AD/A-004 583

FAR-FIELD ANTENNA PERFORMANCE INVESTIGATIONS CONCERNING IN-BAND EFFECTS OF NEAR-FIELD STRUCTURES AND OUT-OF-BAND PHASED ARRAYS

F. L. Cain, et al

Georgia Institute of Technology

Prepared for:

Naval Ship Engineering Center
Naval Sea Systems Command

31 January 1975

REPORT DOCUMENTATION PAGE		READ INSTRUCTIONS BEFORE COMPLETING FORM
1. REPORT NUMBER	2. GOVT ACCESSION NO.	3. RECIPIENT'S CATALOG NUMBER AD/A-004583
4. TITLE (and Subtitle) Far-field Antenna Performance Investigations Concerning In-Band Effects of Near-Field Structures and Out-of-Band Phased Arrays		5. TYPE OF REPORT & PERIOD COVERED Final Engineering Report February 1974-January 1975
		6. PERFORMING ORG. REPORT NUMBER A-1613
7. AUTHOR(s) F. L. Cain, B. J. Cown, E. E. Weaver, and C. E. Ryan		8. CONTRACT OR GRANT NUMBER(s) N00024-74-C-1215
9. PERFORMING ORGANIZATION NAME AND ADDRESS Radar Division, Engineering Experiment Station Georgia Institute of Technology Atlanta, Georgia 30332		10. PROGRAM ELEMENT, PROJECT, TASK AREA & WORK UNIT NUMBERS Project SF 9990140 Task 18079
11. CONTROLLING OFFICE NAME AND ADDRESS		12. REPORT DATE 31 January 1975
		13. NUMBER OF PAGES xxxii plus 311
14. MONITORING AGENCY NAME & ADDRESS(if different from Controlling Office) Naval Ship Engineering Center Naval Sea Systems Command Department of the Navy Washington, D.C. 20360		15. SECURITY CLASS. (of this report) Unclassified
		15a. DECLASSIFICATION/DOWNGRADING SCHEDULE

16. DISTRIBUTION STATEMENT (of this Report)

Approved for Public Release: Distribution Unlimited

17. DISTRIBUTION STATEMENT (of the abstract entered in Block 20, if different from Report)

Same

18. SUPPLEMENTARY NOTES

None

19. KEY WORDS (Continue on reverse side if necessary and identify by block number)

Radar Antennas	Phased Arrays	Dielectrics
Antenna Performance	Out-of-Band Arrays	Coupling
Near-Field Scattering	Statistics	
Obstacles	Median Gain	
Open Masts	Standard Deviation	

20. ABSTRACT (Continue on reverse side if necessary and identify by block number)

This report presents the results of studies involving (1) the effects on far-field antenna performance of obstacles located in the near-field of an antenna, and (2) derivation of statistical models for predicting the out-of-band performance of waveguide phased-array antennas.

In the first area, empirical data were recorded to determine the degrading effects of near-field blocking obstacles and reflecting objects on gain loss (decoupling), beamshift, beamwidth, and sidelobe levels of microwave radar antennas. The data were recorded for two parallel-polarization senses.

Empirical prediction curves were derived as a function of the obstacle's radial distance and angular position relative to the antenna for (1) three sizes of solid cylindrical metal masts, square columns, flat sheets, and corner reflectors, (2) two sizes of open-mast metallic obstacles, and (3) one size of dielectric-coated metal cylinder. An existing computer program for shipboard antenna siting was modified to predict antenna gain loss based on the derived empirical data.

In the second area, a previously-derived basic theoretical statistical model for predicting out-of-band phased-array characteristics was expanded to include arrays of waveguide elements which randomly propagate higher-order modes. Statistical equations were derived to predict and describe the out-of-band radiation pattern characteristics and median gain as a function of the in-band scan angle of the array.

GEORGIA INSTITUTE OF TECHNOLOGY
Engineering Experiment Station
Atlanta, Georgia 30332

FINAL ENGINEERING REPORT

PROJECT A-1613

FAR-FIELD ANTENNA PERFORMANCE INVESTIGATIONS
CONCERNING IN-BAND EFFECTS OF NEAR-FIELD
STRUCTURES AND OUT-OF-BAND PHASED ARRAYS

By

F. L. Cain, B. J. Cown, E. E. Weaver, and C. E. Ryan

CONTRACT N00024-74-C-1215

31 January 1975

Prepared for

NAVAL SHIP ENGINEERING CENTER
CODE 6174D
HYATTSVILLE,MARYLAND 20782
NAVAL SEA SYSTEMS COMMAND 0341
WASHINGTON, D.C. 20360

FOREWORD

Respectfully submitted,

F. L. Cain
Project Director

Approved:

H. A. Ecker
Chief, Radar Division

TABLE OF CONTENTS

TABLE OF CONTENTS (Continued)

LIST OF FIGURES

x

LIST OF FIGURES (Continued)

xiv

LIST OF FIGURES (Continued)

LIST OF FIGURES (Continued)

LIST OF FIGURES (Continued)

LIST OF FIGURES (Continued)

LIST OF TABLES

SECTION I

INTRODUCTION

The topside placement of shipboard antennas to obtain acceptable electromagnetic performance still remains a critical problem. The magnitude of the topside electromagnetic problem arises because of various reasons. Among these are the large number of antennas that must be installed in a limited physical space and the unknown interactions among various antennas due to energy at both in-band and out-of-band frequencies and due to many different obstacles and objects of various geometrical shapes and sizes that exist aboard ships. Although coupling between antennas can sometimes be reduced by taking advantage of blockage due to parts of the ship, the far-field performance of an antenna can be degraded even though such undesired coupling is reduced. Thus, models of both near-field coupling and far-field antenna performance must be considered together when investigating the placement of shipboard antennas. As a result, a concentrated effort by the Naval Ship Engineering Center (NAVSEC) has been under way for several years to systematically use the data and models that have been developed.

Many areas in which additional efforts are required to extend the applicability and usefulness of the prediction methods have been identified. Several of these deficient areas were identified as a result of a three-phase program sponsored by NAVSEC at the Radar Division of the Engineering Experiment Station at Georgia Tech [1,2,3]. That three-phase program, which was largely experimental with the exception of the studies on potential phased-array interference problems, covered several

1

broad categories: (1) refinement of the near-field antenna coupling formula, which included the determination of the effects of main-beam to main-beam antenna coupling with various intervening obstacles present at selected near-field ranges—for both in-band and out-of-band frequencies—and the determination of the effects of main-beam misalignments with and without obstacles present—for both in-band and out-of-band frequencies, (2) determination of the effects of selected near-field obstacles on in-band far-field antenna performance and its correlation to near-field antenna coupling in the presence of intervening obstacles, (3) modification of a computer program for the shipboard siting of antennas to incorporate selected antenna performance data, and (4) phased-array investigations to identify unique problem areas and to study possible techniques to statistically describe antenna characteristics.

Research efforts were subsequently conducted to extend certain important aspects of the work initiated in the previous three-phase program. These efforts are described in this report and involve the following aspects:

(1) extension of the empirically derived antenna performance prediction curves to include both an additional frequency band of operation and the number of near-field obstacles investigated, including those of more complex shape,

(2) incorporation of the antenna performance boresight gain-reduction data (decoupling data) into the existing computer program,

(3) experimental investigations involving an open-mast structure and a dielectrically coated metallic obstacle, and

(4) continuation of the phased-array investigations.

A brief summary of these efforts is given below, and detailed descriptions of each are presented in the following sections. Far-field antenna performance curves were empirically derived to describe the effects of the near-field obstacles on the gain loss (decoupling), beam-shifts, beamwidths, and sidelobe levels. The decoupling data (gain-loss data) were added to the existing computer program. In addition, the computer program was modified to increase the flexibility to (1) permit more convenient and extensive expansion of the gain-loss data files, and (2) permit use of a simplified format for the antenna/obstacle decoupling data. Initial exploratory experiments involving two "open-mast" structures and one dielectrically coated solid metal circular mast were conducted to briefly investigate the effects of these near-field obstacles on the far-field antenna performance. The results indicate that (1) the near-field blockage effects of "open-mast" structures and "solid" obstacles are considerably different, and (2) properly chosen dielectric coatings can be designed to either significantly enhance radar detection and tracking capabilities and/or provide greater isolation between shipboard antennas. The basic statistical model for predicting and analyzing out-of-band EMC/EMI characteristics of future shipboard phased arrays was expanded to become more comprehensive and useful. The effects of out-of-band random variations of the radiation pattern shape and polarization properties of a typical waveguide element were incorporated as inputs to the model to provide more realistic results.

SECTION II

DESCRIPTIONS OF ANTENNAS AND OBSTACLES

A. Test Antennas

The experimental studies that involved the far-field performance of antennas in the presence of near-field obstacles, which were supported under this contract, involved the following three Georgia Tech (GT) antennas:

    (1) GT/AR-4C1,

    (2) GT/AR-PCX, and

    (3) GT/AR-4S1.

All three of these antennas were used in previous near-field investigations involving main-beam to main-beam near-field antenna boresight decoupling tests. Hence, the near-field effects of solid obstacles on the far-field performance of these antennas can be correlated to the previously derived effects on near-field antenna-to-antenna boresight coupling (no near-field antenna-to-antenna coupling involving open masts has been previously conducted). The antennas used in the tests involving the dielectrically-coated cylinder were small pyramidal horn antennas.

The GT/AR-4C1 antenna is a C-band antenna which has a 4-foot paraboloidal dish with a F/D ratio of approximately 0.3 and is fed by a flared waveguide feed. A photograph of the GT/AR-4C1 is shown in Figure 1. The radiation pattern of the GT/AR-4C1 antenna at a frequency of 5500 MHz and for a horizontally polarized signal is shown in Figure 2.

The GT/AR-PCX antenna is an X-band antenna consisting of a cut parabolic cylinder reflector with an offset hoghorn feed that is

5
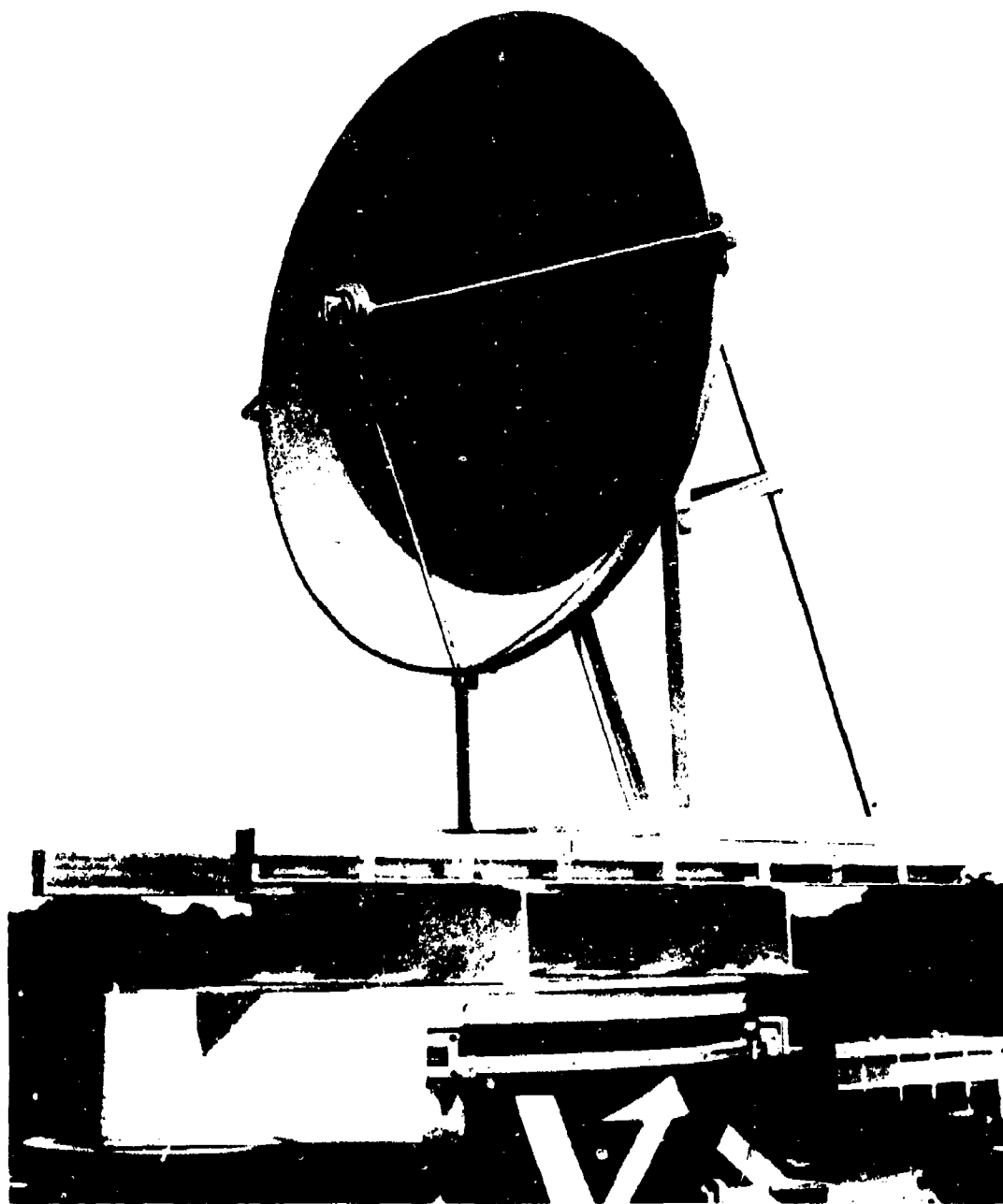
Figure 1. GT/AR-4C antenna mounted on the antenna positioner.
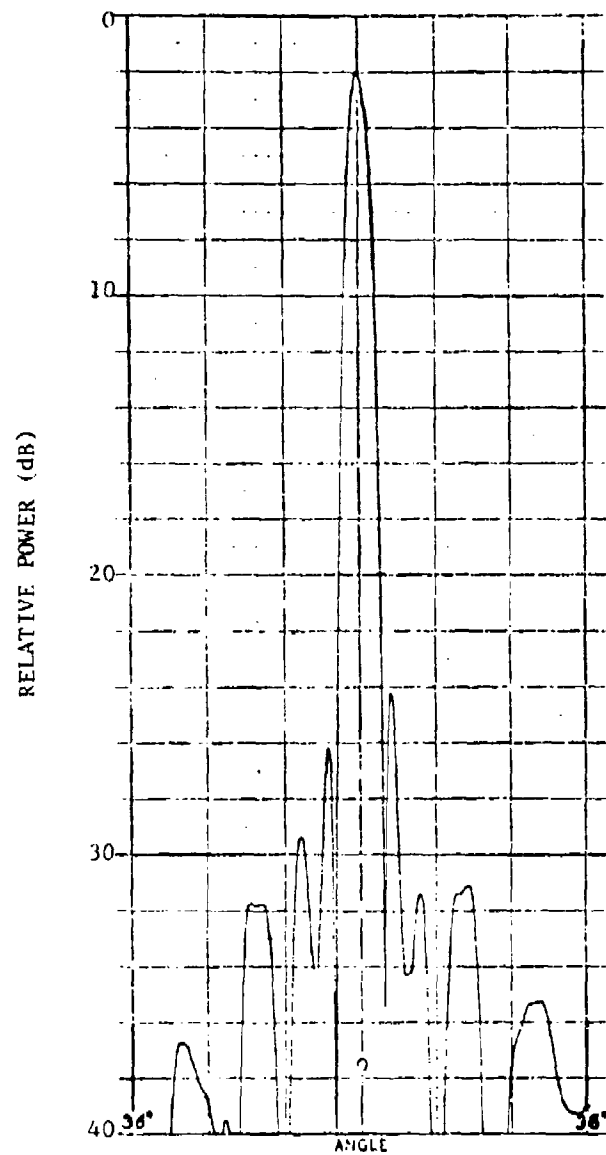
Figure 2. Far-field azimuthal radiation pattern of the GT/AR-4C for horizontal polarization at 5500 MHz. The gain level with respect to an isotropic radiator at the top of the chart is 36 dB.

equipped with "blinders." Blinders are arrays of choke slots which are attached to the E-plane edges of a feed horn to reduce spillover radiation at the sides of reflector antennas. The maximum dimension of this antenna, shown in the photograph in Figure 3, is 4.9 feet. The far-field E-plane pattern of this antenna which was recorded at a frequency of 9600 MHz is shown in Figure 4.

The GT/AR-4S1 is an S-band antenna which has a 4-foot paraboloidal dish with an F/D ratio of about 0.3 and a flared waveguide feed. The appearance of this antenna is essentially the same as that of the GT/AR-4C1, with the exception of the S-band feed horn. The far-field E-plane pattern of this S-band antenna for a frequency of 3000 MHz is shown in Figure 5.

The two pyramidal horn antennas used in the dielectrically-coated cylinder tests were X-band (8.2 to 12.4 GHz) antennas. The aperture dimensions of the transmit and receive antennas were 5.7 by 7.6 inches and 3.0 by 5.0 inches, respectively. The estimated gains of the transmitting and receiving antennas at 10.0 GHz were approximately 22 dB and 19 dB, respectively. The E-plane (5-inch aperture) and H-plane (3-inch aperture) beamwidths of the receiving antenna for parallel polarization were 9.5 degrees and 6.9 degrees, respectively. A photograph of the receiving antenna shown in Figure 6 typifies the appearance of both antennas.

B. Obstacles

The following six different types of obstacles were used in the experimental antenna performance investigations supported under this contract.

8
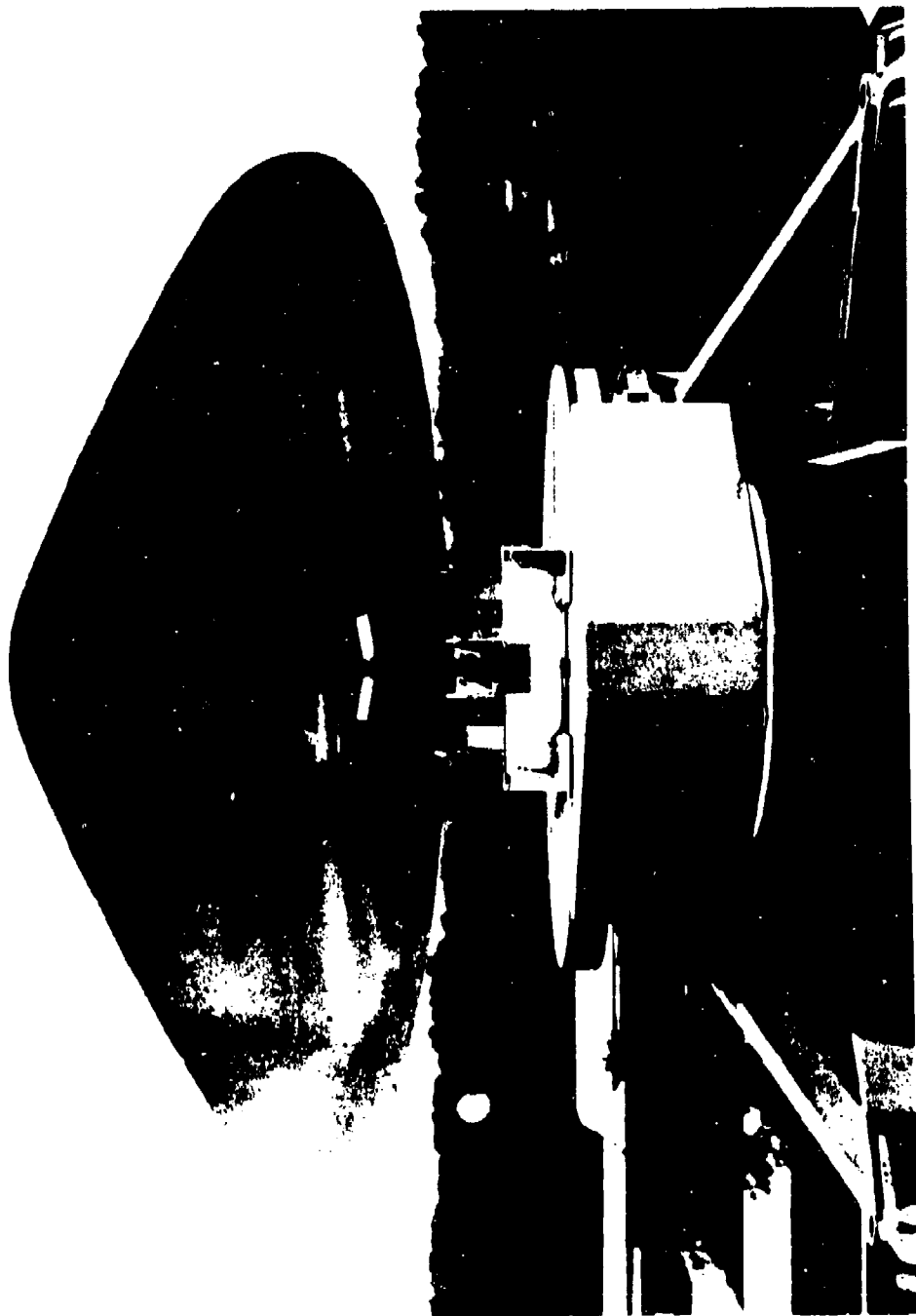
Figure 3.   The GT/AR-PCX antenna mounted on the antenna positioner.

9
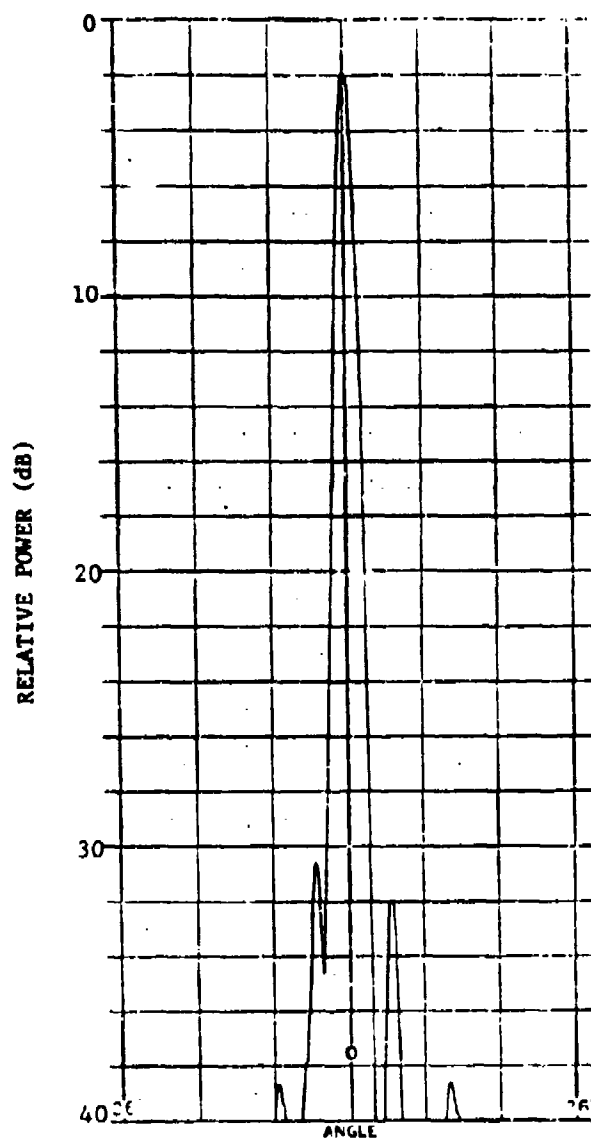
Figure 4. Far-field azimuthal radiation pattern of the GT/AR-PCX for horizontal polarization at 9600 MHz. The gain levels with respect to an isotropic radiator at the top of the chart is 31 dB.
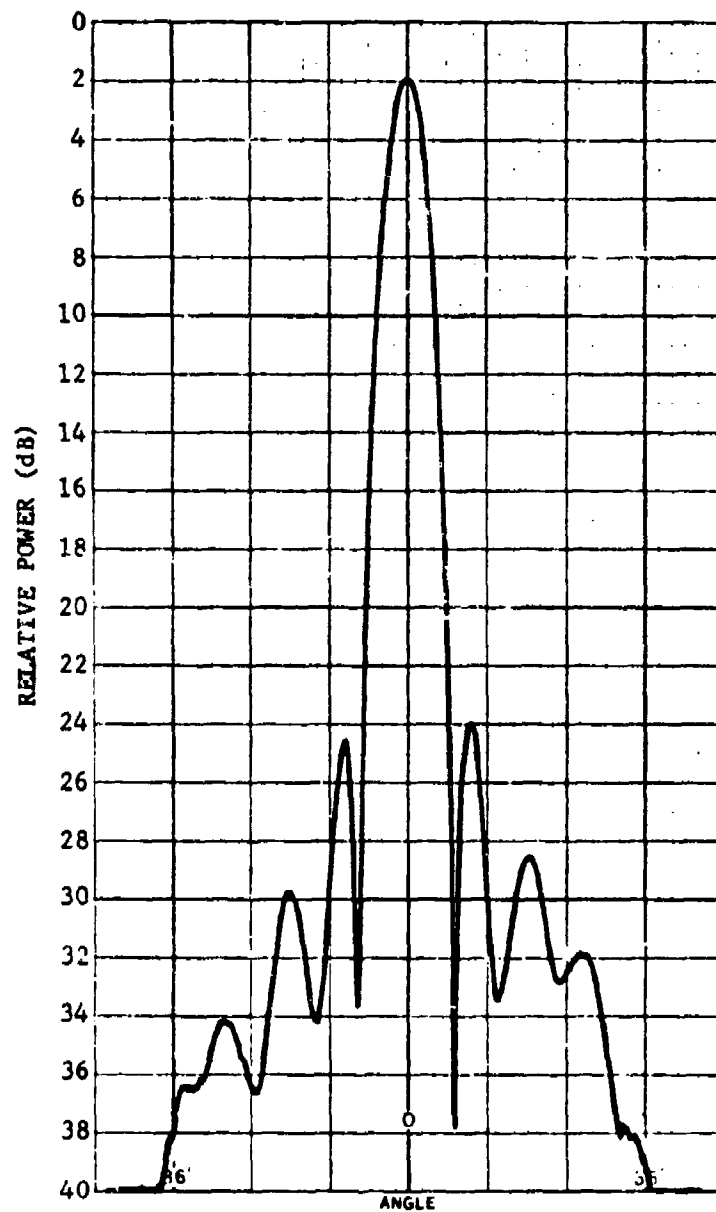
Figure 5. Far-field azimuthal radiation pattern of the GI/AR-4S1 for vertical polarization at 3000 MHz. The gain level at the top of the chart with resepct to an isotropic radiator is 30 dB.
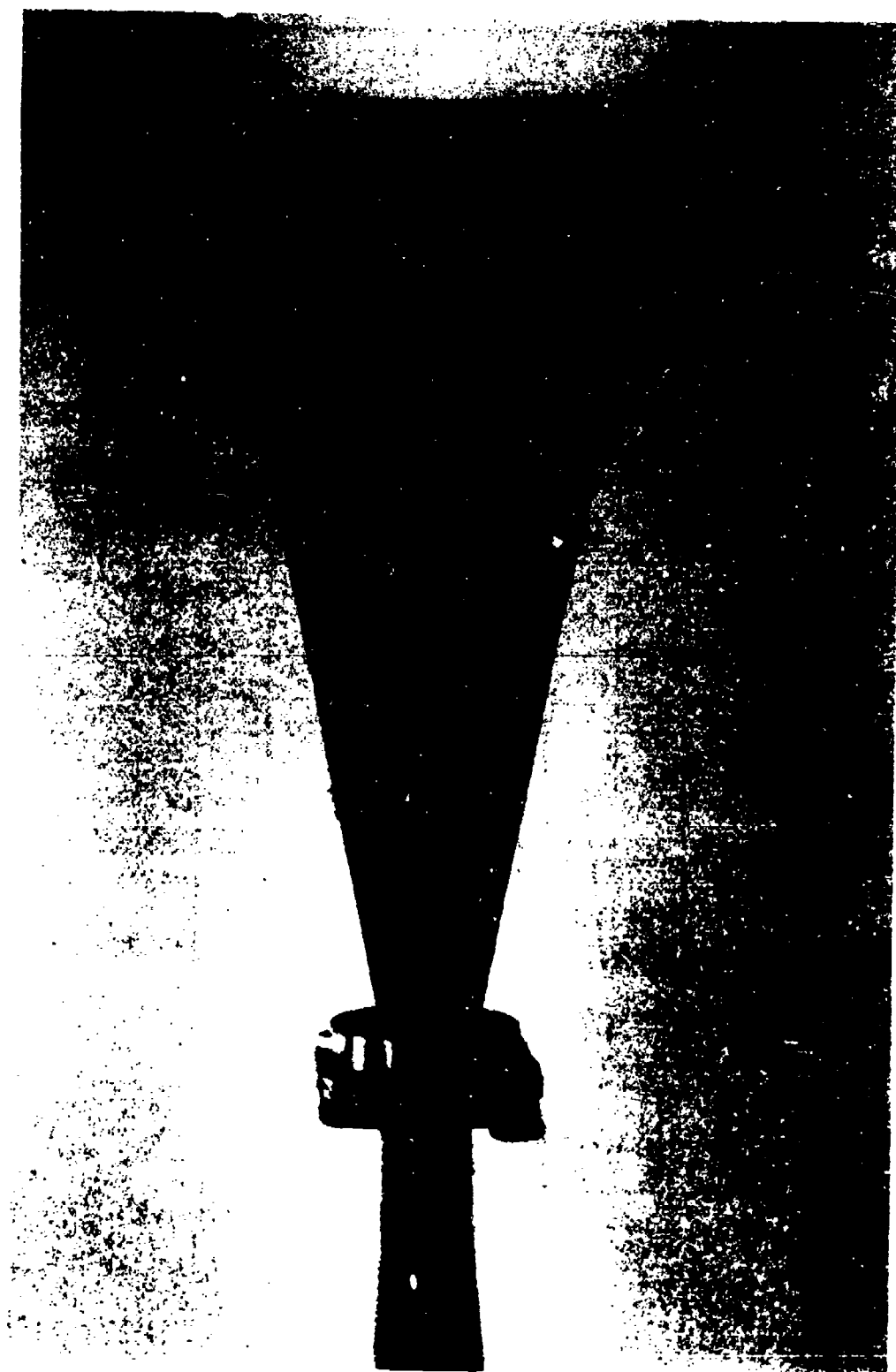
Figure 6. Receiving antenna used in dielectric-coated cylinder tests.

12

1. Circular Metal Masts

Solid metal masts with three different diameters were used: 6-inch diameter, 24-inch diameter, and 48-inch diameter. Each mast was 12 feet high.

2. Flat Metal Sheets

Solid flat metal sheets with three different widths were used: 6-inch width, 24-inch width, and 48-inch width. Each sheet was 12 feet high.

3. 90-Degree Corner Reflector

Solid metal 90-degree corner reflectors with the open side having three different widths were used: 6-inch width, 24-inch width, and 48-inch width. The width of the corner reflector was measured across the open side. Tests with each corner were conducted with the open side both toward and away from the transmitted signal. The corner reflector were designated as Corner No. 1 when the open side was away from the transmitted signal and Corner No. 2 when the open side was toward the transmitted signal. Each corner reflector was 12 feet high.

4. Square Metal Columns

Solid metal square columns with three different widths were used. 6-inch width, 24-inch width, and 48-inch width. The height of each square column was 12 feet high. The flat surface was always parallel with the aperture of the transmitting antenna.

5. Open Masts

Two open-mast structures were fabricated and used: one was 24 inches wide, and the other was 48 inches wide. Each open mast was 12 feet high. The 24-inch wide open-mast structure was constructed of

circular tubing, whereas, flat metal strips were used to construct the 48-inch wide structure. A photograph of these two open masts is shown in Figure 7. A more detailed discussion concerning this selection of open masts is presented in Section VI.

6. Cylinders for Dielectric Tests

A bare metal cylinder and a dielectrically-coated cylinder were constructed for limited experimental tests to investigate the improvement in boresight antenna gain through the use of dielectrics. The bare metal cylinder which was used as a reference was 3.5 inches in diameter and 32 inches high. The dielectrically-coated cylinder, which had an overall diameter of 4 inches, consisted of a 0.25-inch coating of plexiglass on a 3.5-inch diameter metal core. Plexiglass has a dielectric constant and loss tangent of approximately 2.6 and 0.006, respectively. A photograph of the bare metal and dielectrically-coated cylinders is shown in Figure 8.

The selection of the solid metal obstacles was based on the need to investigate basic phenomena associated with typical types of shipboard structures. Technical considerations for these selections are discussed in the Final Report [1] of Contract N00024-71-C-1120. Subsequent Navy programs, such as the Patrol Frigate Electromagnetic Effectiveness Program, emphasized the need for basic antenna performance data involving open-mast structures. To partially fulfill this void, limited tests were conducted with the above two open masts. All of the above obstacles (both solid and open) were used in the tests conducted in S-band, but only the corner reflector, square column, and open-mast obstacles were used in the C-band and X-band tests because the circular
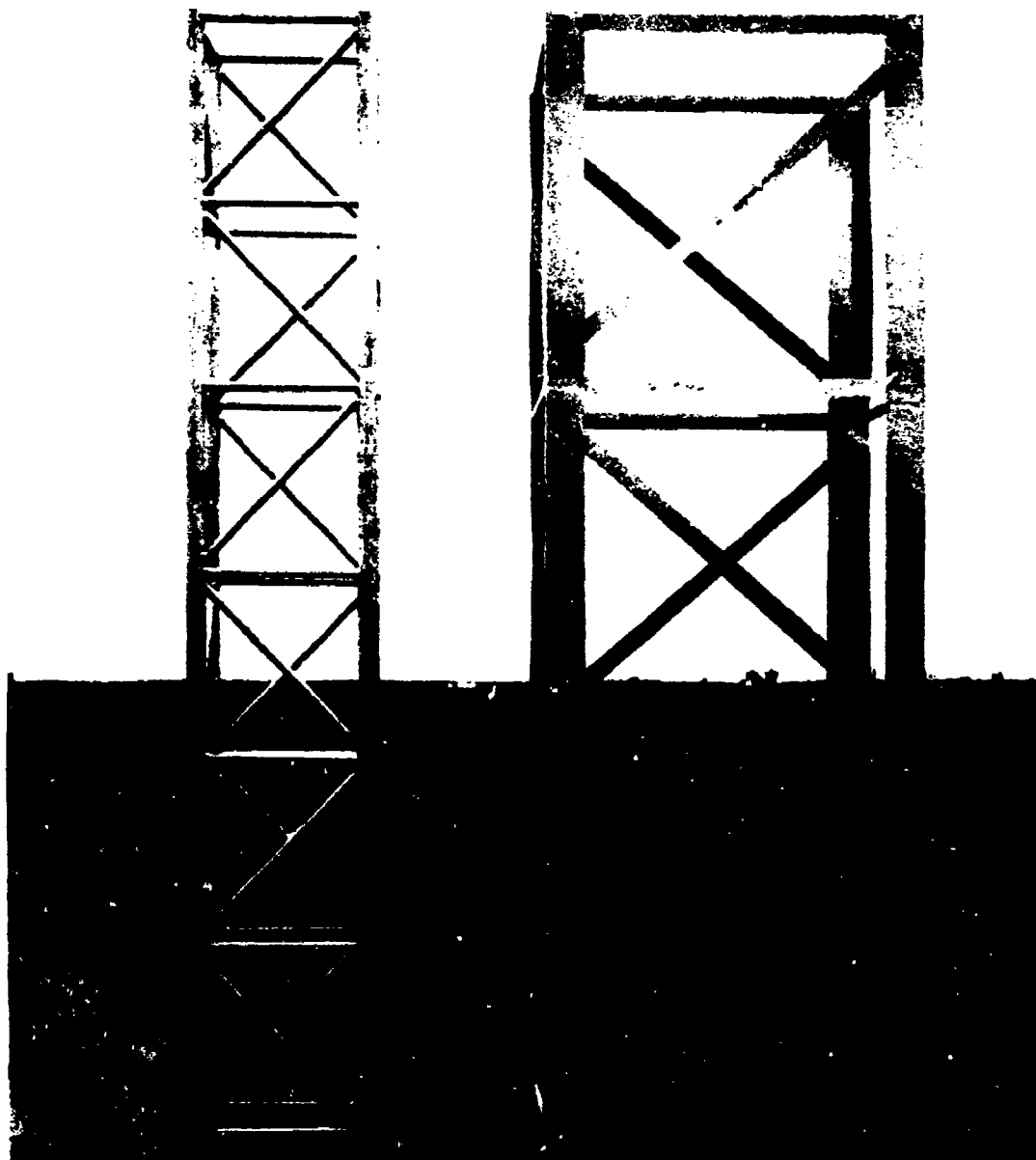
Figure 7.   The 24-inch wide and 48-inch wide open-mast structures
            constructed of circular metal tubing and flat metal
            strips, respectively.
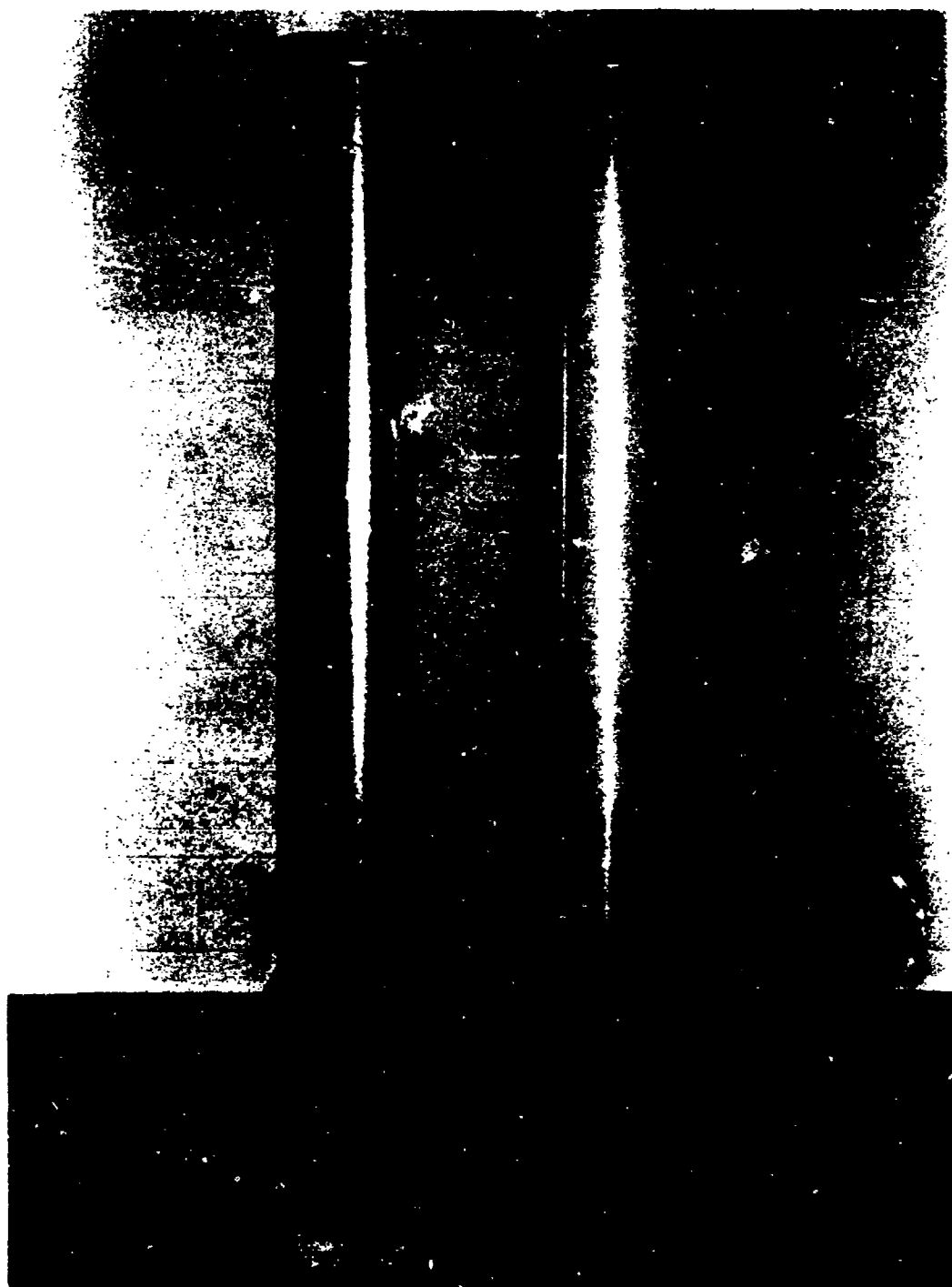
Figure 8. Bare metal reference cylinder and dielectric-coated cylinder used in X-band tests.

masts and flat sheet obstacles were used in similar tests conducted
under Contract N00024-71-C-1120. Because the purpose of the dielec-
trically-coated obstacle tests was to illustrate that an improvement
in antenna gain can be obtained through the use of dielectrics, the
selection of this obstacle was based on the ready availability of
materials and on ease of construction.

SECTION III

INSTRUMENTATION AND MEASUREMENT PROCEDURES

The data were recorded on two different far-field antenna ranges: one was a 700-foot outdoor range and the other was an indoor antenna range. The solid obstacle data and the open-mast data were recorded under controlled conditions on the outdoor range, whereas the data for the dielectrically-coated cylinder were recorded on the indoor range. Descriptions of the instrumentations and the measurement procedures follow.

A. Instrumentation

1. Outdoor Antenna Range

The basic instrumentations at the receiving and transmitting ends of the antenna range are typically illustrated by the block diagrams of Figures 9 and 10, respectively. The antenna receiving site was equipped with an azimuth-over-elevation antenna positioner along with receiving, recording, and data-analyzing equipment. Typical instrumentation for the receiving site for the X-band measurements is illustrated in Figure 9; however, the arrangement was also the same for the C-band and S-band measurements except that the sequence of components consisting of the transition, the variable precision attenuator, the isolator, and the crystal mixer were located between the coaxial cable from the rotary joint and the superheterodyne receiver.

The receiving antenna was mounted on the antenna positioner on top of the tower, and the received X-band RF signal was passed through a precision attenuator and an isolator to a crystal mixer. The IF signal

19
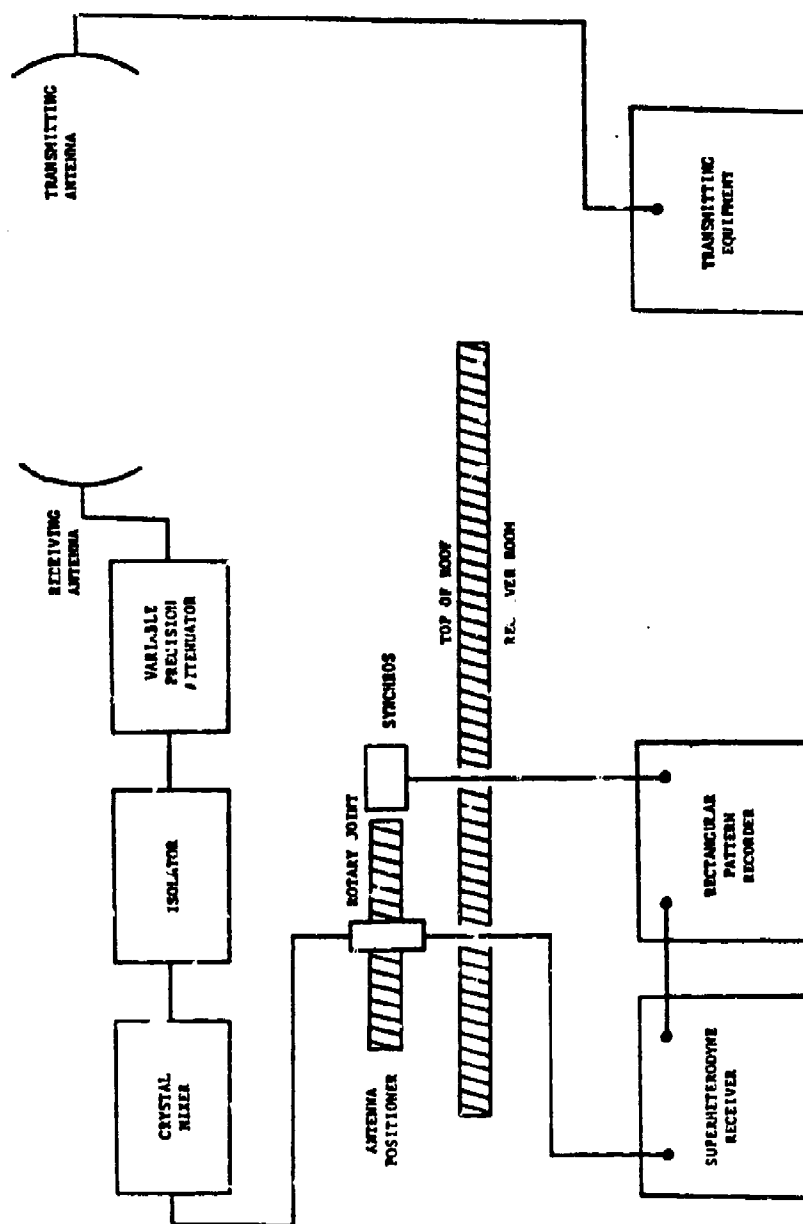
Figure 9. Simplified illustration of typical instrumentation at the receiving end of antenna range.

20
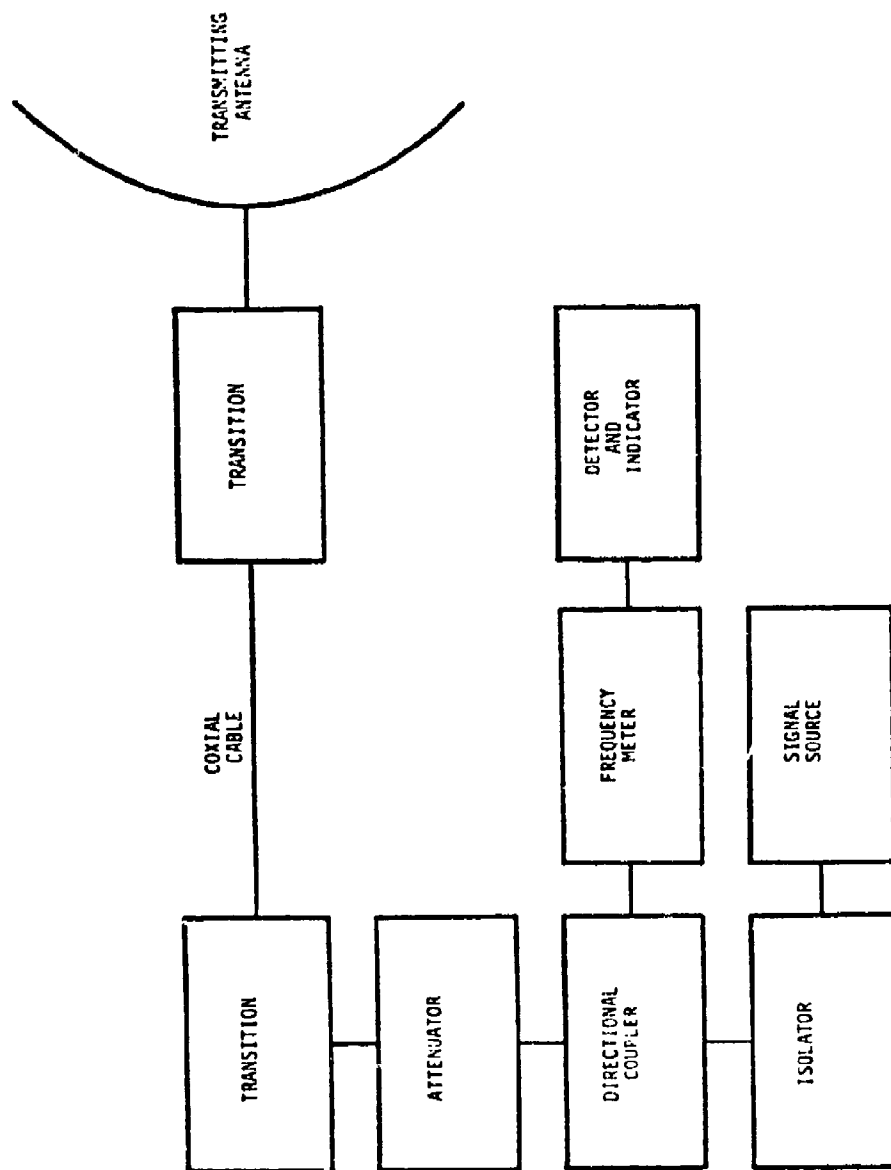
Figure 10. Simplified il stration of typical instrumentation at the transmitting end of antenna range.

at the mixer was passed through a rotary joint at the antenna positioner
to a superheterodyne receiver in the receiver room, and the output of
the receiver was plotted on a rectangular pattern recorder. The C-band
and S-band signals followed the same path as did the X-band signal ex-
cept that the RF signal passed through the rotary joint before reaching
the attenuator, isolator, and crystal mixer, respectively.

The antenna positioner is controlled from the receiver room, and
the position of the chart paper in the pattern recorder is controlled
by a synchro link with the antenna positioner. The positioner controls
are not shown in Figure 9 in order to simplify the illustration. The in-
strumentation arrangement for the transmitting site, as shown in Figure
10, was the same for each of the three frequency bands (S-band, C-band,
and X-band).

2. Indoor Antenna Range

The indoor antenna range instrumentation that was used for the
dielectric-coated obstacle tests is schematically shown in the block
diagram of Figure 11. The X-band sweep generator, which can be preset
to automatically sweep across any desired bandwidth within the 8 GHz to
12 GHz frequency range, generated the signal that was radiated by the
transmitting antenna. When appropriate, the magnitude of the signal
was adjusted either at the source or at the precision attenuator. A
broadband isolator at the output of the generator was used to prevent
any large transient reflections from affecting the output signal or from
damaging the generator. The frequency meter was used to calibrate the
output signal frequency at discrete frequencies within the selected
sweep bandwidth.

22
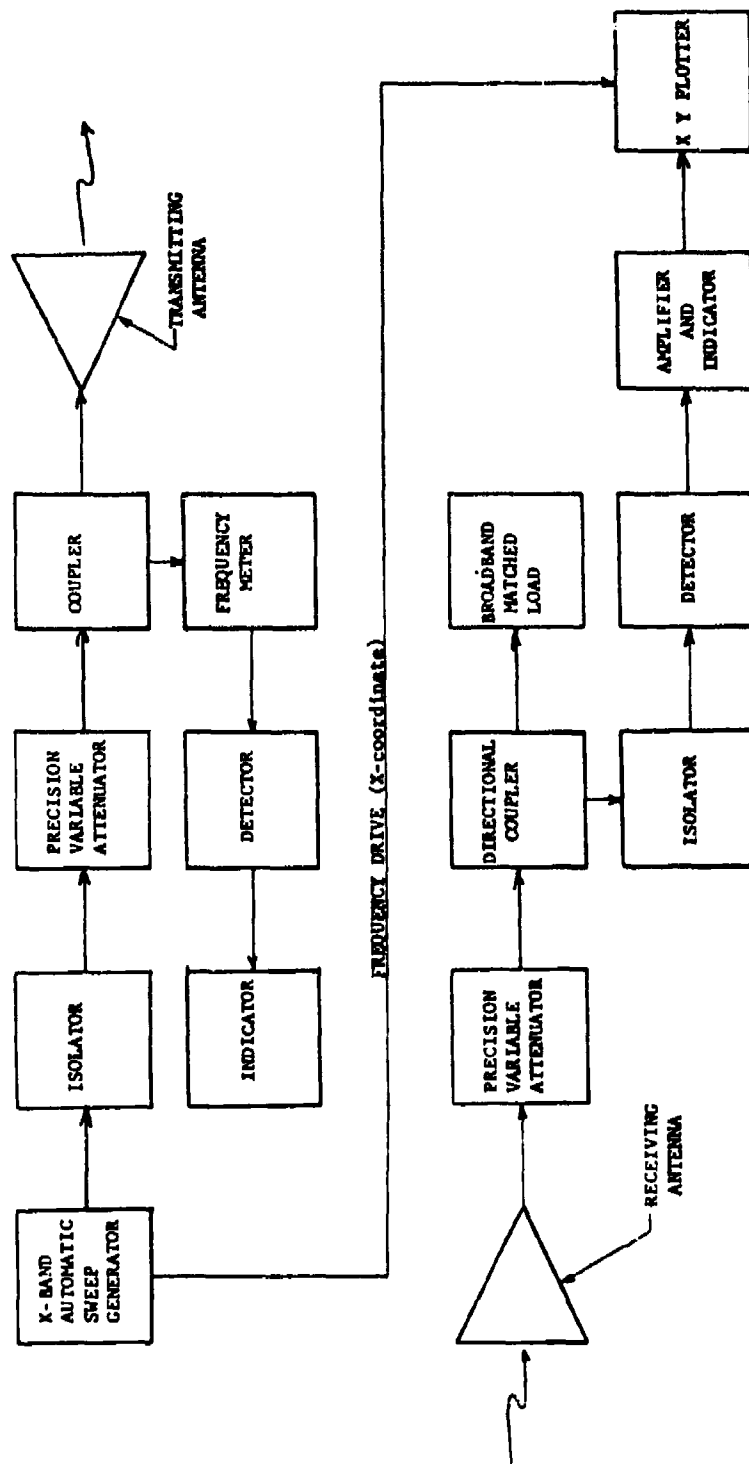
Figure 11. Block diagram of indoor antenna range instrumentation used in dielectric-coated obstacle tests.

At the receiving end of the indoor antenna range, a precision variable attenuator was used for convenience to make small adjustments in the signal level. A directional coupler to tap off a portion of the received signal was used to reduce any interactions between the obstacles blocking the receiving antenna and the detector. An isolator was also used to further damp out any interaction effects. The largest portion of the power intercepted by the receiving antenna was efficiently absorbed in the broadband matched load. The output of the detector was conveniently amplified by the indicating device which then furnished an amplified signal as the driver for the Y-axis of the XY rectangular plotter. The driver for the X-axis (frequency axis) was furnished by the sweep generator, as shown in Figure 11. Consequently, the amplitude of the received signal (Y-axis) was plotted as a function of frequency (X-axis).

B. Measurement Procedures

1. Outdoor Far-Field Procedures

The measurement procedures employed on the outdoor far-field antenna range involved determining the effects of near-field obstacles and objects on the far-field performance of antennas. The transmitting antenna was always located in the far field of the receiving antenna in order to simulate a return signal from a distant target. In these measurements, each obstacle was located at approximately the same distances from the receiving antenna as it was in the corresponding near-field antenna-to-antenna coupling cases investigated under previous contracts [1,2,3]. The antennas and obstacles involved are identified in Section II.

In these tests, the reference receiving-antenna patterns were recorded without an obstacle present to determine the electrical boresight position on the recorded pattern and to obtain a reference level. In all measurements, the aperture of the receiving antenna was located approximately on the axis of rotation of the antenna positioner. After a reference pattern was recorded, an obstacle was placed on bor-sight between the antennas, and then a receiving antenna pattern was recorded over the angular sector of at least $\pm$ 36 degrees from boresight. Each obstacle at each fixed distance from the receiving antenna was then moved in angular increments along an arc whose radius was measured from the center of the aperture of the receiving antenna. The schematic diagram in Figure 12 illustrates the arrangement for the measurement procedure. The photograph of Figure 13 shows a 24-inch mast obstacle at a location on boresight; the transmitting antenna, which is about 700 feet from the receiving antenna, is located on the top edge of the Electrical Engineering Building in the near background. Reference patterns were also taken before, during, and after each sequence of tests for every obstacle to ensure that no variations in the transmitted or received power levels occurred during the measurement sequence.

The obstacle distances from the receiving antenna along each radial direction were varied in major steps of 2 feet, or some multiple, from approximately 4 feet from the aperture of the receiving antenna to a maximum of approximately 20 feet from the aperture of the receiving antenna. At each major obstacle distance, the obstacle was moved in discrete incremental steps about that particular point, and data were recorded for three or four incremental steps about each major obstacle

25
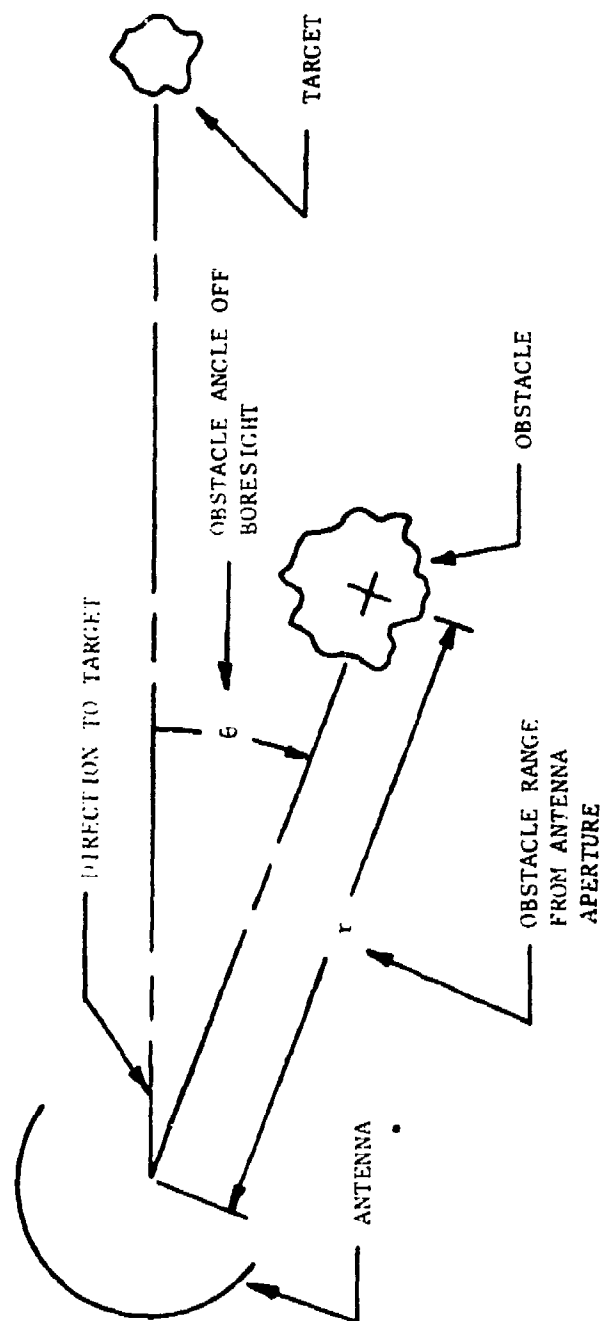
Figure 12. Simplified schematic illustrating far-field performance test variables for a simulated target return.
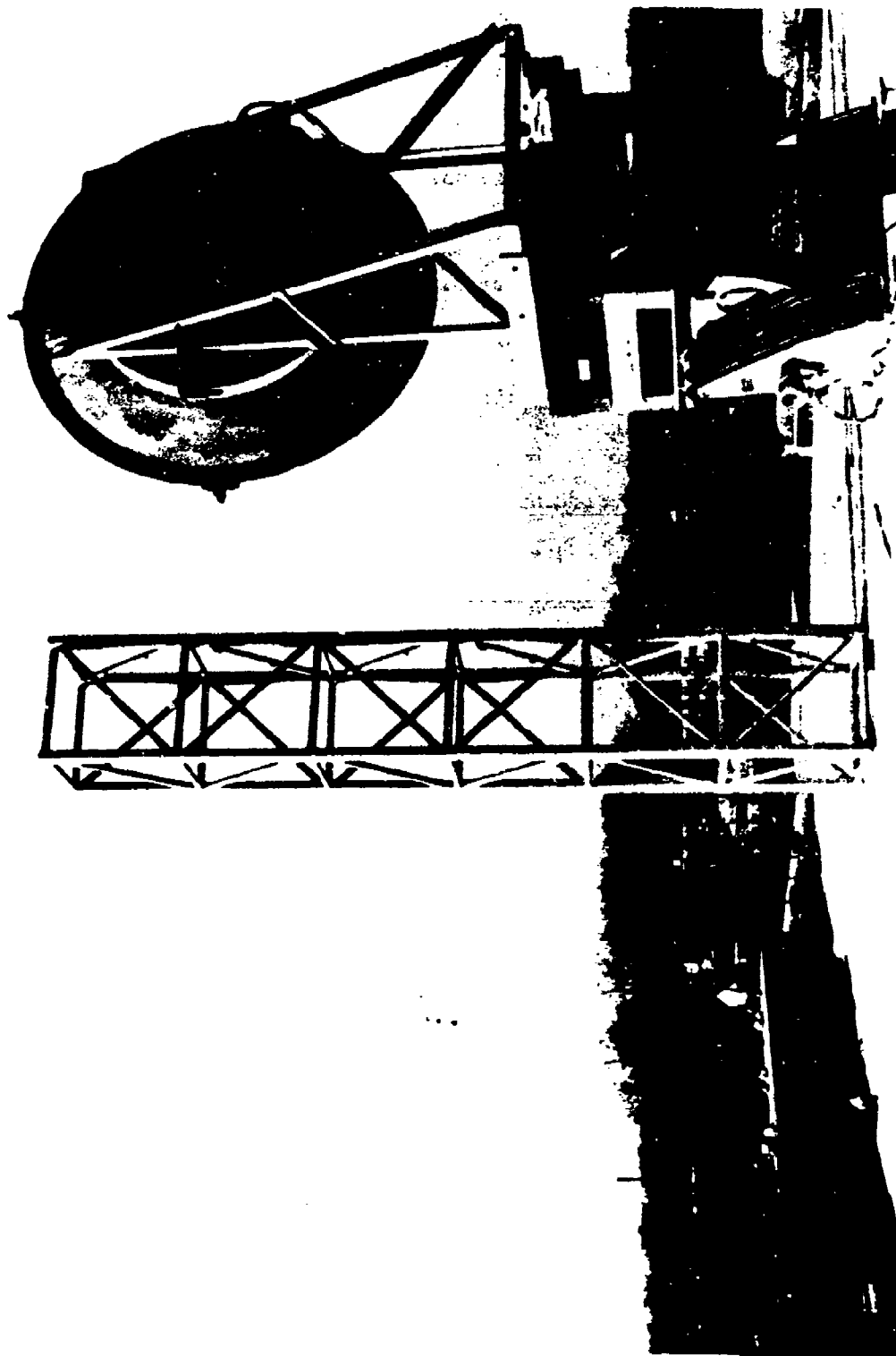
Figure 13. A view of the receiving antenna and the 24-inch wide open-mast structure located on boresight in a far-field antenna performance test.

distance to obtain an average value. Because the decoupling varied periodically as a function of obstacle distance, this procedure produced an envelope from which the maximum variation from the average decoupling value could be determined. The reduction of the maximum received power level due to an obstacle was termed decoupling (or gain loss). In addition, sidelobe, beamwidth, and beamshift information also was recorded as a function of obstacle angle off the boresight direction for these incremental steps. Whenever necessary, the beamwidths for a series of incremental steps were averaged, as discussed in Section V.

2. Indoor Far-Field Procedure

The measurement procedure employed on the indoor far-field antenna range was designed to demonstrate that an improvement in the far-field performance of an antenna in the presence of a solid near-field metallic obstacle can be achieved by coating the obstacle with the appropriate dielectric material. To simulate the return from a distant target, the receive antenna and obstacle always were located in the far field of the transmitting antenna, as indicated in Figure 14 for the highest test frequency used. The cylindrical test obstacles which were placed vertically on a styrofoam mount, also shown in Figure 14, were located along the boresight direction at three different discrete distances (13 inches, 24 inches, and 35 inches) from the receive antenna during the various tests. For each of the three discrete obstacle distances, swept-frequency measurements were recorded.

The swept-frequency procedure involved three steps. Each of the three steps was performed for both linear parallel polarization states:
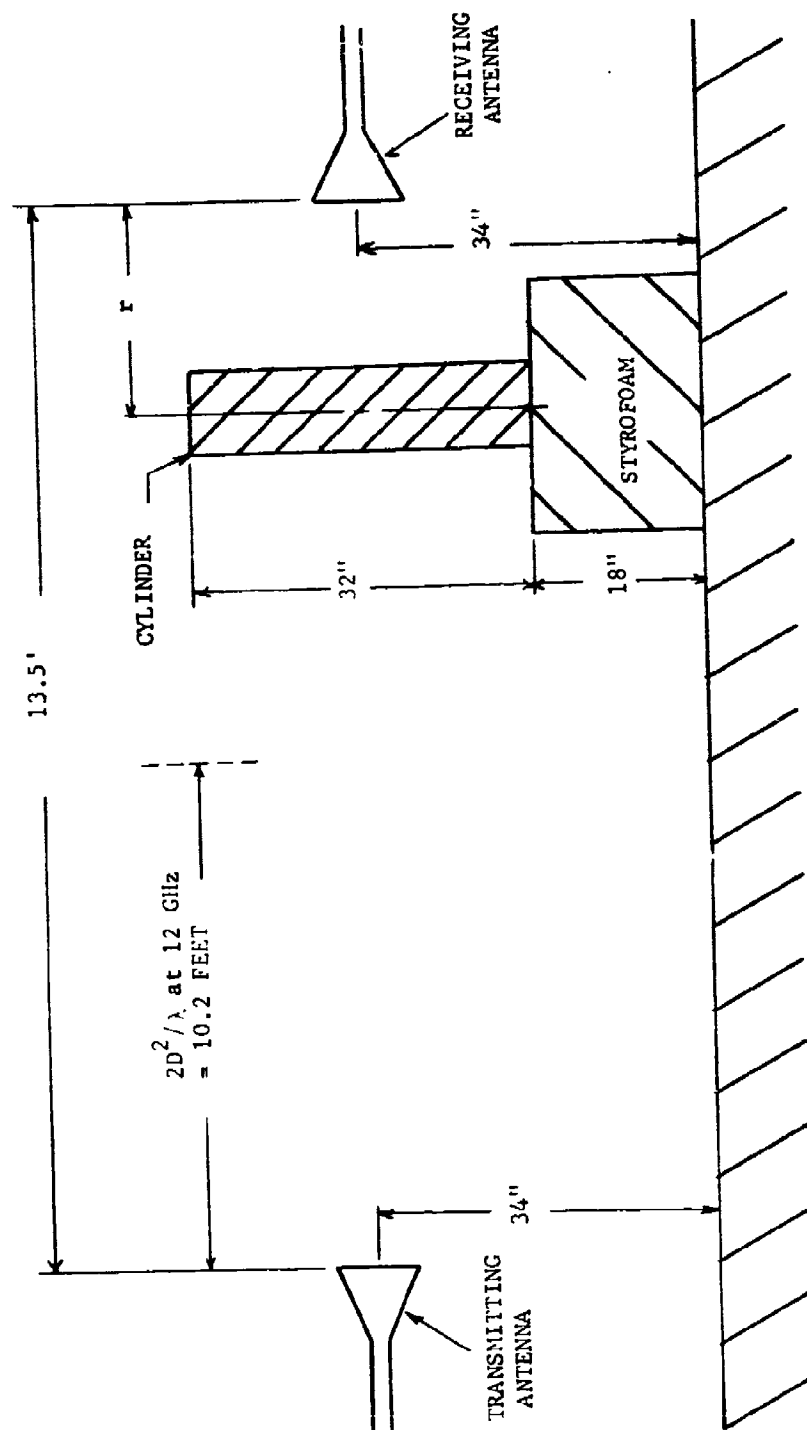
Figure 14. Sketch illustrating antenna range configuration for obstacle measurements involving bare metal and dielectric-coated cylinders.

29

(1) horizontal-transmit horizontal-receive, and (2) vertical-transmit vertical-receive. First, the received power level as a function of frequency (8 GHz to 12 GHz) was recorded as a calibration reference signal. Next, the metallic cylinder was inserted at each of the three positions along the boresight direction of the receiving antenna, and the swept-frequency measurements were again recorded. Finally, the dielectric-coated metallic cylinder was positioned at the same positions as those for the bare metal cylir 'er, and the swept-frequency measurements were again repeated. From the results of these three steps, (1) the effects of the bare metal obstacle on the gain of the receiving antenna was determined, (2) the effects of the dielectric-coated obstacle on the gain was determined, and (3) the differences (improvements) between the bare metal and dielectric-coated obstacles were determined.

When using the swept-frequency measurement technique, small perturbations on each received power versus frequency curve due to interactions between the bare metal (or coated) cylinder occurred. Additional measurements at discrete frequencies (8 GHz, 9 GHz, 10 GHz, 11 GHz, and 12 GHz) were recorded for very small incremental movements about the major obstacle locations from the receive antenna (13 inches, 24 inches, and 36 inches) to verify that the perturbations were the usual deviations from the average curve (curve in which no interactions would occur). The origin of these perturbations due to interactions between the obstacle and antenna is the same as that which is discussed in Section IV as well as in previous reports [1,2,3] for the larger metal obstacles. Therefore, the swept-frequency measurement procedure described above was validated and used.

SECTION IV

MEASUREMENT SENSITIVITY AND REPEATABILITY

A. Introduction

Measurements of far-field antenna performance in the presence of near-field scattering obstacles or reflecting objects have previously been performed only on a limited basis [1]. However, these far-field antenna performance measurements, as well as the near-field antenna-to-antenna coupling measurements previously performed under other contracts [2,3] indicate that the distortion effects due to near-field obstacles are potentially sensitive to precise obstacle position and/or obstacle orientation. Consequently, in order to establish realistic measurement tolerances, it is both necessary and desirable to determine the possible effects on antenna performance data due to small errors in position or orientation of an obstacle. Additionally, a knowledge of the significance of obstacle orientations which differ considerably from the intended test orientations can provide useful insight into distortion effects that often arise in various situations but are not explicitly displayed in the empirically-derived curves.

Although it is not feasible to perform measurements that correspond precisely to every conceivable shipboard situation, brief exploratory investigations were undertaken to investigate the sensitivity and repeatability of the data due to positioning and orientation errors. These investigations involved the following three types of tests:

    (1) small incremental movements of an obstacle along a particular radial direction,

(2) lateral displacements of an obstacle in small incremental

distances in a path perpendicular to the particular radial

direction, and

(3) rotation of an obstacle about its vertical axis which is

perpendicular to the particular radial direction.

The measurements of Test (1) were performed for all solid and open-

mast obstacles for all three test frequencies and polarizations (ver-

tical and horizontal polarizations for 3000 MHz and 5500 MHz, but only

horizontal polarization for 9600 MHz). The measurements of Tests (2)

and (3) were conducted for selected 24-inch and 48-inch obstacles at

the frequency of 5500 MHz for both linear parallel polarizations and

for the 48-inch open mast at the frequency of 9600 MHz for horizontal

polarization. Because no significant variations for any of the 6-inch

obstacles occur at any of these three frequencies if reasonable mea-

surement guidelines are observed and followed, no 6-inch obstacle tests

were conducted.

B. Discussion of Test Results

1. Small Incremental Movements along Boresight and Other Radial Directions

The decoupling values due to the obstacles varied somewhat

with small incremental movements of the obstacles along various radial

directions from the receiving antenna, particularly the boresight di-

rection. Along boresight, these variations from the average decoupling

levels are due to interaction between the receiving antenna and the ob-

stacle and result in a standing wave phenomena. All of the obstacles

exhibited the variations to some extent, with the smallest obstacles

32

having the smallest peak-to-peak variation. For any given obstacle, frequency, and polarization, the peak-to-peak variation in decoupling was progressively smaller either as the obstacle distance along a given radial direction from the antenna increased or as the angle off boresight increased. The repeatability of the measurements for a given obstacle was always within a particular envelope of variations. In order to derive the most reliable empirical decoupling curves, measurements of this type were recorded during the entire course of the program to determine the envelope of the variations for each obstacle at each selected major obstacle distance, as previously described in Section III. The values of the variations from the average decoupling curves are discussed further in Section V.

2. Lateral Displacements

Both C-band and X-band lateral displacement tests were conducted. Several C-band lateral displacement tests for selected solid and open-mast obstacles were conducted at selected angles and radial distances from the receiving antenna, but only one series of tests at X-band with the 48-inch open mast was conducted. Information about the particular tests conducted and the results of those tests are given in the following paragraphs.

C-band tests for all of the 24-inch solid obstacles were conducted at obstacle locations of 4 feet and 8 feet along both the boresight radial and the 10-degree radial directions. Because the sensitivity decreased significantly not only as the obstacle distance from the antenna increased but also as the obstacle angle off boresight increased, tests at obstacle angles larger than 10 degrees off boresight were not

33

conducted. For lateral displacements of 4 inches off the boresight radial direction, approximately 0.5 to 1 dB decrease in decoupling and a slight broadening of the main beam on the order of a few tenths of a degree generally appeared to occur. Lateral displacements of 4 inches off the 10-degree radial vector did not appear to cause a noticeable change in the decoupling level or beamwidth. The tests at the 10-degree angle showed that the data were only slightly sensitive to small lateral displacements of 4 inches or less. Neither a well-defined beamshift nor a significant change in sidelobe level could be discerned for small lateral displacements about either the boresight or 10-degree radial line, although a slight asymmetry in the received pattern for the lateral displacements about the boresight radial direction occurred.

C-band lateral displacement tests for all of the 48-inch solid obstacles were conducted at a distance of 4 feet from the antenna on the boresight radial direction, but tests for only the 48-inch Corner Reflector No. 1 at a distance of 4 feet were conducted for the 10-degree radial direction. Because the tests with the 24-inch obstacles indicated that the sensitivity to lateral displacements and repeatability of measurements are the most critical at a distance of 4 feet along the boresight radial direction, tests with the 48-inch obstacles at larger obstacle distances and angles off boresight were not conducted. Lateral displacements of about 2 inches off the boresight radial direction and off the 10-degree radial direction caused the decoupling level to decrease approximately 2 to 3 dB and 1 dB, respectively. Although the beamshift and beamwidth boresight tests did not exhibit any well-defined trends for these small lateral displacements, the received antenna pattern was

unsymmetrical. For the tests at the 10-degree radial direction, no discernible changes in beamwidth, beamshift, or sidelobe levels occurred.

For open masts, the C-band lateral displacements of 2 inches at positions along the boresight radial direction for either the 48-inch wide or the 24-inch wide open mast did not cause noticeable effects on the antenna performance parameters. No C-band tests for either of the two open masts were conducted for obstacle angle off the boresight direction. For lateral displacements of about 12 inches about the boresight direction, the C-band measured decoupling for the 48-inch open mast increased approximately 1 dB, a slight narrowing of the main beam appeared to occur, and increases in sidelobe levels up to approximately 15 dB occurred. The changes in sidelobe levels varied with polarization and obstacle distance from the receiving antenna. For the 12-inch lateral displacement, no beamshifts were readily apparent. No tests for large lateral displacements were conducted for the 24-inch open mast.

X-band lateral displacement tests with the 48-inch open mast were conducted at a distance of 12 feet along the boresight direction only. The major reason for conducting these X-band lateral displacement tests was to investigate the main-beam asymmetry that occurred when the 48-inch open mast was centered at various distances along the boresight direction. To determine if the asymmetry was due to a slight error in boresight alignment, several lateral displacement tests for distances up to one inch off the boresight direction were performed. For these lateral displacements, no significant pattern differences were apparent. Other special tests, in addition to the obstacle rotation tests presented in the following subsection, are discussed in Section VI.

35

Because positioning accuracies of less than an inch can be achieved, the sensitivity of distortion effects due to small lateral displacements of any of the obstacles tested did not present a problem in measurement accuracy or repeatability.

3. Obstacle Rotations

Antenna performance tests to determine the effects of slight rotation of an obstacle about its vertical axis on obstacle sensitivity and measurement repeatability were performed at 5500 MHz (C-band) for various obstacle distances and angles off boresight direction and at 9600 MHz (X-band) only for the 48-inch open mast at one distance on the boresight direction. For both the 24-inch open mast and the 24-inch solid obstacles (corner reflectors and square column), C-band rotation tests were performed for obstacle locations of 4 feet and 8 feet along both the boresight and the 10-degree radial directions. For the 48-inch open mast and 48-inch solid obstacles (corner reflectors and square column), C-band tests were performed for the 4-foot obstacle-distance along the boresight radial direction. Additional C-band rotation tests for the 48-inch Corner Reflector No. 1 were conducted for an obstacle distance of 6 feet along the boresight, 5-degree, 10-degree, 20-degree, 30-degree, and 40-degree radial directions. The X-band tests were conducted at 12 feet on boresight.

C-band rotational data for the 24-inch and 48-inch solid obstacles were measured for maximum obstacle rotations of 5 degrees because positioning accuracies of less than 1 to 2 degrees are easily maintained during the course of normal tests. For rotations of 5 degrees or less, no discernible changes in the antenna performance characteristics due to

rotation of either the 24-inch solid obstacles or the 24-inch and 48-inch open masts occurred for obstacle locations along boresight and 10-degree radial directio.. Notceable changes did occur, however, for 5-degree rotations of the 48-inch wide square column and corner reflectors. For the maximum rotation of 5 degrees, the decoupling levels for the two 48-inch corner reflector obstacles decreased about 2 dB, whereas, the decoupling level for the square column increased about 2 dB. In adidition, small beamshift and beamwidth changes on the order of $\pm$ 1 degree appeared to occur, but well-defined trends related to the obstacle type or polarization were not apparent. Although small changes of about $\pm$ 1 dB in the sidelobe levels occurred, the exact changes in sidelobe levels depended on the polarization and obstacle type, and no well-established trends were observed. The results of the 5-degree rotation tests for the 48-inch Corner Reflector No. 1 for the 4-foot obstacle-distance along the various radial directions showed a rapidly diminishing sensitivity as obstacle angle off boresight was increased.

The X-band rotational tests with the 48-inch open mast at 12 feet on boresight were conducted for obstacle rotation angles 5 degrees, 10 degrees, and 15 deg.ees. Although no major changes occurred for any of the rotation angles, the overall shape of the distorted pattern did appear to improve slightly. Other X-band special tests concerning pattern shape will be discussed in Section VI.

Based on the results of the three different types of tests discussed under Headings 1, 2 and 3 above, the measured data were repeatable to within small tolerances, which depend on obstacle size and location. The small deviations in positioning or orientation of the test obstacles

37

that occurred during the course of the measurement program were smaller than the relatively extreme situations described in this section, with the exception of the small incremental movements along a radial direction which are necessary in the near-field test situations encountered. Consequently, the results are repeatable to within the envelope of the variations caused by the standing wave or reflection phenomena.

SECTION V

ANTENNA PERFORMANCE DISPLAYS FOR SOLID OBSTACLES

A. Introduction

The ability to predict the effects of obstacles in the near field
of an antenna on the far-field performance of that antenna is an im-
portant capability for improving the electromagnetic effectiveness of
future topside ship designs. The objective of the work reported in
this section is to extend both the knowledge and the range of useful-
ness and applicability of techniques previously developed [1]. Exten-
sive experimental efforts dealing with near-field antenna-to-antenna
coupling in the presence of intervening near-field obstacles previously
were conducted [1,2,3], but only very limited efforts concerning the
effects of those same near-field obstacles on the far-field radiation
characteristics of antennas were conducted. Consequently, additional
far-field antenna performance data were obtained not only to assess the
ability of an antenna to perform its designated function in the pres-
ence of obstacles but to provide the capability to correlate far-field
antenna performance to near-field antenna-to-antenna coupling in the
presence of the same obstacles.

Antenna performance cannot be ignored when one attempts to reduce
electromagnetic interference. Obviously, when the EM engineer considers
a potential antenna location which would minimize the interference with
other antennas or equipment, he cannot locate the antenna at a position
in which obstruction effects would seriously degrade the performance of
the associated equipment even though antenna interference would be

39

minimized. For example, the position of the null of a monopulse or a conically scanned antenna is very important in a tracking mode. Consequently, if an obstacle were located on one side of the line-of-sight between the target and the antenna, the obstacle would affect the return signal from the target more on one side of the antenna pattern than on the other side. Therefore, the pattern null would shift, and a tracking-angle error would result.

To determine the magnitude of the detrimental effects that can be caused by nearby obstacles, a series of antenna performance experiments involving various obstacles at several ranges were conducted for in-band frequencies. The same objects that were used in the corresponding antenna-to-antenna near-field coupling tests were used in the far-field performance tests; however, the transmitting antenna was in the far field since the return signal from a target was simulated. Furthermore, in these tests, it was necessary to rotate the receiving antenna to determine the degradation of the complete main beam as well as the close-in sidelobes. For each distance that each obstacle was located from the receiving antenna, each obstacle was moved along an arc of constant radius from the receiving antenna so that the distortion effects could be determined as a function of obstacle angle.

The effects of the various near-field obstacles on the far-field performance of an antenna are characterized in terms of decoupling (antenna gain loss), beamwidth, beamshift, and close-in sidelobe levels. In many situations, particularly when the width of the near-field obstacle is comparable in size to the aperture of the antenna, the distortion effects on the clear-site antenna pattern are very complex. The

inherent complexity which often occurs demands the use of engineering judgments in interpreting and using these far-field antenna performance descriptors. Use of the various empirical curves should be guided by the radar system accuracy requirements. In general, if all the appropriate empirical performance curves and tables for a given situation are properly interpreted, an engineering description can be obtained.

In this section, data which display the effects of obstacles on the antenna characteristics cited above are presented. In general, each type of data is arranged with increasing frequency, and where appropriate, the order of data is with decreasing size of obstacle. Various trends of the above antenna characteristics can be observed from the data. The major trends of the data, many of which are similar to those reported previously [1], will be pointed out in the following subsections.

B. Main-Beam Boresight-Decoupling Displays

The main-beam boresight-decoupling data are displayed in two different formats. In the first format, displays are presented that permit easy visualization of the manner in which the decoupling values change with increasing obstacle distance from the receiving antenna and that permit easy comparison with near-field antenna-to-antenna boresight decoupling. In the second format, displays with near-field obstacle distance as the parameter are presented that portray the decoupling values as a function of the angle at which the near-field obstacle is removed from the boresight direction.

41

1. Decoupling along Boresight

In Figures 15 through 25, the boresight decoupling for all three sizes of the indicated obstacles is displayed as a function of the obstacle distance, r, from the receiving antenna normalized in far-field units of $2D^2/\lambda$, where D is the horizontal dimension of the receiving antenna and λ is the operating wavelength. The curve parameter for the obstacles is the width of the particular obstacles, W, normalized in terms of the horizontal dimension of the receiving antenna. In Figures 15 through 22, the boresight decoupling for both horizontally and vertically polarized signals is displayed in each figure. In Figures 23 through 25, however, the decoupling for only horizontally polarized signals is displayed because the receiving antenna is not adaptable for operation for other polarizations. In addition to the curves at S-band (3000 MHz) for the corner reflectors and square column reflectors, boresight decoupling curves for the sheet and mast obstacles also are included. Curves for the sheet and mast obstacles for the C-band (5500 MHz) and X-band (9600 MHz) frequencies were reported previously [1].

The overall trend of the data displayed in Figures 15 through 25 is apparent. Some of the individual trends that are obvious are the following. In most cases, greater decoupling occurs for vertically polarized signals than for horizontally polarized signals, but the difference generally decreases as the size of an obstacle decreases. In all cases, the decoupling levels are larger for larger size obstacles than for smaller size obstacles. The slopes of the decoupling curves generally tend to be negative, that is, the decoupling values decrease as the

42
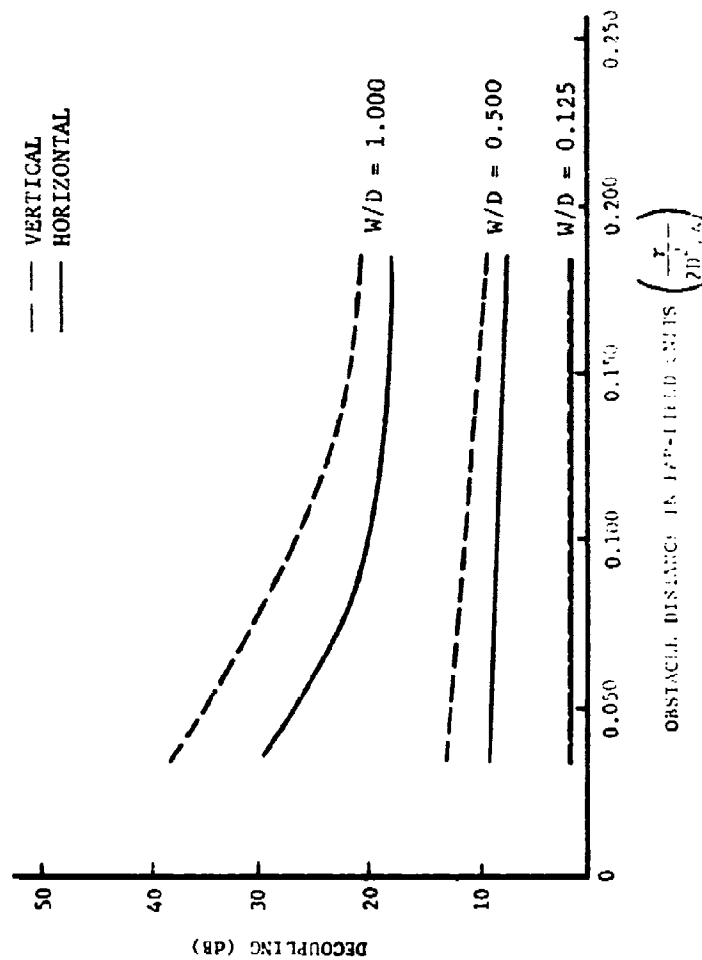
Figure 15. Average boresight decoupling as a function of obstacle distance along boresight direction (target direction) for receiving antenna aperture D for the Mast obstacles of widths W for vertically and horizontally polarized signals at a frequency of 3000 MHz. Receiving antenna is in far field of target.

43
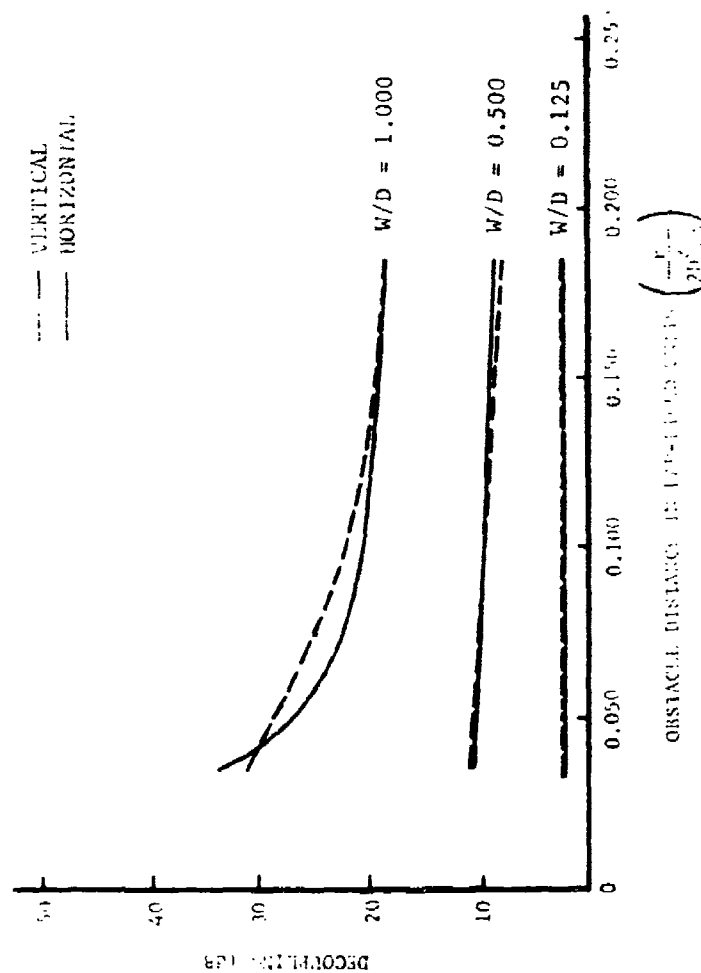
Figure 16. Average boresight decoupling as a function of obstacle distance along boresight direction (target direction) for receiving antenna aperture D for the Sheet obstacles of widths W for vertically and horizontally polarized signals at a frequency of 3000 MHz. Receiving antenna is in far field of target.

44
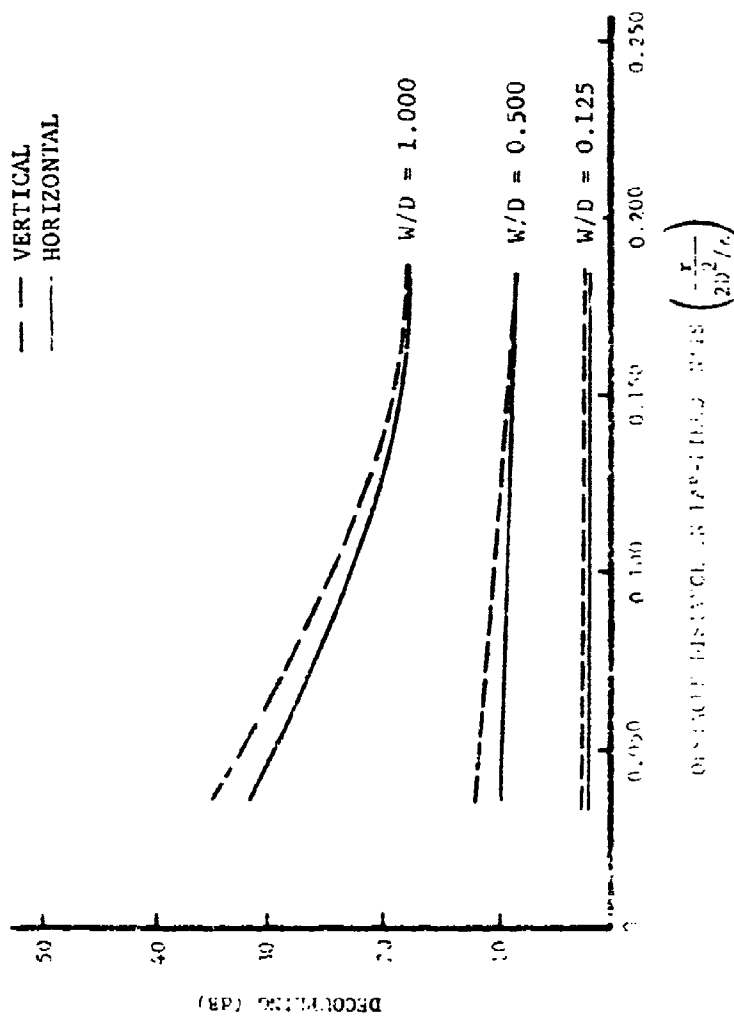
Figure 17. Average boresight decoupling as a function of obstacle distance along boresight direction (target direction) for receiving antenna aperture D for the Corner No. 1 obstacles of widths W for vertically and horizontally polarized signals at a frequency of 3000 MHz. Receiving antenna is in far field of target.
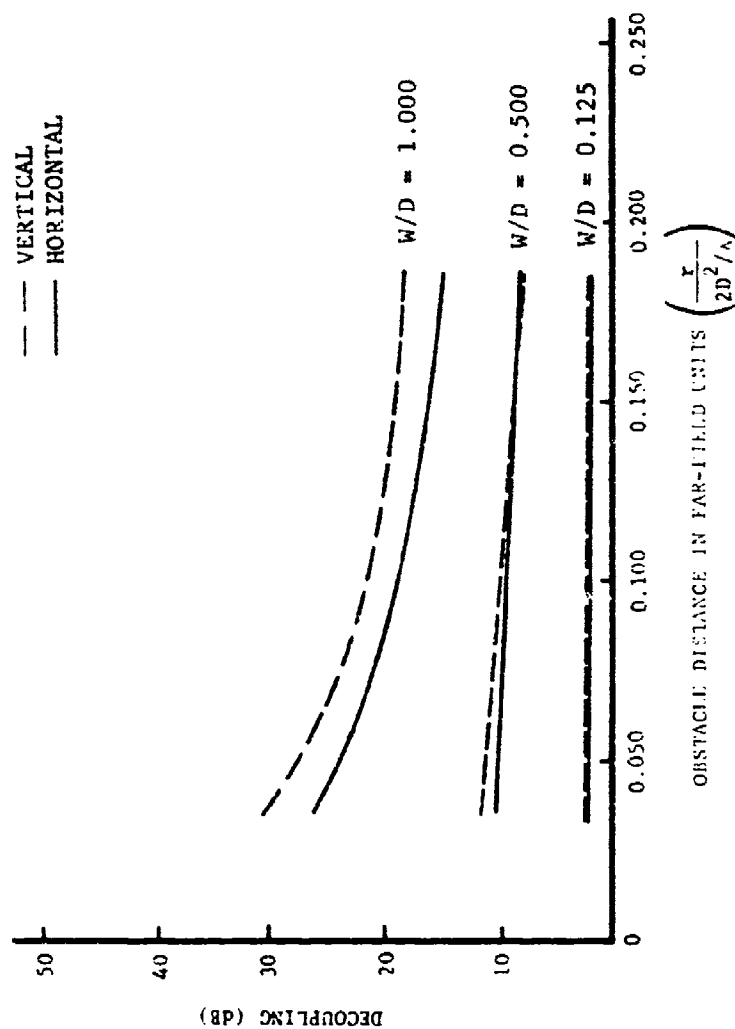
Figure 18. Average boresight decoupling as a function of obstacle distance along boresight direction (target direction) for receiving antenna aperture D for the Corner No. 2 obstacles of widths W for vertically and horizontally polarized signals at a frequency of 3000 MHz. Receiving antenna is in far field of target.
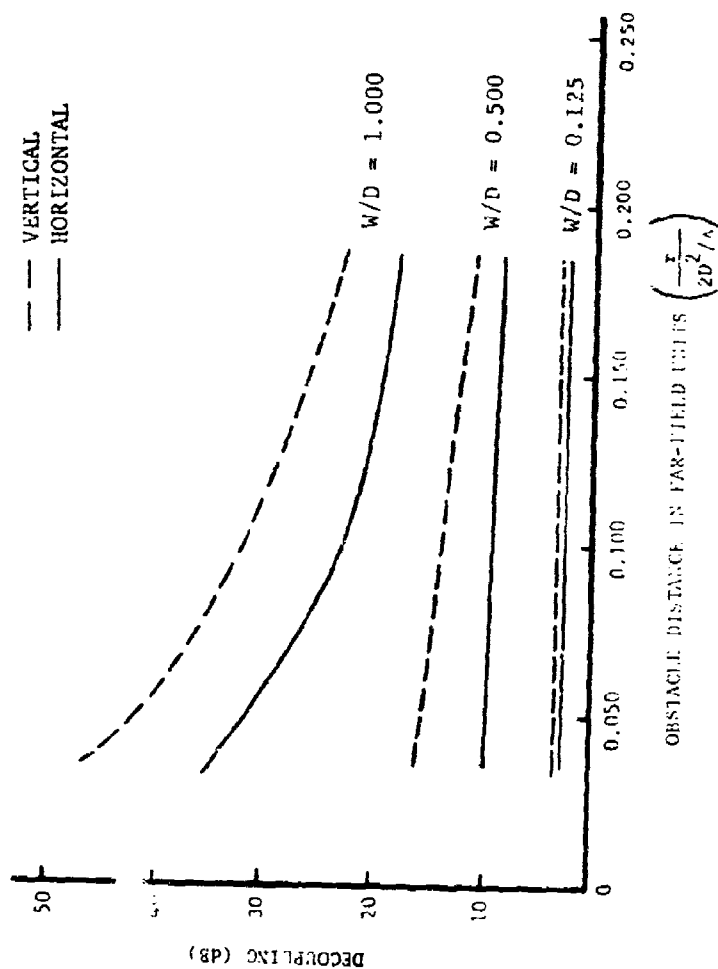
Figure 19. Average boresight decoupling as a function of obstacle distance along boresight direction (target direction) for receiving antenna aperture D for the Square Column obstacles of widths W for vertically and horizontally polarized signals at a frequency of 3000 MHz. Receiving antenna is in far field of target.

47
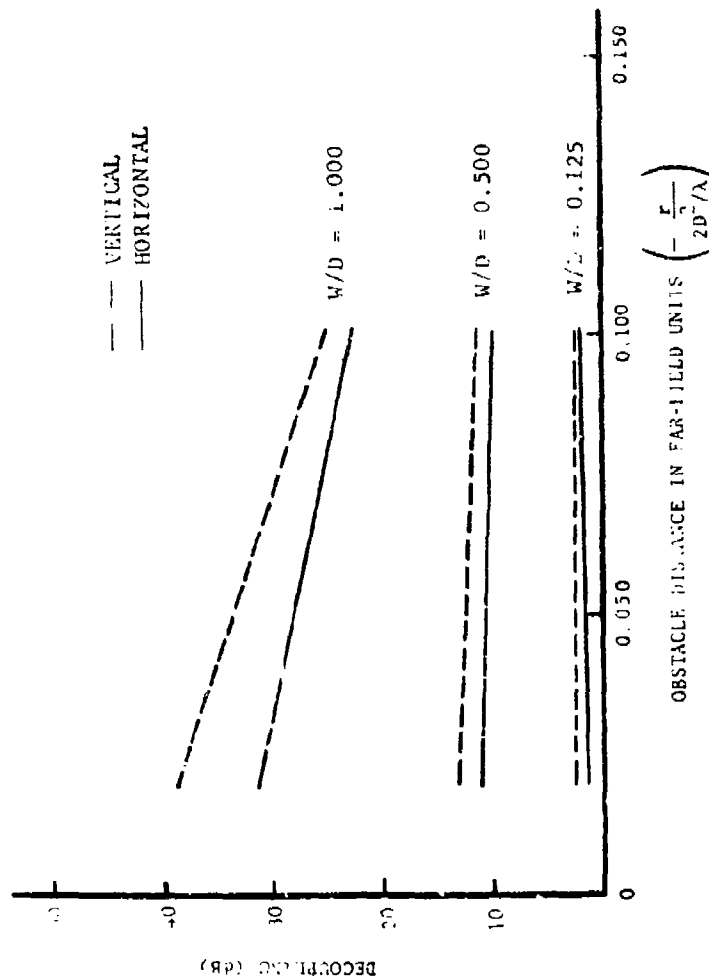
Figure 20. Average boresight decoupling as a function of obstacle distance along boresight direction (target direction) for receiving antenna aperture D for the Corner No. 1 obstacles of widths W for vertically and horizontally polarized signals at a frequency of 5500 MHz. Receiving antenna is in far field of target.

VERTICAL
HORIZONTAL

W/D = 1.000

W/D = 0.500

W/D = 0.125

DECOUPLING (dB)

OBSTACLE DISTANCE IN FAR-FIELD UNITS $\left(\dfrac{r}{2D^2/\lambda}\right)$

50
40
30
20
10
0

0   0.050   0.100   0.150
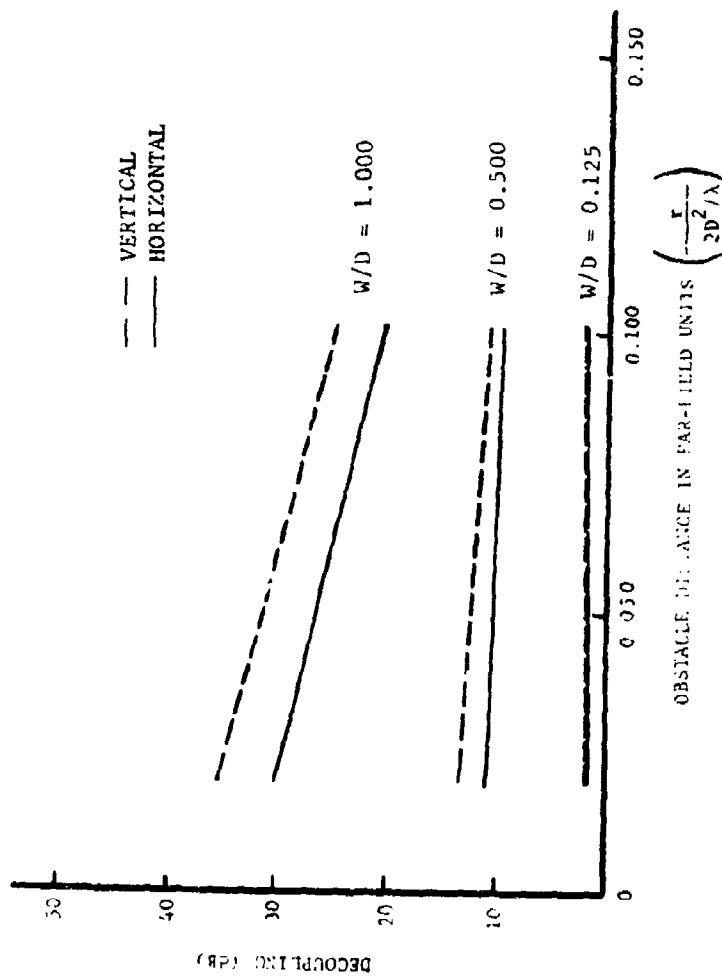
Figure 21. Average boresight decoupling as a function of obstacle distance along boresight direction (target direction) for receiving antenna aperture D for the Corner No. 2 obstacles of widths W for vertically and horizontally polarized signals at a frequency of 5500 MHz. Receiving antenna is in far field of target.
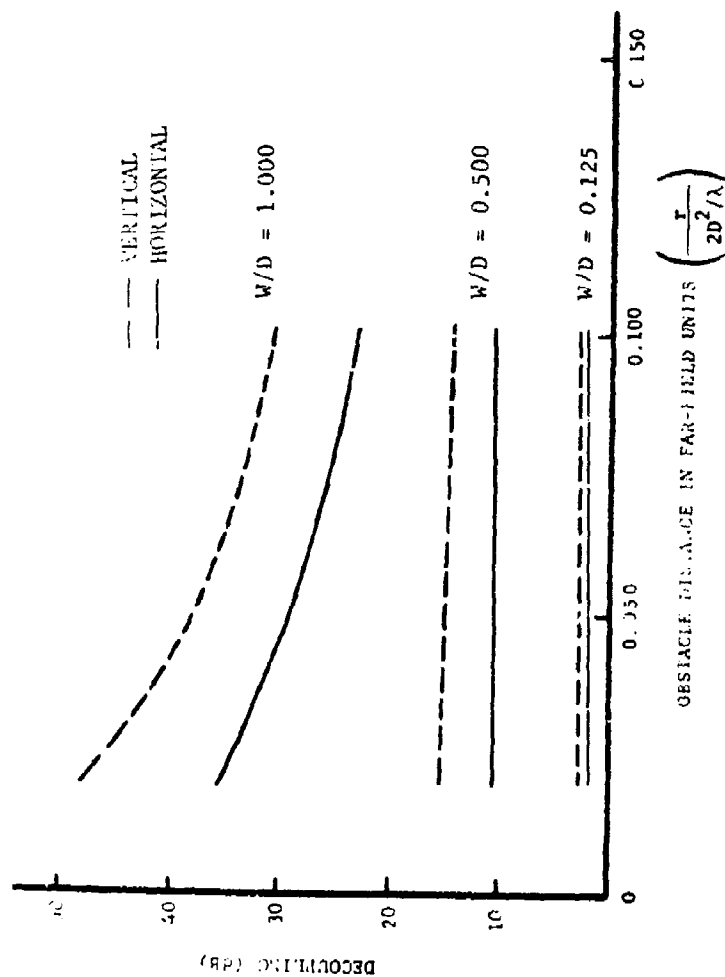
Figure 22. Average boresight decoupling as a function of obstacle distance along boresight direction (target direction) for receiving antenna aperture D for the Square Column obstacles of widths W for vertically and horizontally polarized signals at a frequency of 5500 MHz. Receiving antenna is in far field of target.
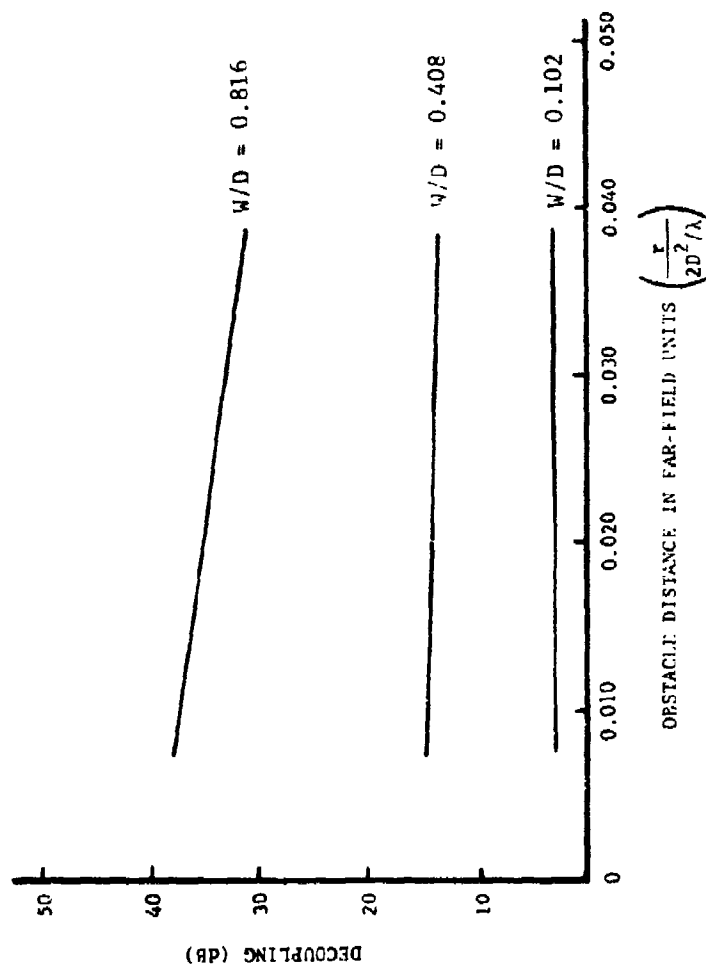
Figure 23. Average boresight decoupling as a function of obstacle distance along boresight direction (target direction) for receiving antenna aperture D for the Corner No. 1 obstacles of widths W for horizontally polarized signals at a frequency of 9600 MHz. Receiving antenna is in far field of target.
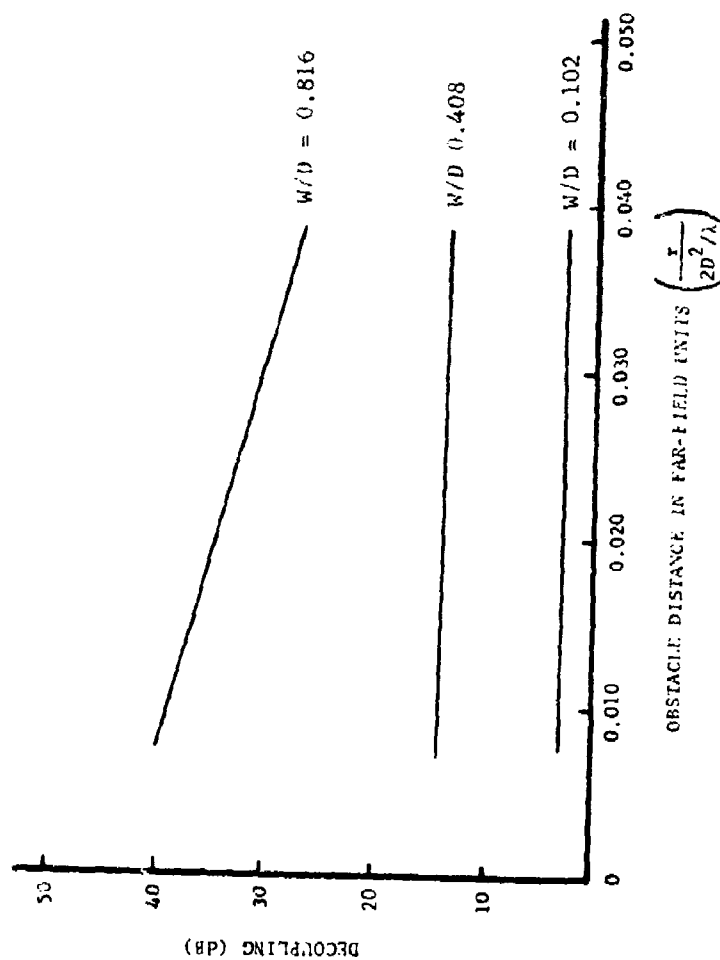
Figure 24. Average boresight decoupling as a function of obstacle distance along boresight direction (target direction) for receiving antenna aperture D for the Corner No. 2 obstacles of widths W for horizontally polarized signals at a frequency of 9600 MHz. Receiving antenna is in far field of target.
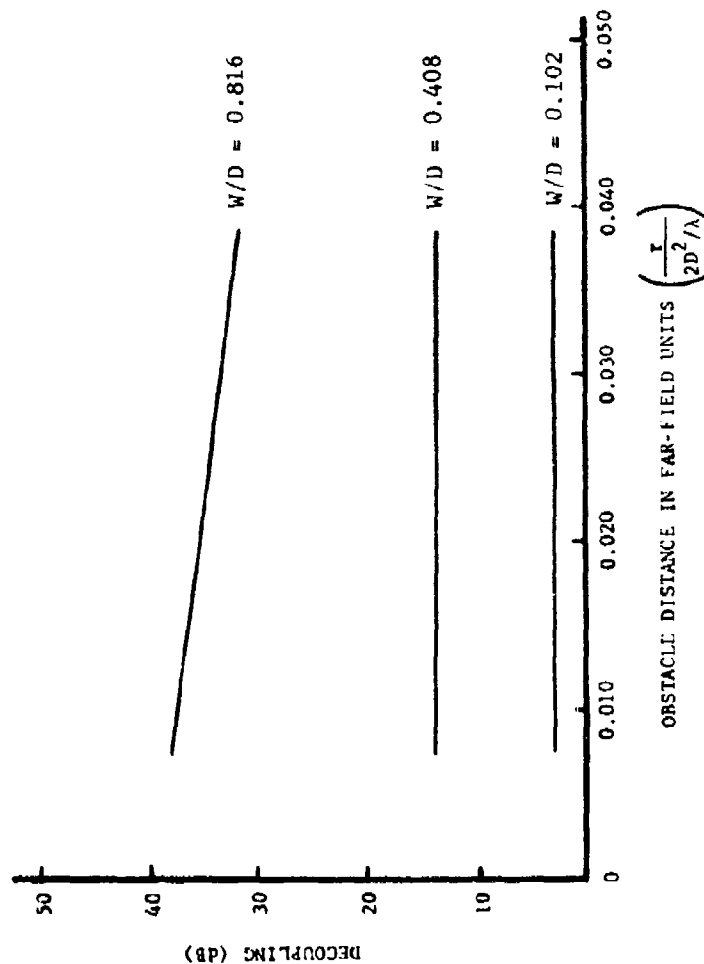
Figure 25. Average boresight decoupling as a function of obstacle distance along boresight direction (target direction) for receiving antenna aperture D for the Square Column obstacles of widths W for horizontally polarized signals at a frequency of 9600 MHz. Receiving antenna is in far field of target.

distance of the obstacle from the receiving antenna increases. These slopes tend to larger values as the size of an obstacle increases. For a given frequency of operation, major differences between decoupling levels are likely to occur for same-size obstacles of different types (for example, a 48-inch mast and a 48-inch square column) if one of the obstacles is a square column whose W/D ratio is one and if the polarization is vertical. The differences become less distinct for horizontal polarization and for smaller W/D ratios for either polarization.

The S-band (3000 MHz) boresight decoupling curves appear to indicate one trend that has not been observed in any of our previously reported work for C-band and X-band frequencies. For large obstacles, $W/D = 1$, the slopes of the curves for both vertically-polarized and horizontally-polarized signals generally are not linear. This new S-band trend implies that the decoupling level as a function of the obstacle distance from the receiving antenna along the boresight direction monotonically decreases and approaches a limiting value. In terms of the far-field units of $2D^2/\lambda$, the maximum obstacle distance from the receiving antenna is considerably greater at the S-band frequency than at either the C-band or X-band frequency. Based on the S-band data, it appears that approximately 0.2 of the far-field distance may be a good rule-of-thumb for the obstacle distance (break-distance) for which the boresight decoupling values approach a constant value. If this rule-of-thumb were true for all microwave frequencies, then a useful technique for application in topside ship design would exist. However, further investigations should be conducted to substantiate this conjecture.

2. Decoupling Versus Obstacle Angle

The decoupling curves for average boresight decoupling as a
function of obstacle angle for various types of obstacles, near-field
obstacle distances, polarizations, and frequencies are presented in
Figures 26 through 46. S-band (3000 MHz) curves are presented for mast
and sheet obstacles as well as corner reflector and square column ob-
stacles. C-band (5500 MHz) and X-band (9600 MHz) empirical curves for
the mast and sheet obstacles were presented in a previous report [1];
therefore, at these two frequencies, curves only for the corner reflec-
tors and square column obstacles are presented.

Observations of the figures indicate several trends. Some of the
trends are self-evident, while others are more subtle. Clearly, as the
obstacle angle off the boresight direction to the target increases, the
decoupling (peak gain loss) decreases for all obstacle sizes, obstacle
distances, polarizations, and frequencies. Also it is evident that a
given level of decoupling is dependent on the width of the obstacle and
the obstacle distance. For a given type of obstacle, for example, it
is evident that a W/D ratio of unity yields a larger decoupling value
than a W/D ratio of 0.5. Along boresight, which is the direction from
the receiving antenna to the target (0° on the graphs), the decoupling
values for the various near-field obstacle ranges are the same as those
displayed in Figures 15 through 25. The polar displays of Figures 26
through 46 show the manner in which the decoupling on boresight decreases
as the obstacle is displaced at an angle off boresight. Therefore, un-
less the behavior of the "roll-off" in decoupling is of particular con-
cern, the trends are also observable from Figures 15 through 25.
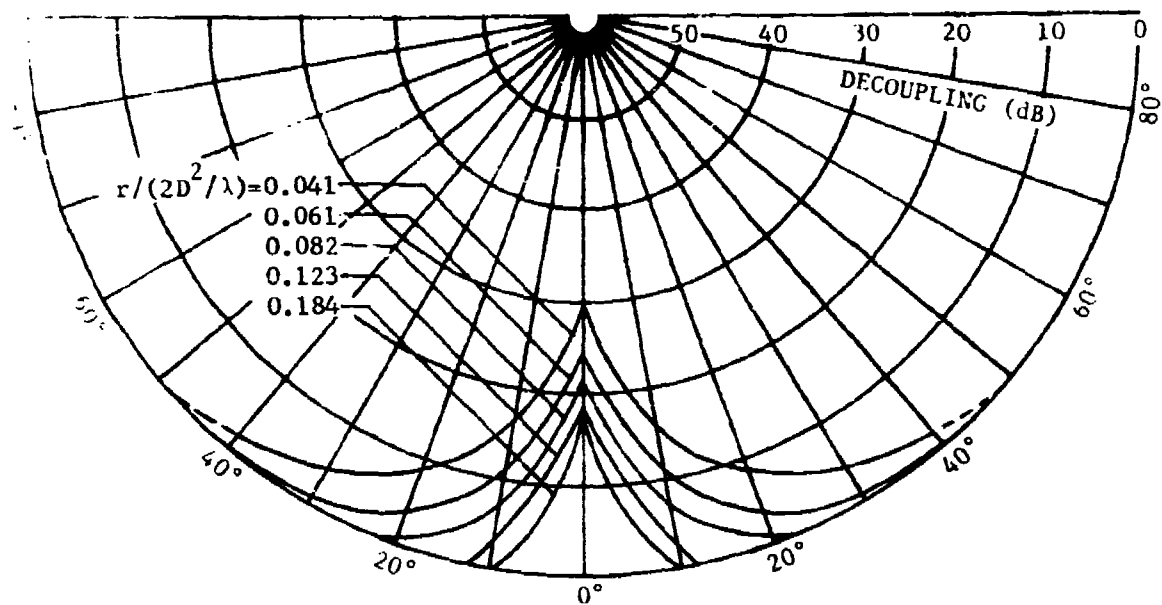
(a) Horizontal Polarization
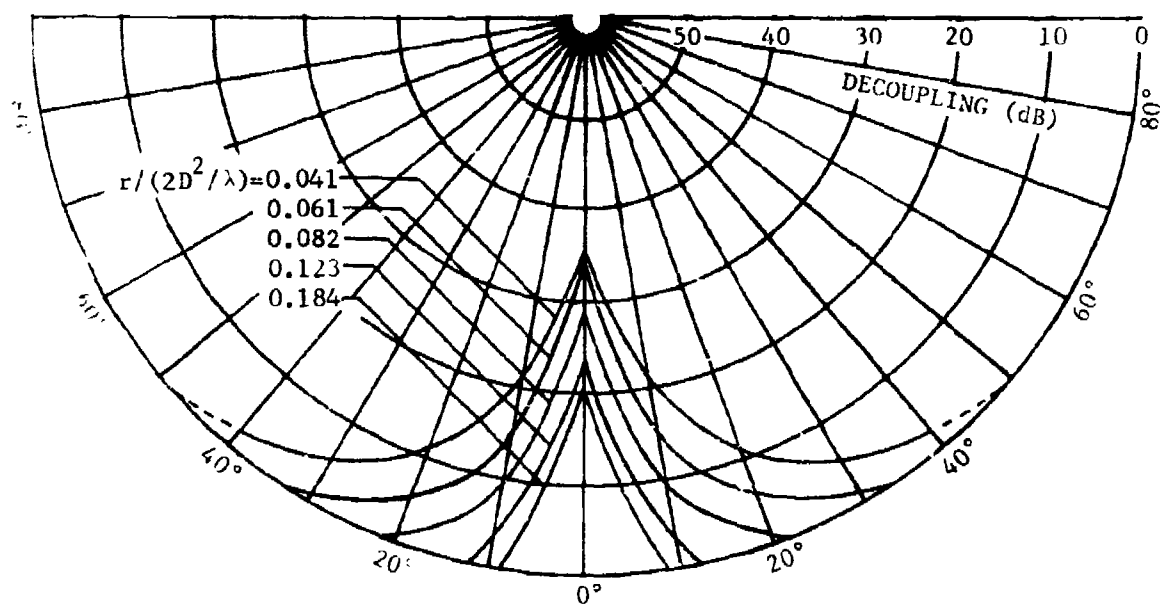
(b) Vertical Polarization

Figure 26. Average boresight decoupling as a function of the angle between obstacle and target direction for the **Mast** obstacle of normalized width **1.0** for indicated normalized obstacle distances from receiving antenna aperture D and for **horizontally** and **vertically** polarized signals at the frequency of **3000** MHz.
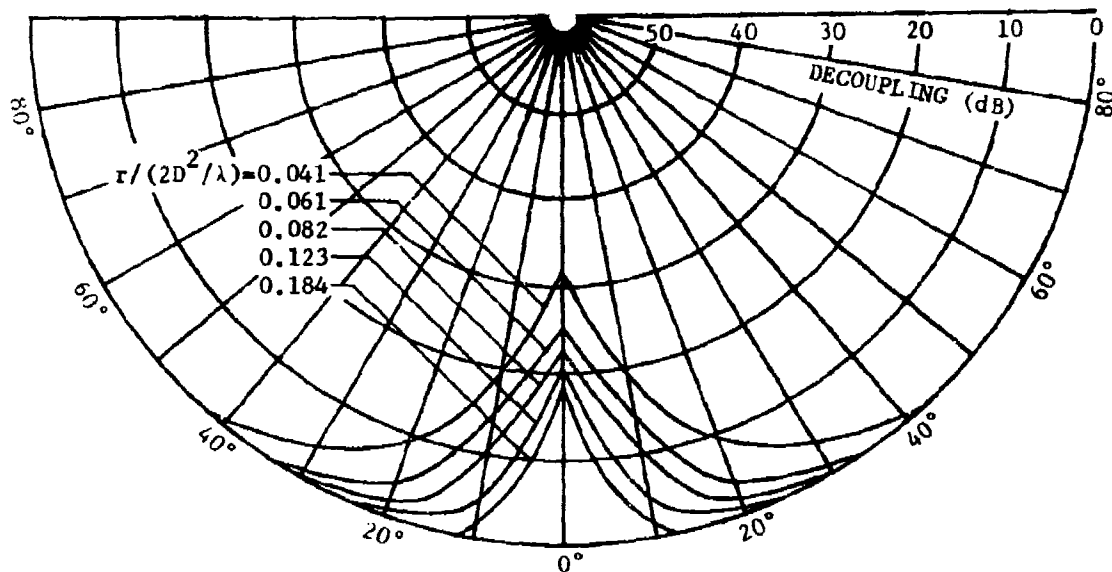
(a) Horizontal Polarization
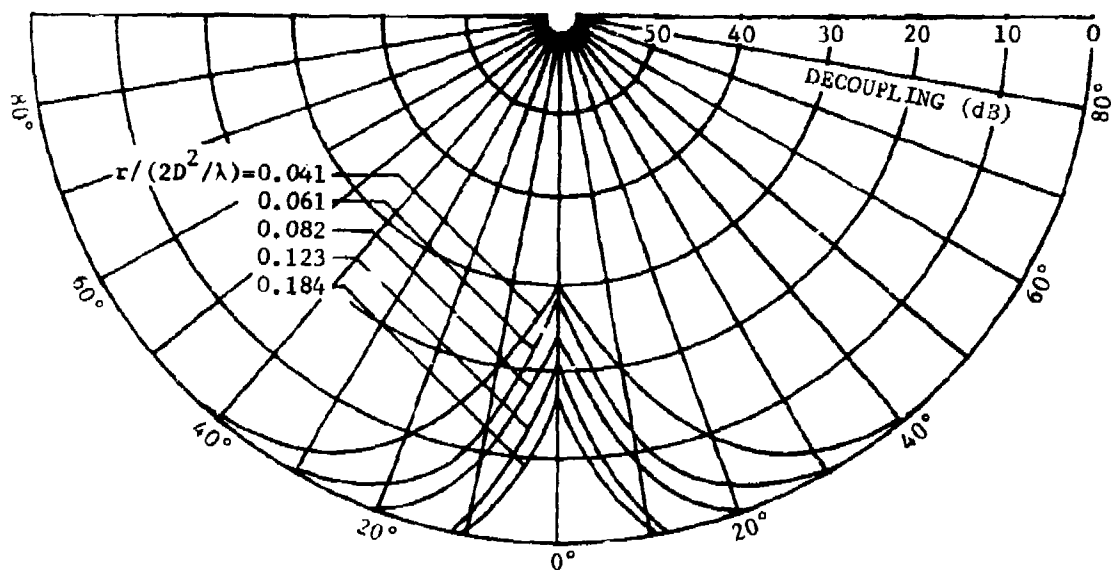
(b) Vertical Polarization

Figure 27. Average boresight decoupling as a function of the angle between
obstacle and target direction for the Sheet obstacle of normalized
width 1.0 for indicated normalized obstacle distances from
receiving antenna aperture D and for horizontally and vertically
polarized signals at the frequency of 3000 MHz.

57
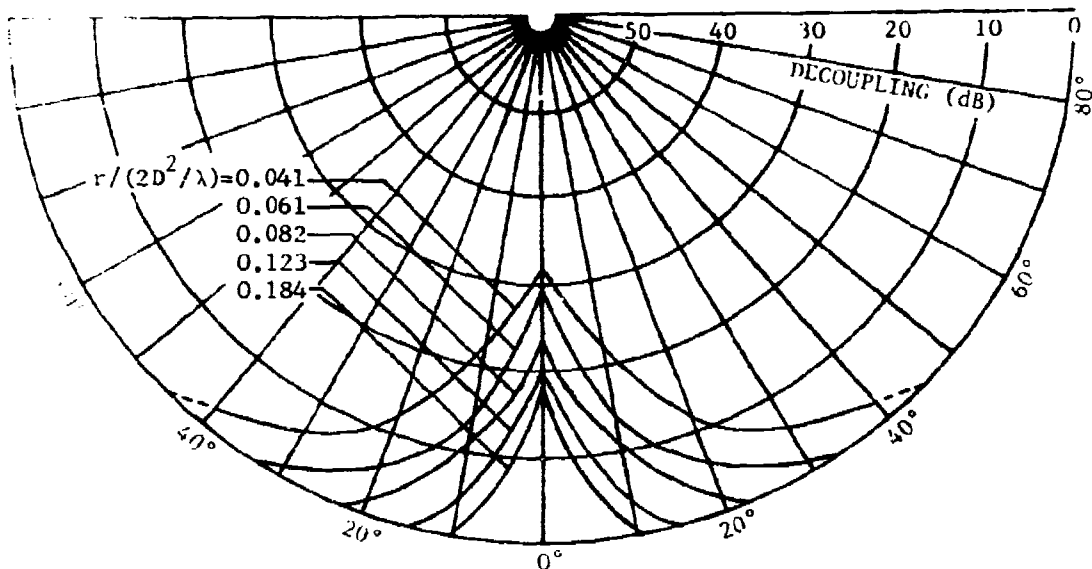
(a) Horizontal Polarization
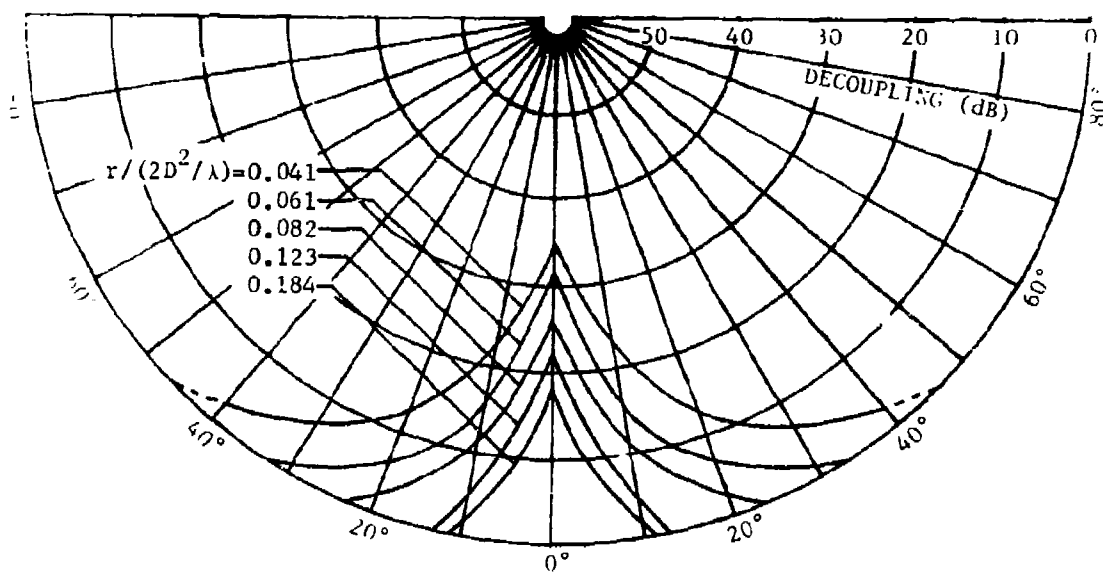
(b) Vertical Polarization

Figure 28. Average boresight decoupling as a function of the angle between obstacle and target direction for the Corner No. 1 obstacle of normalized width 1.0 for indicated normalized obstacle distances from receiving antenna aperture D and for horizontally and vertically polarized signals at the frequency of 3000 MHz.

58
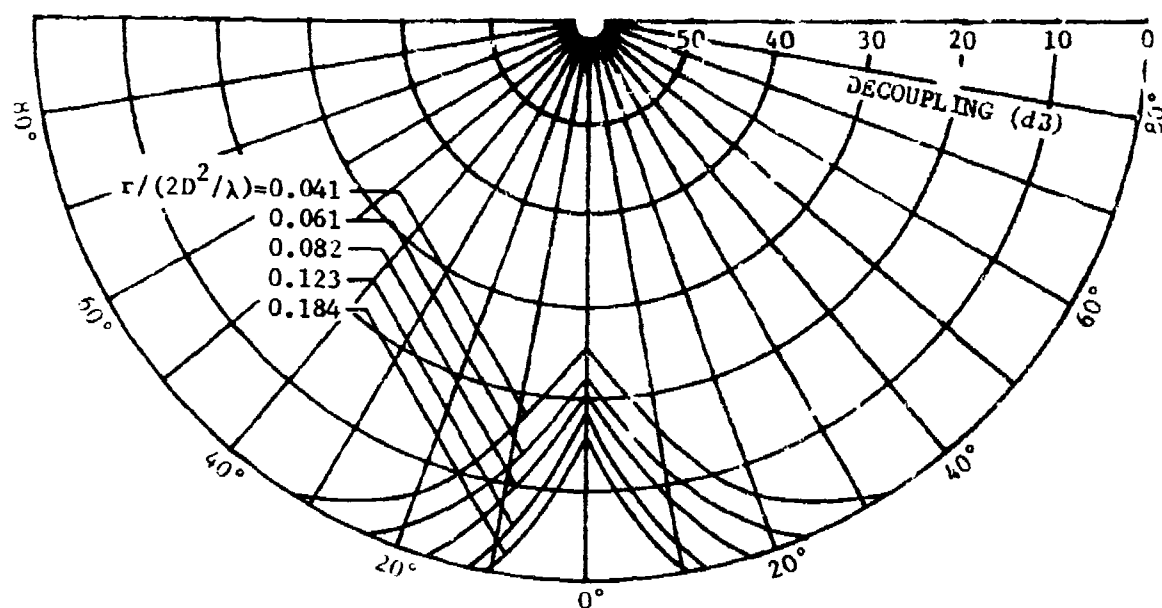
(a)   Horizontal Polarization
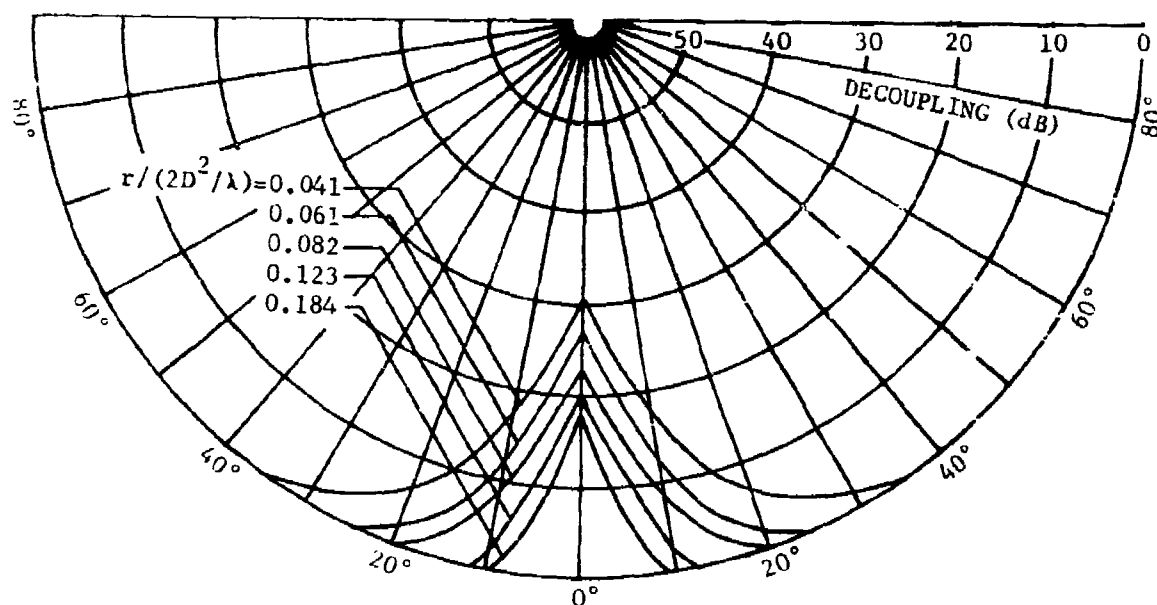
(b)   Vertical Polarization

Figure 29.   Average boresight decoupling as a function of the angle between obstacle and target direction for the Corner No. 2 obstacle of normalized width 1.0 for indicated normalized obstacle distances from receiving antenna aperture D and for horizontally and vertically polarized signals at the frequency of 3000 MHz.

59

(a) Horizontal Polarization

(b) Vertical Polarization

Figure 30. Average boresight decoupling as a function of the angle between obstacle and target direction for the Square Column obstacle of normalized width 1.0 for indicated normalized obstacle distances from receiving antenna aperture D and for horizontally and vertically polarized signals at the frequency of 3000 MHz.

(a) Horizontal Polarization

(b) Vertical Polarization

Figure 31. Average boresight decoupling as a function of the angle between obstacle and target direction for the Mast obstacle of normalized width 0.5 for indicated normalized obstacle distances from receiving antenna aperture D and for horizontally and vertically polarized signals at the frequency of 3000 MHz.
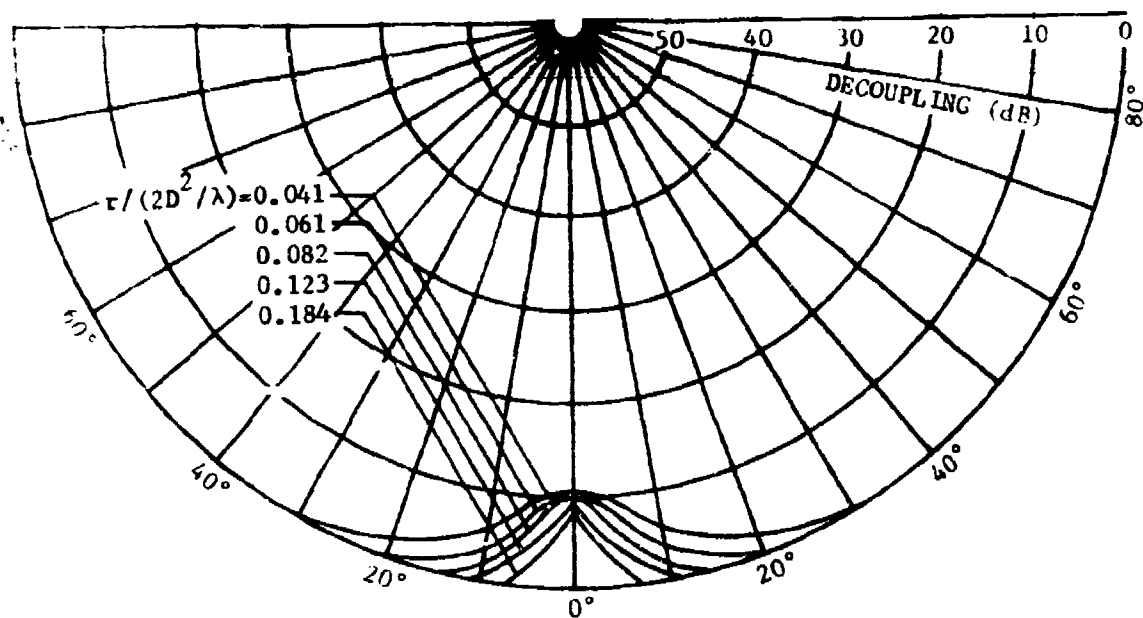
(a) Horizontal Polarization
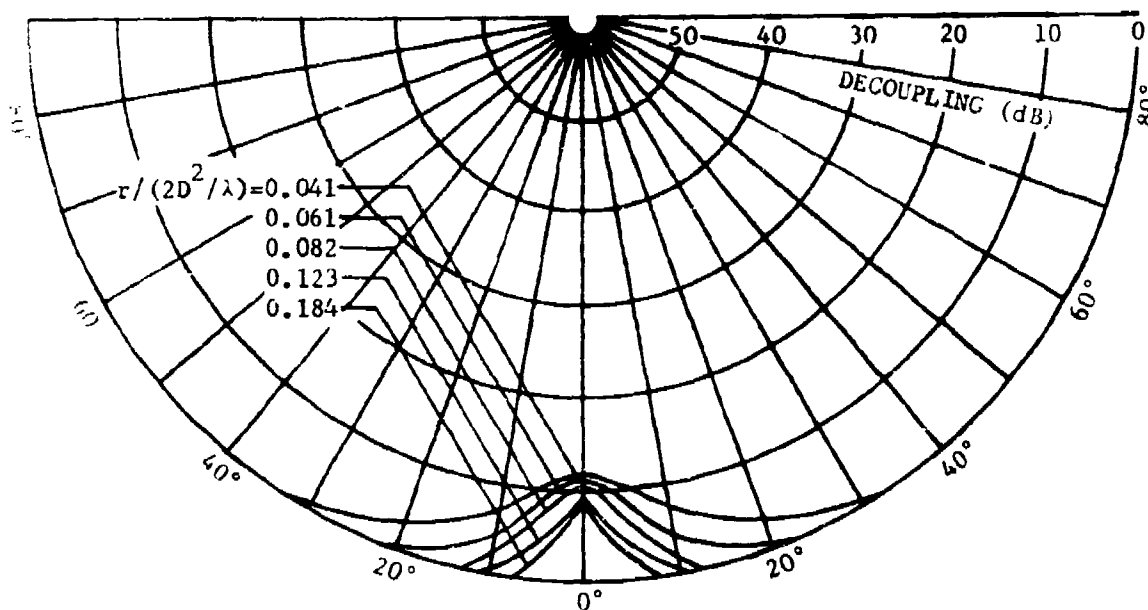
(b) Vertical Polarization

Figure 22. Average boresight decoupling as a function of the angle between obstacle and target direction for the Sheet obstacle of normalized width 0.5 for indicated normalized obstacle distances from receiving antenna aperture D and for horizontally and vertically polarized signals at the frequency of 3000 MHz.

62
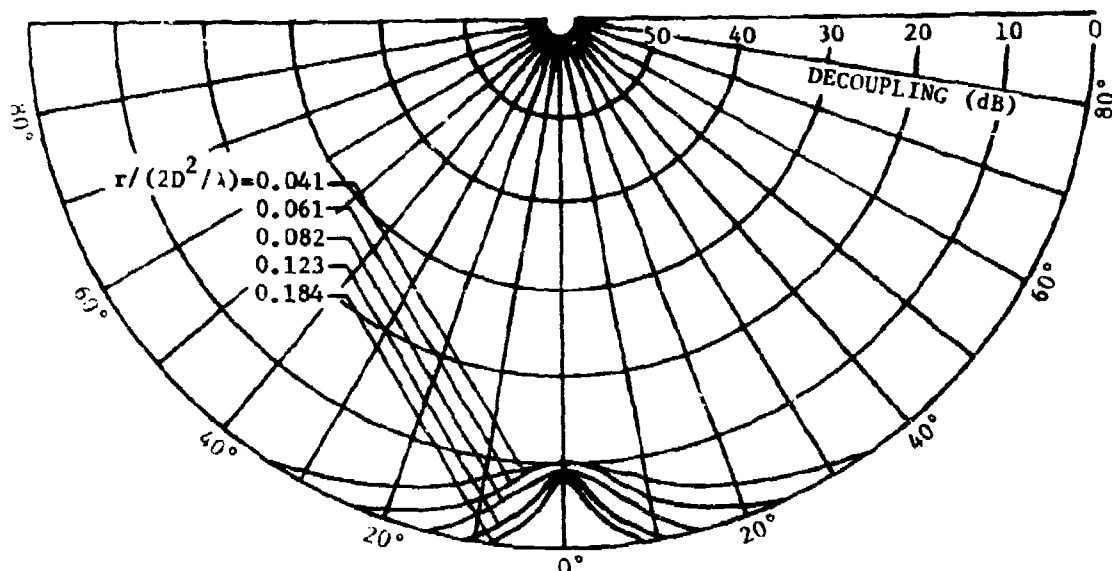
(a) Horizontal Polarization
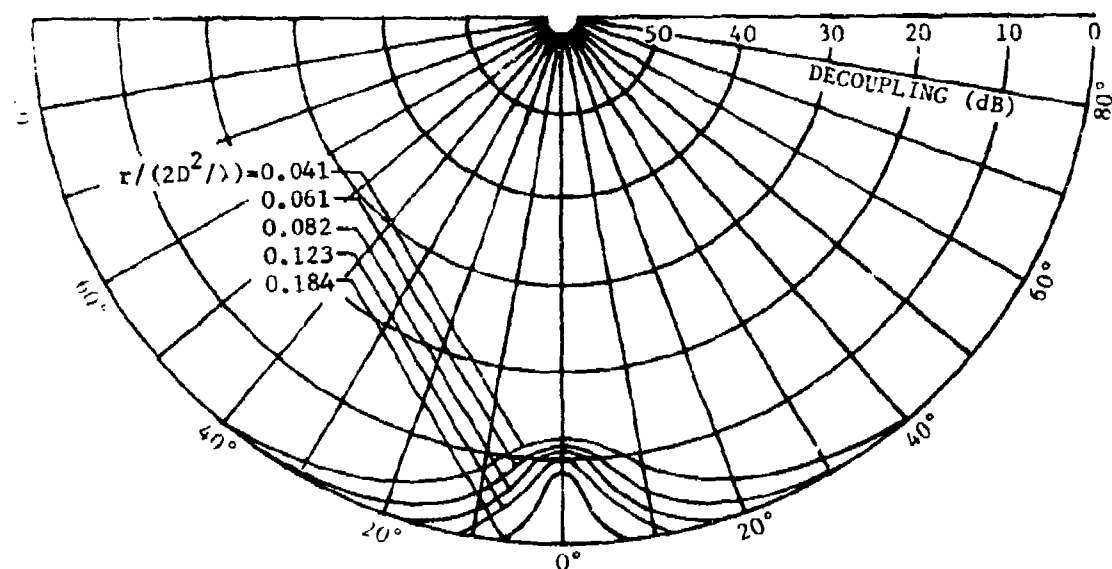
(b) Vertical Polarization

Figure 33. Average boresight decoupling as a function of the angle between obstacle and target direction for the Corner No. 1 obstacle of normalized width 0.5 for indicated normalized obstacle distances from receiving antenna aperture D and for horizontally and vertically polarized signals at the frequency of 3000 MHz.

63
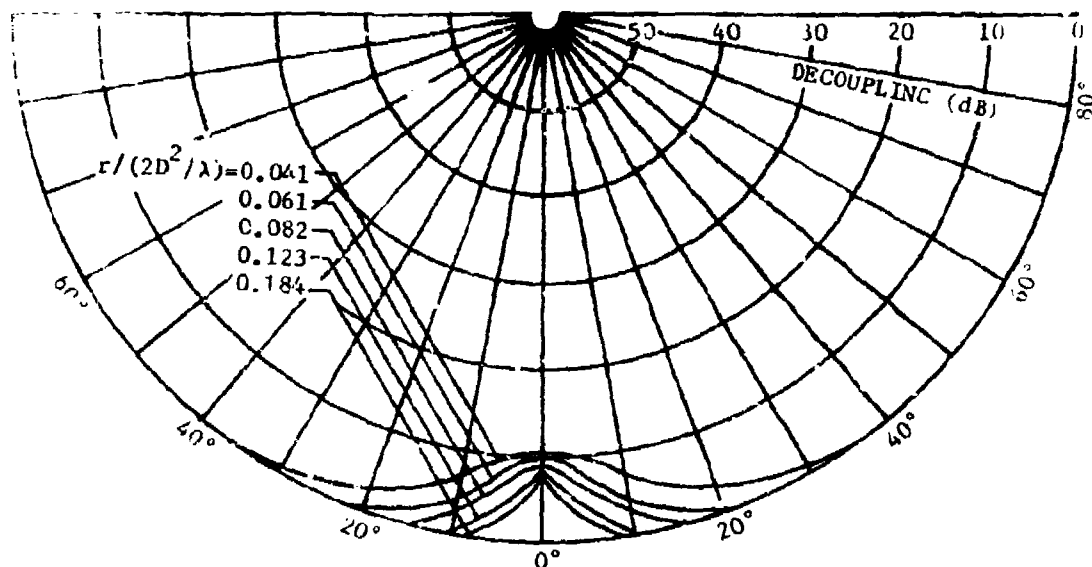
(a)   Horizontal Polarization
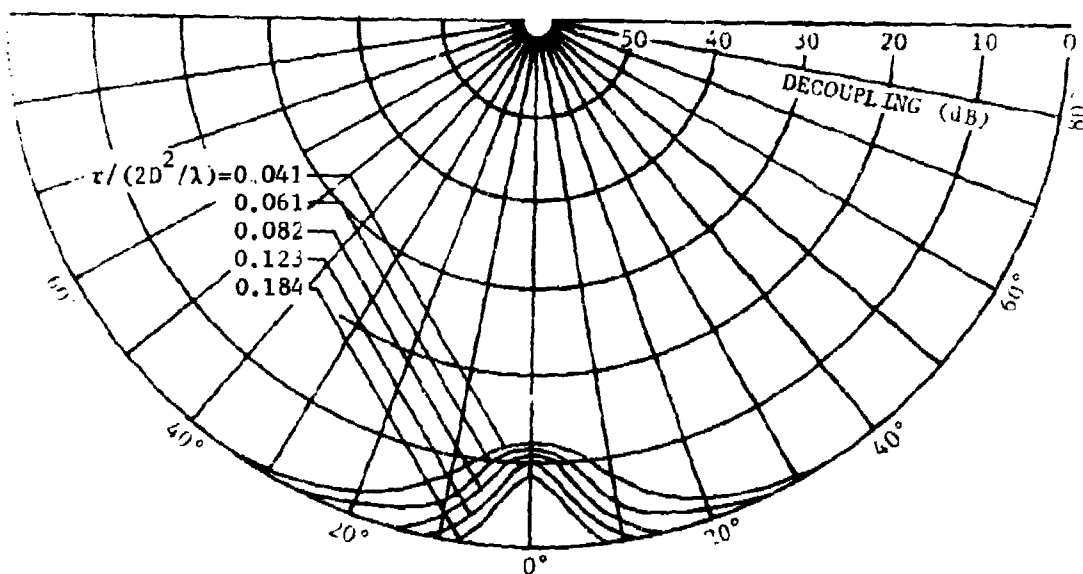
(b)   Vertical Polarization

Figure 34.   Average boresight decoupling as a function of the angle between obstacle and target direction for the Corner No. 2 obstacle of normalized width 0.5 for indicated normalized obstacle distances from receiving antenna aperture D and for horizontally and vertically polarized signals at the frequency of 3000 MHz.

64
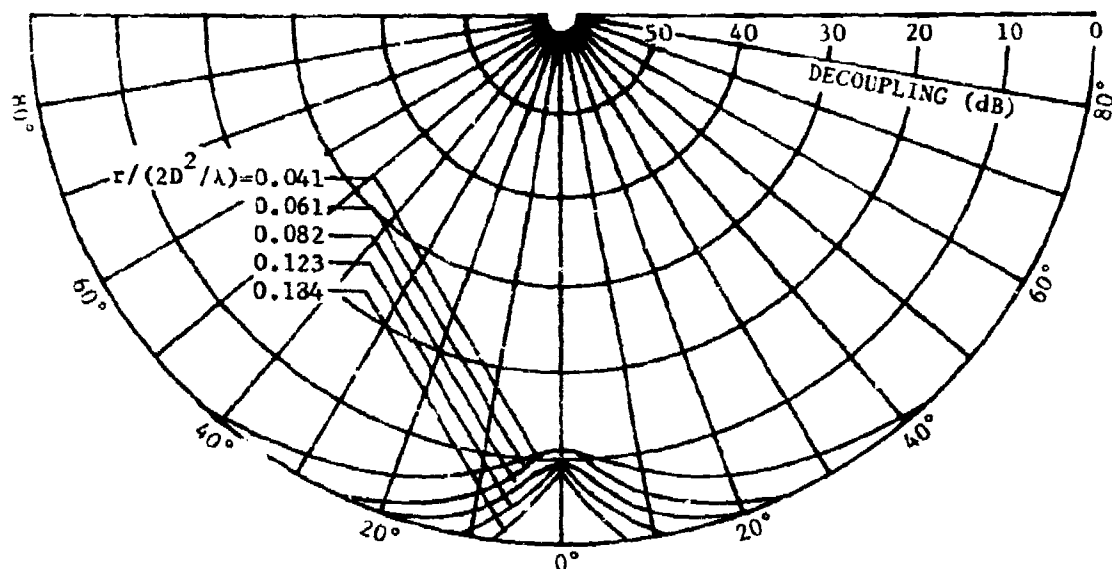
(a) Horizontal Polarization
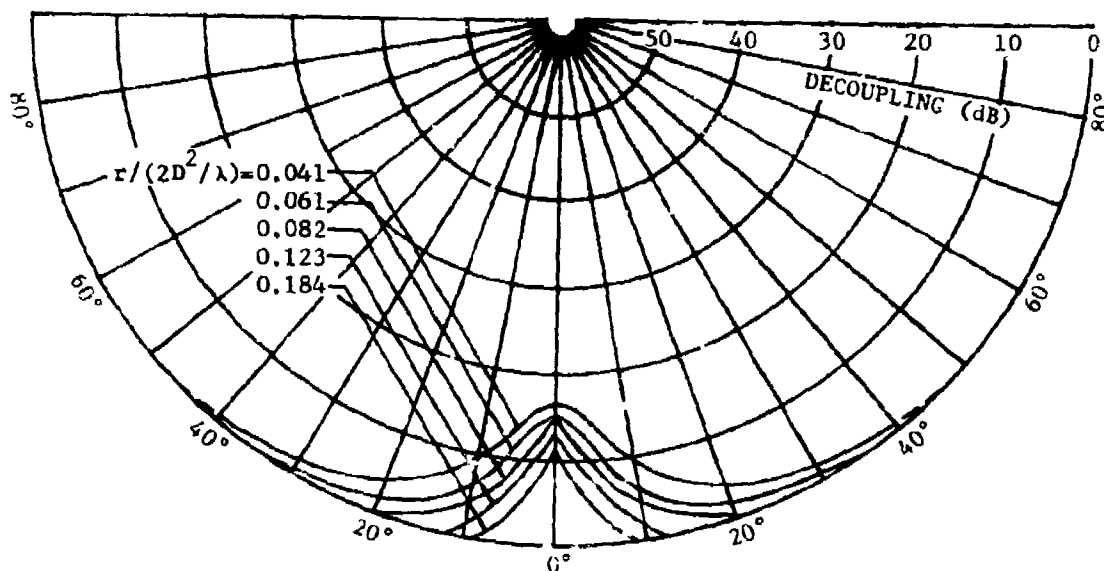
(b) Vertical Polarization

Figure 35. Average boresight decoupling as a function of the angle between obstacle and target direction for the Square Column obstacle of normalized width 0.5 for indicated normalized obstacle distances from receiving antenna aperture D and for horizontally and vertically polarized signals at the frequency of 3000 MHz.
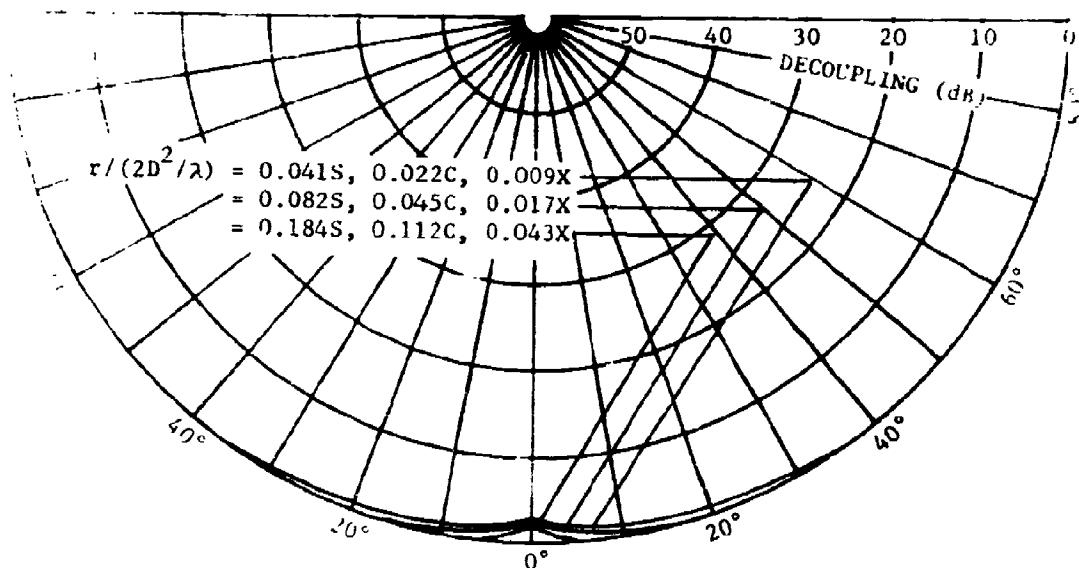
Figure 36. Average boresight decoupling as a function of the angle between obstacle and target direction for all obstacles of normalized width of approximately 0,125 for indicated normalized obstacle distances from receiving antenna aperture D and for horizontally and vertically polarized signals at the frequencies of 3000, 5500, or 9600 MHz.

66
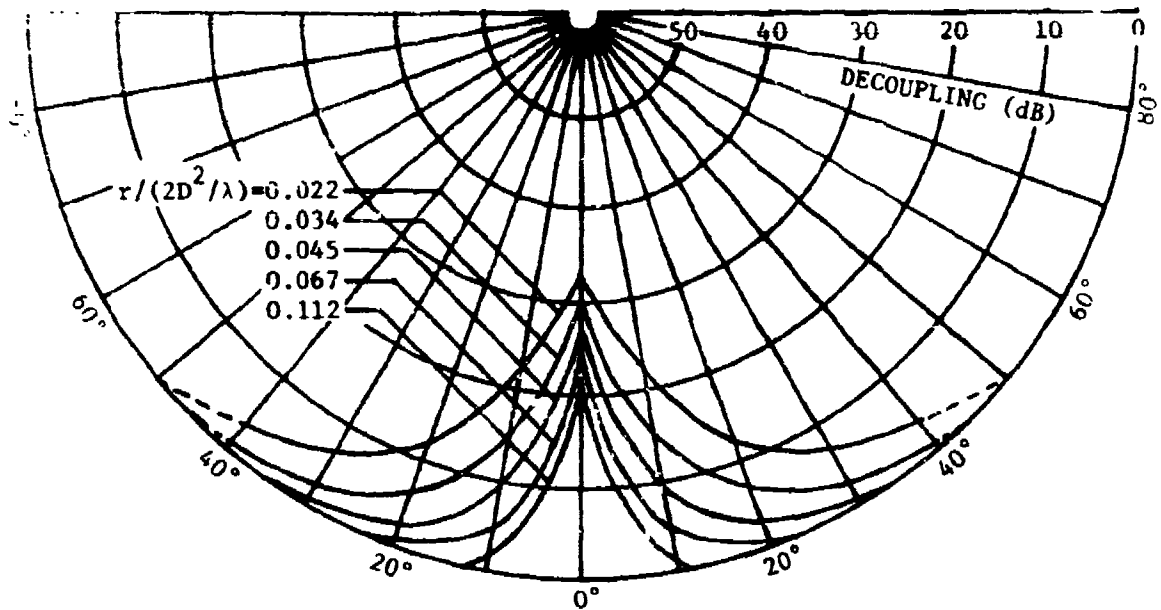
(a) Horizontal Polarization
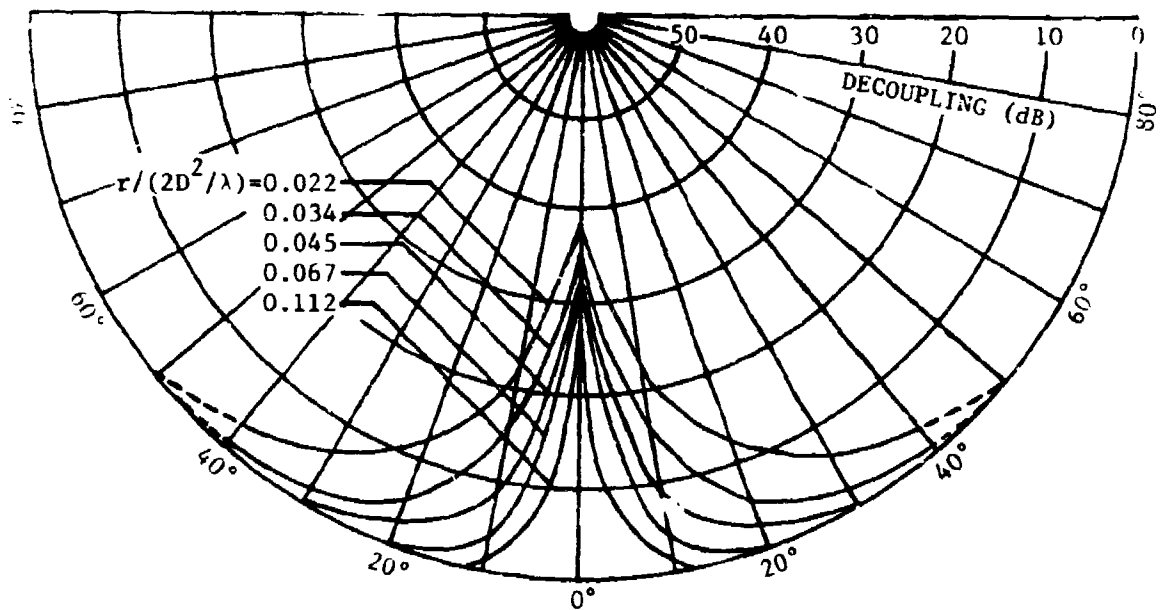
(b) Vertical Polarization

Figure 37. Average boresight decoupling as a function of the angle between obstacle and target direction for the Corner No. 1 obstacle of normalized width 1.0 for indicated normalized obstacle distances from receiving antenna aperture D and for horizontally and vertically polarized signals at the frequency of 5500 MHz.
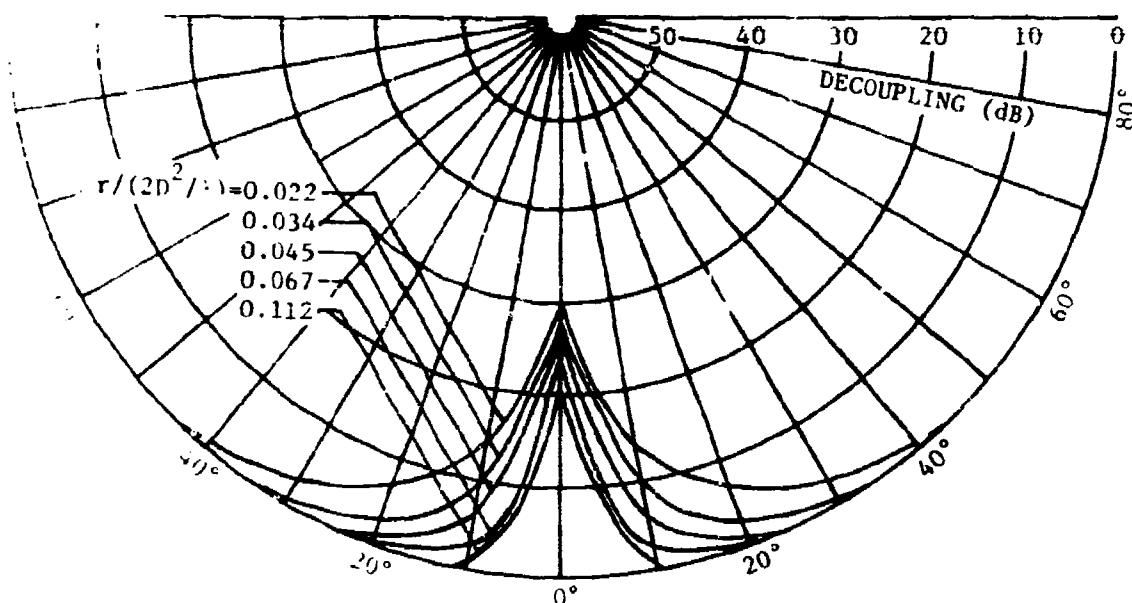
(a) Horizontal Polarization
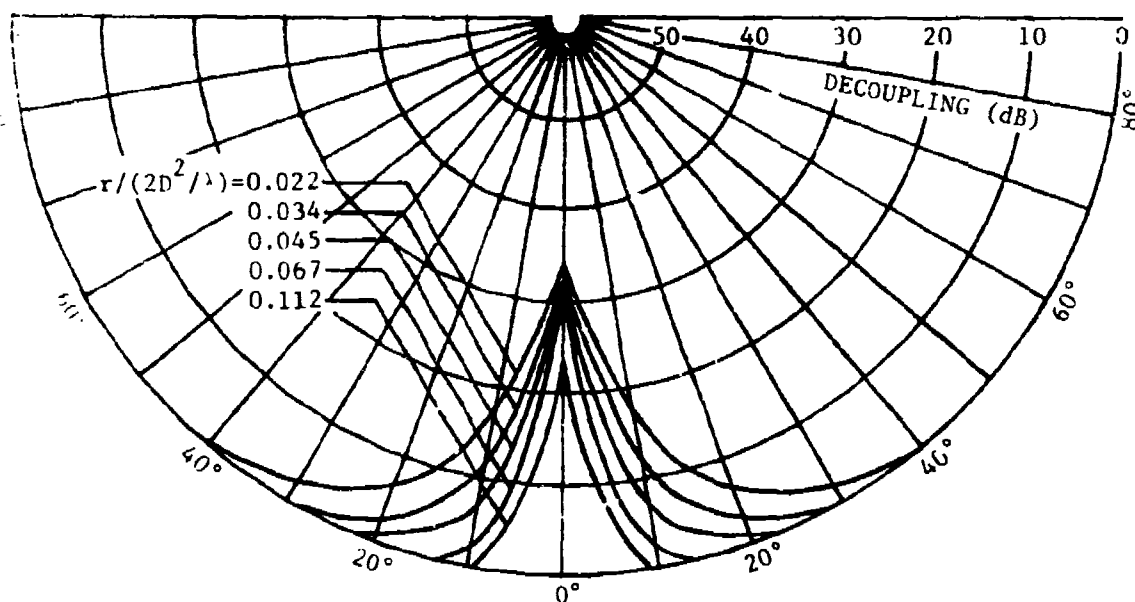
(b) Vertical Polarization

Figure 38. Average boresight decoupling as a function of the angle between obstacle and traget direction for the Corner No. 2 obstacle of normalized width 1.0 for indicated normalized obstacle distances from receiving antenna aperture D and for horizontally and vertically polarized signals at the frequency of 5500 MHz.

68
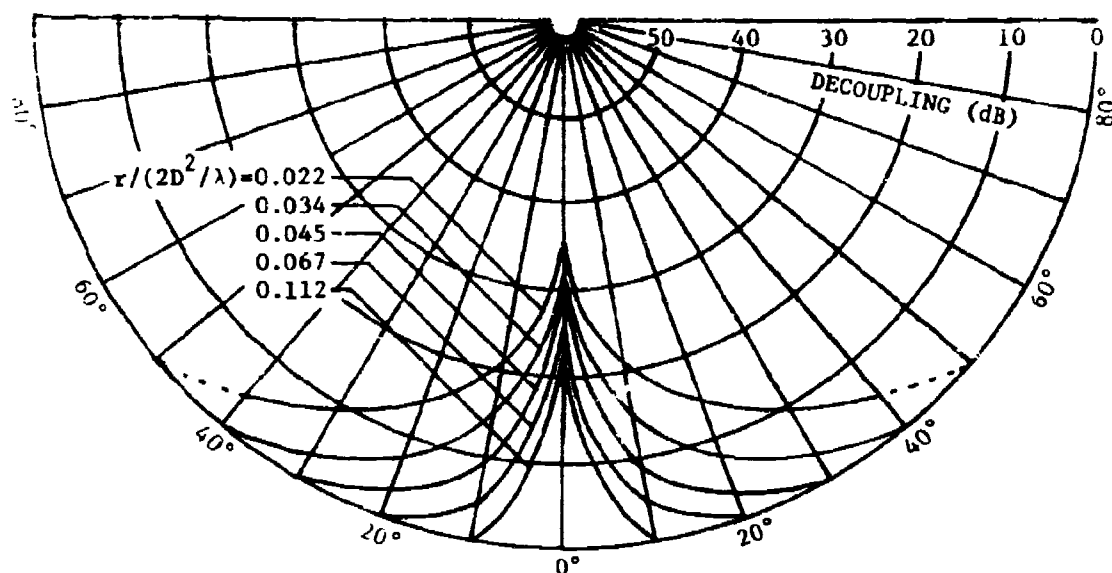
(a) Horizontal Polarization
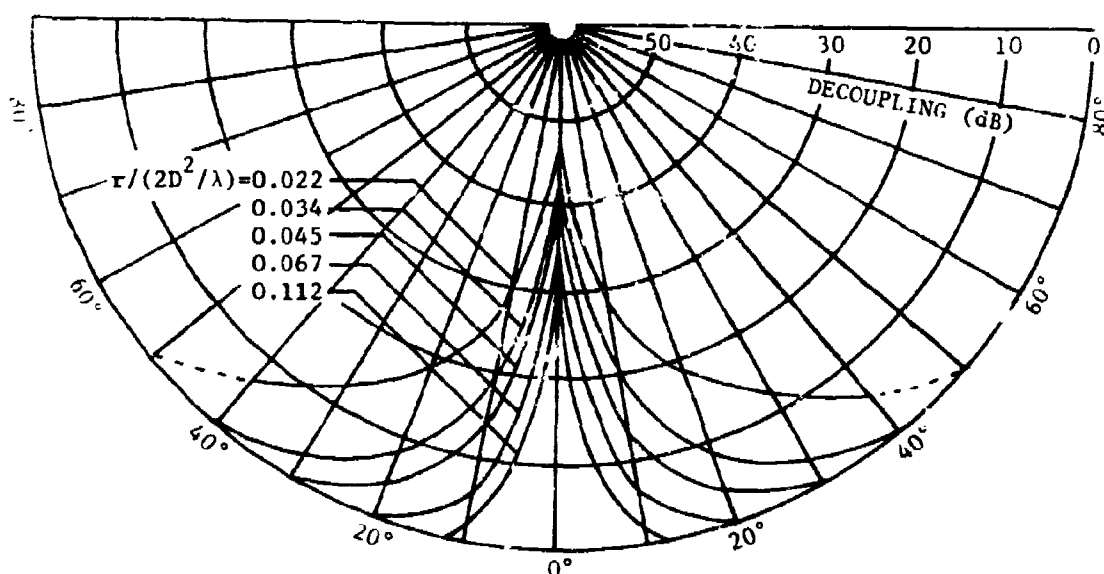
(b) Vertical Polarization

Figure 39. Average boresight decoupling as a function of the angle between
obstacle and target direction for the Square Column obstacle of
normalized width 1.0 for inciated normalized obstacle distances
from receiving antenna aperture D and for horizontally and
vertically polarized signals at the frequency of 5500 MHz.

69
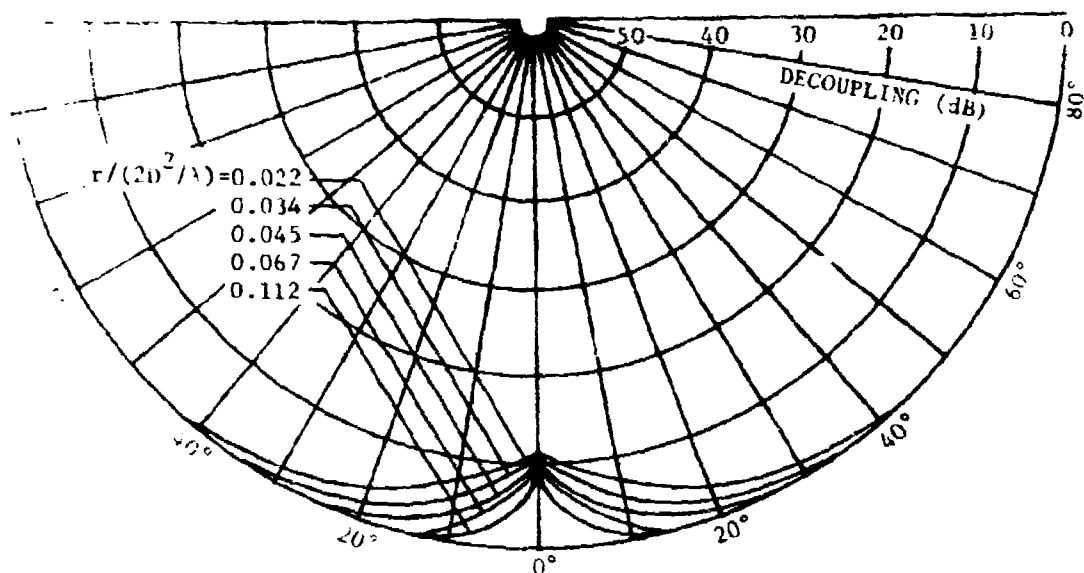
(a) Horizontal Polarization
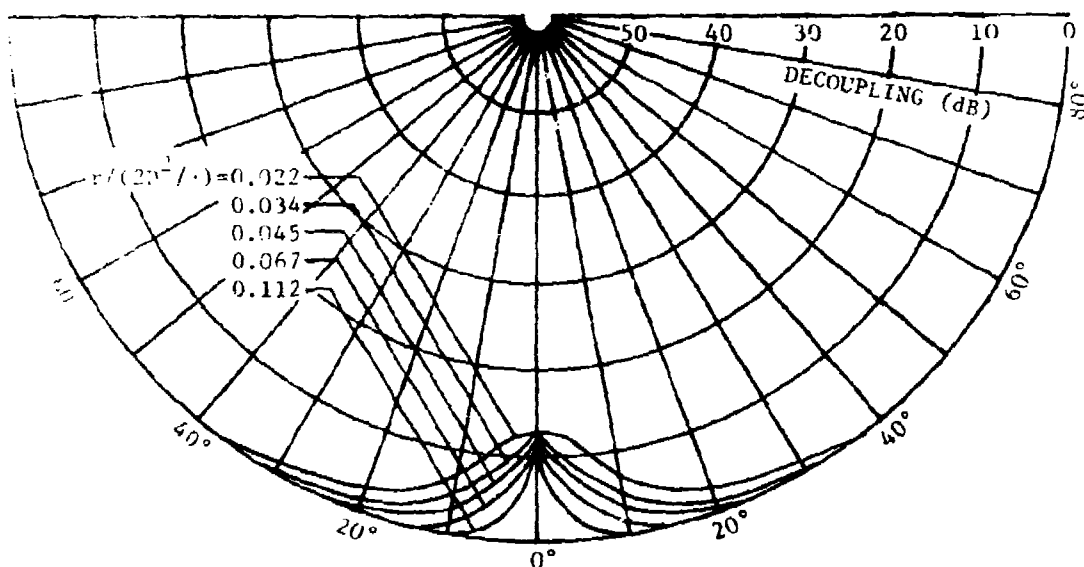
(b) Vertical Polarization

Figure 40. Average boresight decoupling as a function of the angle between obstacle and target direction for the Corner No. 1 obstacle of normalized width 0.5 for indicated normalized obstacle distances from receiving antenna aperture D and for horizontally and vertically polarized signals at the frequency of 5500 MHz.

70
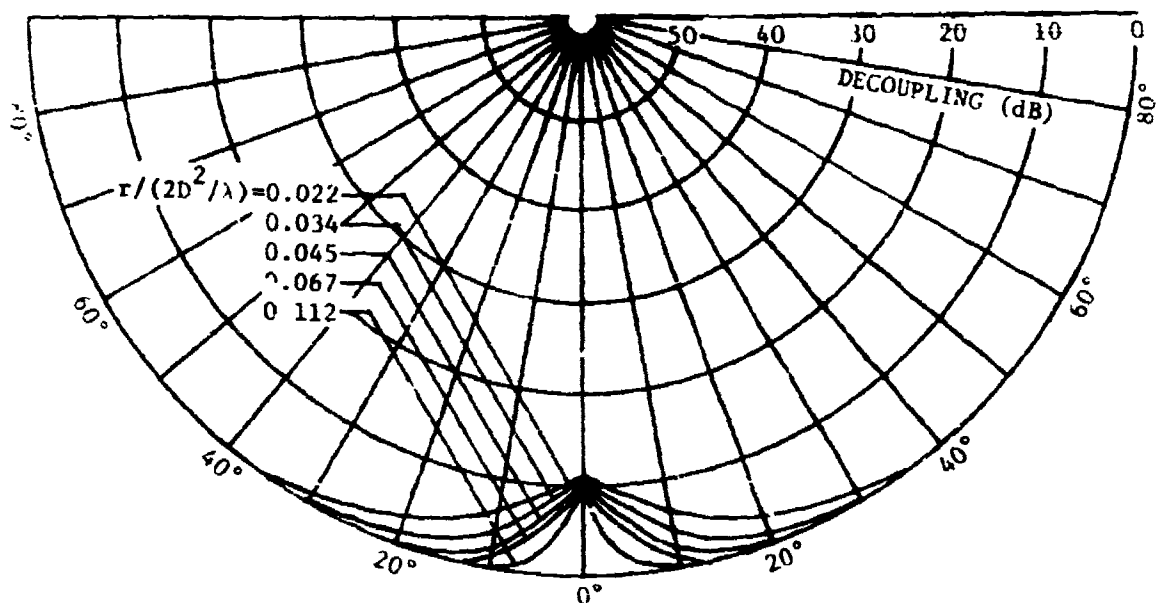
(a) Horizontal Polarization
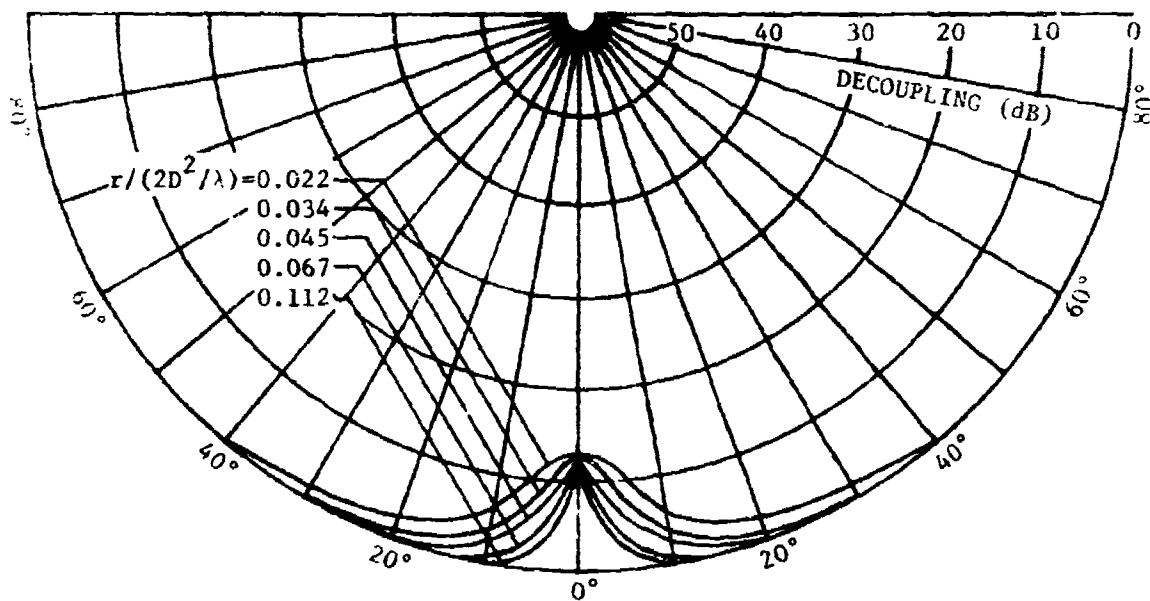
(b) Vertical Polarization

Figure 41. Average boresight decoupling as a function of the angle between obstacle and target direction for the Corner No. 2 obstacle of normalized width 0.5 for indicated normalized obstacle distances from receiving antenna aperture D and for horizontally and vertically polarized signals at the frequency of 5500 MHz.

71

(a) Horizontal Polarization

(b) Vertical Polarization

Average boresight decoupling as a function of the angle between obstacle and target direction for the Square Column obstacle of normalized width 0.5 for indicated normalized obstacle distances from receiving antenna aperture D and for horizontally and vertically polarized signals at the frequency of 5500 MHz.

72

(a) Corner #1
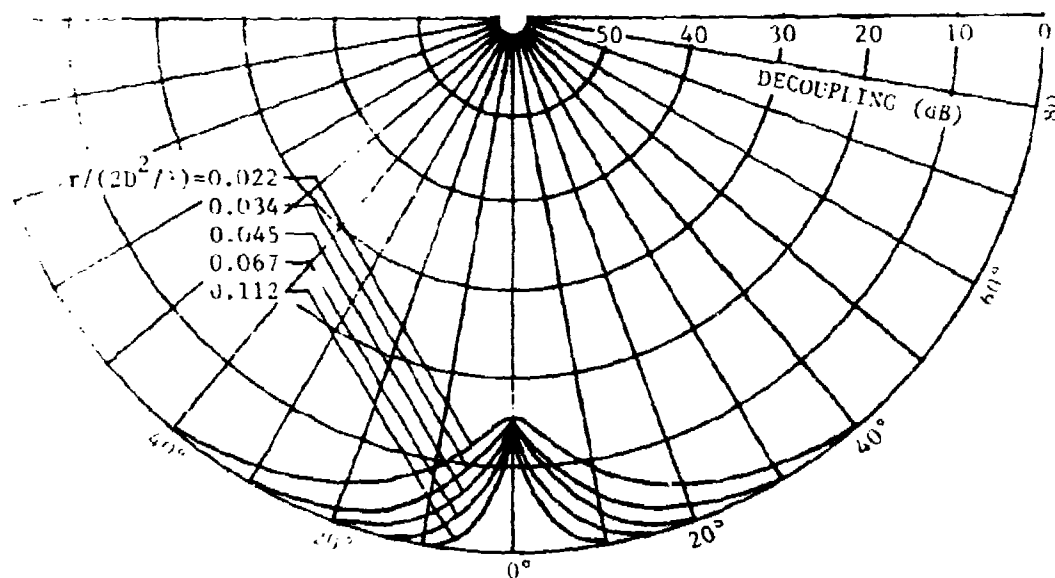
(b) Corner #2

Figure 43. Average boresight decoupling as a function of the angle between obstacle and target direction for Corner No. 1 and Corner No. 2 obstacles of normalized width 0.816 for indicated normalized obstacle distances from receiving antenna aperture D and for horizontally polarized signals at the frequency of 9600 MHz.
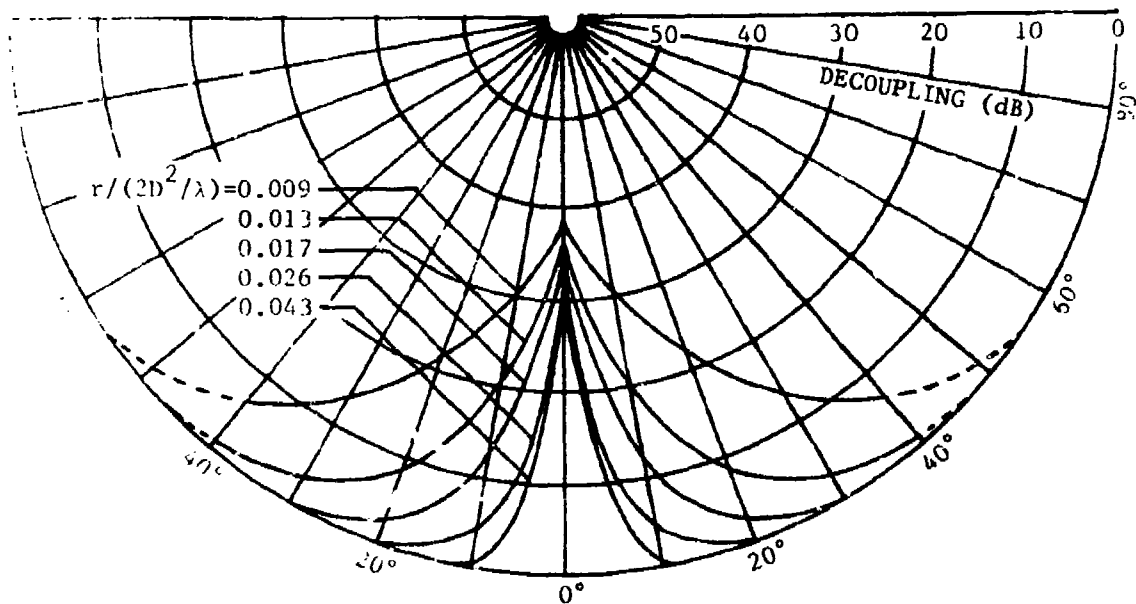
Figure 44. Average boresight decoupling as a function of the angle between obstacle and target direction for the Square Column obstacle of normalized width 0.816 for indicated normalized obstacle distances from receiving antenna aperture D and for horizontally polarized signals at the frequency of 9600 MHz.
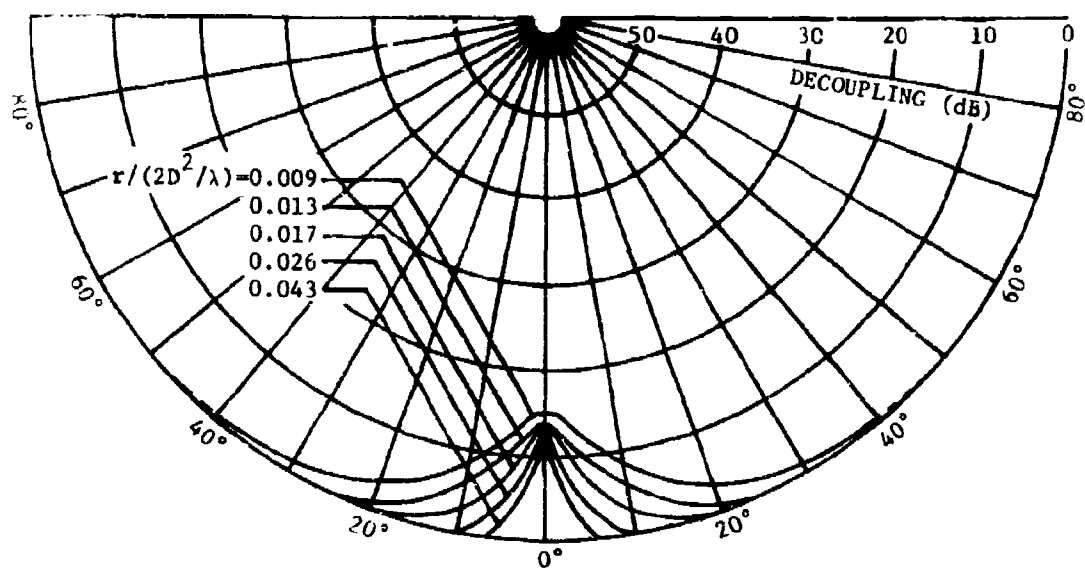
(a) Corner #1
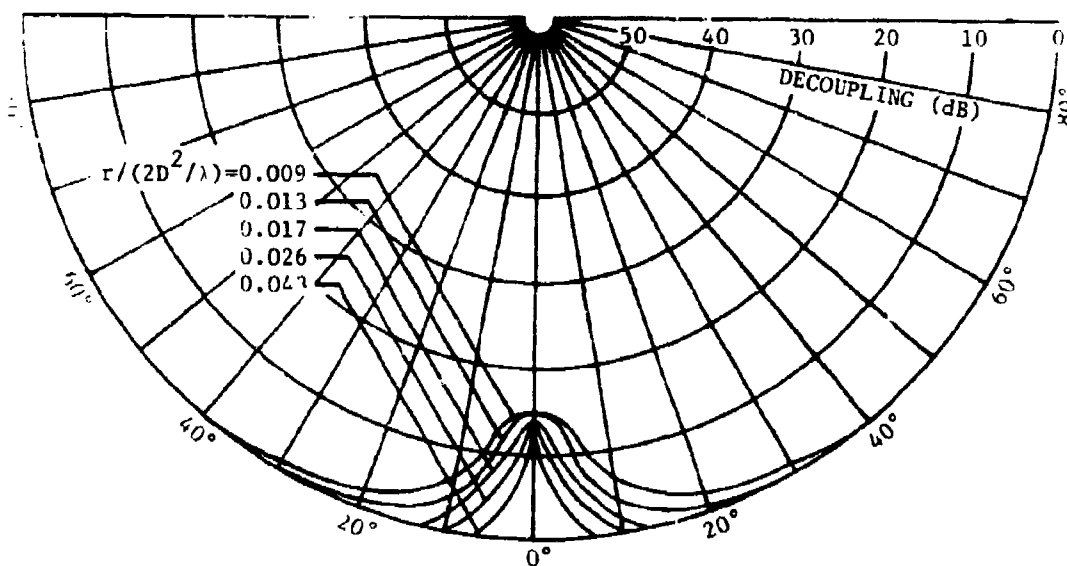
(b) Corner #2

Figure 45. Average boresight decoupling as a function of the angle between obstacle and target direction for Corner No. 1 and Corner No. 2 obstacles of normalized width 0.408 for indicated normalized obstacle distances from receiving antenna aperture D and for horizontally polarized signals at the frequency of 9600 MHz.

75
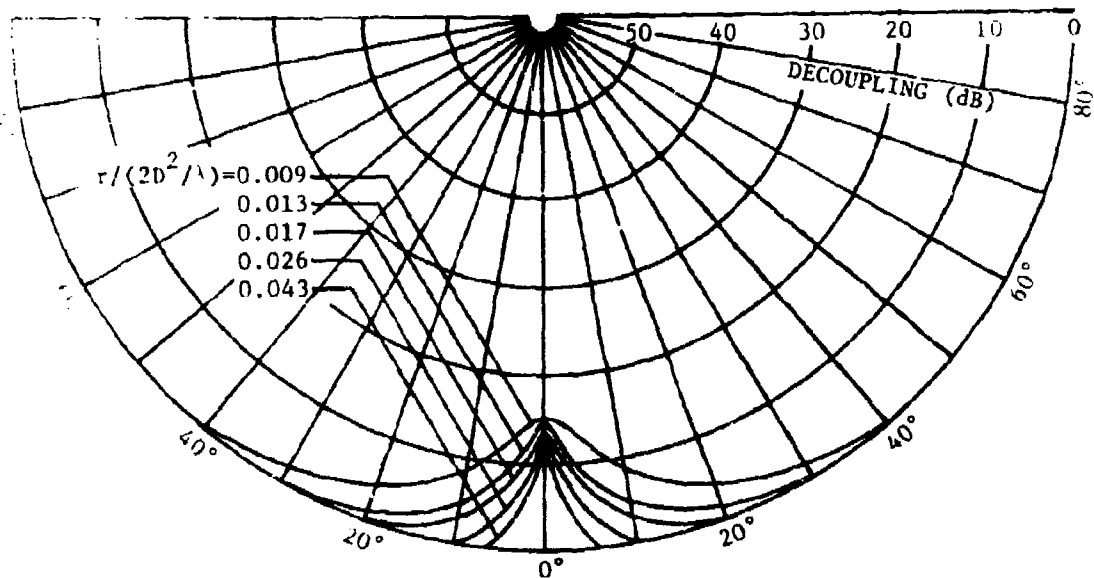
Figure 46. Average boresight decoupling as a function of the angle between obstacle and target direction for the Square Column obstacle of normalized width 0.408 for indicated normalized obstacle distances from receiving antenna aperture D and for horizontally polarized signals at the frequency of 9600 MHz.

In all of the polar displays, the near-field obstacle distance from the receiving antenna extends from about 4 feet to approximately 18 to 20 feet. Because the near-field obstacle distances are characterized in terms of far-field units which are frequency dependent, the obstacle distances in these units for each frequency band (S-band, C-band, and X-band) vary considerably. In many cases, however, the decoupling values for a given normalized obstacle distance (in terms of $2D^2/\lambda$) at 0° for a given set of conditions (for example, same obstacle type, same obstacle size, and same polarization) are usually about the same. Although the electrical distance of a given obstacle from an antenna [in terms of $r/(2D^2/\lambda)$] appears to be a major factor in determining the maximum decoupling at 0°, the physical distance of an obstacle from the receiving antenna (for example, 20 feet) appears to be a major factor in determining the extent of the angular blockage.

These electrical and physical phenomena can be illustrated by referring to the appropriate curves of Figures 28(a) and 43(a). The curves in these two figures were derived from S-band and X-band data for the 48-inch wide Corner Reflector No. 1 for horizontally polarized signals. Although the W/D ratios are slightly different and most of the normalized obstacle distances are widely different, the five physical obstacle distances in units of feet are exactly the same; however, two of the normalized obstacle distances [in terms of $r/(2D^2/\lambda)$] in the two figures are reasonably close to each other. Therefore, the maximum decoupling value at 0° is approximately 32 dB and 30 dB in Figures 28(a) and 43(a), respectively, for normalized obstacle distances of 0.041 and 0.043, respectively. However, note that the extent of the angular

blockage in the two cases is vastly different even though the maximum decoupling is approximately the same. Further, note that if the curves that correspond to a physical distance of approximately 18 to 20 feet in these two figures are consulted [this distance corresponds to normalized distances of 0.184 and 0.43 in Figures 28(a) and 43(a), respectively], the extent of the angular blockage is approximated $\pm 10^\circ$ about boresight (boresight is 0° on the polar plots). If curves corresponding to smaller W/D ratios are consulted, then the total angular blockage for an obstacle distance of 20 feet is less than $\pm 10^\circ$. Therefore, the users of the curves should consider various aspects for best results in siting a shipboard antenna.

Based on the empirical decoupling curves presented in both parts of this subsection, V-B, it appears that as the obstacle distance from the receiving antenna approaches relatively large values, the maximum decoupling approaches a limiting value and the extent of the angular blockage decreases to zero, that is, there is no blockage except at 0° on the polar plot. However, the limiting decoupling value may depend on the size of obstacle, the type of obstacle, the frequency, and the polarization. Additionally, in this limiting case, the obstacle itself must remain in the far-field of the target as the obstacle distance from the receiving antenna increases.

The maximum deviations from the average decoupling curves as a function of obstacle angle and near-field obstacle distance are given in Tables I through IX for the indicated frequencies, polarizations, and obstacle types. Deviations are given for only the largest-size and middle-size obstacles. The maximum deviations for the smallest-size

TABLE I

MAXIMUM DEVIATIONS FROM FAR-FIELD DECOUPLING VALUES IN DECIBELS FOR MAST AND SQUARE COLUMN OBSTACLES AT SELECTED OBSTACLE DISTANCES AND ANGLES FROM BORESIGHT DIRECTION (TARGET DIRECTION) FOR VERTICALLY AND HORIZONTALLY POLARIZED SIGNALS AT THE FREQUENCY OF 3000 MHz

Obstacle Distance*		DEVIATIONS FOR INDICATED OBSTACLE ANGLES θ AND NORMALIZED WIDTHS** OF W/D = 1.0 AND 0.5					
		$\theta = 0°$		$\theta = 5°$		$\theta = 10°$	
r (Feet)	$r/(2D^2/\lambda)$	1.0	0.5	1.0	0.5	1.0	0.5
4	0.041	4.0	1.5	3.0	1.5	1.5	1.0
6	0.061	3.0	1.0	2.0	0.5	1.5	0.5
8	0.082	2.5	1.0	1.5	0.5	1.0	0.5
12	0.123	2.5	1.0	1.0	0.0	0.5	0.0
20	0.184	2.0	1.0	1.0	0.0	0.0	0.0

* r is the distance from the receiving antenna aperture D to the obstacle.
**The normalized width is the ratio of the obstacle width to the receiving antenna aperture width.

TABLE 11

MAXIMUM DEVIATIONS FROM FAR-FIELD DECOUPLING VALUES IN DECIBELS FOR CORNER NO. 1 OBSTACLE AT SELECTED OBSTACLE DISTANCES AND ANGLES FROM BORESIGHT DIRECTION (TARGET DIRECTION) FOR VERTICALLY AND HORIZONTALLY POLARIZED SIGNALS AT THE FREQUENCY OF 3000 MHz

Obstacle Distance*		DEVIATIONS FOR INDICATED OBSTACLE ANGLES θ AND NORMALIZED WIDTHS** OF W/D = 1.0 AND 0.5					
		$\theta = 0°$		$\theta = 5°$		$\theta = 10°$	
r (feet)	$r/(2D^2/\lambda)$	1.0	0.5	1.0	0.5	1.0	0.5
4	0.041	6.0	2.0	2.5	1.5	1.5	1.5
6	0.061	4.0	1.5	2.5	1.5	1.0	1.0
8	0.082	3.5	1.5	1.5	1.0	0.5	0.5
12	0.123	2.5	1.5	1.0	1.0	0.5	0.0
20	0.184	1.5	1.0	0.5	0.5	0.0	0.0

* r is the distance from the receiving antenna aperture D to the obstacle.
**The normalized width is the ratio of the obstacle width to the receiving antenna aperture width.

TABLE III

MAXIMUM DEVIATIONS FROM FAR-FIELD DECOUPLING VALUES IN DECIBELS FOR CORNER NO. 2 AND SHEET OBSTACLES AT SELECTED OBSTACLE DISTANCES AND ANGLES FROM BORESIGHT DIRECTION (TARGET DIRECTION) FOR VERTICALLY AND HORIZONTALLY POLARIZED SIGNALS AT THE FREQUENCY OF 3000 MHz

Obstacle Distance*		DEVIATIONS FOR INDICATED OBSTACLE ANGLES θ AND NORMALIZED WIDTHS** OF W/D = 1.0 AND 0.5					
		$\theta = 0^\circ$		$\theta = 5^\circ$		$\theta = 10^\circ$	
r (Feet)	$r/(2D^2/\lambda)$	1.0	0.5	1.0	0.5	1.0	0.5
4	0.041	1.0	1.0	1.0	0.5	0.5	0.5
6	0.061	1.0	.05	0.5	0.5	0.0	0.0
8	0.082	0.5	0.5	0.5	0.0	0.0	0.0
12	0.123	0.5	0.5	0.0	0.0	0.0	0.0
20	0.184	0.5	0.5	0.0	0.0	0.0	0.0

* r is the distance from the receiving antenna aperture D to the obstacle.
**The normalized width is the ratio of the obstacle width to the receiving antenna aperture width.

81

TABLE IV

MAXIMUM DEVIATIONS FROM FAR-FIELD DECOUPLING VALUES IN DECIBELS FOR SQUARE COLUMN OBSTACLE AT SELECTED OBSTACLE DISTANCES AND ANGLES FROM BORESIGHT DIRECTION (TARGET DIRECTION) FOR VERTICALLY AND HORIZONTALLY POLARIZED SIGNALS AT THE FREQUENCY OF 5500 MHz

Obstacle Distance*		DEVIATIONS FOR INDICATED OBSTACLE ANGLES θ AND NORMALIZED WIDTHS** OF W/D = 1.0 AND 0.5					
		$\theta = 0^{o}$		$\theta = 5^{o}$		$\theta = 10^{o}$	
r (feet)	$r/(2D^2/\lambda)$	1.0	0.5	1.0	0.5	1.0	0.5
4	0.022	3.0	1.5	2.5	0.5	1.0	0.5
6	0.034	2.0	1.5	1.5	0.5	1.0	0.5
8	0.045	2.0	1.0	1.0	0.0	0.5	0.0
12	0.067	2.0	1.0	0.5	0.0	0.0	0.0
20	0.112	2.0	0.5	0.0	0.0	0.0	0.0

* r is the distance from the receiving antenna aperture D to the obstacle.
**The normalized width is the ratio of the obstacle width to the receiving antenna aperture width.

82

TABLE V

MAXIMUM DEVIATIONS FROM FAR-FIELD DECOUPLING VALUES IN DECIBELS FOR CORNER NO. 1 OBSTACLE AT SELECTED OBSTACLE DISTANCES AND ANGLES FROM BORESIGHT DIRECTION (TARGET DIRECTION) FOR VERTICALLY AND HORIZONTALLY POLARIZED SIGNALS AT THE FREQUENCY OF 5500 MHz

Obstacle Distance*		DEVIATIONS FOR INDICATED OBSTACLE ANGLES θ AND NORMALIZED WIDTHS** OF W/D = 1.0 AND 0.5					
		θ = 0°		θ = 5°		θ = 10°	
r (feet)	$r/(2D^2/\lambda)$	1.0	0.5	1.0	0.5	1.0	0.5
4	0.022	5.0	1.0	1.0	0.5	1.0	0.5
6	0.034	2.5	1.0	1.0	0.5	1.0	0.5
8	0.045	1.0	1.0	0.5	0.0	1.0	0.0
12	0.067	1.0	1.0	0.5	0.0	0.0	0.0
20	0.112	1.0	0.5	0.0	0.0	0.0	0.0

* r is the distance from the receiving antenna aperture D to the obstacle.

**The normalized width is the ratio of the obstacle width to the receiving antenna aperture width.

TABLE VI

MAXIMUM DEVIATIONS FROM FAR-FIELD DECOUPLING VALUES IN DECIBELS FOR CORNER NO. 2 OBSTACLE AT SELECTED OBSTACLE DISTANCES AND ANGLES FROM BORESIGHT DIRECTION (TARGET DIRECTION) FOR VERTICALLY AND HORIZONTALLY POLARIZED SIGNALS AT THE FREQUENCY OF 5500 MHz

Obstacle Distance*		DEVIATIONS FOR INDICATED OBSTACLE ANGLES θ AND NORMALIZED WIDTHS** OF W/D = 1.0 AND 0.5					
		$\theta = 0°$		$\theta = 5°$		$\theta = 10°$	
r (feet)	$r/(2D^2/\lambda)$	1.0	0.5	1.0	0.5	1.0	0.5
4	0.022	1.5	0.0	1.0	0.0	0.5	0.0
6	0.034	1.5	0.0	0.5	0.0	0.5	0.0
8	0.045	0.5	0.0	0.0	0.0	0.0	0.0
12	0.067	0.5	0.0	0.0	0.0	0.0	0.0
20	0.112	0.0	0.0	0.0	0.0	0.0	0.0

* r is the distance from the receiving antenna aperture D to the obstacle.
**The normalized width is the ratio of the obstacle width to the receiving antenna aperture width.

TABLE VII

MAXIMUM DEVIATIONS FROM FAR-FIELD DECOUPLING VALUES IN DECIBELS FOR SQUARE COLUMN OBSTACLE AT SELECTED OBSTACLE DISTANCES AND ANGLES FROM BORESIGHT DIRECTION (TARGET DIRECTION) FOR HORIZONTALLY POLARIZED SIGNALS AT THE FREQUENCY OF 9600 MHz

Obstacle Distance*		DEVIATIONS FOR INDICATED OBSTACLE ANGLES θ AND NORMALIZED WIDTHS** OF W/D = 0.816 AND 0.408					
		$\theta = 0°$		$\theta = 5°$		$\theta = 10°$	
r (feet)	$r/(2D^2/\lambda)$	0.816	0.408	0.816	0.408	0.816	0.408
4	0.009	2.5	1.5	1.5	1.0	1.0	0.0
6	0.013	2.5	1.5	1.5	0.5	0.5	0.0
8	0.017	2.0	1.5	1.5	0.0	0.0	0.0
12	0.026	2.0	1.5	0.5	0.0	0.0	0.0
20	0.043	1.5	1.0	0.5	0.0	0.0	0.0

* r is the distance from the receiving antenna aperture D to the obstacle.
**The normalized width is the ratio of the obstacle width to the receiving antenna aperture width.

TABLE VIII

MAXIMUM DEVIATIONS FROM FAR-FIELD DECOUPLING VALUES IN DECIBELS FOR CORNER NO. 1 OBSTACLE AT SELECTED OBSTACLE DISTANCES AND ANGLES FROM BORESIGHT DIRECTION (TARGET DIRECTION) FOR HORIZONTALLY POLARIZED SIGNALS AT THE FREQUENCY OF 9600 MHz

Obstacle Distance*		DEVIATIONS FOR INDICATED OBSTACLE ANGLES θ AND NORMALIZED WIDTHS** OF W/D = 0.816 AND 0.408					
		$\theta = 0^\circ$		$\theta = 5^\circ$		$\theta = 10^\circ$	
r (feet)	$r/(2D^2/\lambda)$	0.816	0.408	0.816	0.408	0.816	0.408
4	0.009	1.5	2.5	1.0	1.0	0.5	0.0
6	0.013	1.5	2.5	1.0	1.0	0.5	0.0
8	0.017	1.0	1.5	0.5	0.0	0.0	0.0
12	0.026	1.0	1.0	0.0	0.0	0.0	0.0
20	0.043	1.0	0.5	0.0	0.0	0.0	0.0

* r is the distance from the receiving antenna aperture D to the obstacle.
**The normalized width is the ratio of the obstacle width to the receiving antenna aperture width.

TABLE IX

MAXIMUM DEVIATIONS FROM FAR-FIELD DECOUPLING VALUES IN DECIBELS FOR CORNER NO. 2 OBSTACLE AT SELECTED OBSTACLE DISTANCES AND ANGLES FROM BORESIGHT DIRECTION (TARGET DIRECTION) FOR HORIZONTALLY POLARIZED SIGNALS AT THE FREQUENCY OF 9600 MHz

Obstacle Distance*		DEVIATIONS FOR INDICATED OBSTACLE ANGLES θ AND NORMALIZED WIDTHS** OF W/D = 0.816 AND 0.408					
		$\theta = 0^{\circ}$		$\theta = 5^{\circ}$		$\theta = 10^{\circ}$	
(feet)	$r/(2D^2/\lambda)$	0.816	0.408	0.816	0.408	0.816	0.408
4	0.009	1.0	0.0	1.0	0.0	1.0	0.0
6	0.013	1.0	0.0	1.0	0.0	0.0	0.0
8	0.017	1.0	0.0	0.5	0.0	0.0	0.0
12	0.026	0.5	0.0	0.5	0.0	0.0	0.0
20	0.043	0.0	0.0	0.0	0.0	0.0	0.0

* r is the distance from the receiving antenna aperture D to the obstacle.
**The normalized width is the ratio of the obstacle width to the receiving antenna aperture width.

obstacles were essentially always less than 0.5 dB, and therefore, are not included in the tables. As the values in the various tables indicate, the greatest deviations occur on boresight at short obstacle distances. As either the obstacle distance increases or the obstacle angle off boresight increases, the deviations decrease.

C. Maximum Sidelobe-Level Displays

In the displays of Figures 47 through 59, the vertical axis (ordinate) of each display is labeled as the maximum radiation lobe from the boresight value instead of the maximum sidelobe. This designation was chosen because for large obstacles (W/D = 1), the main beam scans off the boresight direction when the obstacles are located on or at an angle off boresight. Therefore, under certain conditions, the maximum value of a lobe off the boresight direction can be that of the main lobe which has scanned off boresight direction, and as a result, is not truly a sidelobe. As a consequence of this possible ambiguity, the designation indicated on the displays was chosen. For curves whose W/D ratio is less than unity, every value on each curve represents a sidelobe value. For the curves whose W/D ratio is unity and for obstacle angles on the right-hand side of the abscissa (indicated as right side lobe on each plot), the negative values for the maximum radiation lobe from the boresight value are for shifted main beams. A correlation of any questionable interpretation of these curves with the corresponding beamshift curves in a subsequent subsection will show whether or not the value in question is for a sidelobe or a shifted main beam. If no displays for shifted main beams exist, the value in question will be a sidelobe value.

88
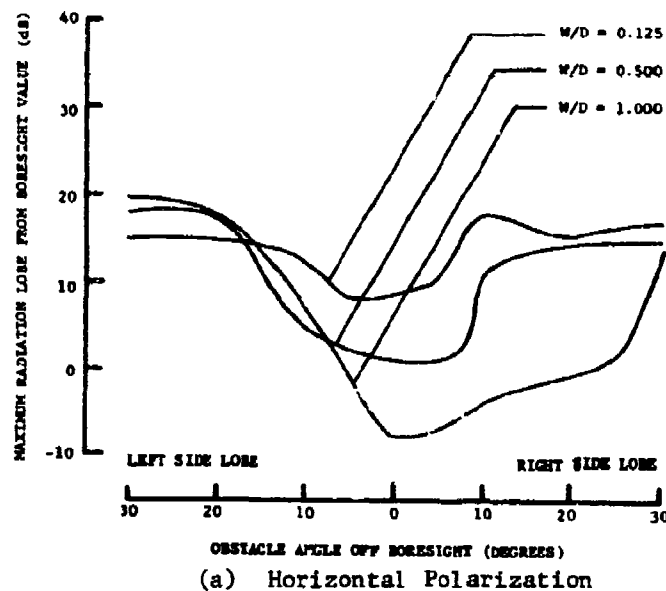
(a) Horizontal Polarization
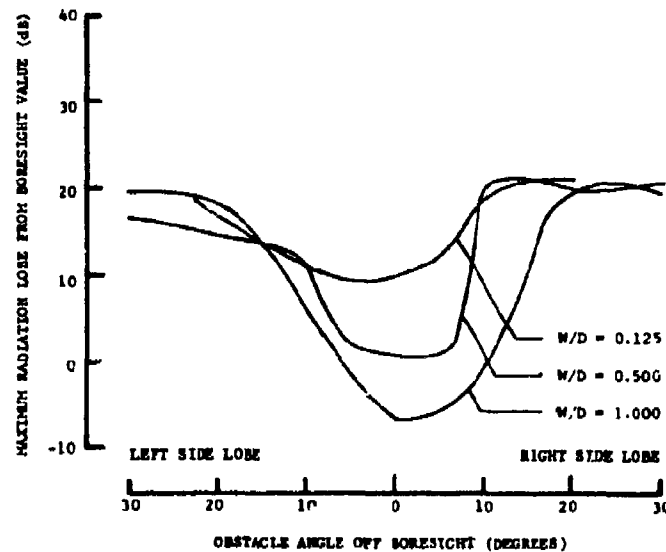
(b) Vertical Polarization

Figure 47. Maximum radiation-lobe levels to the left and right
of boresight as a function of obstacle angle off
boresight for horizontally and vertically polarized
signals for the indicated normalized obstacle widths
at the normalized near-field range of 0.041 at the
frequency of 3000 MHz. The positive values of the
ordinate indicate the level down from boresight
value.
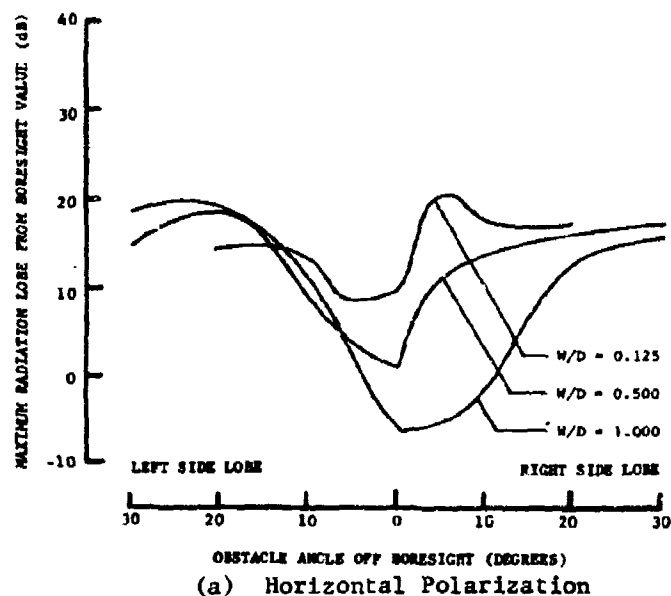
(a) Horizontal Polarization
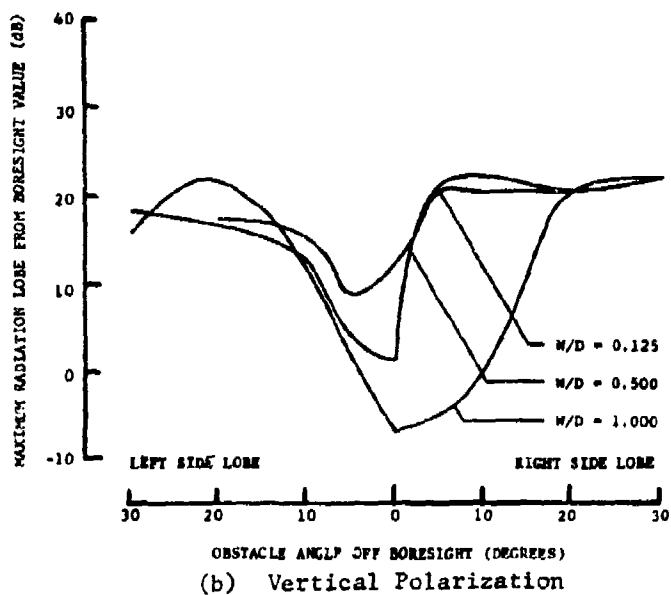
(b) Vertical Polarization

Figure 48. Maximum radiation-lobe levels to the left and right of boresight as a function of obstacle angle off boresight for horizontally and vertically polarized signals for the indicated normalized obstacle widths at the normalized near-field range of 0.061 at the frequency of 3000 MHz. The positive values of the ordinate indicate the level down from boresight value.

(a) Horizontal Polarization

(b) Vertical Polarization
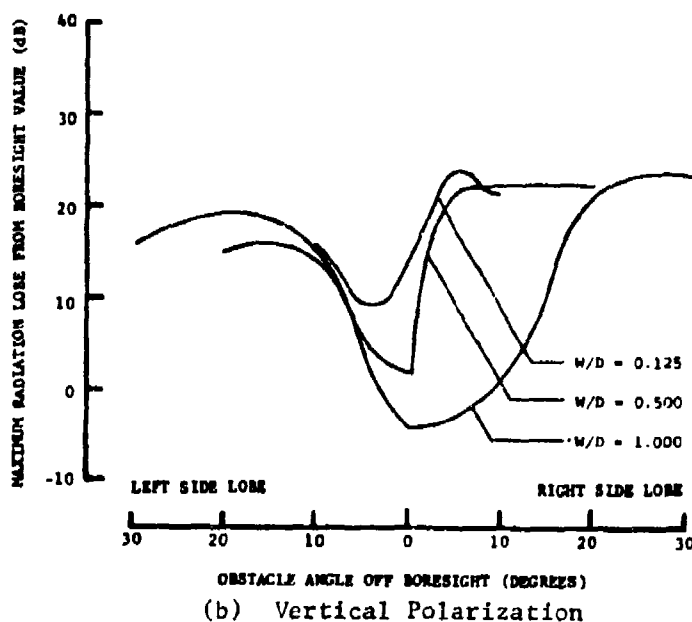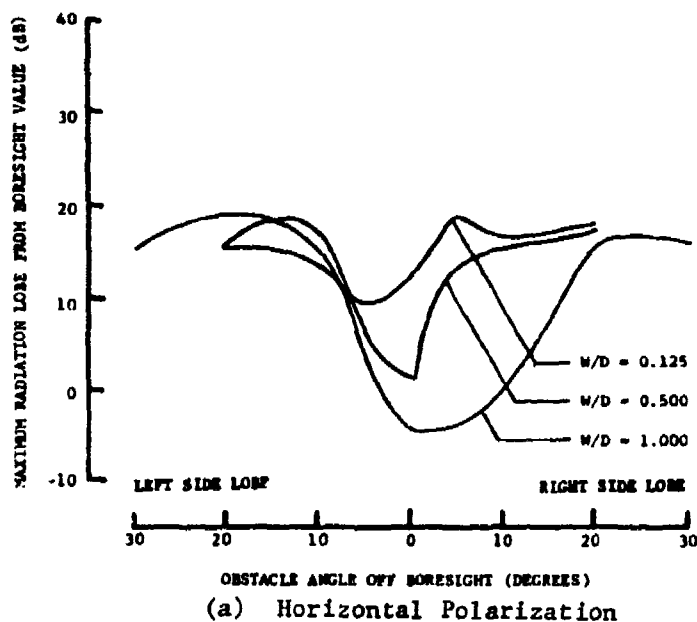
Figure 49. Maximum radiation-lobe levels to the left and right of boresight as a function of obstacle angle off boresight for __horizontally__ and __vertically__ polarized signals for the indicated normalized obstacle widths at the normalized near-field range of __0.082__ at the frequency of __3000__ MHz. The positive values of the ordinate indicate the level down from boresight value.

(a) Horizontal Polarization

(b) Vertical Polarization
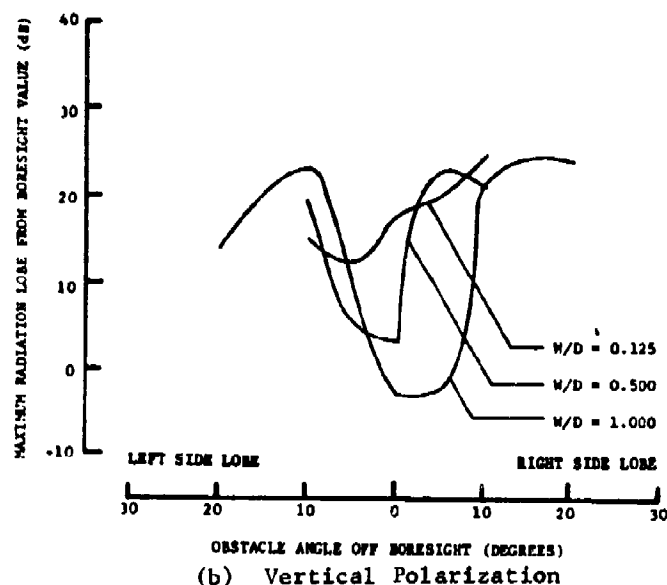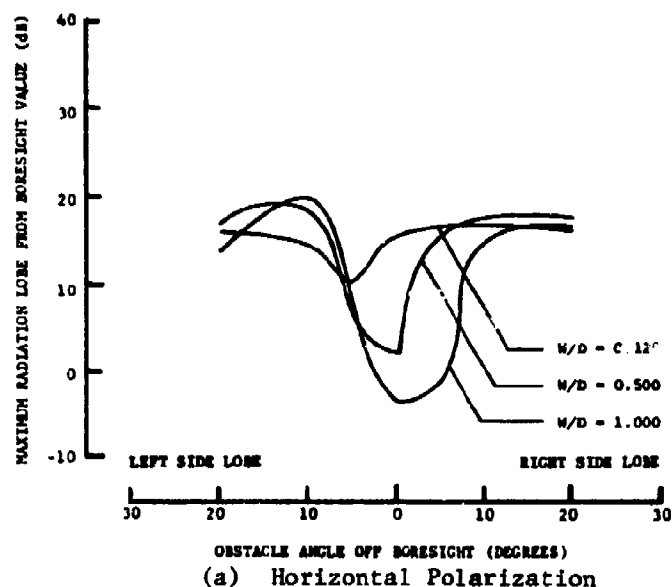
Figure 50.   Maximum radiation-lobe levels to the left and right of
boresight as a function of obstacle angle off boresight
for horizontally and vertically polarized signals for the
indicated normalized obstacle widths at the normalized
near-field range of 0.123 at the frequency of 3000 MHz.
The positive values of the ordinate indicate the level
down from boresight value.

(a) Horizontal Polarization

(b) Vertical Polarization
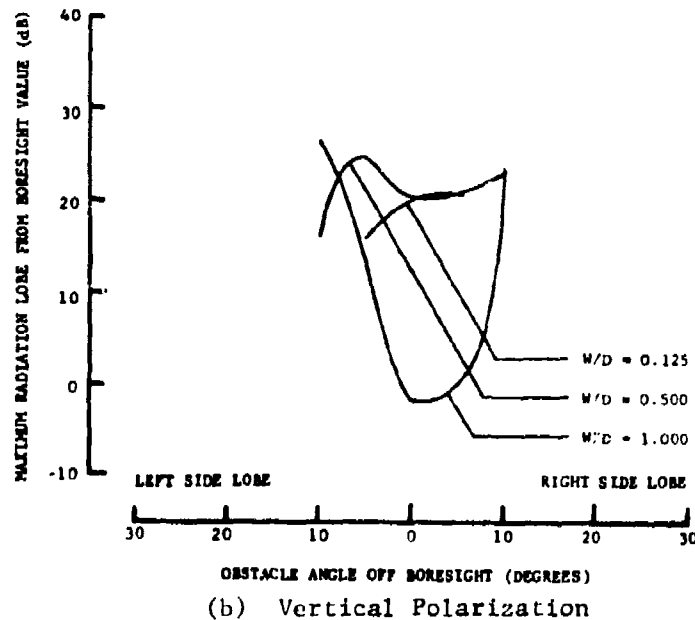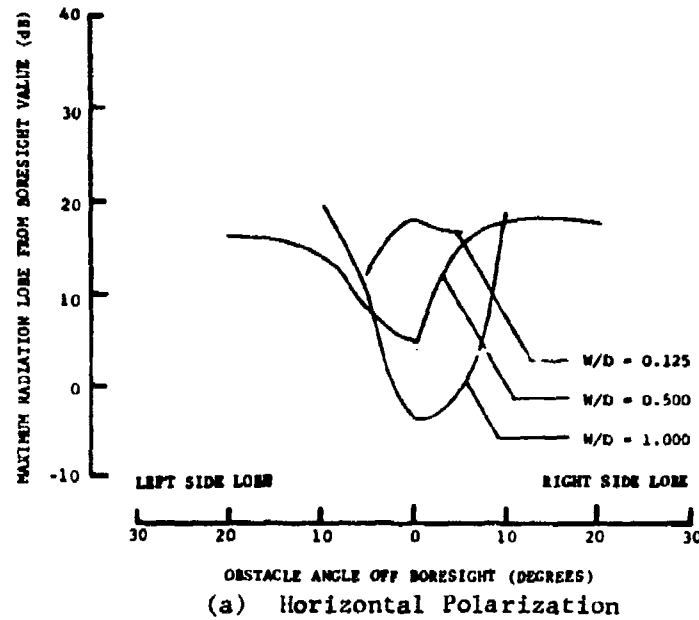
Figure 51. Maximum radiation-lobe levels to the left and right of
boresight as a function of obstacle angle off boresight
for horizontally and vertically polarized signals for the
indicated normalized obstacle widths at the normalized
near-field range of 0.184 at the frequency of 3000 MHz.
The positive values of the ordinate indicate the level
down from boresight value.

93

(a) Horizontal Polarization

(b) Vertical Polarization
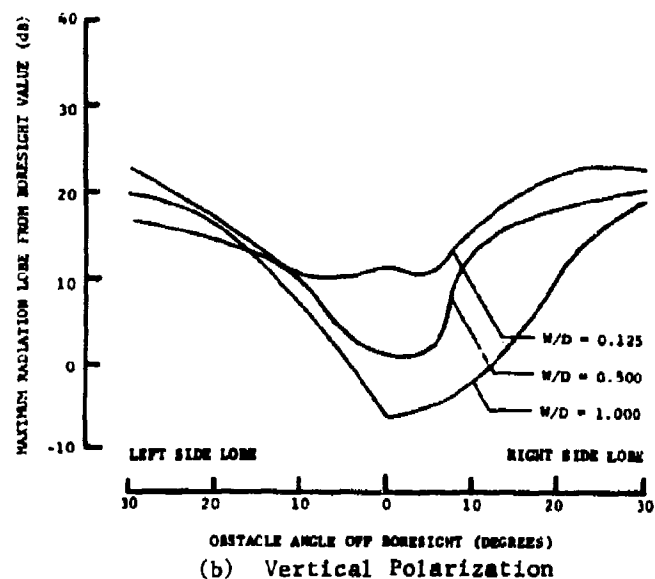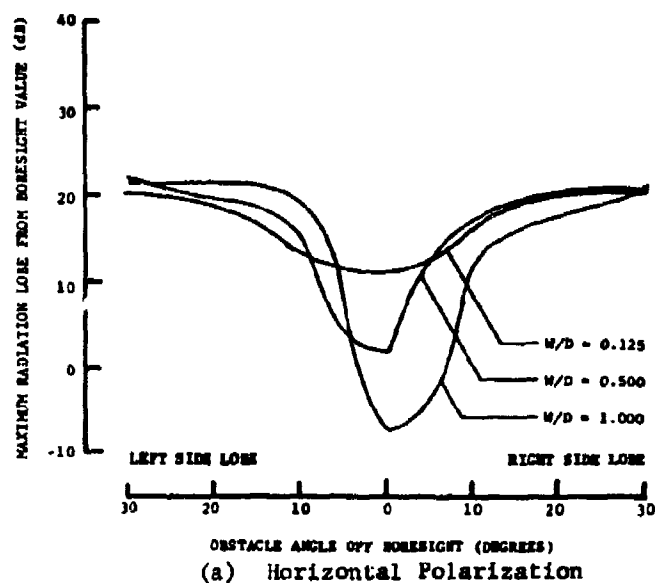
Figure 52. Maximum radiation-lobe levels to the left and right of boresight as a function of obstacle angle off boresight for *horizontally* and *vertically* polarized signals for the indicated normalized obstacle widths at the normalized near-field range of 0.022 at the frequency of 5500 MHz. The positive values of the ordinate indicate the level down from boresight value.

(a) Horizontal Polarization

(b) Vertical Polarization
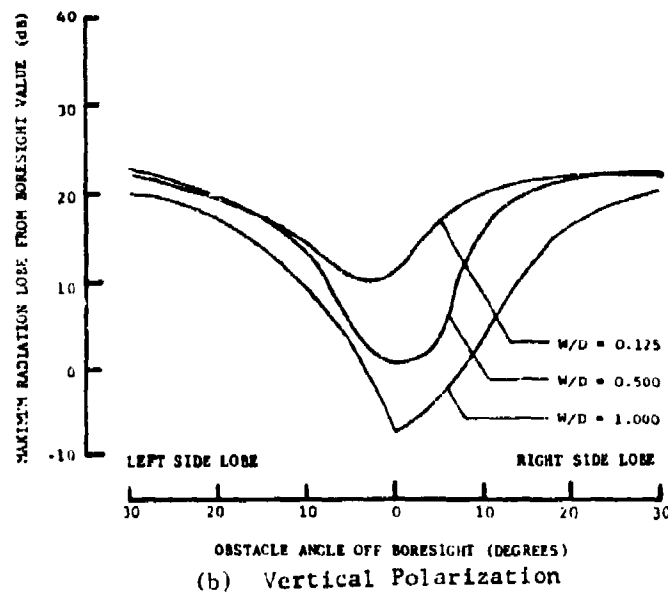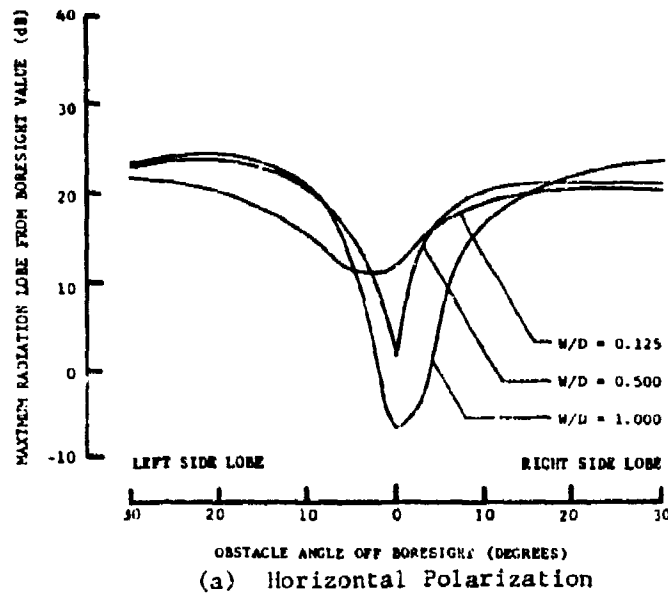
Figure 53. Maximum radiation-lobe levels to the left and right of boresight as a function of obstacle angle off boresight for horizontally and vertically polarized signals for the indicated normalized obstacle widths at the normalized near-field range of 0.034 at the frequency of 5500 MHz. The positive values of the ordinate indicate the level down from boresight value.

95

(a) Horizontal Polarization

(b) Vertical Polarization
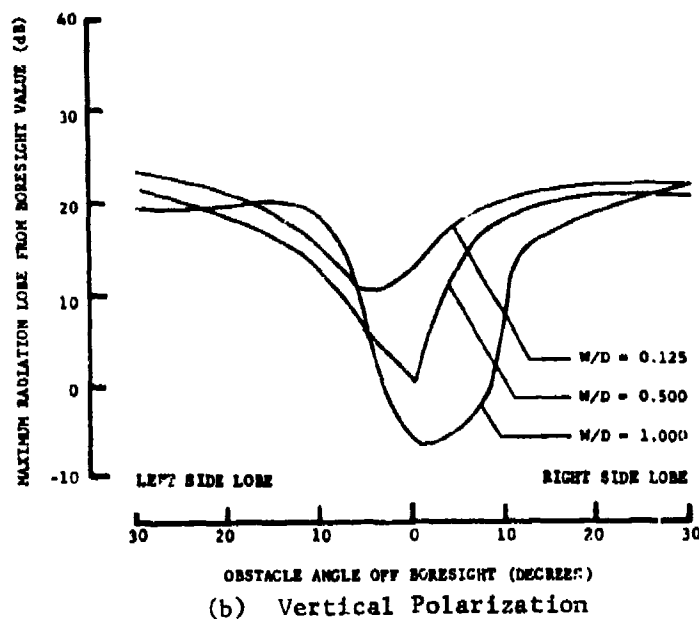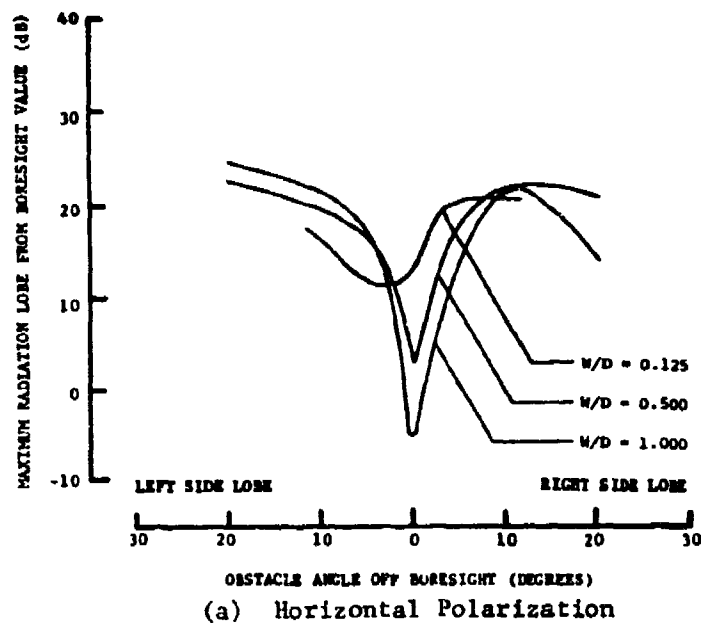
Figure 54. Maximum radiation-lobe levels to the left and right of boresight as a function of obstacle angle off boresight for **horizontally** and **vertically** polarized signals for the indicated normalized obstacle widths at the normalized near-field range of **0.045** at the frequency of **5500** MHz. The positive values of the ordinate indicate the level down from boresight value.

(a)   Horizontal Polarization

(b)   Vertical Polarization
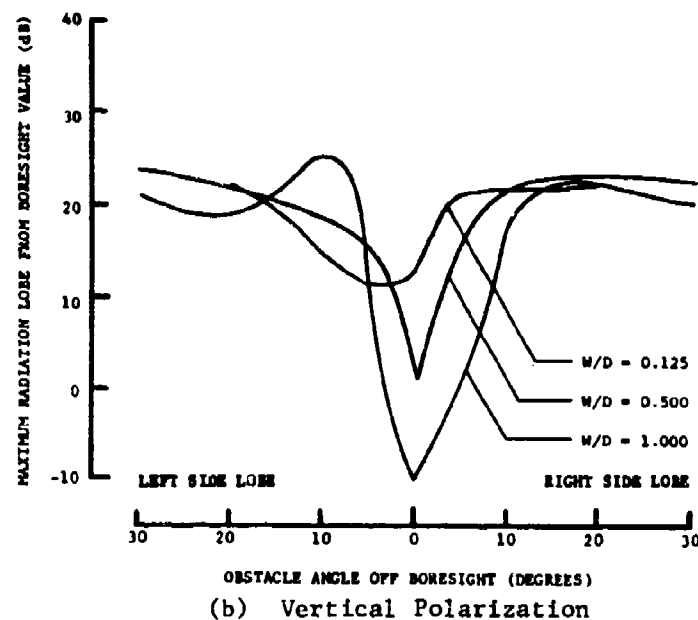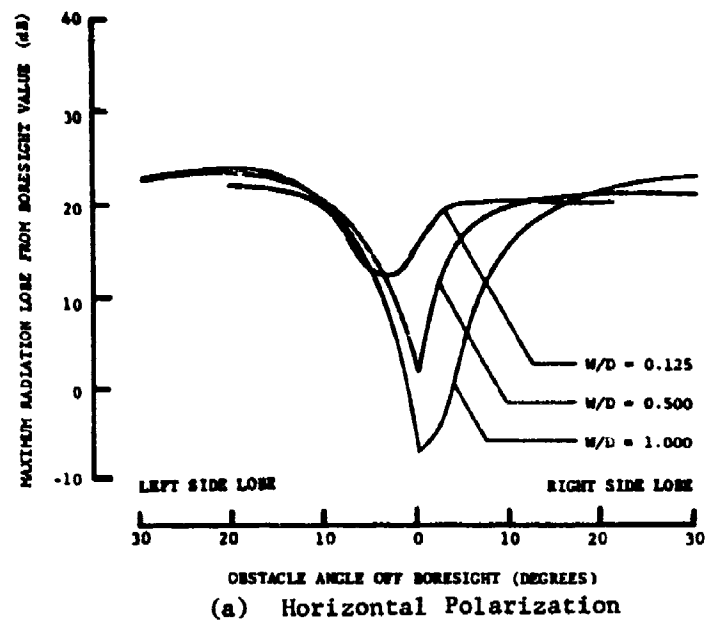
Figure 55.   Maximum radiation-lobe levels to the left and right of
boresight as a function of obstacle angle off boresight
for horizontally and vertically polarized signals for the
indicated normalized obstacle widths at the normalized
near-field range of 0.067 at the frequency of 5500 MHz.
The positive values of the ordinate indicate the level
down from boresight value.

97

(a) Horizontal Polarization

(b) Vertical Polarization
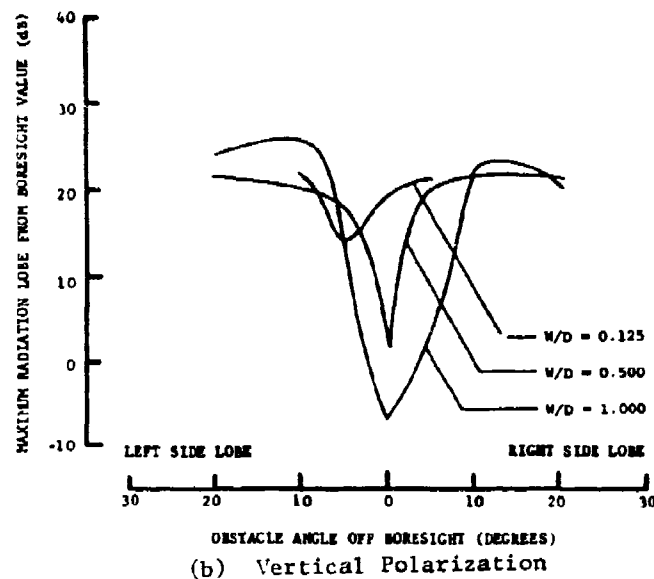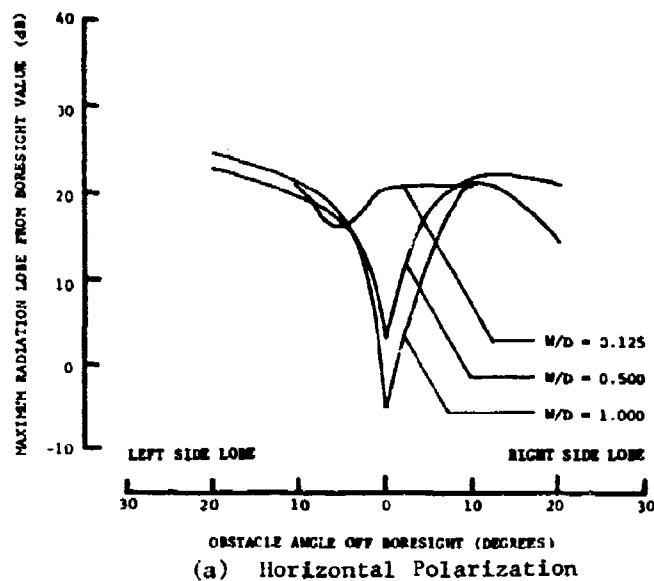
Figure 56. Maximum radiation-lobe levels to the left and right of boresight as a function of obstacle angle off boresight for horizontally and vertically polarized signals for the indicated normalized obstacle widths at the normalized near-field range of 0.112 at the frequency of 5500 MHz. The positive values of the ordinate indicate the level down from boresight value.

(a) $r/(2D^2/\lambda)=0.009$

(b) $r/(2D^2/\lambda)=0.013$
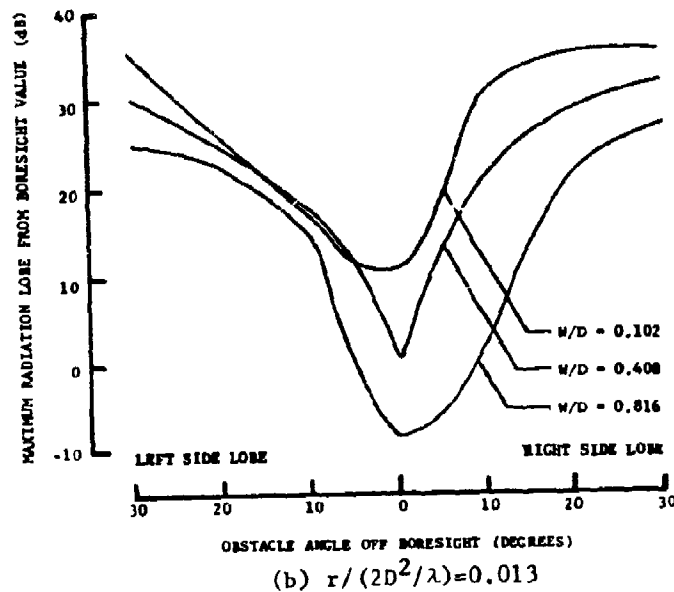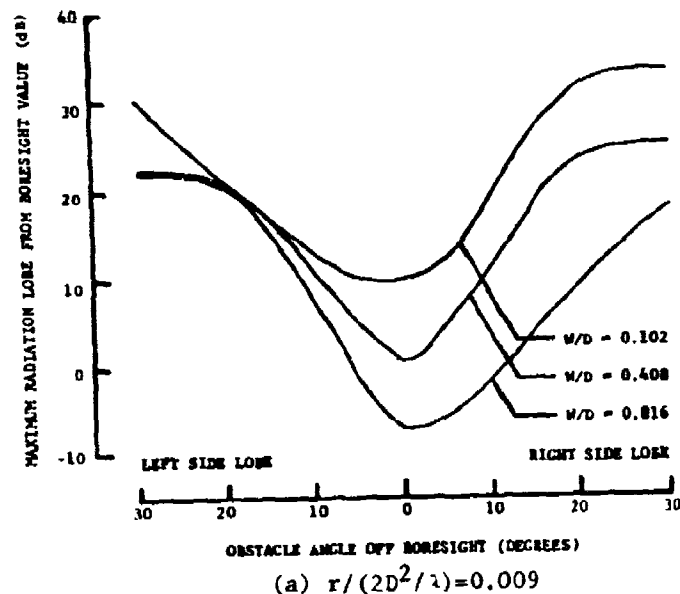
Figure 57. Maximum radiation-lobe levels to the left and right of boresight as a function of obstacle angle off boresight for the horizontally polarized signal for the indicated normalized obstacle widths at the normalized near-field ranges of 0.009 and 0.013 at the frequency of 9600 MHz. The positive values of the ordinate indicate the level down from boresight value.

99

(a) $r/(2D^2/\lambda)=0.017$

(b) $r/(2D^2/\lambda)=0.026$
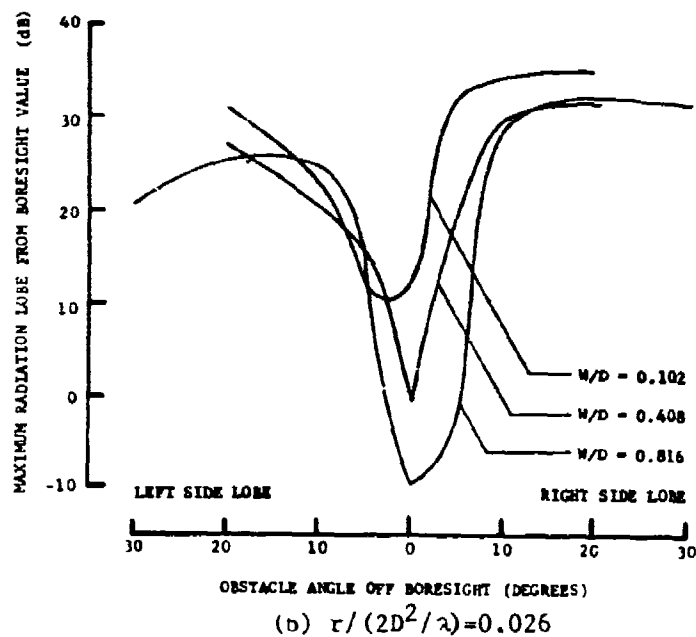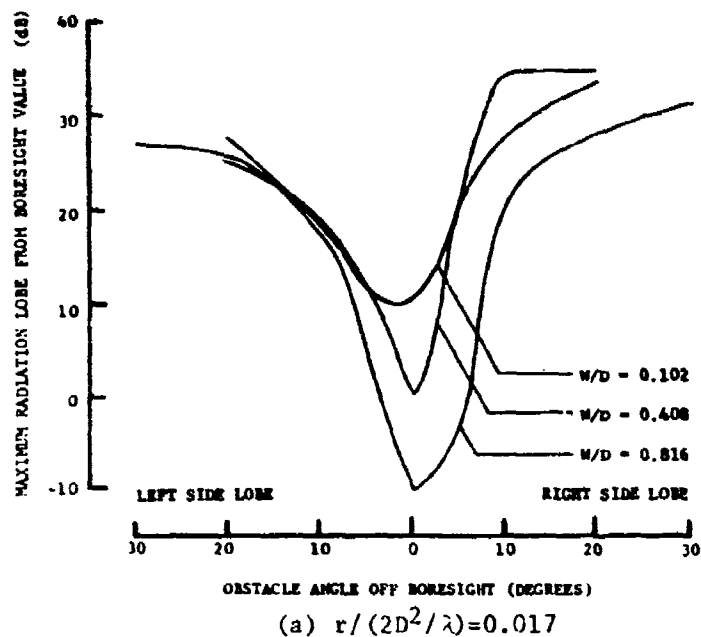
Figure 58. Maximum radiation-lobe levels to the left and right of boresight as a function of obstacle angle off boresight for the horizontally polarized signal for the indicated normalized obstacle widths at the normalized near-field ranges of 0.017 and 0.026 at the frequency of 9600 MHz. The positive values of the ordinate indicate the level down from boresight value.
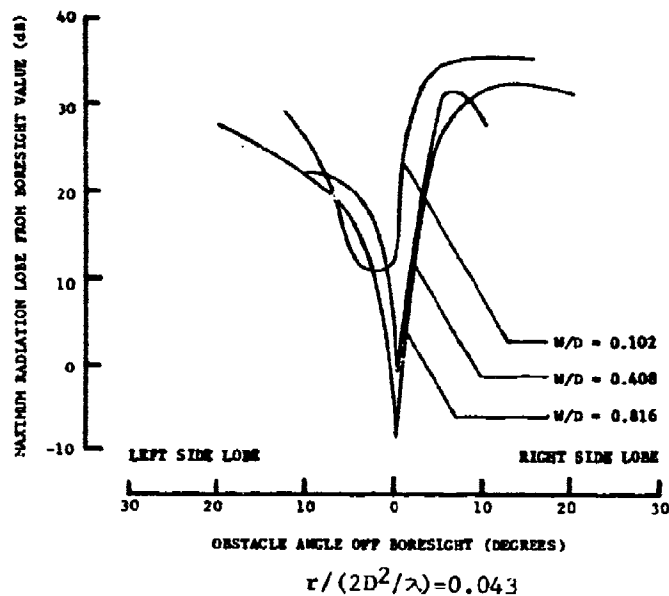
Figure 59. Maximum radiation-lobe levels to the left and right of boresight as a function of obstacle angle off boresight for the horizontally polarized signal for the indicated normalized obstacle width at the normalized near-field range of 0.043 at the frequency of 9600 MHz. The positive values of the ordinate indicate the level down from boresight value.

101

The maximum radiation-lobe levels on both sides of the boresight direction (direction to the target) as a function of the obstacle angle off the boresight direction are displayed in Figures 47 through 59. In these displays, the obstacle angle off boresight is positive both to the right and left of zero degrees. This interpretation must be used because the obstacle was always located on the right-hand side of direction to the target as viewed from the receiving antenna. Therefore, the interpretation of the left sidelobe on the displays is the effect on the left sidelobe of a radiation pattern that an obstacle on the right-hand side of boresight produces. Similarly, the right sidelobe on the displays must be interpreted as the effect on the right sidelobe of a radiation pattern that an obstacle located on the right-hand side of boresight produces, except when a negative value occurs for an obstacle whose W/D equals one as previously explained for the shifted main beam.

The figures are arranged in three groups, and the groups are arranged with increasing frequency. Within each group, the figures are arranged with increasing near-field obstacle distance. In each figure, the results for both polarizations are plotted, and the normalized width of the obstacle is the parameter. Because the raw data indicate that the maximum radiation-lobe levels do not strongly depend on the type of obstacle, each curve of each figure is an average curve derived by averaging the maximum radiation-lobe values of all types of obstacles of a given size. The number of data points included in the calculation of each average value for each obstacle angle varied. In general, approximately 20 to 25 data points, 15 to 20 data points, and 10 to 20

102

data points were used at each obstacle angle when deriving the curves corresponding to W/D ratios of 1.000, 0.500, and 0.125, respectively. The variations from the average curves are summarized in Tables X through XII. For a specified band of variations from the average curve in decibels, the percentage of data points that is within that specified band of variations is indicated in the appropriate table. For an operating frequency of 3000 MHz, for example, 100 percent of the data points was within 3 dB for an obstacle whose normalized width is 0.5 and whose normalized distance from the receiving antenna is 8 feet. Thus, various levels of confidence are indicated in the tables. All of the data points for obstacles of W/D ≈ 0.1 fell within the 3-dB variation band, and thus, are not included in the tables.

The general trends of the curves in each frequency group are similar. As expected, the most severe degradations generally occur in the neighborhood of boresight. In each figure, the positive values for the maximum radiation lobe indicate the values down from the value on antenna boresight. Consequently, the negative values, which only occur for obstacles whose W/D ratio is approximately unity, indicate that maximum radiation lobe values are greater than the boresight values. As the various displays show, the left and right sidelobes are affected differently for a given obstacle angle off boresight as the receiving antenna is rotated in the horizontal azimuthal plane. Also, the displays show that an obstacle located near the antenna affects the maximum radiation level over a larger angular sector than does an obstacle farther away from the antenna.

103

TABLE X

DEVIATIONS OF SIDELOBE DATA FROM THE CORRESPONDING AVERAGE CURVES FOR 3000 MHz FOR THE INDICATED NORMALIZED* OBSTACLE SIZES AND THE INDICATED OBSTACLE RANGES FOR BOTH PARALLEL POLARIZATIONS**

Obstacle Range		Normal Obstacle Width	Percentage of Measured Sidelobe Data That Are within 3 dB and 5 dB of the Corresponding Average Curve***			
			3 dB		5 dB	
r (feet)	$r/(2D^2/\lambda)$	W/D	H	V	H	V
4	0.041	0.5	96	100	100	100
		1.0	89	78	100	88
6	0.061	0.5	88	98	98	100
		1.0	90	98	100	100
8	0.082	0.5	100	100	100	100
		1.0	98	98	100	100
12	0.123	0.5	100	100	100	100
		1.0	100	94	100	100
20	0.184	0.5	100	100	100	100
		1.0	100	100	100	100

* The normalized width is the ratio of the obstacle width, W, to the horizontal width, D, of the receiving antenna.

** H and V designate horizontal and vertical polarizations, respectively.

***The sidelobe data for all obstacles of W/D = 0.125 for all obstacle ranges and both polarizations are within 3 dB of the corresponding average sidelobe curve.

TABLE XI

DEVIATIONS OF SIDELOBE DATA FROM THE CORRESPONDING AVERAGE CURVES FOR 5500 MHz FOR THE INDICATED NORMALIZED* OBSTACLE SIZES AND THE INDICATED OBSTACLE RANGES FOR BOTH PARALLEL POLARIZATIONS**

Obstacle Range		Normal Obstacle Width	Percentage of Measured Sidelobe Data That Are within 3 dB and 5 dB of the Corresponding Average Curve***			
			3 dB		5 dB	
r (feet)	$r/(2D^2/\lambda)$	W/D	H	V	H	V
4	0.022	0.5	91	94	100	100
		1.0	78	64	95	91
6	0.034	0.5	100	100	100	100
		1.0	94	72	98	97
8	0.045	0.5	100	100	100	100
		1.0	88	84	100	100
12	0.067	0.5	100	92	100	100
		1.0	89	82	100	95
20	0.112	0.5	100	97	100	100
		1.0	100	68	100	88

* The normalized width is the ratio of the obstacle width, W, to the horizontal width, D, of the receiving antenna.

** H and V designate horizontal and vertical polarizations, respectively.

***The sidelobe data for all obstacles of W/D = 0.125 for all obstacle ranges and both polarizations are within 3 dB of the corresponding average sidelobe curve.

105

TABLE XII

DEVIATIONS OF SIDELOBE DATA FROM THE CORRESPONDING AVERAGE CURVES FOR 9600 MHz FOR THE INDICATED NORMALIZED* OBSTACLE SIZES AND THE INDICATED OBSTACLE RANGES FOR BOTH PARALLEL POLARIZATIONS**

Obstacle Range		Normal Obstacle Width	Percentage of Measured Sidelobe Data That Are within 3 dB and 5 dB of the Corresponding Average Curve***			
			3 dB		5 dB	
r (feet)	$r/(2D^2/\lambda)$	W/D	H	V	H	V
4	0.009	0.5	68	–	98	–
		1.0	72	–	84	–
6	0.013	0.5	94	–	100	–
		1.0	77	–	90	–
8	0.017	0.5	100	–	100	–
		1.0	83	–	100	–
12	0.026	0.5	100	–	100	–
		1.0	86	–	95	–
20	0.043	0.5	100	–	100	–
		1.0	97	–		–

* The normalized width is the ratio of the obstacle width, W, to the horizontal width, D, of the receiving antenna.

** H and V designate horizontal and vertical polarizations, respectively.

*** The sidelobe data for all obstacles of W/D = 0.104 for all obstacle ranges and both polarizations are within 3 dB of the corresponding average sidelobe curve.

D. Half-Power Beamwidths

The half-power beamwidths as a function of obstacle angle off bore-sight are presented in Figures 60 through 65. The normalized obstacle distance from the receiving antenna is the parameter in these curves. The 3-dB beamwidths for obstacles of normalized widths of approximately one are for the shifted beam as indicated on each ordinate in Figures 60, 63, and 65(a). For normalized obstacle widths of approximately 0.5 and 0.1, the 3-dB beamwidths characterize the beam on boresight. A discussion of shifted beams is given in the following subsection.

For a given obstacle distance, obstacle size, obstacle angle, and polarization, the beamwidths for all the obstacles were averaged to derive the curves of Figures 60 through 65. In the various displays of curves, some of the curves for the largest-size obstacles ($W/D \approx 1$) are shown as a mixture of solid and dashed lines. The dashed lines indicate the situations in which the square column obstacle data were not used in the empirical derivation of the average curves; however, all of the data for the other obstacles were used in the derivation. The solid lines indicate that all obstacle data, including that of the square column, were used. Observations of the various curves show that the portions of the square column data that were not used occurred only for the largest size ($W/D \approx 1$) and that the usage of the square column data depended on the near-field obstacle distance from the receiving antenna and on the obstacle angle off the boresight direction. In general, the shorter the near-field obstacle distance and the smaller the obstacle angle off boresight, the less often were the square column data used in the average-curve derivations.

(a) Horizontal Polarization

(b) Vertical Polarization
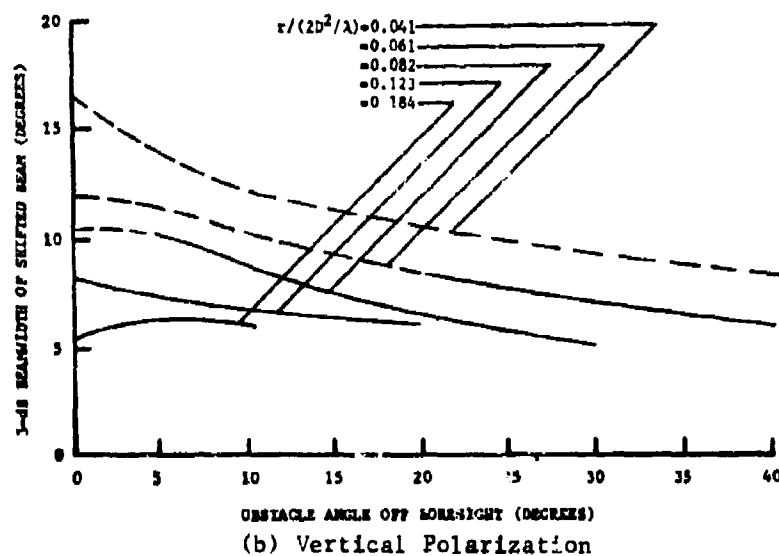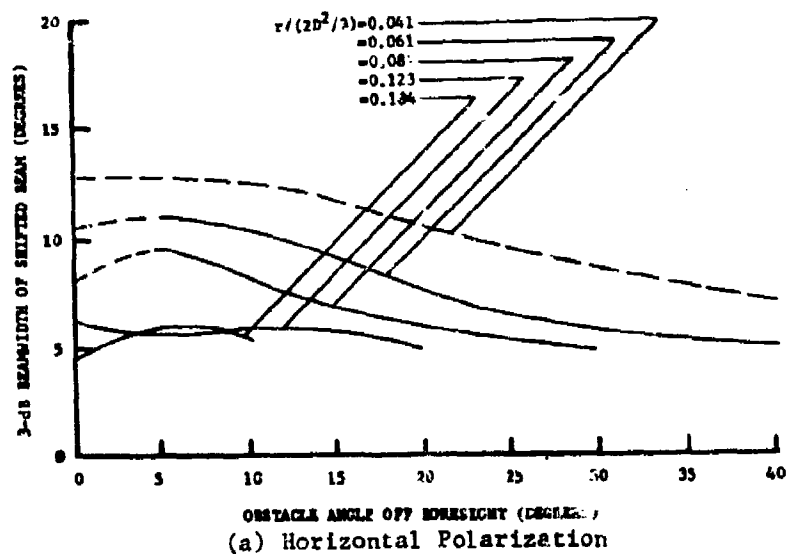
Figure 60. Half-power beamwidth as a function of obstacle angle off boresight for the indicated normalized obstacle distances. For each curve in the family, the levels for each obstacle of normalized width of 1.000 were combined for horizontally and vertically polarized signals at the frequency of 3000 MHz.

108
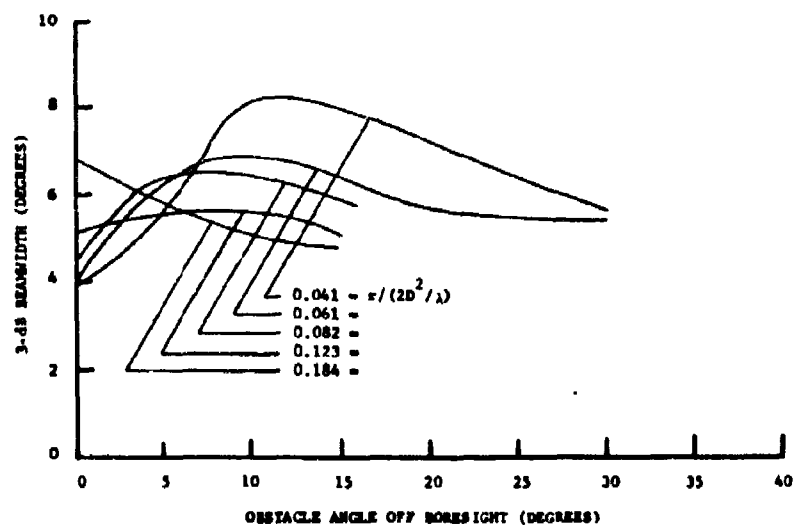
(a) Horizontal Polarization
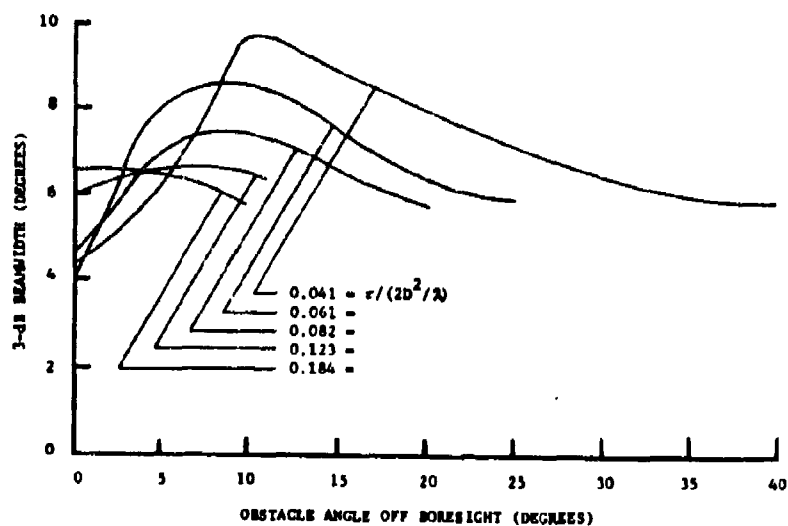
(b) Vertical Polarization

Figure 61. Half-power beamwidth as a function of obstacle angle off
boresight for the indicated normalized obstacle distances.
For each curve in the family, the levels for each obstacle
of normalized width of 0.500 were combined for horizontally
and vertically polarized signals at the frequency of 3000
MHz.

109

(a) Horizontal Polarization

(b) Vertical Polarization
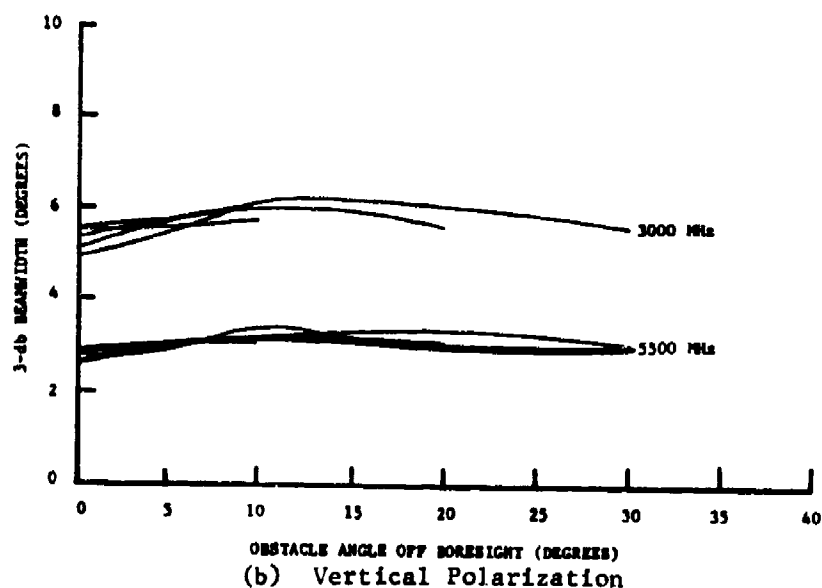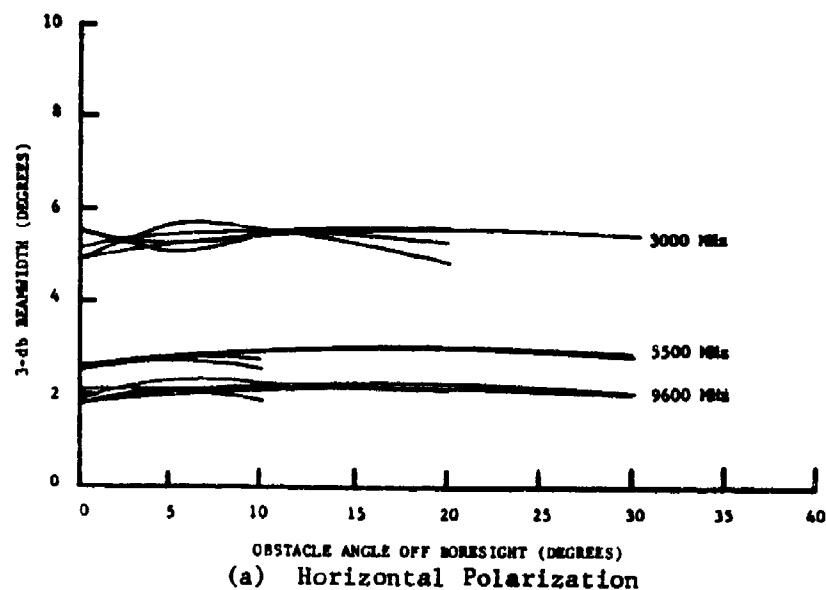
Figure 62.   Half-power beamwidth as a function of obstacle angle off
boresight for _horizontally_ and _vertically_ polarized
signals for the indicated frequencies for all obstacle
distances and for all obstacles whose normalized widths
are approximately _0.125_.

110

(a) Horizontal Polarization

(b) Vertical Polarization
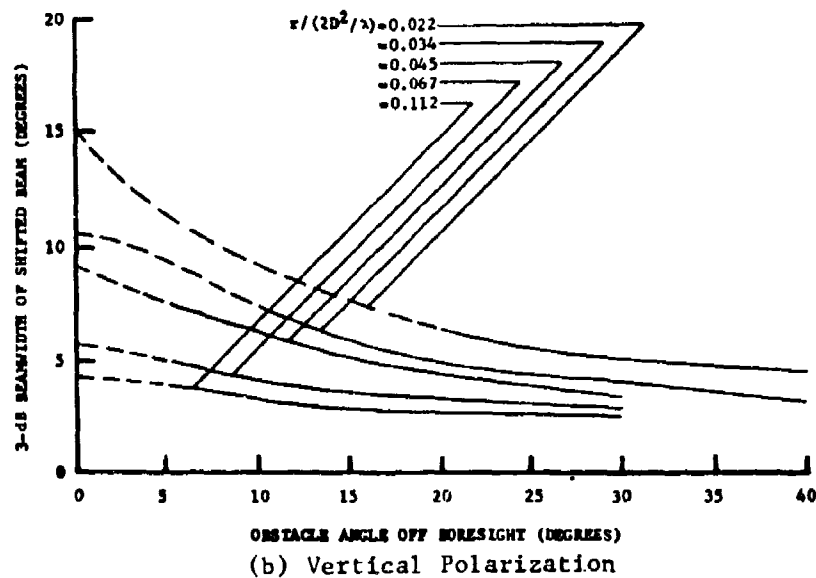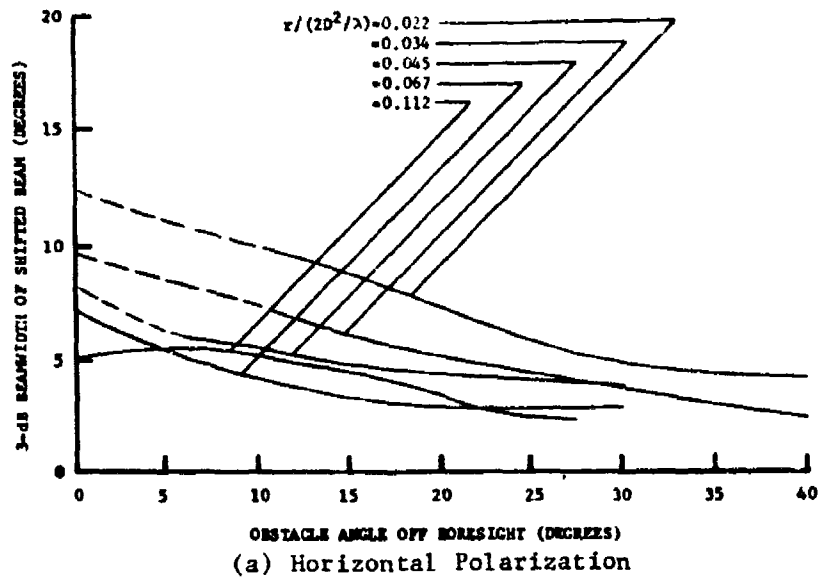
Figure 63. Half-power beamwidth as a function of obstacle angle off boresight for the indicated normalized obstacle distances. For each curve in the family, the levels for each obstacle of normalized width of 1.000 were combined for horizontally and vertically polarized signals at the frequency of 5500 MHz.

111

(a) Horizontal Polarization

(b) Vertical Polarization
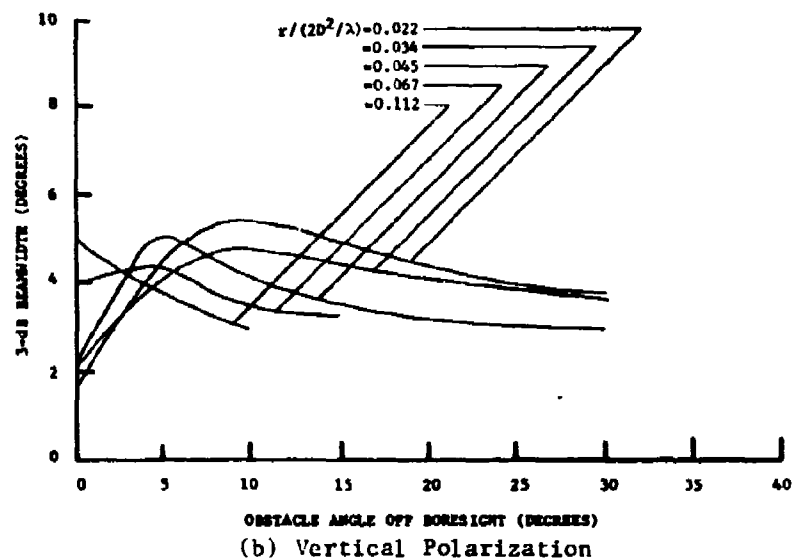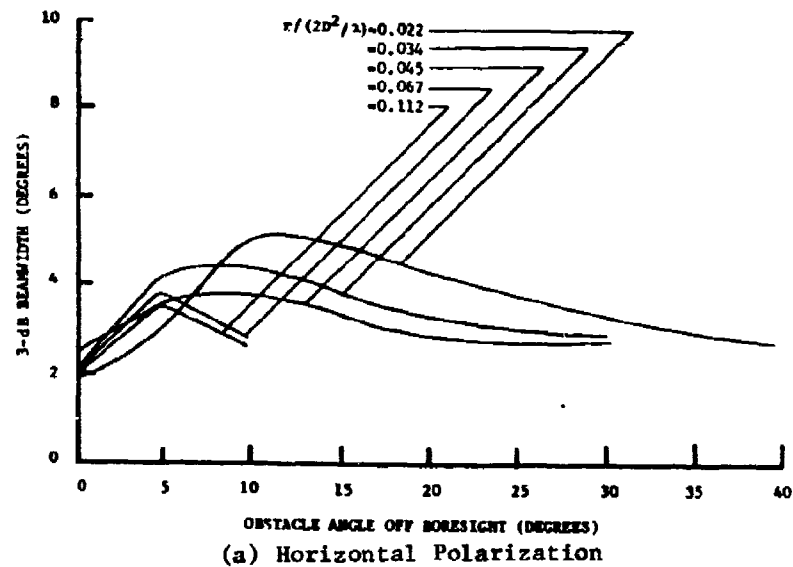
Figure 64. Half-power beamwidth as a function of obstacle angle off boresight for the indicated normalized obstalce distances. For each curve in the family, the levels for each obstacle of normalized width of 0.500 were combined for horizontally and vertically polarized signals at the frequency of 5500 MHz.

112
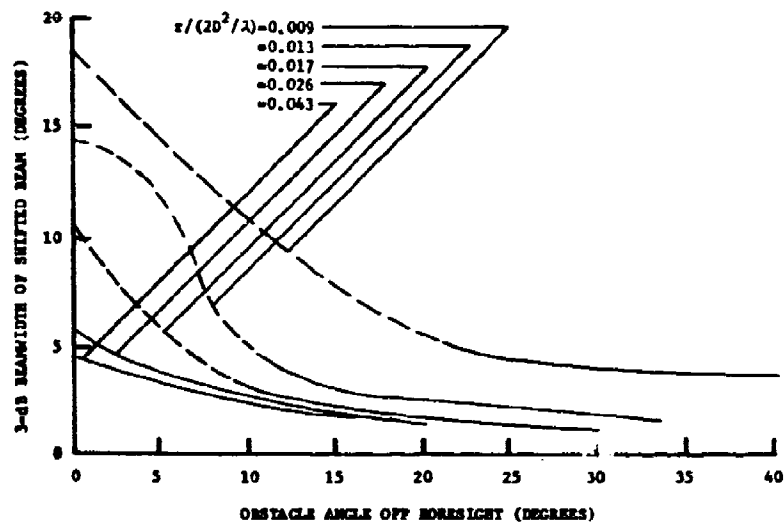
(a) W/D = 0.816
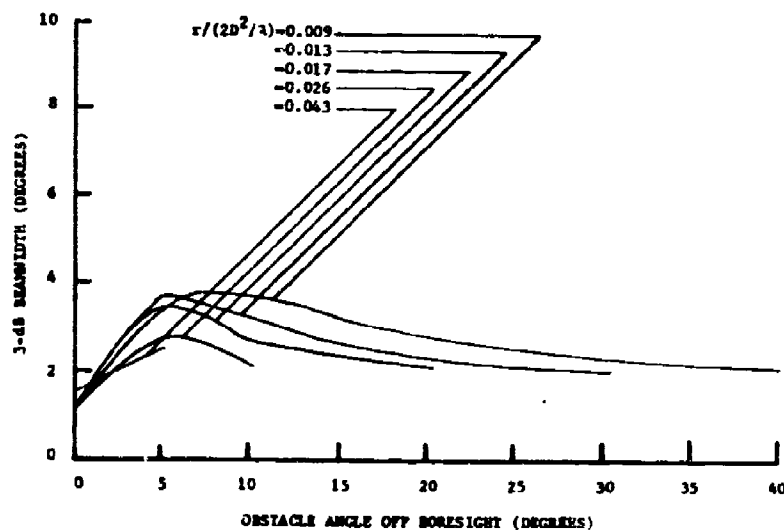
(b) W/D = 0.408

Figure 65. Half-power beamwidth as a function of obstacle angle off boresight for the indicated normalized obstacle distances. For each curve in the family, the levels for each obstacle of normalized widths of 0.816 and 0.408 at the frequency of 9600 MHz.

The square column obstacle located in the near field of an antenna generally affected the far-field antenna pattern to a larger extent than did the other obstacles, particularly for short obstacle distances and small obstacle angles on or off the boresight direction. When the degradations approached a certain stage, no attempts to approximate the 3-dB beamwidths were made. The two antenna patterns in Figures 66(a) and (b) associated with the 48-inch wide square column obstacle (W/D = 1) illustrate the changes that can occur when the near-field distance of the obstacle from the receiving antenna is changed by an incremental amount, typically a fraction of a wavelength. The dashed lines at the top of each pattern indicate the approximations made in order to read the 3-dB beamwidths. For pattern degradations worse than these, the beamwidth data were not included in the empirical derivations of the beamwidth curves, as is indicated by the dashed portions of the curves. In Figure 66, note that the beamwidths are for beams shifted off the boresight direction (0° in the figure).

The maximum deviations from the various average curves are given in Tables XIII and XIV. Although the maximum deviations are relatively small, the largest variations generally occur for obstacle angles close-in to boresight, while the smallest variations generally occur for large obstacle angles off the boresight direction. The square column obstacle generally produced the largest deviations from the various average curves. As the tables show, the variations from the average curves are generally slightly larger for larger W/D ratios. As the obstacle angle increases, the variations from the average curves tend to be smaller for the smaller obstacles.

(b) r = 8 feet + Δλ
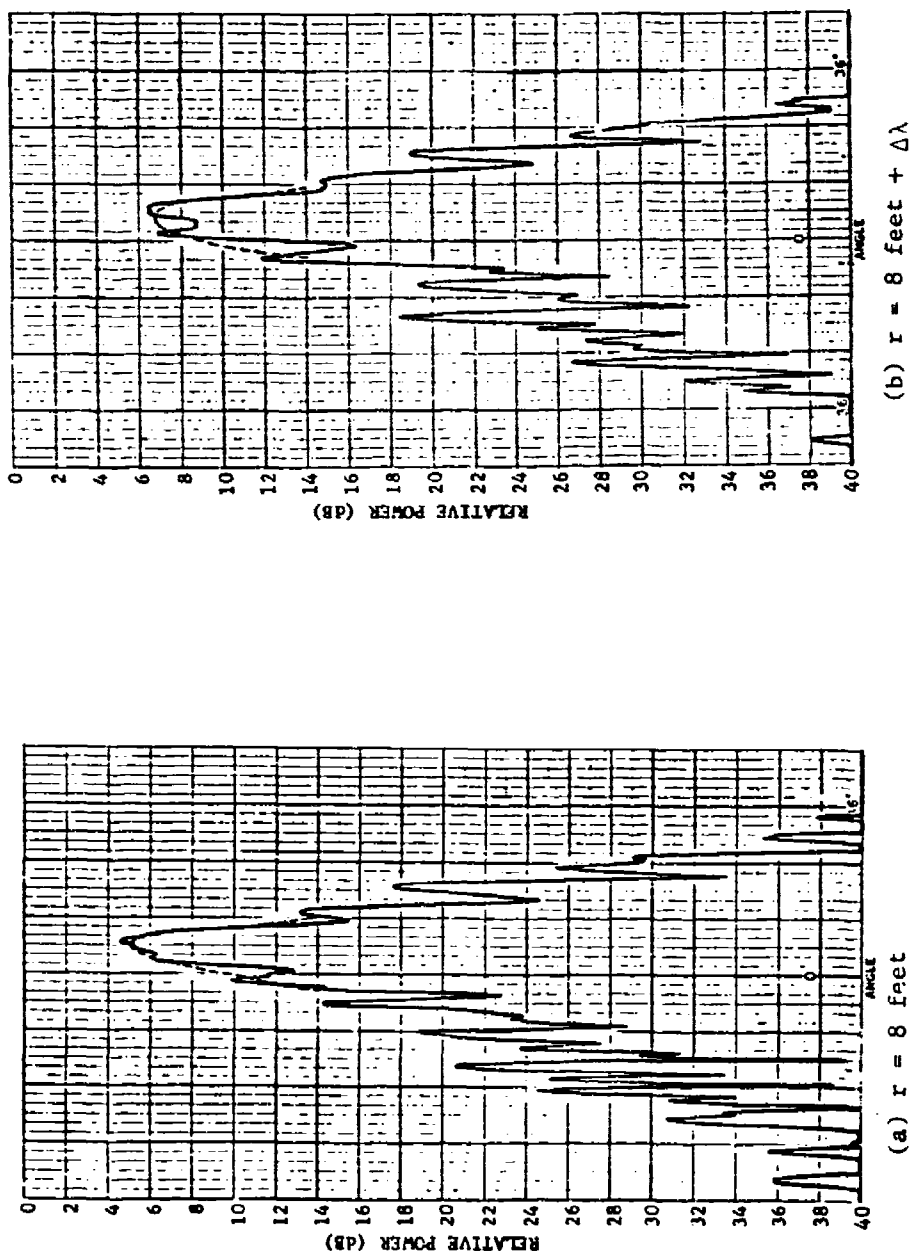
(a) r = 8 feet

Figure 66. These C-band antenna patterns for horizontally polarized signals with the 48-inch square column located at 5 degrees off the boresight direction at a near-field distance of r = 8 feet and r = 8 feet+Δλ illustrate typical worst case conditions in which the 3-dB beamwidths were approximated (by dashed lines in figures). The gain relative to isotropic is 26 dB at the top of the charts.

115

TABLE XIII

MAXIMUM DEVIATIONS OF BEAMWIDTHS FROM AVERAGE CURVES AND OBSTACLE ANGLES WHERE MAXIMUM DEVIATIONS OCCURRED FOR LARGEST-SIZE OBSTACLES FOR INDICATED OBSTACLE DISTANCES AND FREQUENCY BANDS

r(feet)	Obstacle Distance $r/(2D^2/\lambda)$			Maximum Deviation (Degrees)			Obstacle Angle Where Maximum Deviation Occurred (Degrees)		
	S-Band	C-Band	X-Band	S-Band	C-Band	X-Band	S-Band	C-Band	X-Band
(Horizontal Polarization)									
4	0.041	0.022	0.009	2.5	2.5	5.0	10.0	0.0	0.0
6	0.061	0.034	0.013	2.0	2.0	2.5	5.0	0.0	0.0
8	0.082	0.045	0.017	1.5	1.5	2.0	0.0	0.0	0.0
12	0.123	0.067	0.026	1.0	1.0	2.0	0.0	0.0	5.0
20	0.184	0.112	0.043	0.5	1.0	2.0	5.0	0.0	0.0
(Vertical Polarization)									
4	0.041	0.022	0.009	3.0	2.0	—	10.0	0.0	—
6	0.061	0.034	0.013	2.0	1.0	—	0.0	0.0	—
8	0.082	0.045	0.017	2.0	1.0	—	0.0	5.0	—
12	0.123	0.067	0.026	1.5	.5	—	0.0	0.0	—
20	0.184	0.112	0.043	0	.5	—	5.0	0.0	—

TABLE XIV

MAXIMUM DEVIATIONS OF BEAMWIDTHS FROM AVERAGE CURVES AND OBSTACLE ANGLES WHERE MAXIMUM DEVIATIONS OCCURRED FOR MIDDLE-SIZE OBSTACLES FOR INDICATED OBSTACLE DISTANCES AND FREQUENCY BANDS

(Horizontal Polarization)

r(feet)	Obstacle Distance $r/(2D^2/\lambda)$			Maximum Deviation (Degrees)			Obstacle Angle Where Maximum Deviation Occurred (Degrees)		
	S-Band	C-Band	X-Band	S-Band	C-Band	X-Band	S-Band	C-Band	X-Band
4	0.041	0.022	0.009	2.0	1.0	0.5	20.0	10.0	10.0
6	0.061	0.034	0.013	1.5	0.5	0.5	5.0	10.0	10.0
8	0.082	0.045	0.017	1.0	0.5	0.5	5.0	5.0	5.0
12	0.123	0.067	0.026	0.5	0.5	0.5	5.0	10.0	0.0
20	0.184	0.112	0.043	0.5	0.5	0.5	5.0	5.0	5.0

(Vertical Polarization)

r(feet)	Obstacle Distance $r/(2D^2/\lambda)$			Maximum Deviation (Degrees)			Obstacle Angle Where Maximum Deviation Occurred (Degrees)		
	S-Band	C-Band	X-Band	S-Band	C-Band	X-Band	S-Band	C-Band	X-Band
4	0.041	0.022	0.009	2.0	1.5	—	10.0	5.0	—
6	0.061	0.034	0.013	1.5	1.0	—	10.0	5.0	—
8	0.082	0.045	0.017	0.5	0.5	—	5.0	5.0	—
12	0.123	0.067	0.026	1.0	2.0	—	0.0	0.0	—
20	0.184	0.112	0.043	0.5	3.0	—	0.0	0.0	—

Several general trends are apparent from the displays. For the largest-size obstacles (W/D ≈ 1), the beamwidth of the main beam is largest when the obstacle is located on boresight but decreases toward the clear-site beamwidth as the obstacle angle increases. However, for the middle-size obstacles (W/D ≈ 0.5) and smallest-size obstacles (W/D ≈ 0.125), the beamwidths on boresight tend to be less than the clear-site beamwidths, reach maximum values at intermediate angles off boresight, and then approach the clear-site beamwidth values as the obstacle angles further increase. The clear-site 3-dB beamwidths are approximately 5.5 degrees, 3.0 degrees, and 2.0 degrees for 3000 MHz, 5500 MHz, and 9600 MHz, respectively. The various displays also indicate that for a given obstacle angle, the differences between beamwidths as a function of near-field distance are generally greater for larger obstacles than for smaller-size obstacles. As a consequence, all of the curves for the smallest obstacles for all three test frequencies are combined and displayed in Figure 62. Because the spread of beamwidth values as a function of obstacle was so small, the parameters indicating the near-field obstacle distances are not shown in Figure 62.

E. Beamshifts

Experimental tests previously conducted [1] indicated that obstacles located in the near field of an antenna cause an angular shift (or scan) in the pointing direction of the main beam of the antenna. As a result, the return signal from a far-field target appears to be coming from a direction other than the true target direction; conse-

quently, an error in bearing occurs. Additional tests under the current program were conducted to investigate this phenomena further. These tests involved various types and sizes of obstacles. The results indicate that the magnitude of the beamshift strongly depends on the normalized width (ratio of obstacle width to antenna aperture width) of the obstacle and on the obstacle angle off the boresight direction. For small normalized obstacle widths ($W/D \approx 0.1$), no significant beamshifts occur. For W/D ratios of approximately 0.5, small beamshifts, which usually appeared to be much less than 0.5 degree, apparently occurred for obstacle angles near boresight, but no well-defined trends could be definitely established within the measurement accuracy achievable in these particular tests. However, for large obstacles whose W/D ratios are approximately unity, significant beamshifts occur. Consequently, the tests indicate that obstacles whose normalized widths are greater than 0.5 produce significant beamshifts and should be considered in electromagnetic effectiveness performance analyses.

Empirically-derived curves of beamshifts as a function of obstacle angle off the boresight direction (direction to the target) are displayed in Figures 67 through 69 for obstacles whose W/D ratios are approximately unity. The near-field distance of the obstacles from the receiving antenna is the parameter in the families of curves. In each figure, the beamshifts for both vertical and horizontal polarizations are displayed. For each curve at each near-field distance, the data for all obstacles of a given size ($W/D \approx 1$) were averaged for each polarization. As was the case for the beamwidth displays discussed in the previous subsection, the dashed lines in Figures 67 through 69

119

(a) Horizontal Polarization

(b) Vertical Polarization
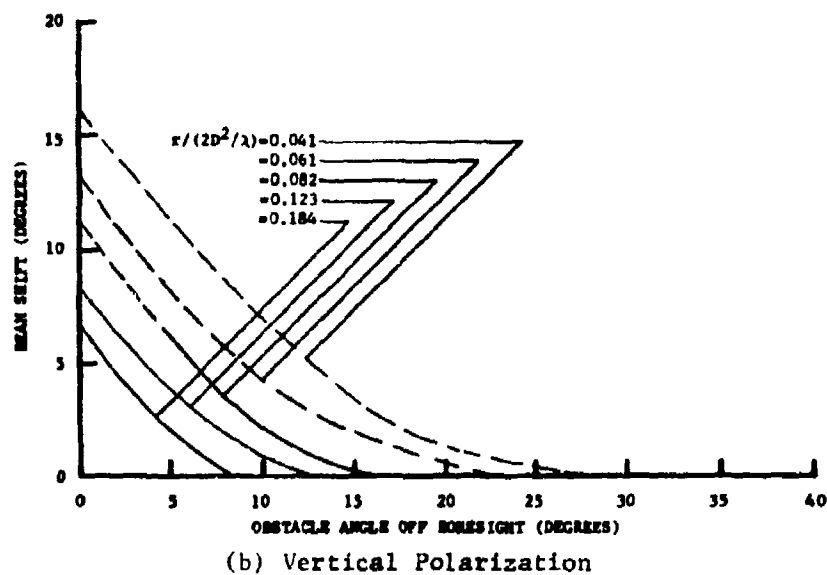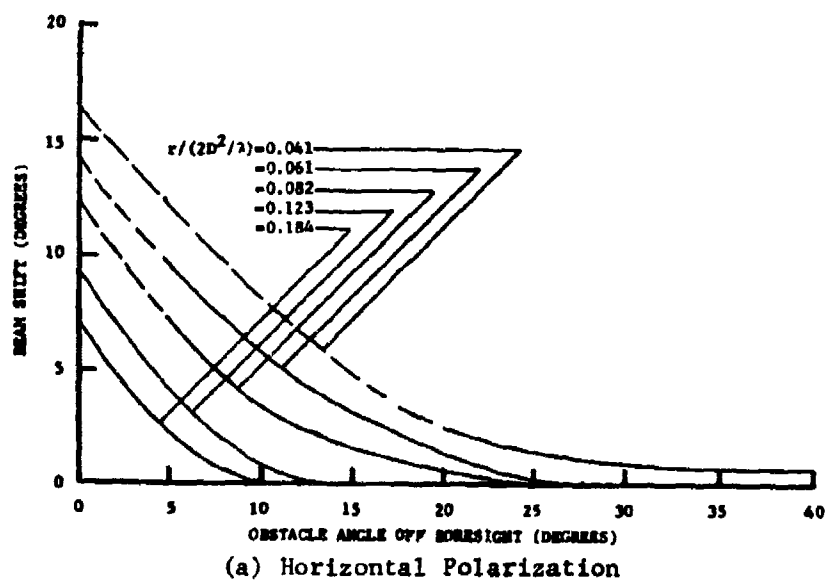
Figure 67. Beamshift as a function of obstacle angle off boresight for the indicated normalized obstacle distances. For each curve in the family, the levels for each obstacle of normalized width of 1.000 were combined for horizontally and vertically polarized signals at the frequency of 3000 MHz.

120

(a) Horizontal Polarization

(b) Vertical Polarization
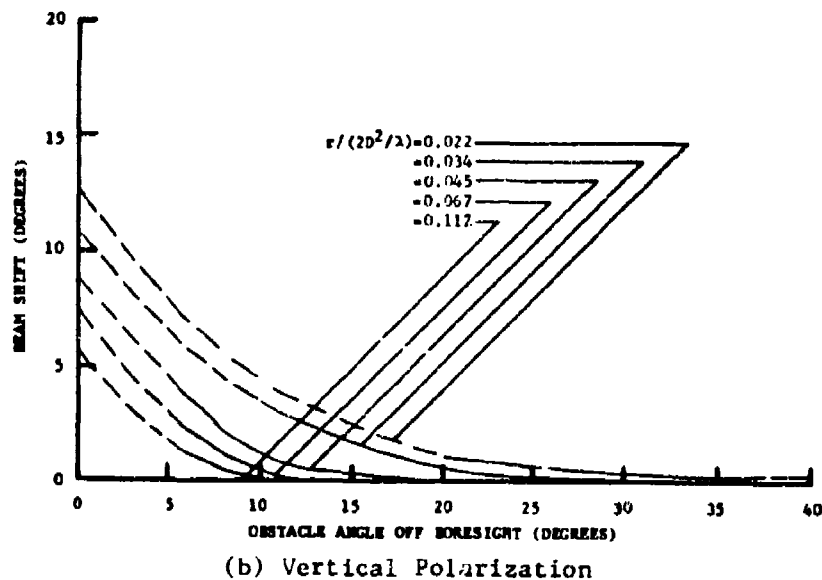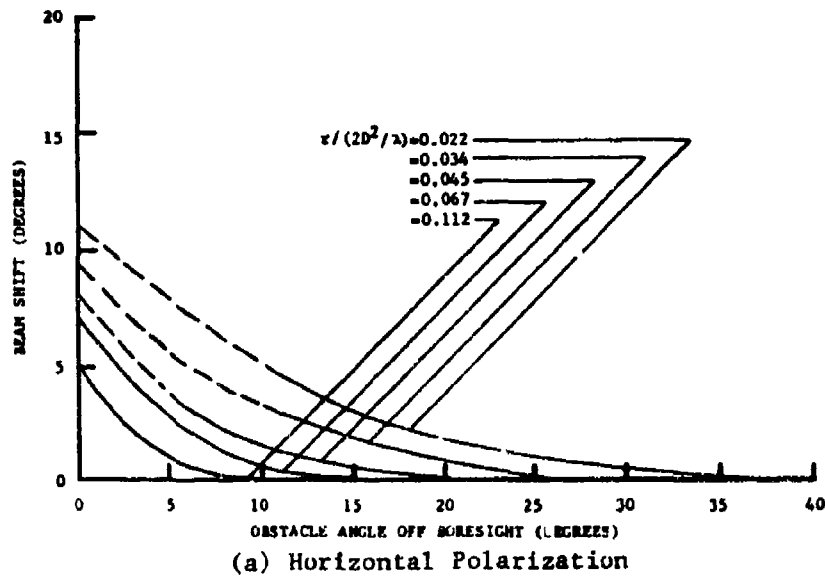
Figure 68. Beamshift as a function of obstacle angle off boresight
for the indicated normalized obstacle distances. For
each curve in the family, the levels for each obstacle
of normalized width of 1.000 were combined for horizontally
and vertically polarized signals at the frequency of 5500
MHz.

121
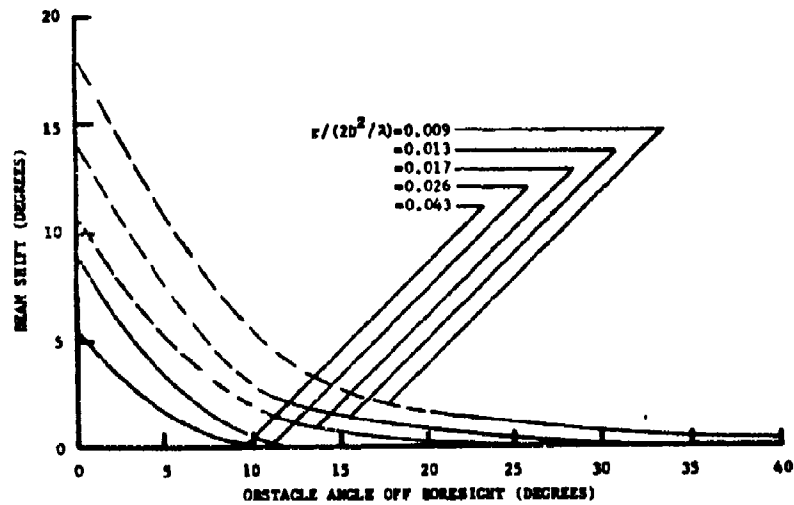
Figure 69. Beamshift as a function of obstacle angle off boresight for the indicated normalized obstacle distances. For each curve in the family, the levels for each obstacle of normalized width of 0.816 were combined for horizontally polarized signals at the frequency of 9600 MHz.

indicate that the square column obstacle data were not used; however, the solid portion indicates that all data were used in the empirical derivation of the average curves. The maximum deviations from the average curves are given in Table XV. The largest deviations, which are small relative to the beamshift, occur for obstacle angles close-in to boresight.

The sequence of antenna patterns shown in Figure 70 typically illustrates the manner in which the main beam shifts. For an obstacle angle of 20 degrees, the main beam is essentially aligned on the bore-sight direction (direction to the target) as shown in Figure 70(a). As the obstacle angle off the boresight direction is decreased to 10 degrees, the main beam shifts approximately 3 degrees off the boresight direction and the gain on boresight is also reduced, as shown in Figure 70(b). As the obstacle angle off boresight decreases further, the main beam shifts farther off boresight and the left sidelobes begin to rise significantly, as shown in Figure 70(c). As the obstacle angle decreases to zero degrees (that is, the obstacle is located directly between the antenna and the target), the main beam shifts farther off the boresight direction, and the magnitude of the left sidelobe increases to the same level as that of the shifted main beam, as shown in Figure 70(d). If one considered only Figure 70(d), an apparent ambiguity would exist and several interpretations could logically be made. The pattern could be interpreted as two main beams (because sidelobes are generally considered to be minor lobes), as distorted sidelobes with the main lobe on boresight, or as a shifted main lobe which is the interpretation adopted in this report. The important point, however, is that

TABLE XV

MAXIMUM DEVIATIONS OF BEAMSHIFTS FROM AVERAGE CURVES AND OBSTACLE ANGLES WHERE MAXIMUM DEVIATIONS OCCURRED FOR LARGEST-SIZE OBSTACLES FOR INDICATED OBSTACLE DISTANCES AND FREQUENCY BANDS

(Horizontal Polarization)

r(feet)	Obstacle Distance $r/(2D^2/\lambda)$			Maximum Deviation (Degrees)			Obstacle Angle Where Maximum Deviation Occurred (Degrees)		
	S-Band	C-Band	X-Band	S-Band	C-Band	X-Band	S-Band	C-Band	X-Band
4	0.041	0.022	0.009	2.0	1.5	1.0	0.0	10.0	0.0
6	0.061	0.034	0.013	1.0	1.0	1.0	5.0	5.0	5.0
8	0.082	0.045	0.017	1.0	0.5	0.5	5.0	5.0	5.0
12	0.123	0.067	0.026	1.0	0.5	0.5	0.0	0.0	5.0
20	0.184	0.112	0.043	1.0	0.5	0.5	0.0	0.0	0.0

(Vertical Polarization)

r(feet)	Obstacle Distance $r/(2D^2/\lambda)$			Maximum Deviation (Degrees)			Obstacle Angle Where Maximum Deviation Occurred (Degrees)		
	S-Band	C-Band	X-Band	S-Band	C-Band	X-Band	S-Band	C-Band	X-Band
4	0.041	0.022	0.009	1.5	1.0	--	0.0	0.0	--
6	0.061	0.034	0.013	1.0	1.0	--	0.0	0.0	--
8	0.082	0.045	0.017	0.5	0.5	--	0.0	10.0	--
12	0.123	0.067	0.026	0.5	0.5	--	0.0	0.0	--
20	0.184	0.112	0.043	0.0	0.5	--	0.0	0.0	--
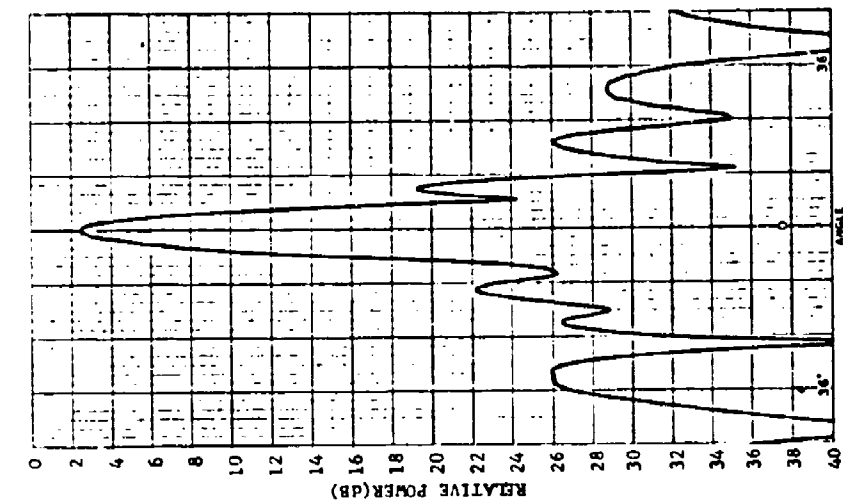
(b) Obstacle Angle = 10°

(a) Obstacle Angle = 20°

Figure 70. Sequence of vertically polarized S-band antenna patterns illustrating the typical manner in which the main beam shifts as the obstacle angle off boresight decreases from (a) 20° to (b) 10° to (c) 5° to (d) 0° for an obstacle (Corner No. 2) distance of 8 feet from the receiving antenna. The gains at the top of the charts relative to isotropic are 30 dB for (a) and (b) and 20 dB for (c) and (d). (continued)

125
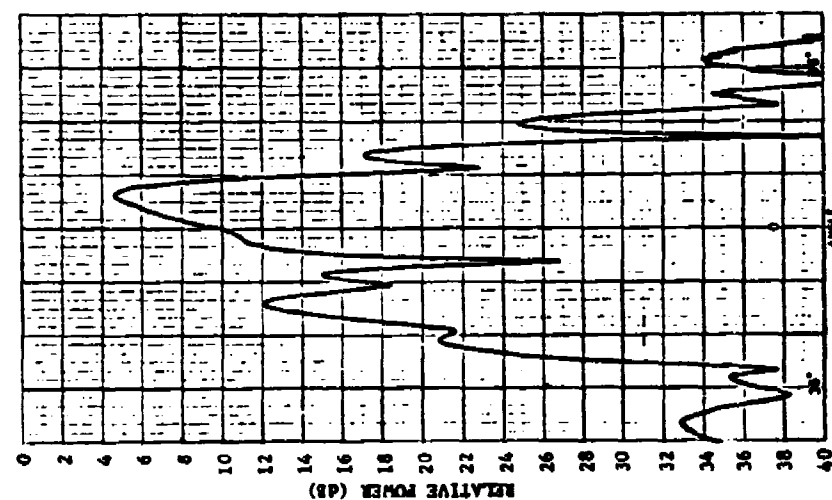
(c) Obstacle Angle = 5°   (d) Obstacle Angle = 0°

Figure 70. Sequence of vertically polarized S-band antenna patterns illustrating the typical manner in which the main beam shifts as the obstacle angle off boresight decreases from (a) 20° to (b) 10° to (c) 5° to (d) 0° for an obstacle (Corner No. 2) distance of 8 feet from the receiving antenna. The gains at the top of the charts relative to isotropic are 30 dB for (a) and (b) and 20 dB for (c) and (d). (continued)

126

the user of the various empirical curves interpret and use the information in the proper context. For a given situation, one can consult the various curves (decoupling, sidelobe, beamwidth, and beamshift curves) to obtain a vivid picture of the behavior of the antenna pattern.

SECTION VI

OPEN-MAST INVESTIGATIONS

A. Introduction

The urgent need for open-mast data has been vividly demonstrated in previous investigations [4]. Estimates of open-mast blocking effects on the main-beam gain previously have been based on aperture blocking theory that is normally used only in the design of directive antennas for clear-site operation. Under certain conditions, these engineering estimates are reasonably valid for predicting the decoupling, as subsequent data show. However, the utility of this particular theoretical technique is very limited in its scope for predicting the effects of obstacles on other antenna performance characteristics, particularly for obstacle locations off the boresight direction (the direction from the receiving antenna to the target in the far field).

Limited open-mast investigations were conducted to acquire information similar to that acquired for totally enclosed, solid-metal, near-field obstacles. The open-mast type of intervening near-field obstacles is one of the few remaining major types of obstacles in which very little experimental or theoretical information exists. Although the scope of the open-mast experimental investigations that were conducted in the work performed under this contract was very limited, much useful information was obtained. In addition, several areas where additional information is needed in order to resolve anomalies as well as to extend the current knowledge and to complete the sets of empirical curves for estimating far-field antenna performance characteristics were identified.

129

In order to accurately predict future topside effects, other investigations in addition to those presented in this report will be necessary not only to provide information to reduce degradations to far-field antenna performance but also to provide information concerning intraship EM compatibility because much more antenna-to-antenna coupling can exist for open-mast configurations.

B. Open-Mast Design Considerations

To accomplish as much as possible under the limited scope of the work outlined in this contract, two types of open-mast structures were selected, designed, fabricated, and tested at the frequencies of 3000 MHz, 5500 MHz, and 9600 MHz. Several factors were considered in the selection and design of the open masts. These factors include the following:

1) selection of realistic geometry for open-mast structure,

2) frequency scaling based on a known ratio of open-mast to antenna aperture size, in wavelengths, of a currently proposed Naval antenna/mast configuration,

3) number of masts needed if frequency scaled to three test frequencies,

4) direct comparisons of results of open masts to solid obstacles of equal widths,

5) ability to compare effects of total obstacle width to total projected aperture blockage,

6) tube design versus flat strip design for elements of mast,

7) weight considerations, and

8) construction costs.

The geometry selected for the open mast was approximately similar to that used on the Patrol Frigate (PF). Although the cross members and diagonals of each mast were oriented the same as those for the PF, the four support columns at the four corners of the open mast were oriented exactly vertically instead of slightly slanted off the vertical direction as were the PF supports. Thus, the overall appearances of each test mast and of the PF open mast are those of a truncated rectangular structure and a truncated pyramidal structure, respectively. However, both the rectangular and pyramidal structures will present approximately the same projected blockage to the receiving antenna because only a small portion of the total height of the mast is viewed by the receiving antenna. Consequently, construction costs were reduced at no significant sacrifice in measurement results.

Scaling based on the ratio of the size of the PF mast to the aperture size of its L-band antenna was considered but not adopted. In order to design open masts with the same PF mast/antenna ratio for measurements at test frequencies of 3000 MHz, 5500 MHz, and 9600 MHz, a mast for each frequency would have been necessary. Furthermore, because the members of the masts (horizontal members, vertical members, and diagonal members) would have required dimensional sizes not available commercially, construction costs would have been prohibitive. In addition, if frequency scaling were adopted, the one mast per test frequency that would result would not permit investigations of other important aspects such as the effects of different percentages of projected aperture blockages at each test frequency and the effects of different mast widths at each test frequency.

131

The approximate geometrical configuration of the PF open-mast structure at the height comparable to that of the L-band antenna of the PF was scaled by factors of 2/7 and 4/7 to yield open-mast widths of 24 inches and 48 inches, respectively. These 24-inch and 48-inch wide open masts project a blockage of about 22 percent and 28 percent, respectively, onto the aperture of a 4-foot paraboloidal dish antenna, as shown in Figure 71(a) and (b). The dashed lines indicate the difference of construction that would have occurred had the exact geometry of the PF been scaled. Although many aspects of the effects of open masts on antenna performance should eventually be investigated, it was determined that a much needed insight could be gained from the experimental data obtained with these 24-inch and 48-inch wide open-mast structures. Because the widths of these two open-mast structures coincide with some of the widths of the solid obstacles that were tested, the data can be compared directly. Furthermore, the selection of these open-mast structures permit the effects of different distributions of aperture blockages to be observed. In addition, the effects of the total percentage of aperture blockage can be observed not only between the two open masts but also between a given open mast and a solid obstacle. Based on aperture blocking alone, for example, one would expect that a solid 6-inch obstacle which blocks approximately 16 percent of the aperture of the 4-foot dish antenna would affect the performance of the antenna about the same as the 24-inch open mast which blocks approximately 22 percent of the total aperture area. However, one probably would not expect that a 24-inch ope mast and a 24-inch solid obstacle would yield the same effects si · the solid

132
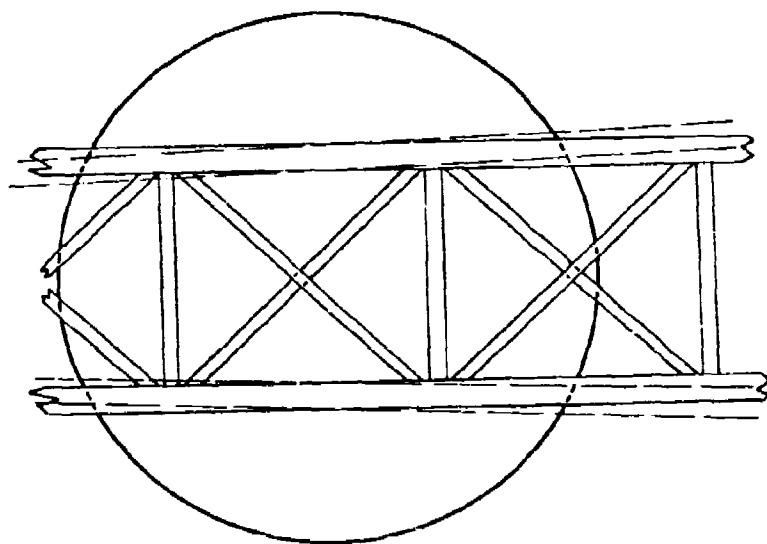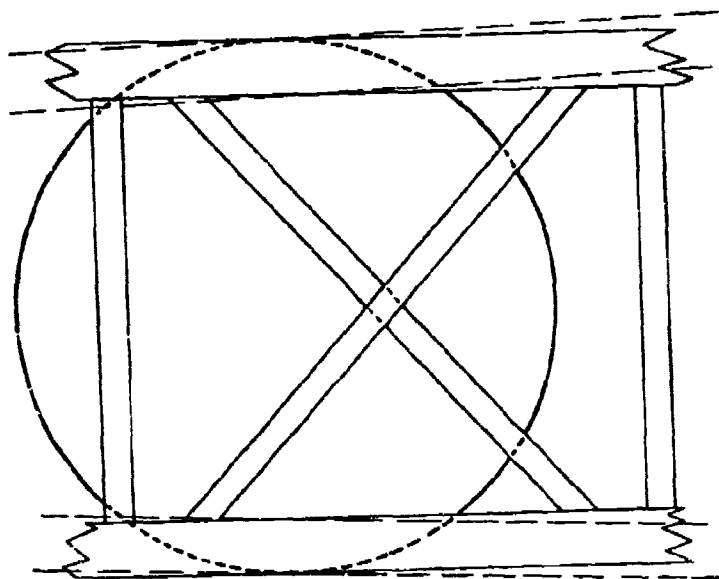
(b) 48-inch mast

(a) 24-inch mast

Figure 71. Projection of the 24-inch mast and the 48-inch mast onto the aperture of a 4-ft paraboloidal dish antenna.

133

obstacle blocks over 50 percent of the total aperture area.

Serious consideration was focused on whether circular tubing, square tubing, or flat strips should be selected as the basic members for constructing the open-mast structures. Although it was known that the scattering from an individual element of each type could be different, the total scattering effects of the combined elements which comprise the entire complex open-mast structures were not known. Therefore, it was decided to construct the 24-inch wide open mast of circular tubing and the 48-inch wide mast of reinforced flat metal strips. Because the weight of the flat strips was less than that of tubing and because the complexity of construction using strips was less, the flat-strip construction for the 48-inch wide open mast was chosen.

C. Special Tests

In addition to the sensitivity and repeatability tests described in Section IV, two additional types of investigation involving open masts were conducted to gain a better insight into the various ways that open masts can affect the far-field performance of an antenna. One type of investigation involved a series of tests at C-band (5500 MHz) with each open mast rotated 45 degrees (about its vertical axis) from the usual obstacle test orientation. The second type involved a series of tests at X-band (9600 MHz) in which the effects of various combinations and arrangements of the basic element members of the 48-inch open-mast structure were investigated.

1. C-Band Tests

For the C-band tests at 5500 MHz, summaries of the antenna performance characteristics for horizontal and vertical polarizations

are presented in Tables XVI and XVII for the 24-inch and 48-inch open masts, respectively. As indicated in the tables data for the 24-inch open mast were recorded for two obstacle distances from the receiving antenna (4 feet and 8 feet) along the boresight direction to the target (0°) and along a radial direction 10 degrees off the boresight direction, but data for the 48-inch mast were recorded at only one obstacle distance (4 feet) on boresight. In all cases, however, data were recorded for each obstacle situated both in its normal orientation (0°) and in its rotated orientation (45°).

Various interesting observations can be made from the tables. Comparisons of the various decoupling data indicate that rotation of a given mast has very little effect. Although small, the changes in decoupling that do occur due to rotation appear to be greater for the 48-inch open mast than for the 24-inch mast. The tables also show that a 45-degree rotation of either mast produces only small changes in the 3-dB beamwidths of the antenna. However, there appears to be a tendency for the beamwidth to increase very slightly when the 24-inch mast is rotated 45 degrees and to decrease slightly when the 48-inch mast is rotated 45 degrees. No beamshift changes occurred, and therefore, were not included in the tables.

The 45-degree obstacle rotation apparently produced greater changes in the sidelobes than in any of the other antenna performance characteristics. Rotation of the 24-inch open mast to 45 degrees causes the sidelobes to decrease significantly (lower sidelobes) in most cases, but a similar rotation of the 48-inch mast causes the sidelobe levels to increase (higher sidelobes). Several factors are apparently responsible

135

TABLE XVI

SUMMARY OF ANTENNA PERFORMANCE CHARACTERISTICS FOR SPECIAL TESTS AT 5500 MHz FOR 24-INCH OPEN MAST ROTATED 0° AND 45° FOR EACH OF TWO DIFFERENT OBSTACLE DISTANCES, OBSTACLE ANGLES, AND POLARIZATIONS

Obstacle Distance (Feet) From Antenna	Radial Direction (Degrees) From Boresight	Decoupling (dB) Rotation 0°	45°	Left Sidelobe (dB) Rotation 0°	45°	Right Sidelobe (dB) Rotation 0°	45°	Beamwidth (Degrees) Rotation 0°	45°
(Horizontal Polarization)									
4	0	4.0	4.0	11.5	18.0	10.0	17.0	2.5	2.7
4	10	3.5	3.5	12.5	19.0	11.0	14.0	2.7	2.9
8	0	4.0	4.0	12.5	18.0	11.5	16.0	2.8	2.6
8	10	2.5	2.0	13.5	19.0	12.0	21.0	2.7	3.0
(Vertical Polarization)									
4	0	4.5	5.0	9.0	23.0	9.0	23.0	3.2	3.2
4	10	3.5	4.0	10.5	12.0	10.5	16.0	3.2	3.3
8	0	4.0	5.5	10.0	16.0	9.0	20.0	3.2	3.2
8	10	3.0	2.0	12.5	13.0	14.0	18.0	3.0	3.2

136

TABLE XVII

SUMMARY OF ANTENNA PERFORMANCE CHARACTERISTICS FOR SPECIAL TESTS AT 5500 MHz FOR 48-INCH OPEN MAST ROTATED 0° AND 45° FOR INDICATED OBSTACLE DISTANCE, OBSTACLE ANGLE, AND TWO POLARIZATIONS

Obstacle Distance (Feet) From Antenna	Radial Direction (Degrees) From Boresight	Decoupling (dB) Rotation 0° 45°	Left Sidelobe (dB) Rotation 0° 45°	Right Sidelobe (dB) Rotation 0° 45°	Beamwidth (Degrees) Rotation 0° 45°
			(Horizontal Polarization)		
4	0	3.5 5.5	17.5 6.0	14.0 6.0	3.2 2.0
			(Vertical Polarization)		
4	0	3.5 6.0	15.0 7.0	12.5 7.0	3.8 2.5

for this behavior. A 45-degree rotation of either mast increases the total width of the projected blockage to 1.41 times its initial width for no rotation. Therefore, a combination of different widths, different total cumulative projected blockages, and different distributions of projected blockages for an aperture distribution function that is also tapered apparently causes this type of behavior. These results indicate that when sidelobe levels are critical, careful consideration should be given to typical factors such as the orientation as viewed from the antenna and the construction geometry of the open mast. For example, decisions such as whether to select an open mast of triangular or square cross-sectional shape (as viewed from the vertical axis of a mast) even though the width of each side is the same must be carefully made. Many apparent subtleties are perhaps very important.

2. X-Band Tests

Several special X-band tests at 9600 MHz were conducted with the 48-inch open mast to investigate the effects of various elements of the mast on the radiation characteristics of the GT/AR-PCX antenna. Particularly at X-band, and to a much smaller extent at S-band and C-band frequencies, a very noticeable pattern asymmetry occurred when the 48-inch open mast was located on boresight in the near field of the antenna. Because the various strips which comprise the open mast could be either removed or reoriented, controlled tests were conducted to observe and compare the near-field effects of each different mast configuration. The small stiffeners on which the various strips were attached can be seen at bottom portion of the 48-inch mast shown in Figure 7 of Section II, these metal stiffeners are 1 inch wide. The vertical strips

at each corner of the mast are 5.0 inches wide, the horizontal strips are 2.5 inches wide, and the diagonal strips are 2.5 inches wide. As viewed from a normal direction to the vertical mast, only one diagonal is on the front side of the mast, and only one diagonal is on the back side of the mast. In the normal configuration, if the front and back diagonals were projected onto a plane, they would be at right angles to each other.

A summary of the pertinent results of the tests is given in Table XVIII. Because there were neither significant beamshifts nor significant changes in beamwidths for any of these open-mast tests, only the decoupling and sidelobe levels are included in the summary.

A number of noteworthy observations are evident from the summary of test results. In the normal open-mast configuration, the main-beam shape and close-in sidelobes were noticeably asymmetrical, as the unequal sidelobe levels of Test Condition 1 of Table XVIII indicate. When the front diagonal strip was removed, the decoupling decreased and the pattern symmetry improved somewhat as indicated by the right and left sidelobes of Test Condition 2. When both the front and back diagonal stripes were removed from the mast, the decoupling decreased considerably, and good main-beam symmetry occurred as also indicated by the symmetrical sidelobe levels. Note for Test Condition 5 that when all of the strips were removed that considerable improvements in both the decoupling and sidelobes occurred; for this case very good main-beam symmetry also resulted.

The results of Test Condition 4 in Table XVIII strongly indicate that the diagonal members are major contributors that can produce asym-

TABLE XVIII

SUMMARY OF X-BAND OPEN-MAST SPECIAL TESTS AT 12-FOOT DISTANCE ON BORESIGHT DIRECTION

TEST CONDITION*	DECOUPLING (dB)	LEFT SIDELOBE (dB)	RIGHT SIDELOBE (dB)
1. Normal Configuration	9.0	9.0	5.5
2. Front Diagonal Strip Removed	7.0	10.0	11.0
3. Front and Back Diagonal Strips Removed	3.5	16.0	17.0
4. All Vertical and Horizontal Strips Removed:			
(a) Front and Back Diagonal Strips in Normal Position	6.5	11.0	6.5
(b) Front Diagonal Strip Removed	4.5	10.0	16.5
(c) Front and Back Diagonal Strips Rotated 90°	6.5	7.0	12.5
(d) Front Diagonal Strip Removed and Back Diagonal Strip Rotated 90°	5.0	12.5	10.5
(e) Both Diagonal Strips on Back of Mast	7.0	11.0	15.5
5. All Vertical, Horizontal, and Diagonal Strips Removed (Only Framework Stiffeners Remain)	3.0	23.5	22.0

*The mast is viewed from the receiving antenna. Therefore, the front of the mast is nearer to the aperture of the receiving antenna than is the back of the mast.

140

metrical antenna patterns. When the front and back diagonals were in their normal position and orientation (vertical and horizontal members removed), as in Test Condition 4(a), poor pattern symmetry resulted even though a small improvement in decoupling occurred. Further, when the front and back diagonals were rotated 90°, the pattern asymmetries on each side of the main lobe reversed, as indicated by the reversal in sidelobe levels of Test Condition 4(c); note, however, that the decoupling of Test Conditions 4(a) and 4(c) remained the same. Finally, when both diagonals were positioned on the same side of the mast, as in Test Condition 4(e), the decoupling remained at about the same value but one of the right sidelobe levels improved (as compared with Test Condition 4(a) where one diagonal is on the front and one is on the back of the mast). Thus, although the projected blockages onto the aperture of the antenna for Conditions 4(a) and 4(c) were identical, an interaction among members apparently occurred. Of all the cases of Test Condition 4, the best symmetry occurred for Test Condition 4(d).

D. Open-Mast Displays

The format for presentation of the open-mast, near-field, empirical curves is similar to that of the solid obstacles. However, no open-mast curves for either beamshifts or beamwidths are included because changes, if any, that occurred for the various test conditions were usually not detectable. Further, no tables for deviations from the average decoupling values are given because the deviations were always less than about 0.5 dB.

l. Decoupling along Boresight

The empirical curves for the decoupling along the boresight direction due to the presence of the 24-inch wide and 48-inch wide open-mast obstacles in the near field of the GT/AR-4S1, GT/AR-4C1, and GT/AR-PCX antennas are presented in Figures 72 through 74. As was the case for the solid obstacles, curves for both polarizations in each figure for 3000 MHz and 5500 MHz are presented, but only curves for horizontal polarization are presented for 9600 MHz because the X-band antenna can accommodate only horizontally polarized signals. The boresight decoupling (gain loss) is displayed as a function of the obstacle distance, r, from the receiving antenna normalized in terms of far-field units of $2D^2/\lambda$, where D is the horizontal dimension of each antenna and λ is the operating wavelength.

The overall trend of the data displayed in Figures 72 through 74 for the open masts is considerably different than that for the solid obstacles. For the open masts, there is usually only minor differences between W/D ratios of 0.5 and 1.0. Also, very minor differences occur between the data for horizontally and vertically polarized signals. Further, the decoupling levels for the 24-inch and 48-inch open masts, particularly for the S-band and C-band signals, are approximately the same as those for 6-inch solid obstacles. Finally, the behavior of the X-band curve for the 48-inch open mast (W/D = 0.816) is irregular. The projection of the asymmetrical blockage onto the aperture of the fan beam antenna (GT/AR-PCX), the possible dependence on polarization, and the possible sensitivity to the angle of arrival of the EM wave from the target may contribute to this irregularity.

142
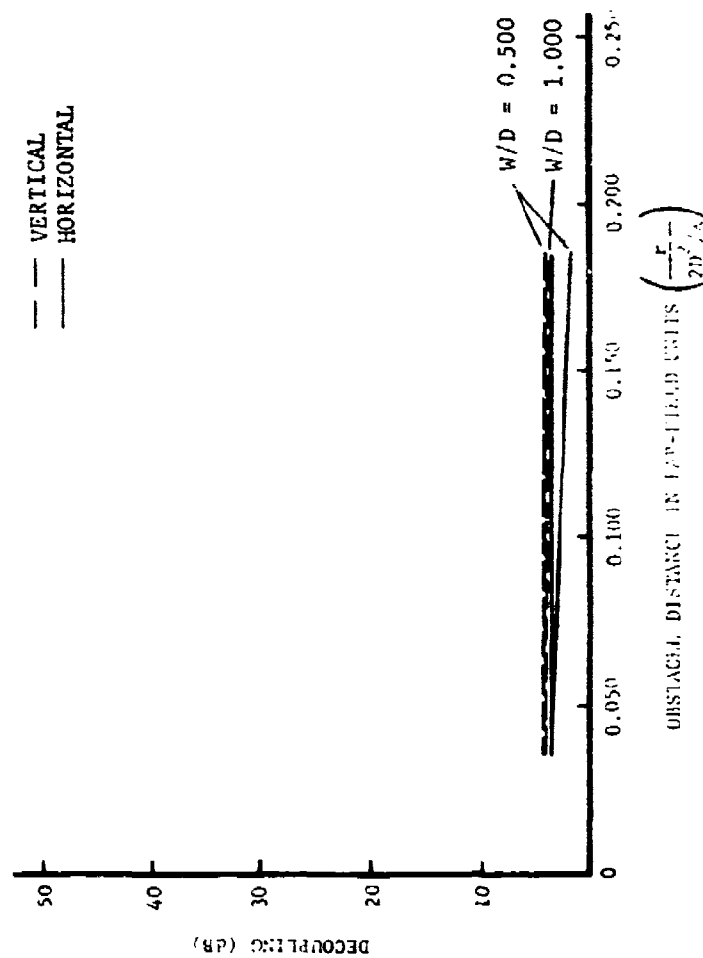
Figure 72. Average boresight decoupling as a function of obstacle distance along boresight direction (target direction) for receiving antenna aperture D for the Open Mast obstacles of widths W for horizontally and vertically polarized signals at a frequency of 3000 MHz. Receiving antenna is in far field of target.

143
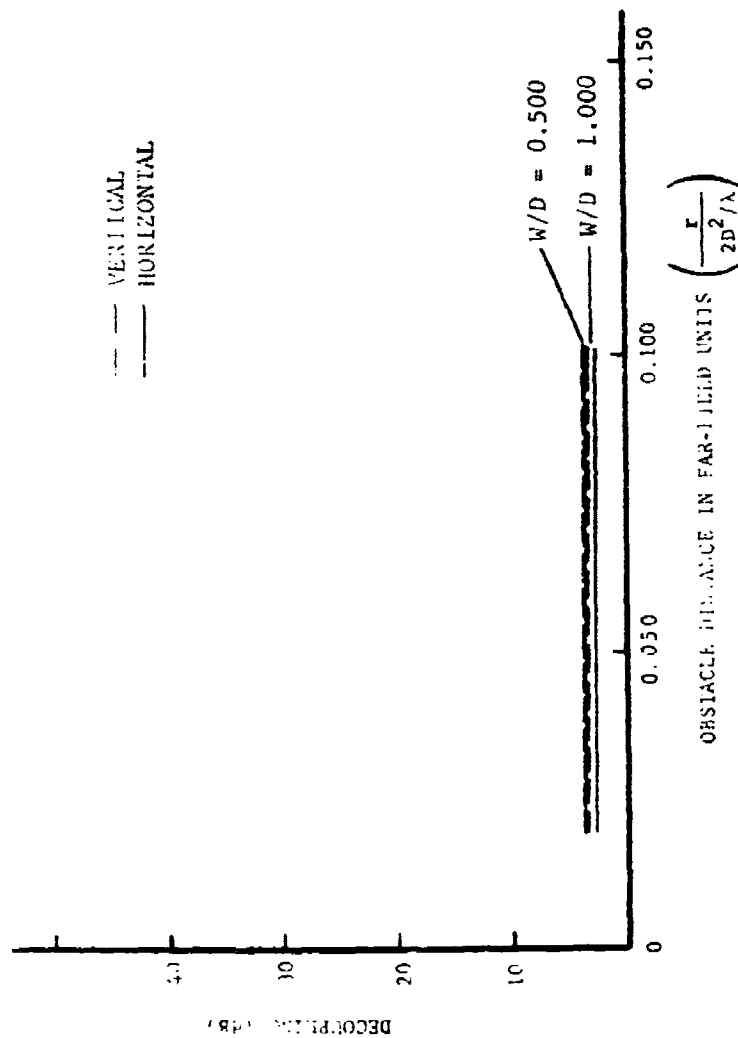
Figure 73. Average boresight decoupling as a function of obstacle distance along boresight direction (target direction) for receiving antenna aperture D for the Open Mast obstacles of widths W for horizontally and vertically polarized signals at a frequency of 5500 MHz. Receiving antenna is in far field of target.

144
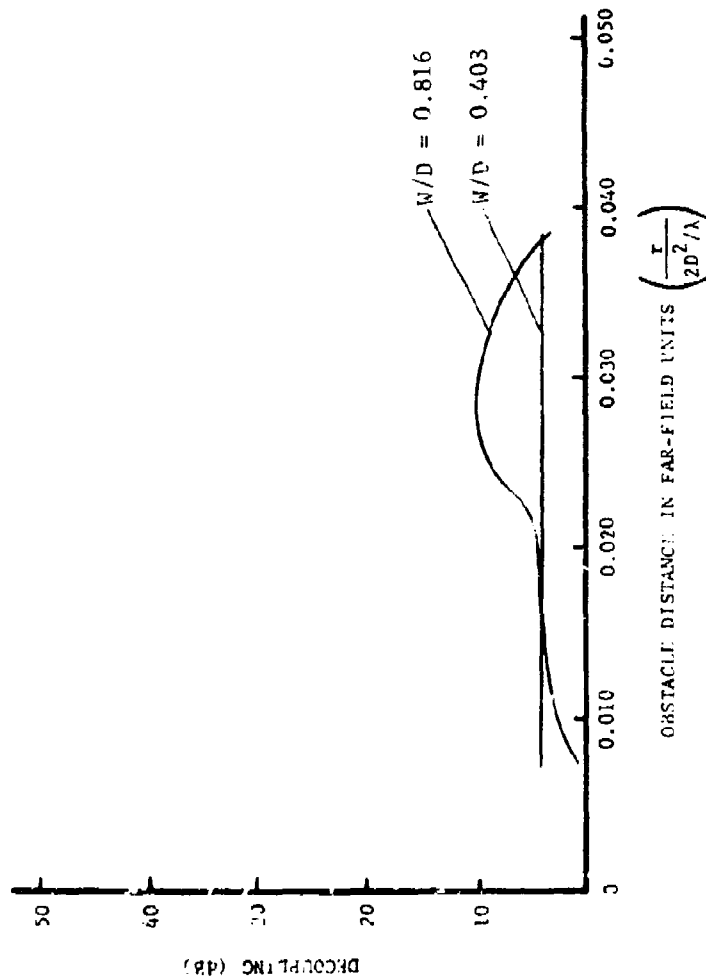
Figure 74. Average boresight decoupling as a function of obstacle distance along boresight direction (target direction) for receiving antenna aperture D for the Open Mast obstacles of widths W for horizontally polarized signals at a frequency of 9600 MHz. Receiving antenna is in far field of target.

OBSTACLE DISTANCE IN FAR-FIELD UNITS $\left(\dfrac{r}{2D^2/\lambda}\right)$

DECOUPLING (dB)

W/D = 0.816

W/D = 0.403

2. Decoupling Versus Obstacle Angle

The decoupling curves for average boresight decoupling as a function of the obstacle angle for the two open masts for the various obstacle distances, polarizations, and frequencies are presented in Figures 75 through 80. As the curves in the figures show, the decoupling levels for the various situations for open masts do not always decrease monotonically to zero as the obstacle angle increases. This behavior is in direct contrast to the curves for solid obstacles. The most consistent trend appears to be that the peak decoupling value occurs at progressively larger obstacle angles as the near-field obstacle distance decreases. In addition, the peak values of the irregular curves tend to occur at smaller obstacle angles for smaller W/D ratios. These trends appear to be logical if one considers the manner in which asymmetrical aperture blocking occurs as an open mast is progressively moved to larger obstacle angles. Unusual, however, is the fact that the C-band curves of Figure 78 show a behavior similar to that for solid obstacles. The manner in which the various curves behave indicates both frequency and polarization dependences. The information contained in the curves in Figures 75 through 80 is not only significant and useful but is also very indicative that much more information is needed to more adequately predict open-mast effects on antenna performance.

3. Maximum Sidelobe-Level Displays

The maximum sidelobe levels on both sides of the main beam as a function of the angle that the obstacle is displaced from the direction to the target (boresight direction) are shown in Figures 81 through 90. It is important to note in the displays that the obstacle angle off
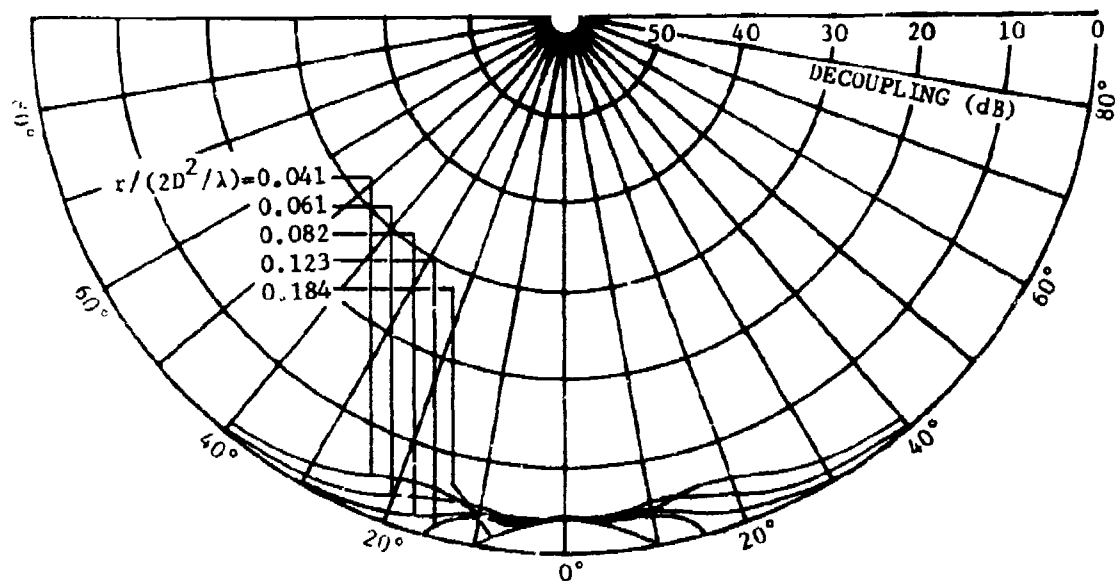
(a) Horizontal Polarization
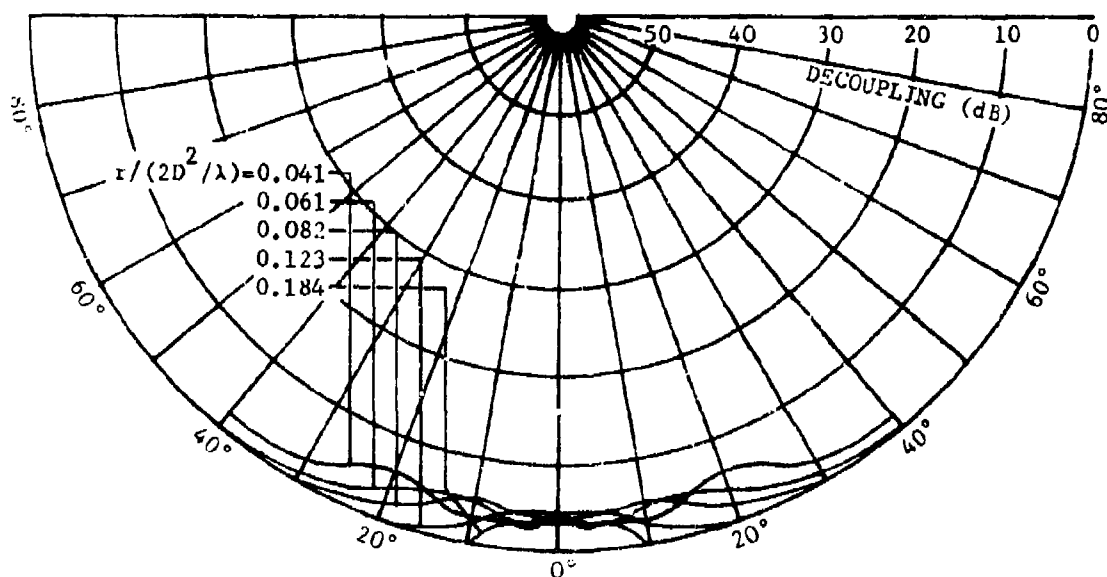
(b) Vertical Polarization

Figure 75. Average boresight decoupling as a function of the angle
between obstacle and target direction for the Open Mast
obstacle of normalized width 1.0 for indicated normalized
obstacle distances from receiving antenna aperture D and
for horizontally and vertically polarized signals at the
frequency of 3000 MHz.
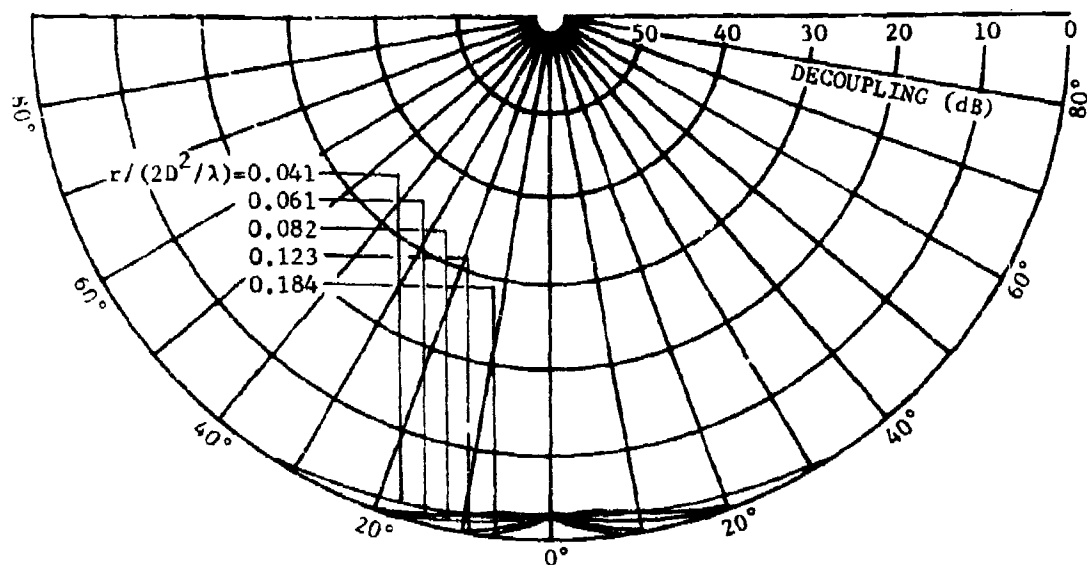
(a) Horizontal Polarization
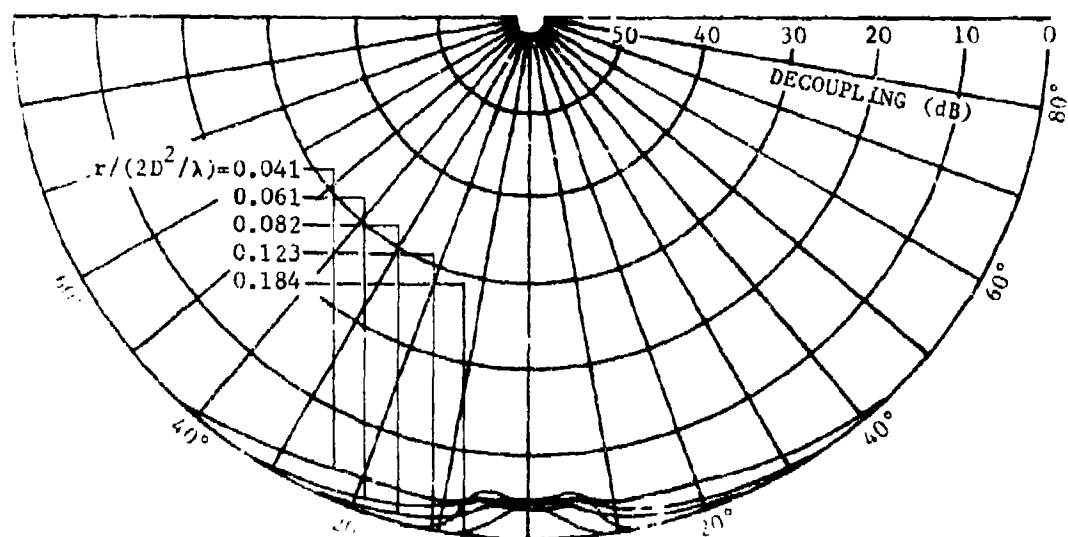
(b) Vertical Polarization

Figure 76. Average boresight decoupling as a function of the angle between obstacle and target direction for the Open Mast obstacle of normalized width 0.5 for indicated normalized obstacle distances from receiving antenna aperture D and for horizontally and vertically polarized signals at the frequency of 3000 MHz.
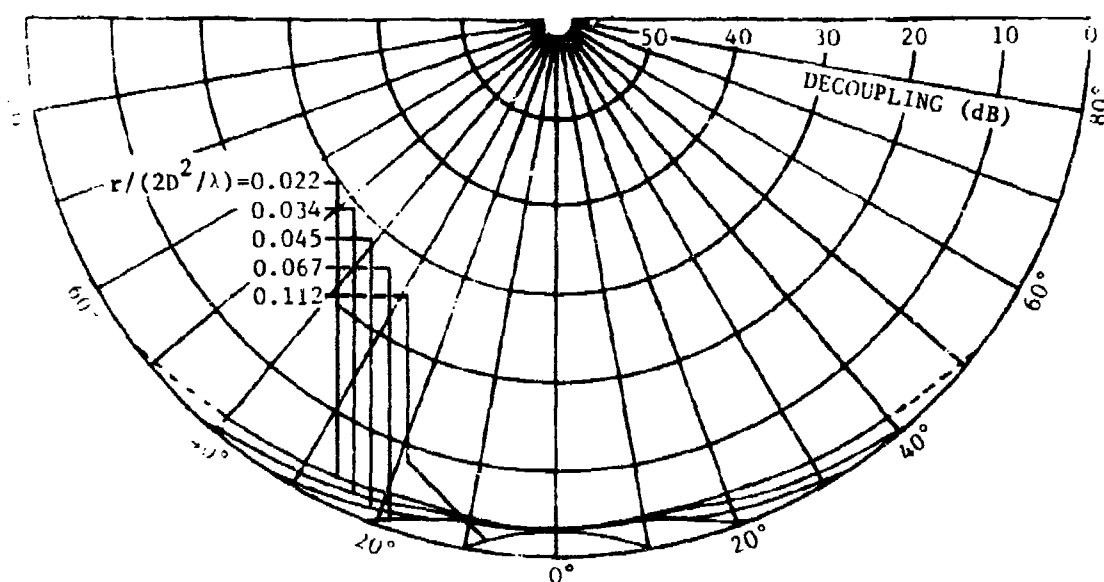
(a)   Horizontal Polarization
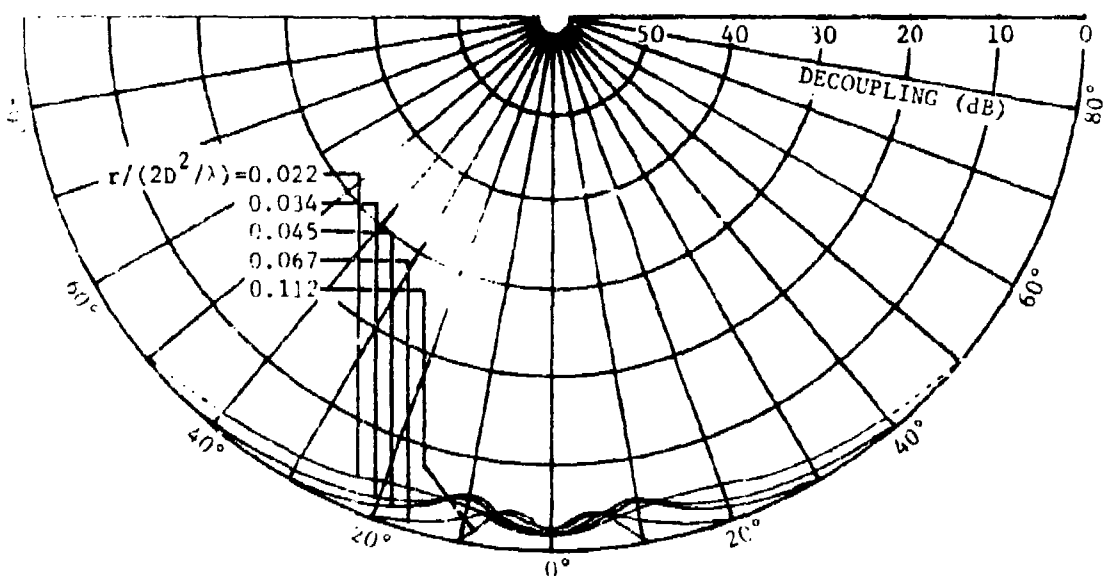
(b)   Vertical Polarization

Figure 77.   Average boresight decoupling as a function of the angle
between obstacle and target direction for the Open Mast
obstacle of normalized width 1.0 for indicated normalized
obstacle distances from receiving antenna aperture D and
for horizontally and vertically polarized signals at the
frequency of 5500 MHz.
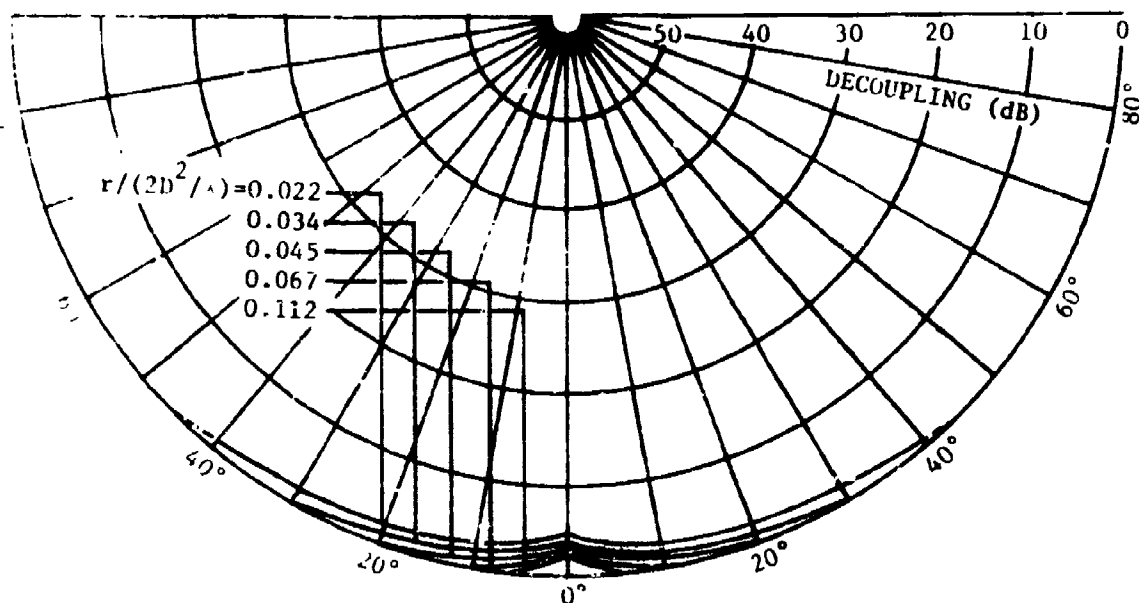
(a) Horizontal Polarization
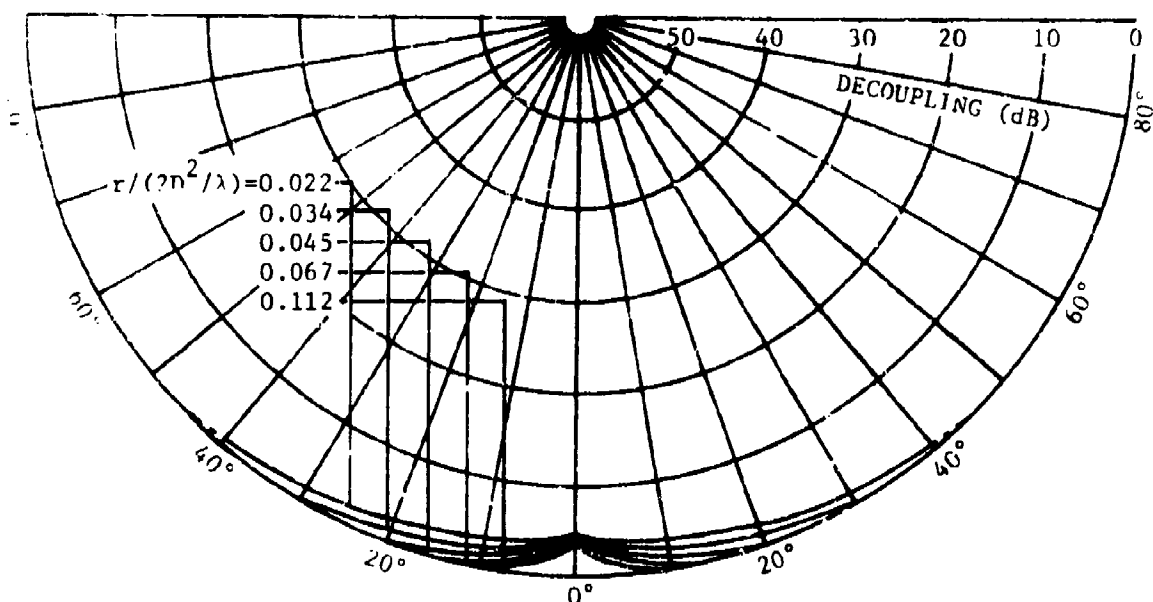
(b) Vertical Polarization

Figure 78. Average boresight decoupling as a function of the angle
between obstacle and target direction for the Open Mast
obstacle of normalized width 0.5 for indicated normalized
obstacle distances from receiving antenna aperture D
and for horizontally and vertically polarized signals
at the frequency of 5500 MHz.

150
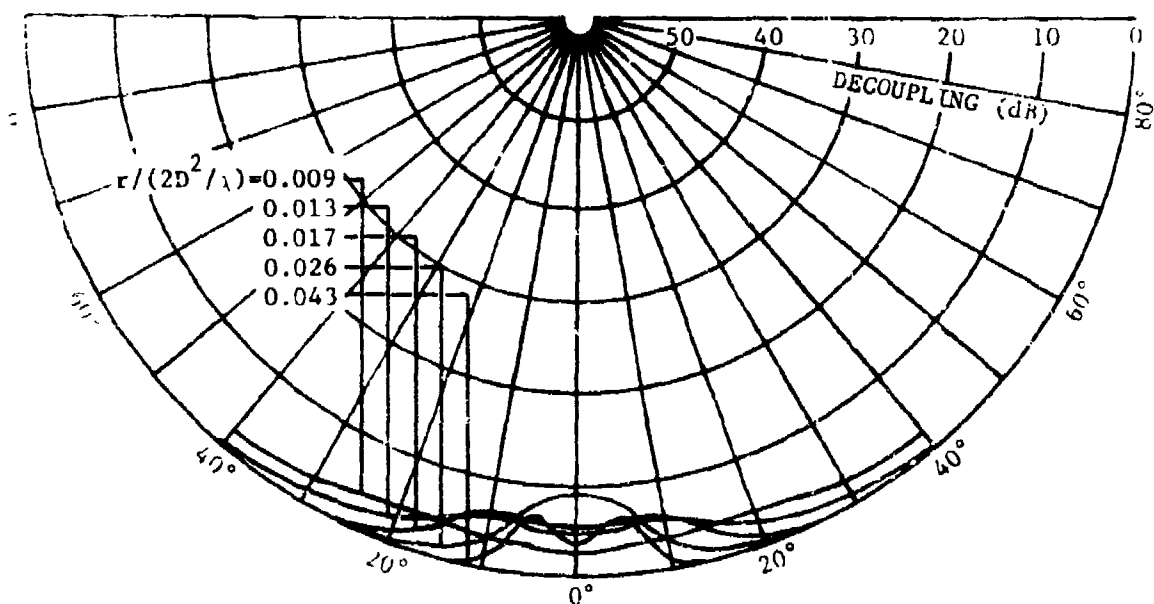
Figure 79. Average boresight decoupling as a function of the angle between obstacle and target direction for the Open Mast obstacle of normalized width 0.816 for indicated normalized obstacle distances from receiving antenna aperture D and for horizontally polarized signals at the frequency of 9600 MHz.
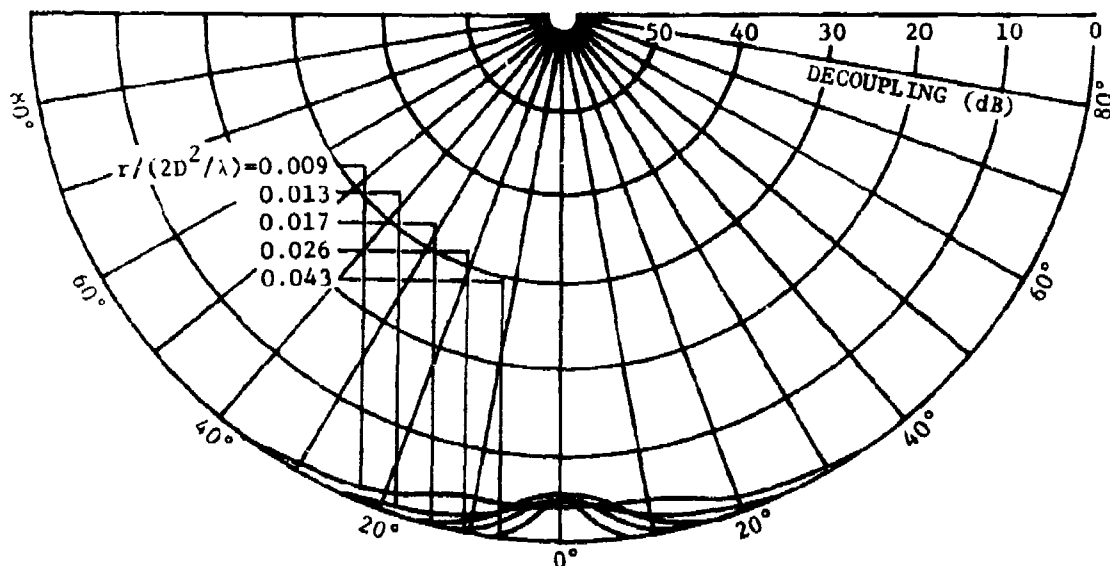
Figure 80. Average boresight decoupling as a function of the angle between obstacle and target direction for the Open Mast obstacle of normalized width 0.408 for indicated normalized obstacle distances from receiving antenna aperture D and for horizontally polarized signals at the frequency of 9600 MHz.

152
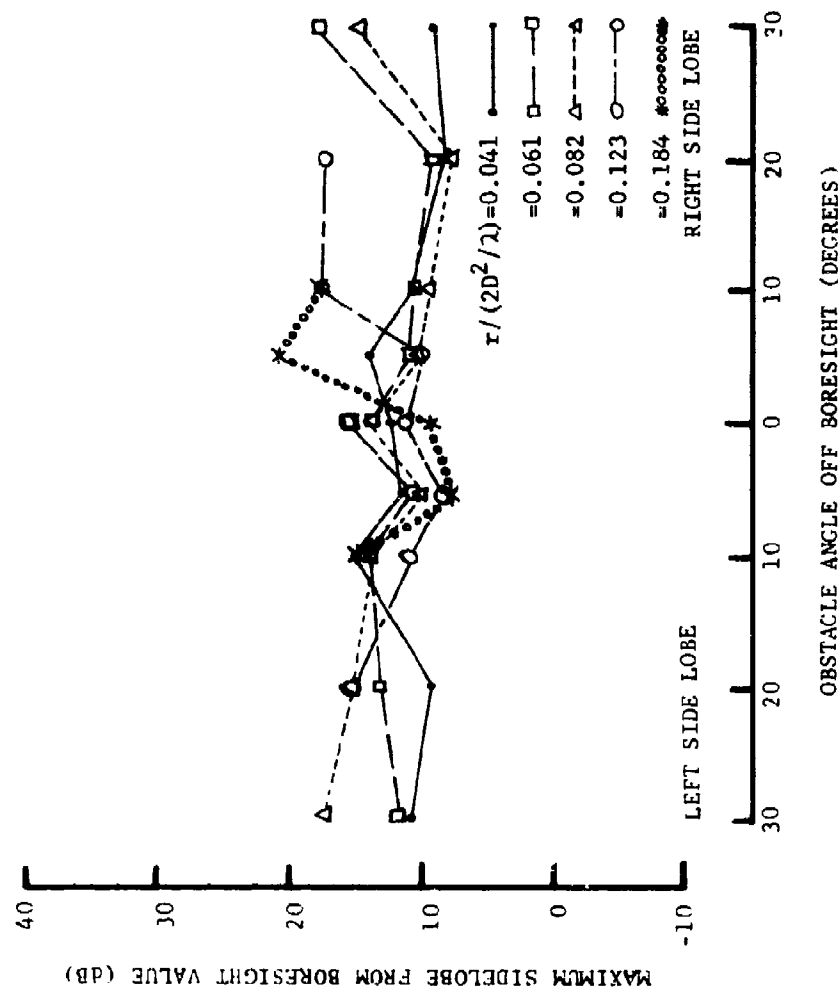
Figure 81. Maximum sidelobe level to the left and right of boresight as a function of obstacle angle off boresight; the positive values of the ordinate indicate the level down from the boresight value. Each curve in the family is for the open mast obstacle of normalized width 1.000 at the indicated normalized obstacle distances for Horizontal-polarized signals at a frequency of 3000 MHz.

OBSTACLE ANGLE OFF BORESIGHT (DEGREES)
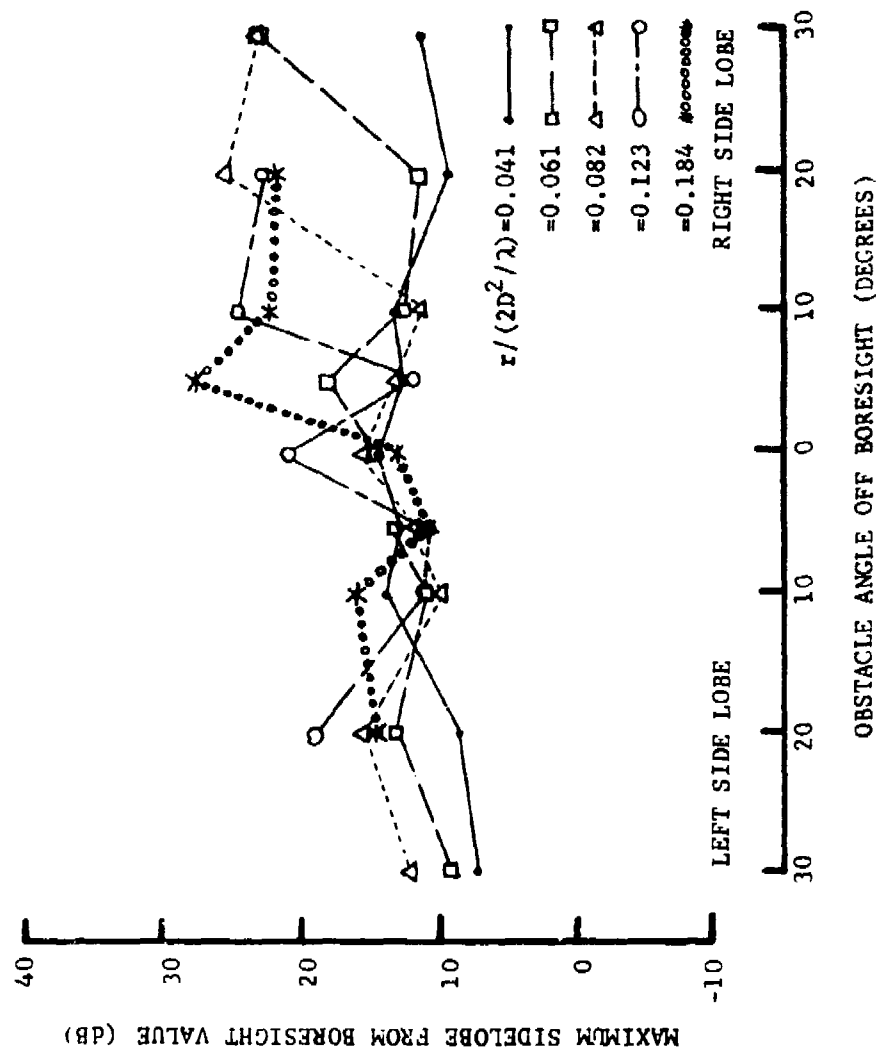
Figure 82. Maximum sidelobe level to the left and right of boresight as a function of obstacle angle off boresight; the positive values of the ordinate indicate the level down from the boresight value. Each curve in the family is for the open mast obstacle of normalized width 1.000 at the indicated normalized obstacle distances for Vertical-polarized signals at a frequency of 3000 MHz.

154

OBSTACLE ANGLE OFF BORESIGHT (DEGREES)
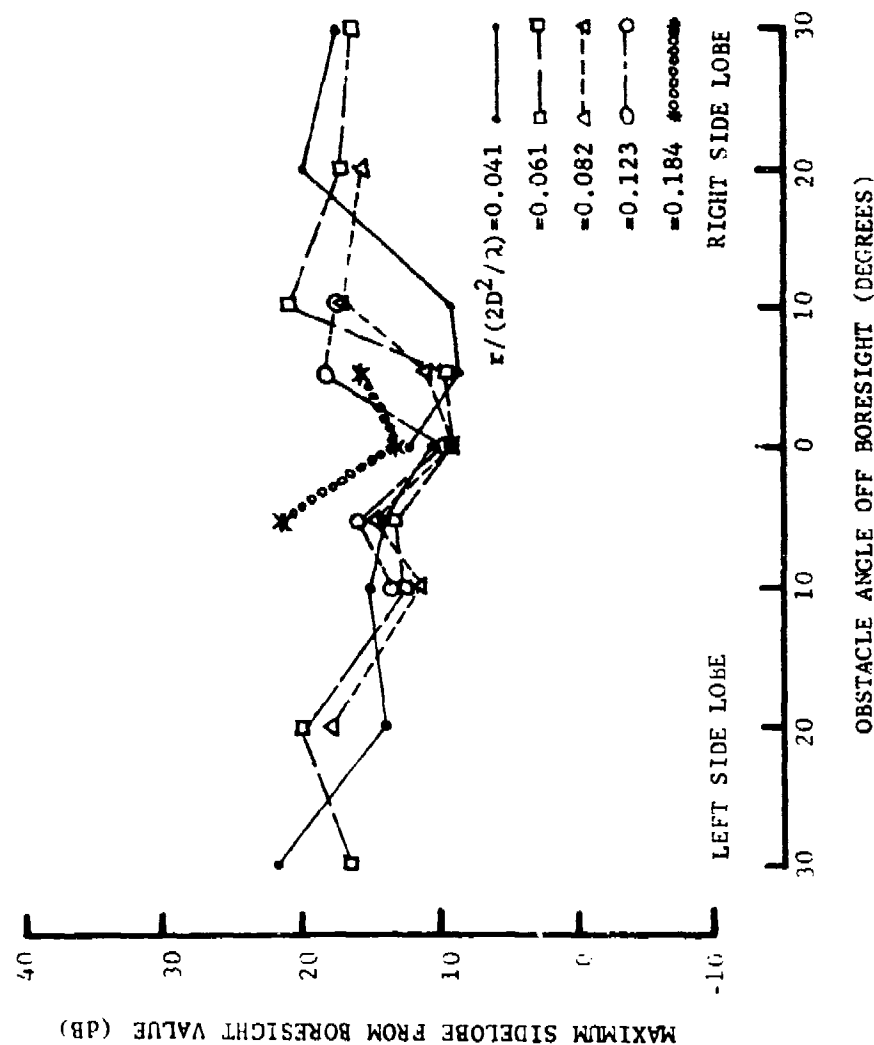
Figure 83. Maximum sidelobe level to the left and right of boresight as a function of obstacle angle off boresight; the positive values of the ordinate indicate the level down from the boresight value. Each curve in the family is for the open mast obstacle of normalized width 0.500 at the indicated obstacle distances for Horizontal-polarized signals at a frequency of 3000 MHz.
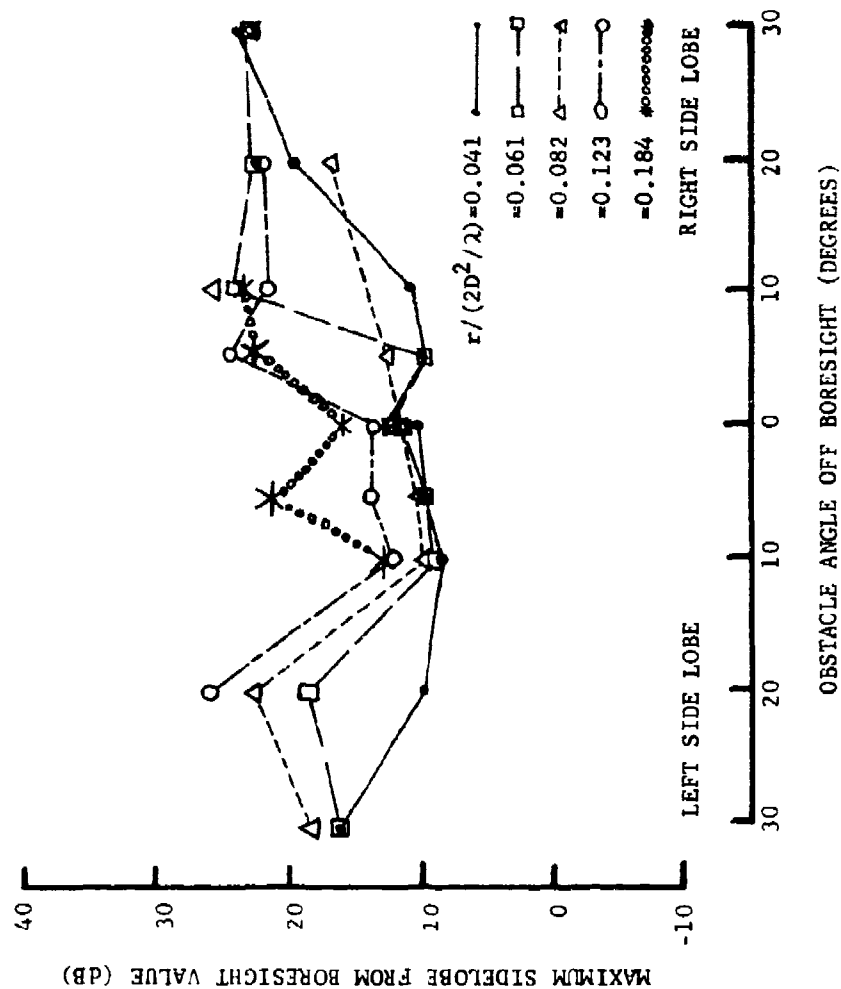
Figure 84. Maximum sidelobe level to the left and right of boresight as a function of obstacle angle off boresight; the positive values of the ordinate indicate the level down from the boresight value. Each curve in the family is for the open mast obstacle of normalized width 0.500 at the indicated normalized obstacle distances for Vertical-polarized signals at a frequency of 3000 MHz.
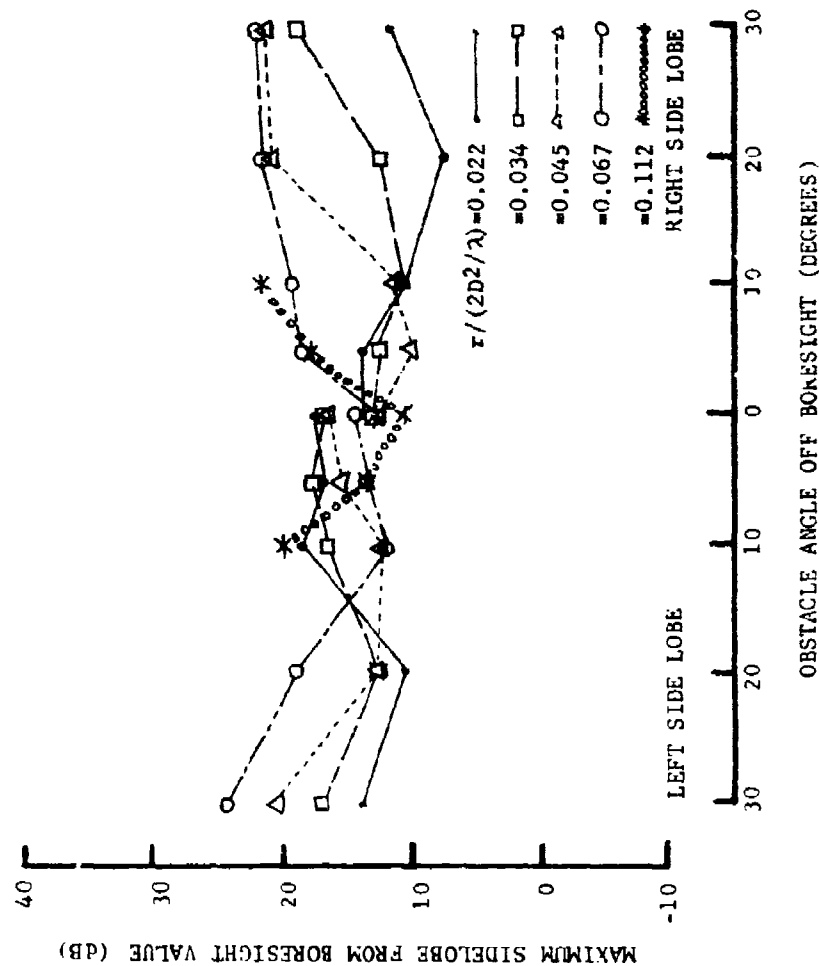
Figure 85. Maximum sidelobe level to the left and right of boresight as a function of obstacle angle off boresight; the positive values of the ordinate indicate the level down from the boresight value. Each curve in the family is for the open mast obstacle of normalized width 1.000 at the indicated normalized obstacle distances for Horizontal-polarized signals at a frequency of 5500 MHz.

157
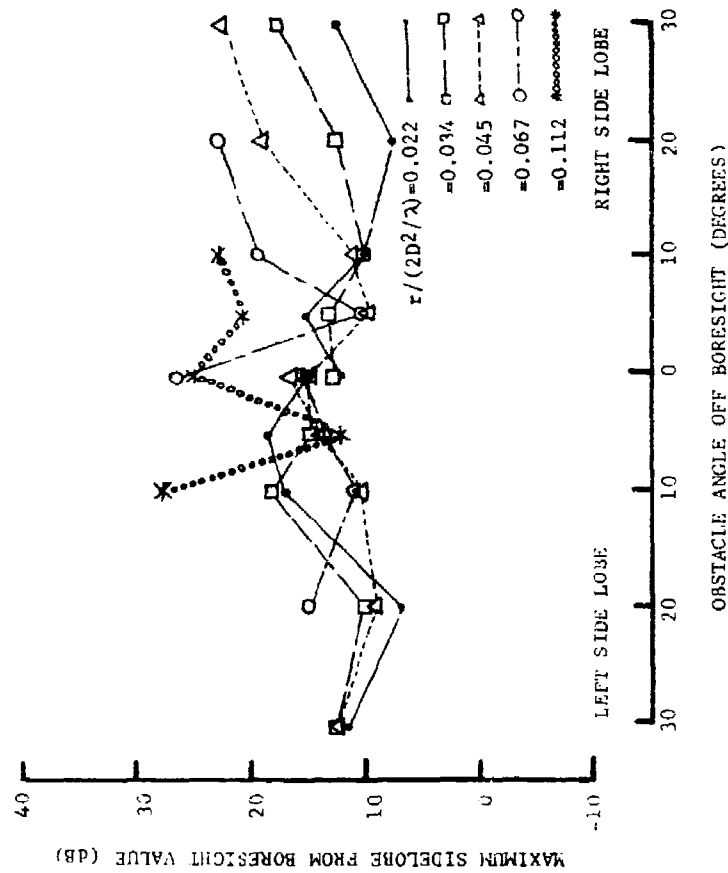
Figure 86. Maximum sidelobe level to the left and right of boresight as a function of obstacle angle off boresight; the positive values of the ordinate indicate the level down from the boresight value. Each curve in the family is for the open mast obstacle of normalized width 1.000 at the indicated normalized obstacle distances for Vertical-polarized signals at a frequency of 5500 MHz.

158
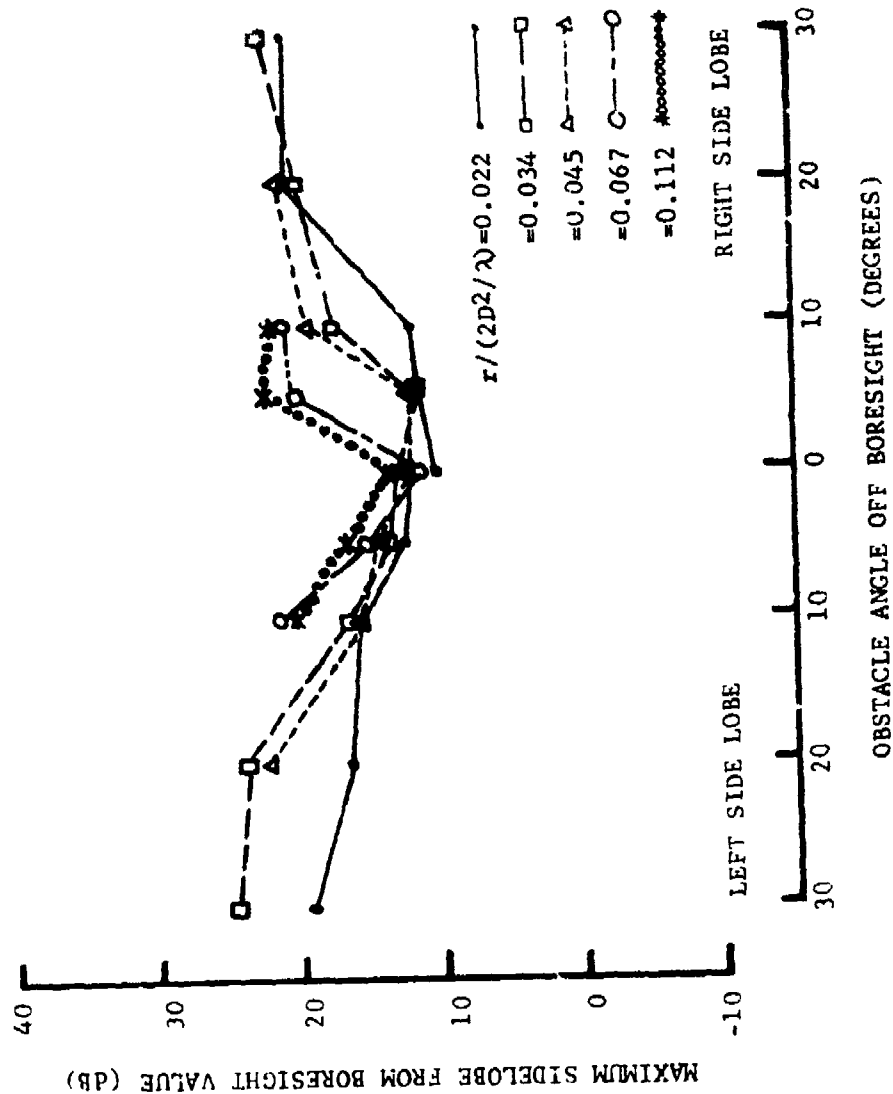
Figure 87. Maximum sidelobe level to the left and right of boresight as a function of obstacle angle off boresight; the positive values of the ordinate indicate the level down from the boresight value. Each curve in the family is for the open mast obstacle of normalized width 0.500 at the indicated normalized obstacle distances for Horizontal-polarized signals at a frequency of 5500 MHz.
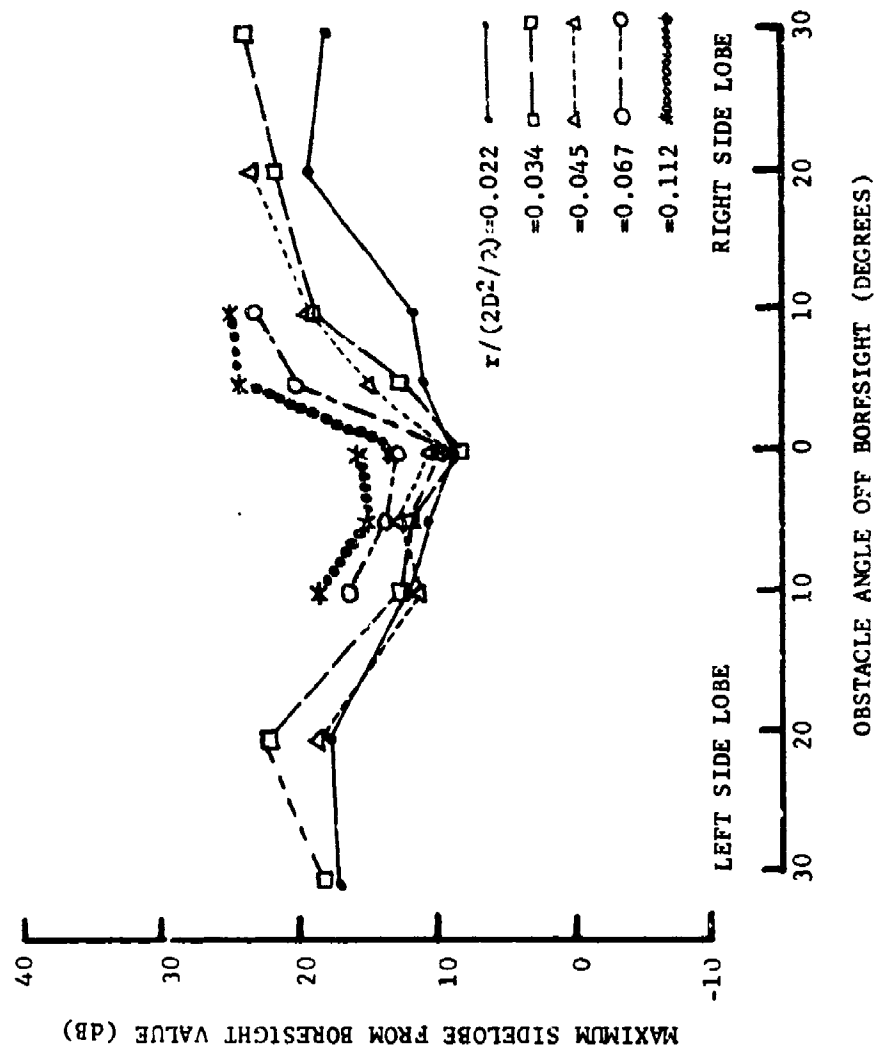
Figure 88. Maximum sidelobe level to the left and right of boresight as a function of obstacle angle off boresight; the positive values of the ordinate indicate the level down from the boresight value. Each curve in the family is for the open mast obstacle of normalized width 0.500 at the indicated normalized obstacle distances for Vertical-polarized signals at a frequency of 5500 MHz.
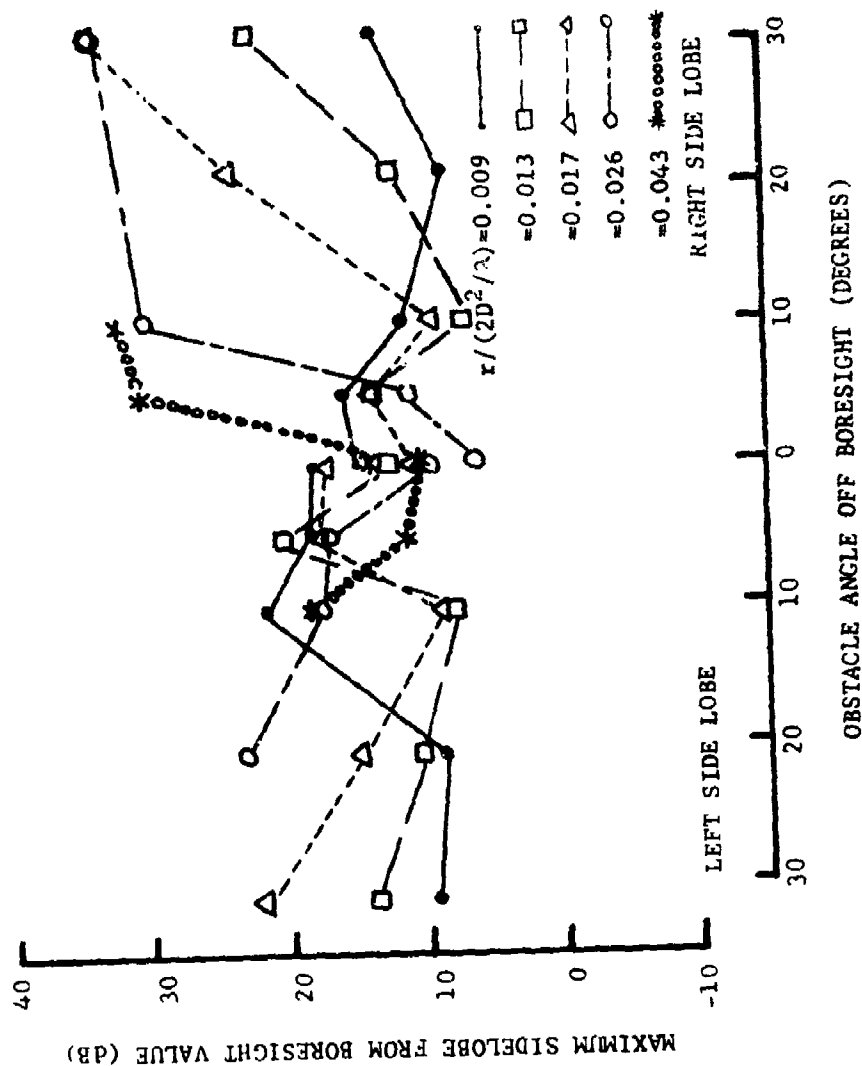
Figure 89. Maximum sidelobe level to the left and right of boresight as a function of obstacle angle off boresight; the positive values of the ordinate indicate the level down from the boresight value. Each curve in the family is for the open mast obstacle of normalized width 0.816 at the indicated normalized obstacle distances for Horizontal-polarized signals at a frequency of 9600 MHz.
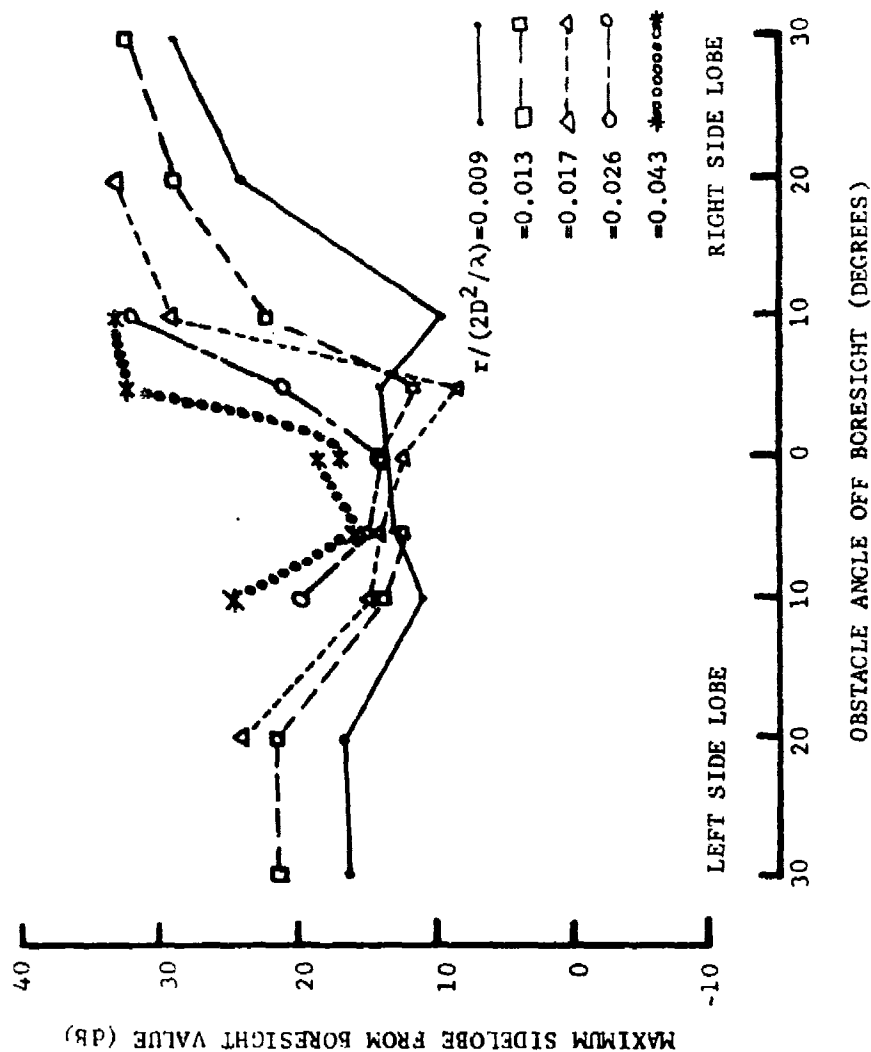
Figure 90. Maximum sidelobe level to the left and right of boresight as a function of obstacle angle off boresight; the positive values of the ordinate indicate the level down from the boresight value. Each curve in the family is for the open mast obstacle of normalized width 0.408 at the indicated normalized obstacle distances for Horizontal-polarized signals at a frequency of 9600 MHz.

162

boresight is positive both to the left and to the right of zero degrees. That is, the obstacle is always located on the right-hand side of the direction to the target as viewed from the receiving antenna. Therefore, the interpretation of the left sidelobe on the displays is the effect on the left sidelobe of a radiation pattern that an obstacle on the right-hand side of boresight produces. Similarly, the interpretation of the right sidelobe is the effect on the right-hand sidelobe of a radiation pattern that the same obstacle on the right-hand side of boresight produces.

Several general trends are apparent from the curves of Figures 81 through 90. In general, the manner in which an individual curve varies depends on the clear-site antenna pattern, the width of the open mast, and the near-field distance from the receiving antenna. For example, one can observe from the figures that the right-hand sidelobe approaches a much lower level (relative to the boresight value of the antenna pattern) for the X-band antenna than for the C-band or S-band antennas. This phenomenon occurs because the close-in sidelobes of the clear-site X-band antenna pattern are much lower than those of the other two antennas, as the antenna patterns shown in Section II indicate. For shorter near-field obstacle distances, the sidelobes are affected over larger obstacle angles, as one would expect. Also, shorter obstacle distances and greater obstacle widths generally produce greater effects on the sidelobes over larger obstacle angles. In general, the left-hand sidelobes are more adversely affected for greater obstacle angles than are the right-hand sidelobes. The fact occurs because the left sidelobe of the receiving antenna pattern is directed toward the transmitting

antenna (target) at the same time the main beam of the receiving antenna
pattern is directed toward an open-mast obstacle, which is always on
the right-hand side of a straight line between the physical locations
of the transmitting and receiving antennas.

It is instructive to note the general limits of the various groups
of sidelobe curves. In general, the sidelobes are 10 dB down, or better,
from the boresight value; this fact is true for both the 24-inch wide
and 48-inch wide open masts. This behavior is in direct contrast to
that for solid obstacles of corresponding widths for which a wide varia-
tion in sidelobe levels occurs, particularly for small obstacle angles.
The sidelobe levels for these two different open masts compare more
closely to 6-inch wide solid obstacles than to either 24-inch or 48-inch
wide solid obstacles. For a given frequency and open-mast width, no
well-defined distinction between the cases for horizontal and vertical
polarizations can readily be made.

SECTION VII

COMPUTER PROGRAM FOR SHIPBOARD SITING OF ANTENNAS

The computer program for shipboard siting of antennas [5,6] is continually being adapted to make it more useful and flexible. In the research accomplished under the program described in this report as well as that under previous work [2], efforts have centered on computer program modifications to describe the gain loss caused by obstacles which block directive antennas. The determination of gain loss versus antenna pointing angle is accomplished using a measured data base and an interpolation scheme. The present data base consists of data in the S, C, and X radar bands for solid obstacles as well as two open-mast structures. A description of these obstacles is given in Section II. Some of the data already have been useful in the estimation of the effective radar coverage of both search and tracking antennas on the Patrol Frigate [4].

The modifications and additions made to the computer program under this research effort extend its range of application in practical shipboard antenna/obstacle blocking problems. In particular, the addition of the open-mast data significantly enhances the computer-program capability. The additions and modifications are summarized below:

(1) Additional measured data were added to the data tables;

(2) The program input/output was modified to permit operator selection of type of obstacles, such as cylindrical

mast, open mast, etc.;

(3)   The data format was revised to simplify expansion of the data tables; and

(4)   The computer program was modified to make more efficient use of core storage.

The modifications will be addressed in more detail in the subsequent discussions.

A block diagram of the computer program for shipboard siting of antennas, which was derived under a previous program [2], is shown in Figure 91. The numbers denote the sequence of program execution. The specific modifications that were made to this block diagram are discussed in the following paragraphs.

During the first program modification, only one type of obstacle data was available and, therefore, operator selection of an obstacle type was not needed. With the addition of the data for various types of obstacles, a problem was encountered as to how the obstacle decoupling data should be paired with the obstacle type encountered. Therefore, the obstacle type was chosen as an operator input to allow the operator to decide which data best suit the antenna blockage situation. For example, a square column may best be simulated by using data for Corner No. 1 if the antenna views the square column from an angle that is 45 degrees with respect to one of its flat sides. Also this choice allows the operator to test various types of obstacles at a given location to optimize antenna performance. To implement this feature,

Figure 91. Over-all flow diagram of the computer-aided-ship-design (CASD) computer program after first modification for including obstacle blocking data.

167
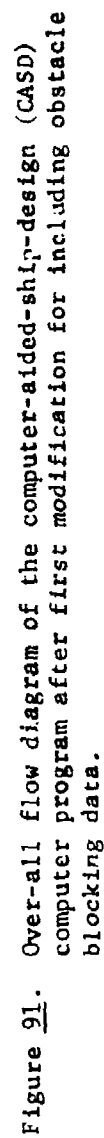
Subroutines MAIN and START were modified. Subroutine CONVRT is now called from Subroutine START instead of from Subroutine MAIN.

The mast type specification was added to the input data that are required in Subprogram START. This specification is now part of the antenna data specification ANDATA (I,J) which is indexed by

I = Antenna number (1≤ I≤ N, N = number of antennas)

J = Data Code

1 = Aperture Width

2 = Frequency

3 = Polarization

4 = Type of Mast Data.

The program modifications are shown in Figure 92. These updates were necessary because Subroutine START reads the operator input, and thus the obstacle type should be entered before Subroutine CONVRT is called. Therefore, Subroutine CONVRT need only read the data needed for the particular obstacle type, antenna, frequency, and polarization. Also, Subroutine CONVRT was modified to convert only the selected obstacle type data from decibel format (DATADB) to power blockage format (FFDATA). Since the data block FFDATA is one dimension less than data block DATADB, a saving in storage is effected. This saving is accomplished by converting only the data for the specific obstacle type being studied. This procedure also minimizes the number of modifications required in subsequent subroutines.

The "free-field" format of the data in the data block DATADB was

168

Figure 92. Over-all flow diagram of the computer-aided-ship-design (CASD) computer program after second modification.
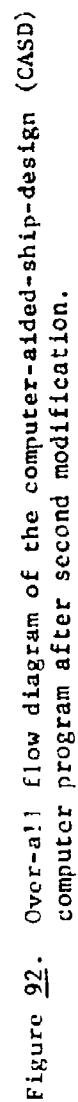
also altered. The data format of the previous program required only that each data number (field) be separated by a comma. This format is very convenient for entering data, because a keypunch or teletype operator need not conform to a predetermined fixed format. However, when one tries to compare the data in the "free-field" format with data in a second independent list, difficulties are encountered due to the lack of pattern in the location of the entries on a data printout. Therefore, all the "free-field" entries were converted to the selected "free-field" format of

$$\pm \text{ XX.X, } \pm \text{ Y.YY, etc.,}$$

where the $\pm$ XX.X, $\pm$ Y.YY denote the blockage data in dB and the comma is the field delimiter. This format requires that all entries contain the same number of characters and be separated by commas so that the data appear columned when listed. This "free-fixed" field format retains the advantages of the free field with respect to addition of new data and allows the data to be cross-checked using the editor features of a time-shared computer system. In addition, the format of each line of obstacle decoupling data was altered to include an obstacle identifier. Figure 93 is a comment section of Subroutine DECPCV. This figure lists the parameters used to identify a data line. A sample line of data is shown below.

    DATA DATADB (3,1,4,3,1,2)/-26.1, -13.3, -4.20, -0.80, 0.00/

From Figure 93 the sample data line parameters (MSTP, M,L,K,J,I) can

```
      COMMON/ANTENN/XANT(6),YANT(6),ZANT(6),JANT,ANDATA(6,4)
      COMMON/CRVMST/CRVMST(6,6),IERROR,XVECU(6),YVECU(6),
     #              ZVECU(6),RANGE(6),WIDTH(6),WRATIO(6),CVMTSL(6,6)
      COMMON/CRVFIT/XCV(7),YCV(7),TSLP(7),N
      COMMON/FFDATA/DATADB(5,5,3,2,3),FFDATA(5,5,3,2,3),
     #              RD(20),WD(20)
C     COMMON/FFDATA CONTAINS FAR FIELD DATA AND CORRESPONDING
C                   PARAMETERS USED BY 'DECPCV' IN THE INTERPOLATION.
C                   THE FAR-FIELD DATA WAS GENERATED AT GEORGIA
C                   TECH.  IT IS STORED IN
C                   'DATAGT' ALONG WITH RD(N) VALUES AND WD(N) VALUES.
C                   DATADB(MSTP,M,L,K,J,I) CONTAINS THE FAR-FIELD
C                                    DATA IN DB.
C                   MSTP=OBSTACLE TYPE
C                       1=CYLINDRICAL MAST
C                       2=SQUARE COLUMN (SQUARE MAST)
C                       3=CONVEX CORNER (CORNER #1)
C                       4=CONCAVE CORNER (CORNER #2)
C                       5=OPEN MAST
C                   I=FREQUENCY
C                       1=9600 MHZ
C                       2=5500 MHZ
C                       3=3000 MHZ
C                   J=POLARIZATION
C                       1=HORIZONTAL
C                       2=VERTICAL
C                   K=WIDTH-RATIO
C                       1 FOR 9600=0.099 FOR 5500&3000=0.125
C                       2 FOR 9600=0.408 FOR 5500&3000=0.500
C                       3 FOR 9600=0.816 FOR 5500&3000=1.000
C                   L=RANGE
C                       1=4.00 FEET
C                       2=6.00 FEET
C                       3=8.00 FEET
C                       4=12.00 FEET
C                       5=20.00 FEET
C                   M=ANGLE
C                       1= 0.0 DEGREES
C                       2= 5.0 DEGREES
C                       3=10.0 DEGREES
C                       4=20.0 DEGREES
C                       5=30.0 DEGREES
C                   FFDATA(M,L,K,J,I) CORRESPONDS TO DATADB EXCEPT
C                                    THAT IT IS IN POWER.
C                   RD(N) CONTAINS THE NUMBER OF RANGES AND ACTUAL
C                        RANGES CORRESPONDING TO THE DATA IN
C                        DATADB AND FFDATA. (SEE L=RANGE)
C                            RD(1)=NUMBER OF RANGES.
C                   WD(0) CONTAINS THE NUMBER OF WIDTH-RATIOS AND
C                        ACTUAL WIDTH-RATIOS CORRESPONDING TO
C                        THE DATA IN DATADB AND FFDATA.(SEE K=WIDTHE
C                        RATIO)
C                            WD(1)=NUMBER OF WIDTH-RATIOS.
```

Figure 93. Comment section of subroutine DECPCV showing explanation of data format.

be identified as:

    MSTP = 3 = Convex corner (Corner #1),

      M = 1 = Initial angle of 0.0 degrees,

      L = 4 = Obstacle displacement of 12 feet,

      K = 3 = Width Patio 9600=0.816 for 5500&3000 MHz=1.000,

      J = 1 = Horizontal polarization, and

      I = 2 = 5500 MHz data.

The numbers between the slashes in the data line are decoupling values for the angles 0, 5, 10, 20, and 30 degrees respectively. The original program included data for the circular cylinder type of obstacle (MSTP=1) and for the X- and C-band frequencies (IFREQ=1,2, respectively).

The data base has been expanded to include the four additional obstacle types at the C-, X-, and S-band frequencies and additional circular cylinder data for S-band. Figure 94 depicts graphically the type of obstacle and the direction of propagation of the energy incident upon the obstacle. The current data base represents an approximate 750 percent expansion of the original data base.

The method of appropriate data selection, interpolation between stored data points, curve fitting, and output curve plotting remains the same as that derived in the original modification [2]. The current program also retains the same output curve plots and data formats. A minor point is that no provision is presently incorporated to display the obstacle type on the output plots. Because the obstacle data to be employed must be operator specified as input data, this limitation is not considered to be a serious deficiency; however, it is anticipated
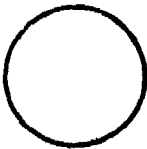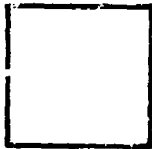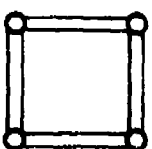
COMPUTER IDENTIFIERS	PROPAGATING SIGNAL DIRECTION	OBSTACLE TYPE	RECEIVING ANTENNA
MSTP = 1	→	CYLINDRICAL MAST	)
MSTP = 2	→	SQUARE COLUMN	)
MSTP = 3	→	CONVEX CORNER (#1)	)
MSTP = 4	→	CONCAVE CORNER (#2)	)
MSTP = 5	→	OPEN MAST	)

Figure 94. Schematic illustration of obstacle type and their respective computer identifiers.

that this output will be provided during a subsequent update of the

computer program.

SECTION VIII

DIELECTRIC-COATED OBSTACLE INVESTIGATIONS

A. Introduction

Previous theoretical and experimental studies conducted by Georgia Tech [7] indicate that applying dielectric coatings to metal obstacles is one possible technique for improving ship topside electromagnetic effectiveness of directive antennas. A limited theoretical investigation for one specific dielectric-coated metal mast indicated that, in general, significant improvements are possible. In particular, a one-way improvement of 20 dB in the field strength at the near-field point of interest behind the obstacle for vertical polarization and an isolation of 15 dB at the same near-field point for horizontal polarization were predicted. Analyses of the equations, as well as limited data, further indicated that the selection of other parameters could conceivably result in even greater field-strength enhancement and/or isolation. Also, indications from those previous studies were that solid dielectric rods and hollow dielectric tubes of various cross-sectional shapes potentially could be very useful in reducing antenna blockage.

Based on those results, a small, exploratory, measurements program was conducted under the present contract to experimentally investigate the decoupling effects of dielectric coatings on metal masts. Although the extensive theoretical and experimental investigations that are needed to completely define and characterize the potential beneficial scattering properties of dielectric-coated masts are outside the scope of the present investigations, the potential usefulness of dielectric

175

coatings for improving far-field antenna performance and for improving near-field isolation of near-field antenna pairs was further illustrated from these investigations. Because the scope of the present research effort was limited, the measurements were necessarily restricted to antennas and circular masts of small electrical dimensions, for which relatively small improvements in boresight performance are predicted. Although much larger improvements would be obtained with larger masts and antennas, the exploratory measurements program demonstrates the principle, but does not represent either the optimum case or the upper bound on the performance which might be obtained for larger masts and/ or different parameters.

B. Theoretical Considerations

Pertinent theoretical considerations concerning scattering by dielectric-coated masts are summarized to emphasize important aspects. Although this brief analysis does not constitute the in-depth study necessary to completely characterize the effects of dielectric-coated obstacles on antenna performance, it does provide useful insight into the sensitivity of dielectric-coated obstacle effects to various obstacle parameters and provides guidelines for wisely selecting the obstacles to be tested experimentally.

The theoretical analysis is based on the exact modal solutions to the wave equation for scattering of a linearly-polarized plane wave perpendicularly incident on an infinitely-long dielectric-coated mast [8]. The geometry and variables for this situation are depicted in Figure 95. The various symbols shown in the figure denote the following variables and parameters:
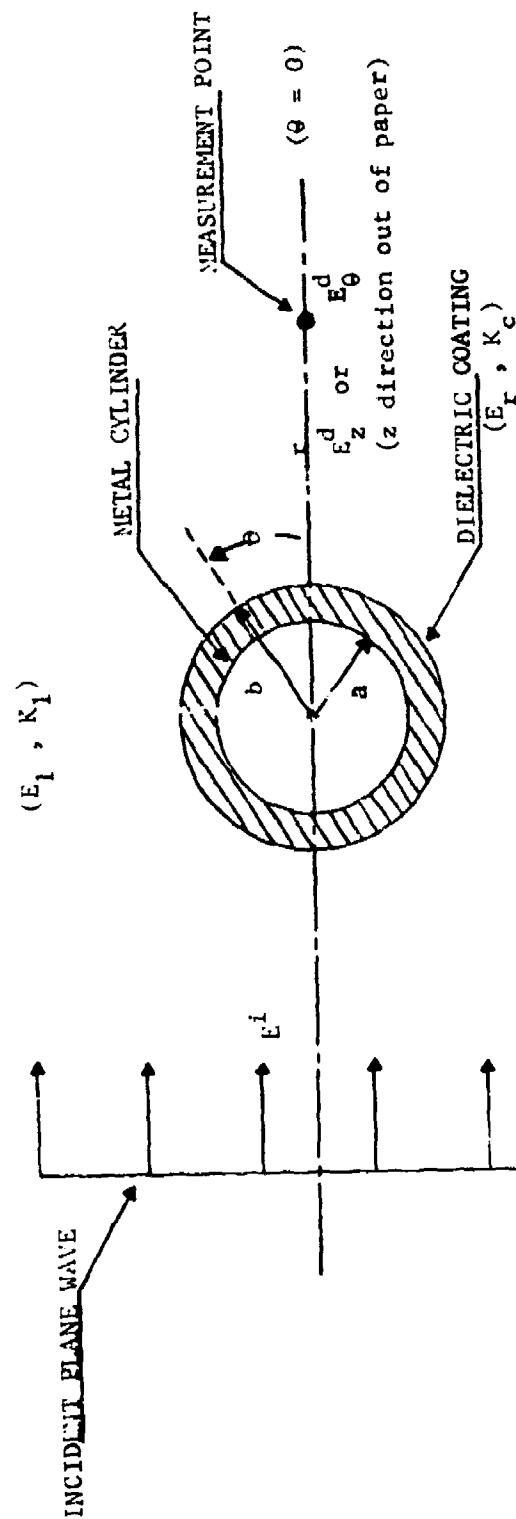
Figure 95. Sketch depicting geometry and variable for scattering of an incident electromagnetic plane wave by a dielectric-coated mast.

177

E^i = incident electric field,

$E^d(r,\theta)$ = resultant diffracted electric field at the near-field point defined by coordinates (r, θ),

r = distance from vertical axis of mast to the near-field point of interest,

θ = angular coordinate of near-field point,

z = coordinate parallel to cylinder axis,

K_1 = propagation constant of incident wave,

K_c = propagation constant inside the dielectric coating,

ε_r = complex dielectric constant of coating relative to vacuum,

ε_1 = dielectric constant of free space,

a = radius of metal mast, and

b = outer radius of dielectric coating.

The expressions for the resultant field $E^d(r,\theta)$ are obtained by solving the Helmholtz wave equation in cylindrical coordinates subject to appropriate boundary conditions at the interfaces. The wave equation expressed in terms of polarization (parallel or perpendicular) is solved subject to the appropriate boundary conditions, which require continuity of tangential electric and magnetic fields across the air-dielectric interface and vanishing of the tangential electric field on the surface of the metal mast.

The solutions for the resultant diffracted field E_z^d for vertical polarization and E_θ^d for horizontal polarization are, respectively,

$$E_z^d(r,\theta) = \sum_{n=0}^{\infty} e_n(i)^n J_n(K_1 r) \cos(n\theta) \qquad (1)$$

178

$$+ \sum_{n=0}^{\infty} e_n A_n H_n^{(1)} (K_1 r) \cos n\theta \quad ,$$

and

$$E_\theta^d (r,\theta) = \sum_{n=0}^{\infty} e_n (j)^n J_n^{'}(K_1 r) \cos (n\theta) \qquad (2)$$

$$+ \sum_{n=0}^{\infty} e_r B_n H_n^{'}(K_1 r) \cos (n\theta) \quad ,$$

where

e_n	$=$	Neumann's number ($e_n = 1$ for $n = 0$, $e_n = 2$ otherwise) ,
$J_n (K_1 r)$	$=$	Bessel function of the first kind and order n,
$H_n^{(1)}(K_1 r)$	$=$	Bessel function of the third kind and order n (Hankel function),
A_n	$=$	scattering coefficients for vertical polarization, and
B_n	$=$	scattering coefficients for horizontal polarization.

E_θ^d is obtained from H_z^d by the Maxwell curl relation. The prime in the equations denotes differentiation with respect to the argument. The equations are valid everywhere in the region of space exterior to the dielectric-coated mast, in both the near field and the far field. In the limit as the coating thickness goes to zero, the radii a and b are equal, and the scattering coefficients respectively reduce to the correct expressions for an uncoated mast of radius a (or b) for vertical and horizontal polarization, respectively.

Examination of the equations for the dielectric-coated mast shows the explicit dependence of the resultant electric field on frequency,

179

polarization, dielectric constant and loss tangent, coating thickness, and the diameter of the metal mast. However, the complexity of the equations prevents a qualitative analysis of trends based on a casual inspection. In order to study the effects of various parameters on the scattering properties of the coated mast, a computer must be used to calculate the electric field strength at selected near-field points along the boresight ($\theta = 0$) direction for selected coated and uncoated masts.

The results of preliminary calculations explicitly showed that the diffracted electric field intensity can be favorably altered by certain thicknesses of dielectric coating. In particular, for the properly chosen coating thickness, the diffracted electric field for either polarization state can be significantly increased or reduced relative to the diffracted electric field intensity at the same near-field point for an uncoated metal mast. Further, it appears that the beneficial effects of a coating are greater for larger metal masts and that the optimum coating thickness depends on the dielectric constant. Additional indications are that for a given frequency, the diffracted electric field intensity behind coated and uncoated masts increases smoothly as the near-field distance is increased, and that the magnitude of the difference between the electric field intensities at a given frequency for coated and uncoated masts decreases for longer near-field distances. This latter fact indicates that the beneficial effects of dielectric coatings are greater for shorter near-field distances where they are needed most.

C. Experimental Investigations

The results of measured data for a particular dielectric-coated mast and an uncoated metal mast are presented an discussed. As mentioned in Section II, the metal mast diameter is about 3.5 inches, the overall diameter of the dielectric-coated mast is about 4.0 inches, and the inner diameter of the coated mast is the same size as the bare metal mast. The thin 0.25-inch thick dielectric coating has a dielectric constant and loss tangent of approximately 2.6 and 0.006, respectively, over the X-band frequency range from 8 to 12 GHz. The ratios of the mast diameter of the uncoated and coated masts to receiving antenna aperture (W/D ratios) were 0.7 and 0.8, respectively, for vertical polarization, while for horizontal polarization the W/D ratios were 1.2 and 1.3, respectively. These different ratios for the two polarizations occur because tne antenna aperture dimensions are different in. the two principal planes.

The experimental results of the swept-frequency measurements of decoupling by the coated and uncoated masts are displayed in Figures 96 through 107. Figures 96 through 101 are for vertically polarized signals and Figures 102 through 107 are for horizontally polarized signals. For each polarization, the figures are sequenced according to increasing near-field obstacle distance from the receiving antenna. Finally, the figure at the top of each page displays the results of measured decoupling for both the coated and uncoated masts, and the figure at the bottom of each page displays the magnitude of the difference in decoupling between the coated and uncoated masts.
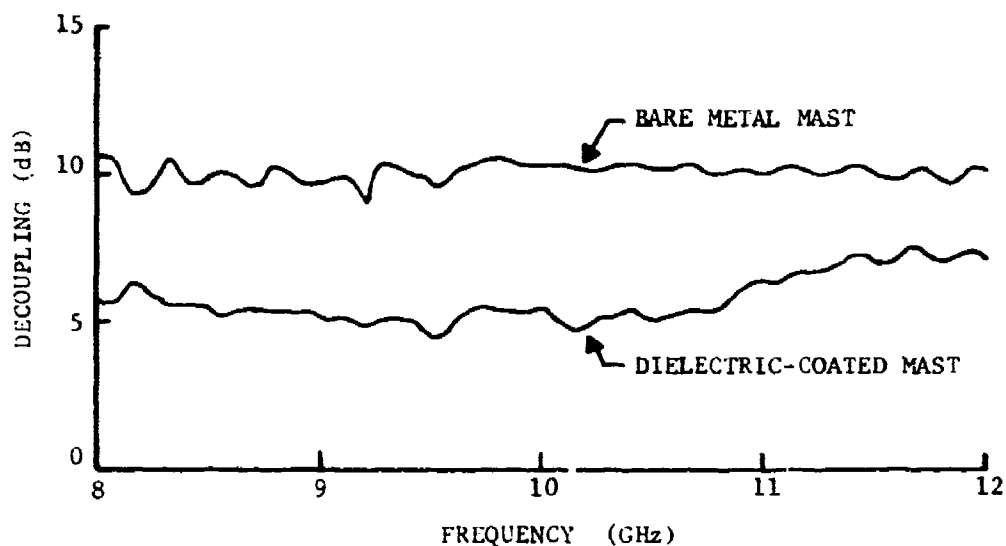
Figure 96. Boresight decoupling as a function of frequency for
both the bare metal mast and the dielectric-coated
mast for obstacle distance of 0.26 through 0.38 of
$(2D^2/\lambda)$ for vertically polarized incident signals.
The W/D ratios for the bare metal mast and coated
mast are 0.7 and 0.8, respectively.
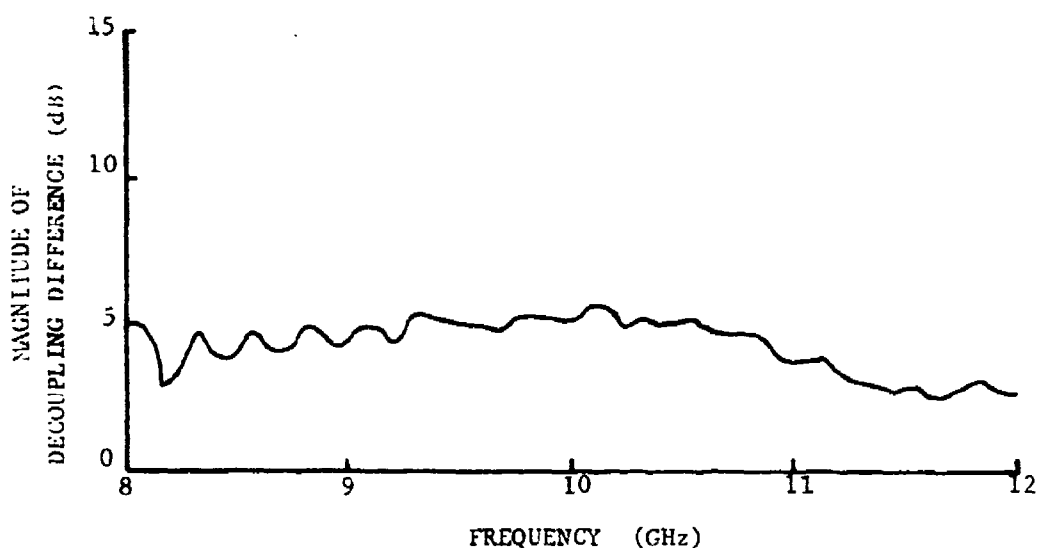
Figure 97. Magnitude of the boresight decoupling difference as
a function of frequency for measured mast decoupling
data presented in Figure 96.
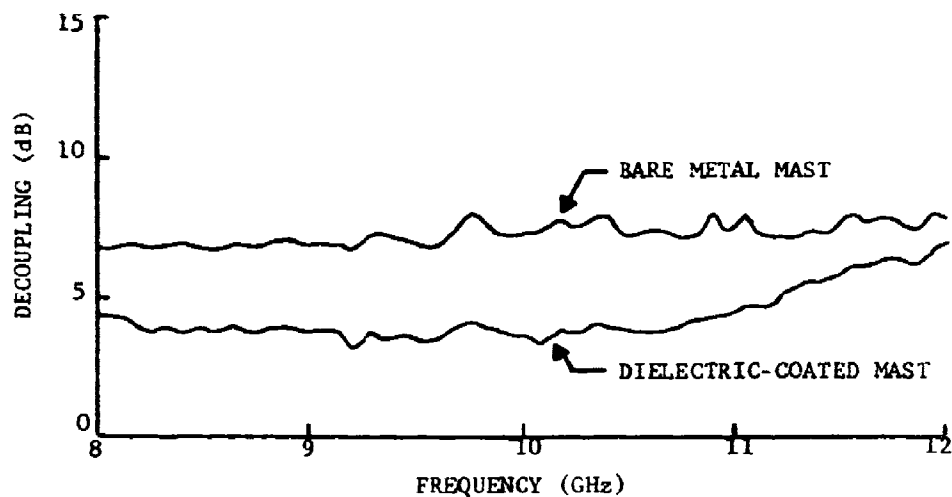
Figure 98. Boresight decoupling versus frequency for both the bare metal mast and the dielectric-coated mast for obstacle distances of 0.47 through 0.71 of $(2D^2/\lambda)$ for vertically polarized incident signals. The W/D ratios for the bare metal mast and the dielectric-coated mast are 0.7 and 0.8, respectively.
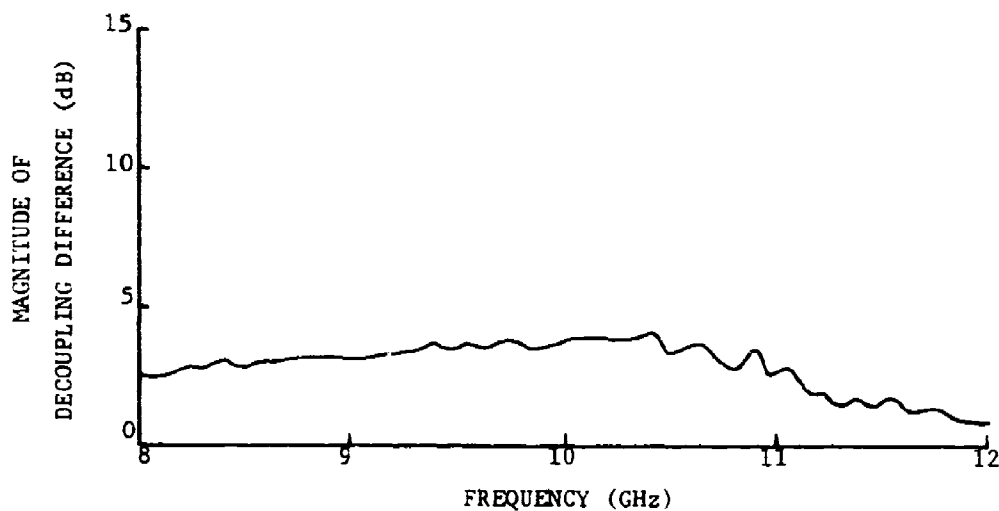
Figure 99. Magnitude of decoupling difference versus frequency for measured mast decoupling data presented in Figure 98.

183
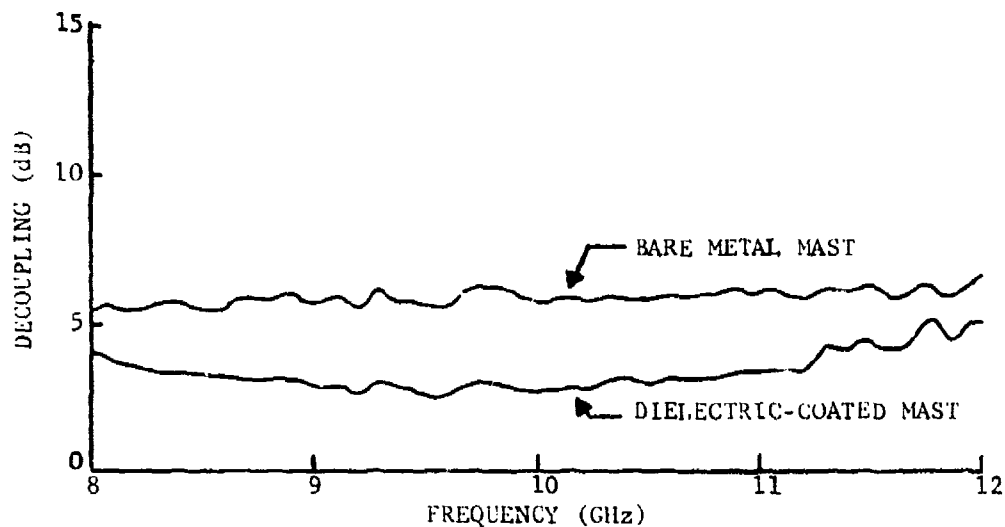
Figure 100. Boresight decoupling versus frequency for both the bare metal mast and the dielectric-coated mast for obstacle distance of 0.71 through 1.1 of $(2D^2/\lambda)$ for vertically-polarized incident signals. The W/D ratios for the bare metal mast and the dielectric-coated mast are 0.7 and 0.8, respectively.
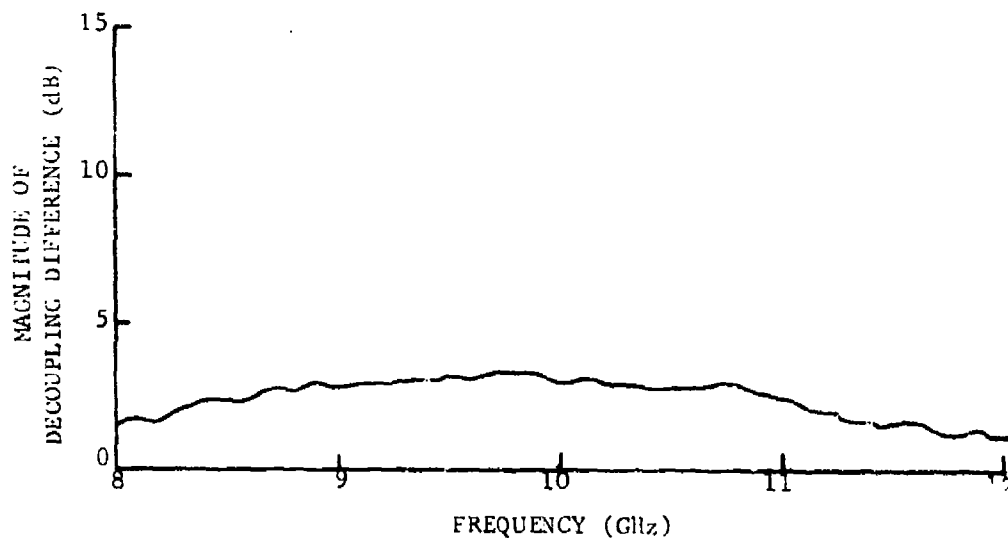
Figure 101. Magnitude of the decoupling difference for the measured data presented in Figure 100.
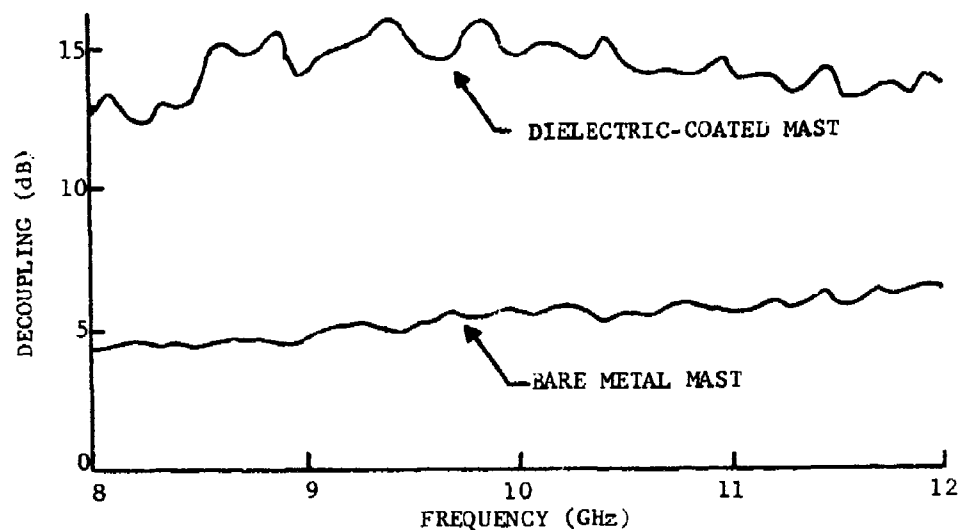
Figure 102. Boresight decoupling versus frequency for both a bare metal mast and dielectric-coated mast for obstacle distance of 0.25 through 0.38 of $(2D^2/\lambda)$ for horizontally polarized incident signals. The W/D ratios for the bare metal mast and coated mast are 1.2 and 1.3, respectively.
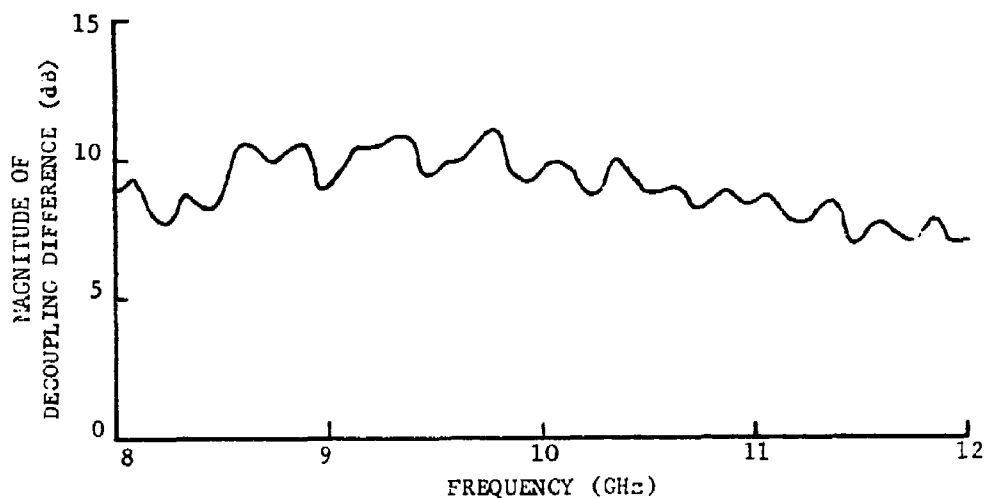
Figure 103. Boresight decoupling difference versus frequency for measured mast decoupling data presented in Figure 102.
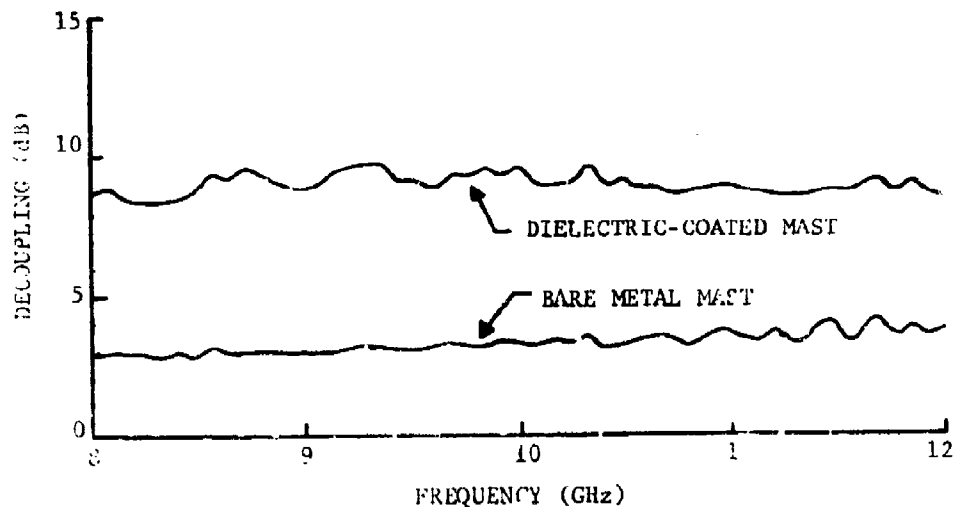
Figure 104. Boresight decoupling versus frequency for both the bare metal mast and dielectric-coated mast for obstacle distance of 0.47 through 0.71 of $(2D^2/\lambda)$ for horizontally-polarized incident signals. The W/D ratios for the bare metal mast and coated mast are 1.2 and 1.3, respectively.
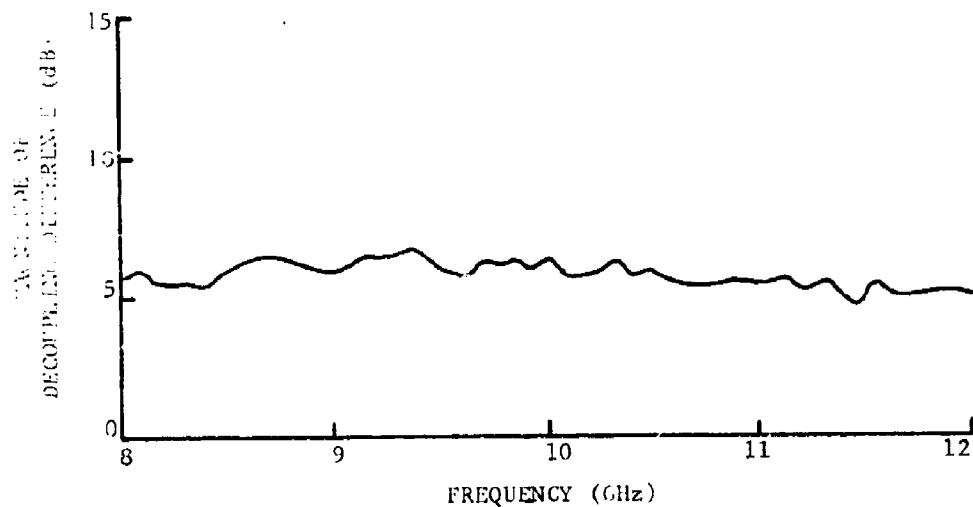
Figure 105. Magnitude of the decoupling difference versus frequency for measured mast data presented in Figure 104.

186
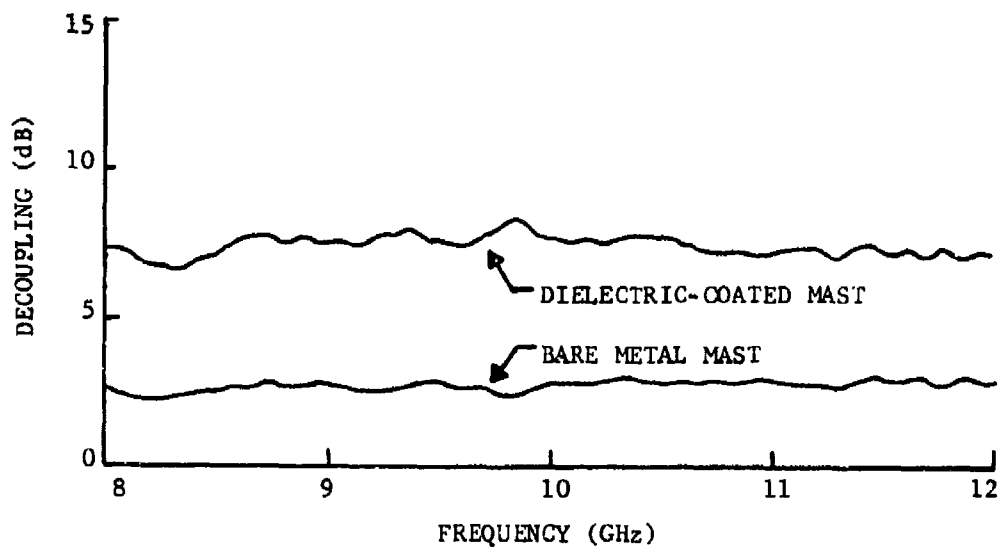
Figure 106. Boresight decoupling versus frequency for both the bare metal mast and the dielectric-coated mast for obstacle distance of 0.71 through 1.1 of $(2D^2/\lambda)$ for horizontally polarized signals. The W/D ratios for the bare metal mast and the dielectric-coated mast are 1.2 and 1.3, respectively.
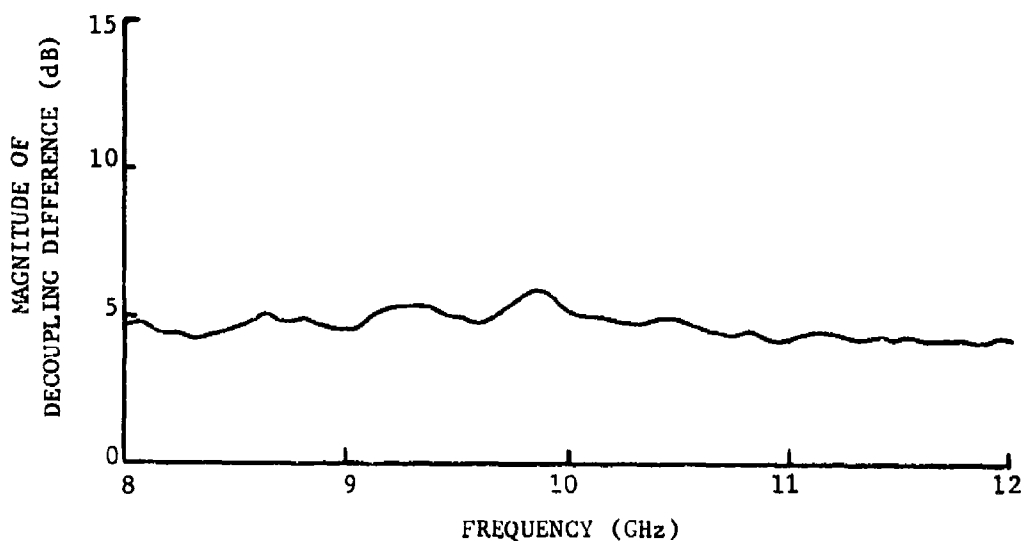
Figure 107. Magnitude of the decoupling difference versus frequency for measured mast data presented in Figure 106.

The measurement results presented in the figures for this partic-
ular dielectric-coated mast show well-defined trends. Inspection of
Figures 96 through 101 for vertically polarized incident signals shows
that the decoupling for the dielectric-coated mast is always less than
the decoupling for the bare metal mast for each of the three near-field
obstacle distances. Thus, the forward diffracted field is enhanced by
the coating for vertical polarization. Inspection of Figures 102
through 107 for horizontally polarized incident signals shows that the
decoupling for the dielectric-coated mast is always greater than the
decoupling for the bare metal mast for the same three near-field ob-
stacle distances. Therefore, the strength of the forward diffracted
field is diminished by the coating for horizontal polarization. These
experimentally-observed polarization trends for this particular choice
of dielectric-coated mast parameters are consistent with the estimates
based on theoretical considerations.

The magnitude of the decoupling difference between the coated and
uncoated masts for either incident polarization depends on both the
near-field obstacle distance and the frequency. For a given frequency,
the magnitude of the decoupling difference for either polarization is
greatest for the shortest near-field obstacle distance and decreases for
larger near-field obstacle distance. For example, the decoupling dif-
ferences for vertical polarization at 10 GHz are about 5 dB and 3 dB
for the shortest and longest near-field obstacle locations, respectively.
For horizontal polarization, decoupling differences of about 9.5 dB
and 5 dB were recorded for the shortest and longest near-field obstacle
locations, respectively. The measured and estimated values of decoupling

difference for both polarizations for the shortest near-field obstacle distance are in reasonable agreement. For each near-field obstacle location for either polarization, the decoupling difference varies as a function of frequency, with the highest value of decoupling difference generally occurring in the neighborhood of 10 GHz and decreasing as the operational frequency approaches either end of the frequency interval, which is consistent with theory. Small deviations in the decoupling difference occur as the frequency is swept over the frequency range from 8 to 12 GHz; these deviations are due to the fact that the individual decoupling curves as a function of frequency for both the dielectric-coated and bare metal masts each exhibits small undulations of typically less than $\pm$ 1 dB as the frequency changes.

In order to investigate the nature of the small undulations in decoupling as the frequency was continuously changed, decoupling measurements were performed for several discrete frequencies for an obstacle distance of 13 inches. The average decoupling values and maximum deviations from the average values for frequencies of 8, 9, 10, 11, and 12 GHz are presented in Table XIX. A comparison of the values for each discrete frequency in the table with the corresponding swept-frequency decoupling curves of Figure 96 shows that the average value and deviations are consistent with the swept-frequency results. Thus, the small undulations are primarily caused by the changes in near-field obstacle distance in terms of $2D^2/\lambda$ as the frequency changes. Note that the deviations for the coated mast are about the same magnitude or smaller than those for the bare metal mast for the same obstacle distance, polarization, and frequency, which indicates that the dielectric-coated

189

TABLE XIX

MEASURED VALUES OF DECOUPLING AND DEVIATIONS AT SELECTED FREQUENCIES FOR THE DIELECTRIC-COATED MAST
AND THE UNCOATED BARE METAL MAST FOR OBSTACLE DISTANCE OF 13 INCHES AND VERTICAL POLARIZATION

FREQUENCY (GHz)	OBSTACLE DISTANCE $\left(\dfrac{r}{2D^2/\lambda}\right)$	COATED Average (dB)	COATED Deviation (dB)	UNCOATED Average (dB)	UNCOATED Deviation (dB)
8.0	0.38	5.7	1.0	9.8	1.5
9.0	0.34	5.5	1.0	10.0	1.2
10.0	0.30	4.8	1.0	10.1	1.2
11.0	0.28	6.0	0.7	10 1	1.0
12.0	0.26	8.4	0.7	10.2	1.0

190

mast does not cause unusual reflections in the direction of the receiving antenna for the situations tested.

D. Summary

The potential beneficial effects of dielectric coatings on metallic obstacles for improving antenna performance and/or isolation depend on both the diffracted electric field of the metallic mast and the aperture illumination function of the antenna. The calculation of the power received by a finite-sized receiving antenna would require integration of the convolution product of the diffracted field with the aperture illumination function, over the entire receiving antenna aperture. Because the diffracted fields of the masts were calculated only at a single point on the boresight axis, the full significance of the coating on the antenna performance or on the isolation of two antennas was not precisely determined. Based on past experience involving near-field obstacle effects on microwave antennas and certain theoretical aspects concerning the structure of diffracted radiation behind obstacles, it appears that the diffracted electric field intensity on boresight may be a reasonably good approximate descriptor of the enhancement or the isolation which would occur for electrically small or moderate-sized mast-antenna combinations of a few wavelengths in width. However, for electrically larger mast-antenna combinations on the order of about 10 wavelengths or larger in width, knowledge of the boresight electric field intensities may not be an adequate descriptor and aperture integration may be necessary in order to achieve acceptable engineering estimates.

The measured data presented have demonstrated that dielectric coatings on circular metal masts can be used to significantly alter the power received by a receiving antenna. For the particular electrically-small dielectric-coated mast and antenna combination tested in this exploratory measurements program, a maximum one-way increase at 10 GHz of about 5.2 dB in received power above the bare metal mast results was achieved for vertically polarized incident signals, while the received power for horizontally polarized signals at 10 GHz was decreased about 9.5 dB below that for the bare metal mast. The experimental data further show that these beneficial effects of the coating, namely enhancement of vertical polarization and increased isolation of horizontally polarized signals, exist over the entire frequency range from 8 to 12 GHz for all of the near-field obstacle locations. An important observation is that the beneficial effects of a dielectric coating for a given frequency for both polarizations appear to be greater for shorter near-field obstacle locations, which is where the most improvement is needed because the degrading effects of bare metal obstacles are typically most severe at the short near-field locations.

Although the experimental results are very encouraging, theoretical considerations indicate that even greater benefits can be achieved with different choices of dielectric-coated mast parameters. In particular, calculations performed for one specific dielectric-coated mast during a prior investigation indicated that enhancement and increased isolation in excess of 20 dB can be achieved for electrically larger masts with properly chosen coating parameters. That brief study further indicated that the polarization and frequency responses can be changed by a

different choice of parameters. Additionally, it appears that the discriminating use of dielectric tubes and rods as well as coated obstacles of various cross-sectional shapes and configurations could lead to beneficial applications. However, these possibilities are based on limited studies which require further theoretical and experimental investigations to determine their potential usefulness.

E. Examples of Potential Applications

The properties of properly chosen dielectric coatings to enhance or diminish the electric field strength behind solid metal mast obstacles can be very useful in shipboard applications. Suppose for example that a high power, vertically-polarized, transmitting antenna must operate in the presence of a mast superstructure located within the near field of the transmitting antenna. Further suppose that at a nearby location, a very sensitive horizontally-polarized receiving antenna is located within the azimuthal sweep sector of the high power antenna but at a slightly lower elevation angle. The cross polarization component of the transmitting antenna, which often may be large enough to interfere with the sensitive receiving antenna, could be significantly reduced at the receiving antenna by applying a properly-chosen dielectric coating on the mast element. The same coating would enhance propagation of the vertically-polarized component of the transmitting antenna, which is its preferred polarization. Thus, an increase in the detection range could be achieved while a decrease in the interference with the sensitive horizontally-polarized receiving antenna could also be achieved.

As a second illustrative example, suppose that a certain search and track radar antenna is located such that a portion of its azimuthal sweep

path is blocked by a mast element. A second antenna whose azimuthal sweep path is not blocked by the mast element and whose frequency of operation is at the second harmonic frequency of the first radar is located slightly forward of the mast element and at a lower elevation than the first radar. It is desired to reduce the blockage effects of the mast on the first radar, but not decrease the isolation of main beam-to-sidelobe coupling which the mast provides between the antennas. Both criteria could evidently be met by a properly chosen dielectric coating which presents a "window" to the frequency band of the first radar while causing attenuation of signals at and near the second harmonic frequency. Thus, detection range of the first radar could be improved while actually decreasing the amount of second harmonic component which is "seen" by the second radar.

The possibility of using dielectric materials in this manner is based on very limited investigations in which many important aspects of the scattering properties of dielectric coatings and obstacles could not be addressed. For example, very little is currently known about the scattering properties of dielectric obstacles in directions other than the forward direction. Obviously, it would do little good to improve antenna performance and/or isolation for one set of antennas and then to have unwanted reflections or diffractions in other directions severely degrade the performance of other antennas. However, if such reflections were known to occur, then solutions could possibly be achieved by various strategems. Much more information regarding the sensitivity of scattering properties of dielectric obstacles to various parameters such as dielectric constant, loss tangent, coating thickness, size and shape of

194

the obstacle, frequency, and polarization state is also needed in order
to avoid possible pitfalls and to achieve the maximum benefits/cost
ratio.

SECTION IX

PHASED-ARRAY STUDY

A. Introduction

Previous experimental and theoretical investigations concerning problem areas of shipboard phased-array antennas have indicated conventional analyses may be inadequate to handle this serious EMC problem area [1-3]. In particular, those limited experimental investigations indicated that the propagation of higher-order modes at out-of-band frequencies cause phased arrays containing ferrite phase shifters not only to respond differently at out-of-band frequencies but also to exhibit random behavior [2]. A subsequent exploratory theoretical study indicated that statistical analysis techniques can be used to describe and predict the out-of-band radiation patterns. As a result of those investigations, a basic statistical model for EMC prediction and analyses was developed for an array of isotropic radiators whose phase shift and amplitude excitation vary randomly [3].

The purpose of the current phased-array study is to investigate the feasibility of extending the basic statistical model to an array of waveguide radiating elements whose out-of-band response is random. This extension is very desirable since many real-world phased arrays are comprised of waveguide radiating elements which can support the propagation of modes at out-of-band frequencies. Each mode, which can have a randomly-varying amplitude and phase shift as a function

197

of phase shifter bias voltage, can give rise to polarization components that are orthogonal to the dominant in-band TE_{10} mode. Consequently, the polarization state, scanning properties, peak gain, and median gain of the out-of-band far-field patterns will vary randomly and will depend on the modal content. Thus, an expanded statistical model which can be used to describe and predict these out-of-band array characteristics is a desirable analysis tool. However, the complex nature of randomly-varying out-of-band phenomena involving multi-modal energy propagation precludes from the current efforts the extensive in-depth analyses required to completely characterize planar arrays of mutually-interacting waveguide elements. Therefore, these feasibility investigations for extending the basic model were conducted for a linear array of non-interacting waveguide elements. The results of the study demonstrate both the feasibility and utility of the expanded statistical model and permit further refinements and extensions in future efforts.

B. Approach

The approach taken to extend the statistical model for predicting the response of phased arrays to encompass a linear array of out-of-band waveguide radiating elements and to interpret the results involved the following major steps:

(1) theoretical development of statistical equations for analyzing a phased-array antenna comprised of out-of-band waveguide elements for which the modal content and inter-element phase shift vary randomly,

198

(2)   computer-generation of graphical displays of the far-field
antenna patterns and of their respective statistical median
gains and standard deviations of the out-of-band phased-
array antenna patterns over the front 180-degree azimuthal
sector, and

(3)   interpretation of EMC implications of results.

In step (1), theoretical equations were derived to statistically
analyze the out-of-band azimuthal antenna patterns of a randomly-
excited linear array of waveguide elements as a function of both the
in-band scan angles and the statistics of the elements. In the
analyses, the in-band phase shift response is assumed both linear
and non-random, and the signal amplitude is assumed both constant
and non-random. For the out-of-band signals, which can generally be
propagated in more than one mode, the amplitudes and phase shifts of
the various modes vary randomly. Thus, the expressions derived for
the statistical-average antenna patterns depended on the assumptions
made regarding the statistical distributions of out-of-band signal
parameters. However, the majority of the theoretical analyses was
conducted under the assumptions that the random-mode signal amplitudes
are uniformly distributed and the random-mode phase shifts are dis-
tributed with a Gaussian probability distribution. Further assump-
tions regarding the statistical parameters are made to derive prac-
tical simplified equations for analyzing average antenna pattern
characteristics such as scanning, peak gain levels, sidelobe statistics,

median gain, and standard deviation.

In Step (2), computer techniques were used to (1) calculate and display average antenna patterns based on the theoretical equations, (2) calculate and display individual antenna patterns for given random amplitude and phase excitations of the allowed mode signals, and (3) compute the median gain and standard deviation over the front 180-degree azimuthal sector, as a function of both the in-band scan angle and the element statistics. Both types of patterns (average patterns and individual randomly-excited patterns) were studied to provide insight into the important out-of-band pattern characteristics as a function of scan angle and modal content. In order that the calculations be as realistic as possible, experimental data derived from the Phase II measurements program involving a ferrite phase shifter were used, where possible, to guide the selection of statistical parameters. The 180-degree median gain and standard deviation were calculated and analyzed to further determine their suitability as EMC descriptors since the results of the Phase III theoretical study indicated that they would be good descriptors.

In Step (3), possible EMC implications of this study are considered and discussed. These considerations include (1) the EMC significance of the dependence of out-of-band grating lobes, main beam, and median gain on the modal content, and (2) the utility of statistical analyses techniques in describing and predicting these out-of-band pattern characteristics in shipboard applications in order to improve electromagnetic effectiveness.

C.   Theoretical Development of Statistical Equations

The far-field antenna pattern of a randomly-excited array exhibits random behavior which is a function of the randomly-varying parameters of the array. Consequently, the array antenna has many different antenna patterns. and it is not possible to predict which pattern would be present if a particular instantaneous measurement could be recorded. Thus, the magnitude of potential EMC hazards is magnified because of the inherent uncertainity in the electromagnetic characteristics of the antenna when any of its parameters are random. The potential EMC problems are particularly acute for phased-array antennas comprised of waveguide radiating elements because of higher-order mode propagation. The pattern structure and gain levels depend on the relative magnitudes and phases of the higher-order mode signals which are present in the waveguide elements. However, the relative magnitudes and phases of the signals propagated in the various allowed modes vary randomly with the phase shifter bias voltage which is determined from the desired in-band scanning criteria [2]. In short, the array pattern statistics depend on the element mode statistics and the in-band scan angle. Therefore, equations are needed which predict the array pattern statistics in terms of the higher-order mode statistics and in-band scan angle. The necessary equations can be derived via the same statistical analysis techniques used in the previous exploratory phased-array study for a randomly-phased array of isotropic radiators [3].

The mathematical outputs of the statistical analyses are (1) expressions for the statistical-average array pattern and its associated

angle-dependent functions of the mode statistics and in-band scan angle, (2) expressions for the cumulative probability distribution of the array pattern as a function of mode statistics and in-band scan angle, and (3) approximate expressions for estimating the 180-degree spatial median gain and standard deviation of the array pattern. The statistical-average array-pattern is the weighted average of all the possible individual random antenna patterns of a single randomly-excited antenna. Equivalently, the average array-pattern can also be interpreted as the average of the individual antenna patterns of an ensemble of similarly-constructed arrays. The spatial standard deviation defines the limits above and below the average pattern within which 68% of the power at that particular spatial angle would lie. The cumulative probability distribution is an expression which defines the probability that the power will lie within specified limits. The median gain over the front sector is the average decibel value (for a Gaussian distribution) of an entire antenna pattern over the sector, and the standard deviation associated with the median gain is a single spatially-invariant standard deviation.

The spatial standard deviation and the cumulative probability distribution are primarily of value in this study to obtain estimates of the front-sector median gain and associated standard deviation as functions of in-band scan angle and mode statistics, whereas the average antenna pattern and the front-sector median gain and standard deviation evidently have direct application as EMC prediction tools for out-of-band phased arrays. The average pattern equation is useful in studying the relative gain levels and scanning properties of out-

202

of-band grating lobes and main beam, as well as overall pattern shape and sidelobe tendencies, as a function of mode statistics and in-band scan angles. The front sector median gain and standard deviation are concise, powerful statistical descriptors of overall pattern tendencies, and therefore, may be very useful in EMC applications.

In addition to the average pattern and the front sector statistics, a knowledge of the detailed structure of a representative individual random antenna pattern can provide useful insight into random array pattern characteristics. In particular, the details of sidelobe structure are displayed in individual random patterns. The individual random patterns also provide a basis for validation of the average pattern and the estimates of the front sector statistics. Consequently, analytical expressions for individual random patterns, which arise during the analyses, were retained for later use in the calculations presented in subsection D.

1. Preliminary Technical Considerations

Statistical analyses involve the application of certain mathematical operations on initially deterministic equations. Consequently, the resulting statistical equations generally involve all of the non-random variables of a system plus the statistical parameters of the variables which are assumed random. Therefore, it is desirable in a statistical approach to first study and understand the deterministic significance of key variables. In the current study, certain aspects of out-of-band mode propagation and the antenna patterns of waveguide elements which propagate the various modes are important factors which will permeate the statistical equations. Therefore, it is advantageous

to initially consider the propagation of higher-order modes and the antenna patterns of elements that propagate the higher-order modes.

a. Higher-Order Mode Propagation

For a given out-of-band frequency, the power may generally be propagated in more than one mode. The possible modes which can exist in X-band waveguide for the in-band frequency of 9 GHz and the out-of-band frequencies of 14.5, 15.7, and 18 GHz are shown in Table XX. Thus, the power may be split among two, three, or five modes for these respective out-of-band frequencies. Because each mode has a distinct electric field configuration, the characteristics of the resulting element pattern of a waveguide radiating element will depend on modal content. If more than one mode is present at a given out-of-band frequency, the resultant element pattern will be a linear superposition of the individual element patterns for each mode.

The different field configurations of the various modes are depicted conceptually in Figure 108 to illustrate the characteristics of the modes. As seen in the figure, the TE_{10} and TE_{20} have only a y-directed electric field component, whereas the TE_{01} has only the orthogonal x-directed electric field component. However, the TE_{11} and TM_{11} have both parallel and cross components of electric field. For the TE_{10} and TE_{01} modes, the phase across the aperture is constant. For the TE_{20}, TE_{11}, and TM_{11} modes, the electric field lines either side of the vertical centerline of the aperture are 180-degrees out of phase. The electric fields on opposite sides of the horizontal centerline are 180-degrees out of phase and also equal in magnitude

TABLE XX

ALLOWED MODES OF PROPAGATION FOR X-BAND
AIR-FILLED WAVEGUIDE FOR THE INDICATED
IN-BAND AND OUT-OF-BAND FREQUENCIES

Frequency	Allowed Higher Order Modes In Air-Filled X-Band Waveguide
9.0 GHz	TE_{10}
14.5 GHz	TE_{10} TE_{20}
15.7 GHz	TE_{10} TE_{20} TE_{01}
18.0 GHz	TE_{10} TE_{20} TE_{01} TE_{11} and/or TM_{11}

(a) TE$_{10}$ MODE

(b) TE$_{20}$ MODE

(c) TE$_{01}$ MODE

(d) TE$_{11}$ MODE
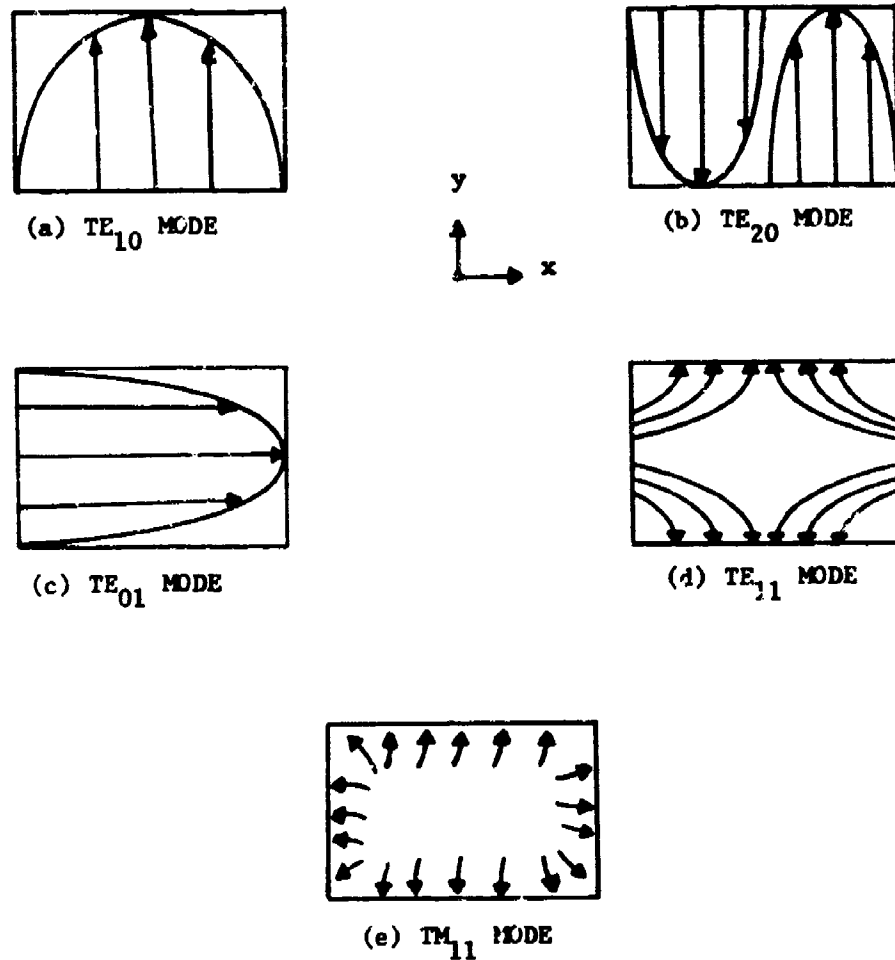
(e) TM$_{11}$ MODE

Figure 108. Conceptual view of the transverse electric fields of the indicated waveguide modes.

for both the TE_{11} and TM_{11} modes. Consequently, the y-component of the antenna patterns for each of these two modes is zero in the entire azimuthal plane defined by the magnetic field vector of the TE_{10} mode. Since attention is confined to the azimuthal plane during the remainder of this study, expressions involving the parallel (y-directed) component of the TE_{11} and TM_{11} modes will not be needed.

Analytical expressions for the spatial distributions of the electric fields of the various modes in the waveguide which do contribute to the far-field azimuthal plane are derived in the literature [9]. If the coordinates of the waveguide are chosen as shown in Figure 109, the equations for the transverse fields of the individual indicated modes are given as

$$E_y^{10} = (\frac{\omega\mu a}{\pi})H_z^{10} \cos [\pi \frac{x}{a}] \exp [-j(\beta^{10}z + \frac{\pi}{2})] \ , \tag{3}$$

$$E_y^{20} = (\frac{2\omega\mu a}{\pi})H_z^{20} \sin [2\pi \frac{x}{a}] \exp [-j(\beta^{20}z - \frac{\pi}{2})] \ , \tag{4}$$

$$E_x^{01} = (\frac{\omega\mu b}{\pi})H_z^{01} \cos [\pi \frac{y}{b}] \exp [-j(\beta^{01}z - \frac{\pi}{2})] \ , \tag{5}$$

$$E_x^{11} = \frac{\omega\mu \frac{\pi}{b}}{(\frac{\pi}{a})^2 + (\frac{\pi}{b})^2} H_z^{11} \sin [\pi \frac{x}{a}] \cos [\pi \frac{y}{b}] \exp [-j(\beta^{11}z - \frac{3\pi}{2})], \text{ and} \tag{6}$$

$$_mE_x^{11} = \frac{\beta^{11}\frac{\pi}{a}}{(\frac{\pi}{a})^2 + (\frac{\pi}{b})^2} \ _mE_z^{11} \sin [\pi \frac{x}{a}] \cos [\pi \frac{y}{b}] \exp [-j(\beta^{11}z - \frac{\pi}{2})] \tag{7}$$
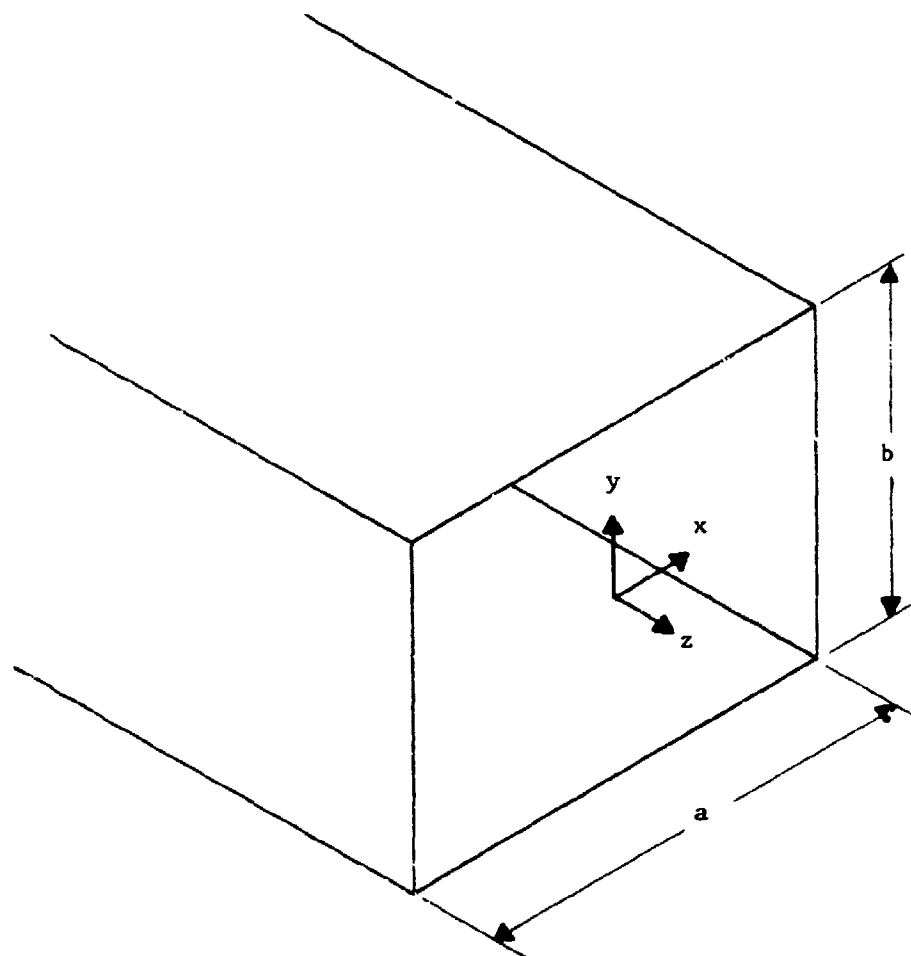
Figure 109.　Illustration depicting a waveguide element and coordinate geometry.

where

a = wide dimension of waveguide,

b = narrow dimension of waveguide,

H_z^{mn} = the z component of the magnetic field amplitude when a prescribed amount of power propagates in the mn^{th} TE mode,

$_mE_z^{mn}$ = the z component of electric field when a presecribed amount of power propagates in the mn^{th} TM mode, and

$_\beta^{mn}$ = propagation constant of the mn^{th} mode.

The factors multiplying the trigonometric functions in Equations (3) through (7) determine the maximum electric field amplitude of each mode for a given amount of power flow in the particular mode. These maximum amplitudes, denoted as $|E_{oy}^{10}|$, $|E_{oy}^{20}|$, $|E_{ox}^{01}|$, $|E_{ox}^{11}|$, and $|_mE_{ox}^{11}|$ for the TE$_{10}$, TE$_{20}$, TE$_{01}$, TE$_{11}$, and TM$_{11}$, respectively, exp·essed in terms of power flow of each mode are given as

$$|E_{oy}^{10}| = \frac{\omega\mu a}{\pi}\sqrt{\frac{P^{10}}{\frac{ab}{4}Z_f\left(\frac{\lambda_c^{10}}{\lambda}\right)^2\sqrt{1-\left(\frac{\lambda}{\lambda_{10}}\right)^2}}} \quad , \tag{8}$$

$$|E_{oy}^{20}| = \frac{2\omega\mu a}{\pi}\sqrt{\frac{P^{20}}{\frac{ab}{8}Z_f\left(\frac{\lambda_c^{20}}{\lambda}\right)^2\sqrt{1-\left(\frac{\lambda}{\lambda_c^{20}}\right)^2}}} \quad , \tag{9}$$

209

$$\left|E_{ox}^{01}\right| = \frac{\omega\mu b}{\pi} \sqrt{\frac{p^{01}}{\frac{ab}{4} Z_F \left(\frac{\lambda_c^{01}}{\lambda}\right)^2 \sqrt{1 - \left(\frac{\lambda}{\lambda_c^{01}}\right)^2}}} \quad , \tag{10}$$

$$\left|E_{ox}^{11}\right| = \frac{\omega\mu \, \frac{\pi}{b}}{\left(\frac{\pi}{a}\right)^2 + \left(\frac{\pi}{b}\right)^2} \sqrt{\frac{p^{11}}{\frac{ab}{8} Z_F \left(\frac{\lambda_c^{11}}{\lambda}\right)^2 \sqrt{1 - \left(\frac{\lambda}{\lambda_c^{11}}\right)^2}}} \quad , \text{ and} \tag{11}$$

$$_m\left|E_{ox}^{11}\right| = \frac{\beta^{11} \left(\frac{\pi}{a}\right)}{\left(\frac{\pi}{a}\right)^2 + \left(\frac{\pi}{b}\right)^2} \sqrt{\frac{Z_F \, _m p^{11}}{\frac{ab}{8} \left(\frac{\lambda_c^{11}}{\lambda}\right)^2 \sqrt{1 - \left(\frac{\lambda}{\lambda_c^{11}}\right)^2}}} \quad , \tag{12}$$

where

p^{mn} = the power flow in the z direction for the mnth TE mode,

$_p^{mn}$ = the power flow in the z direction for the mnth TM mode,

$_c^{mn}$ = cutoff wavelength of mnth mode, and

Z_F = impedance of the air dielectric in the waveguide.

The equations for the peak electric field amplitudes provide relationships for the electric field amplitude as a function of modal power. These relationships are needed to subsequently determine the random variations in electric field amplitude when prescribed random variations in modal power occur.

When the power flowing in each mode varies randomly, the peak electric field intensity of each mode varies randomly, as Equations (8) through (12) show. The statistical behavior of the random amplitude variations is related to the random power variations via the equations. In this study, the random power of each mode is assumed to have a uniform probability density, which is

$$H_i(p_i^{mn}) = \frac{dp_i^{mn}}{\Delta p_i^{mn}} \quad , \tag{13}$$

where Δp_i^{mn} is the width of the interval over which the power flow of the mn^{th} mode of the ith element varies randomly. Because the total power flow is the sum of the power flowing in each mode, the total power flow also varies randomly and may assume any value that does not exceed the input power flow incident on the ferrite phase shifter. In order to satisfy the constraint on total power flow and to establish a basis for investigating the signficance of different modal contents, the statistical average value of the total power flow is assumed to be one-half of the input power. Thus, the average value of power flow for each mode may assume any value which satisfies the criteria that the sum of the average power flowing in the various modes be equal to one-half the input power.

The random phase shifts induced by the ferrite phase shifter for each modal component of power flow can be accounted for by including a randomly varying phase shift factor in the exponential terms in

211

Equations (3) through (7). The phase shift for each mode is assumed to follow a Gaussian probability density defined as

$$f(\alpha_i^{mn}) = \frac{1}{\sqrt{2\pi}\ \sigma_i^{mn}} \exp\left[-\frac{(\alpha_i^{mn} - \bar{\alpha}_i^{mn})^2}{2(\sigma_i^{mn})^2}\right] \quad , \tag{14}$$

where $\bar{\alpha}_i^{mn}$ and σ_i^{mn} are the mean value and standard deviation, respectively, of the phase shift for mn^{th} mode in the ith element.

b. Element Patterns

The far-field patterns of the various individual modes are obtained via the Fourier transforms of the corresponding transverse electric fields given in Equations (3) through (7). In the current study, attention is confined to H-plane azimuthal cuts in the principal plane as conventionally defined for a vertically polarized signal. The resulting transformed fields can be expressed in the following form:

$$E_i^{mn}(\theta) = A_i^{mn} F_i^{mn}(\theta) \exp[-j(\gamma_i^{mn} + \alpha_i^{mn})] \quad , \tag{15}$$

where

$E_i^{mn}(\theta)$ = electric field intensity at angle θ,

A_i^{mn} = electric field amplitude factor,

$F_i^{mn}(\theta)$ = electric field pattern factor,

$\gamma_i^{mn} = \beta_i^{mn} z +$ multiples of π, and

α_i^{mn} = phase shift induced by the phase shifter.

The electric field amplitude factor, A_i^{mn}, is the product of the peak electric field intensity in the aperture of the waveguide element,

212

given in Equations (8) through (12), with the mode transmission co-efficient at the interface between the waveguide aperture and free space.

The element power pattern factor is obtained from Equation (15) as the square of $F_i^{mn}(\theta)$. The resulting expressions for the element power patterns are given as

$$[F^{10}(\theta)]^2 = \left| \frac{(\pi/2) \cos [\pi(a/\lambda) \sin \theta]}{[(\pi/2)^2 - (\pi(a/\lambda) \sin \theta)^2]} \right|^2 \qquad \text{for } TE_{10}, \qquad (16)$$

$$[F^{20}(\theta)]^2 = \left| \frac{(\pi/2) \sin [\pi(a/\lambda) \sin \theta]}{[(\pi)^2 - (\pi(a/\lambda) \sin \theta)^2]} \right|^2 \qquad \text{for } TE_{20}, \qquad (17)$$

$$[F^{01}(\theta)]^2 = \left| \frac{\sin [\pi(a/\lambda) \sin \theta]}{[\pi(a/\lambda) \sin \theta]} \right|^2 \qquad \text{for } TE_{01}, \text{ and} \qquad (18)$$

$$[F^{11}(\theta)]^2 = \left| \frac{[\pi(a/\lambda) \sin \theta] \cos [\pi(a/\lambda) \sin \theta]}{[(\pi/2)^2 - (\pi(a/\lambda) \sin \theta)^2]} \right|^2 \text{ for } TE_{11} \text{ and } TM_{11} \qquad (19)$$

where all symbols are as previously defined. Sketches of the element patterns are displayed in Figure 110. As noted previously, the patterns shown for the TE_{10} and TE_{20} modes are polarized in the vertical, or y, direction, whereas the sketches for the TE_{01}, TE_{11}, and TM_{11} are for the cross-polarized pattern. If more than one mode is present, the electric fields given by Equation (15) must be superimposed to derive the resultant patterns.

2. Statistical Equations

a. Average Patterns

The derivation of statistical expressions to characterize the out-of-band response of a randomly-excited array requires the application of certain mathematical operations on the conventional
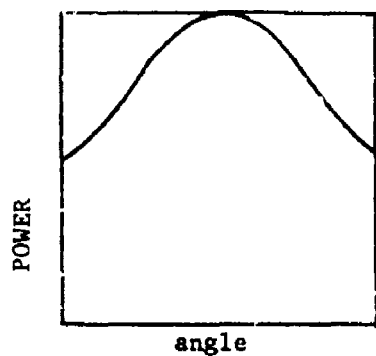
(a) TE$_{10}$ ANTENNA PATTERN
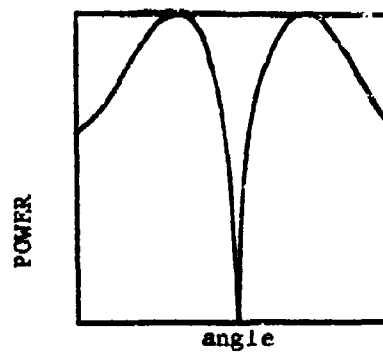
(b) TE$_{20}$ ANTENNA PATTERN
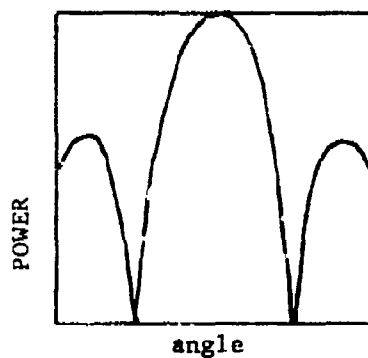
(c) TE$_{01}$ ANTENNA PATTERN
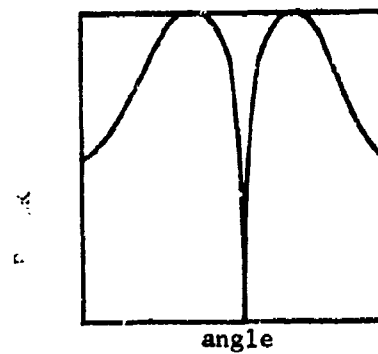
(d) TE$_{11}$ ANTENNA PATTERN

Figure 110.   Sketches of the antenna patterns of the indicated modes.

phased-array equation based on initially deterministic (non-random) parameters. Thus, the statistical expressions will generally depend on all of the variables contained in the conventional expression, plus the statistical parameters of the variables which are assumed random.

The phased-array equation for the out-of-band antenna pattern of a linear array of waveguide radiating elements will ultimately involve (1) the isotropic array pattern factor, and (2) the element patterns of each out-of-band propagating mode. Since certain of the higher-order modes have electric field configurations with components both parallel and orthogonal to the in-band TE_{10} mode, the resultant array antenna pattern will generally have both a parallel pattern and a cross-polarized pattern. The conventional array equation can be written as

$$P(\theta) = \left| \sum_{i=1}^{I} \sum_{m,n} A_i^{mn} F_i^{mn}(\theta) \exp\{j(i-1)\Psi + \gamma_i^{mn} + \alpha_i^{mn}\} \right|^2 , \qquad (20)$$

where $\Psi = \left[2(d/\lambda)\sin\theta\right]$ and the other symbols are as previously defined. $P(\theta)$ is either the parallel or cross-polarized array pattern. To obtain the parallel pattern, the summation over the indexes m and n includes only the mn^{th} TE and TM modes which have parallel electric field components. Similarly, the cross pattern is obtained by summing only over the mn^{th} modes which have cross-polarized electric field components. A sketch illustrating the array geometry is depicted in Figure 111.

The statistical-average pattern for the out-of-band array whose
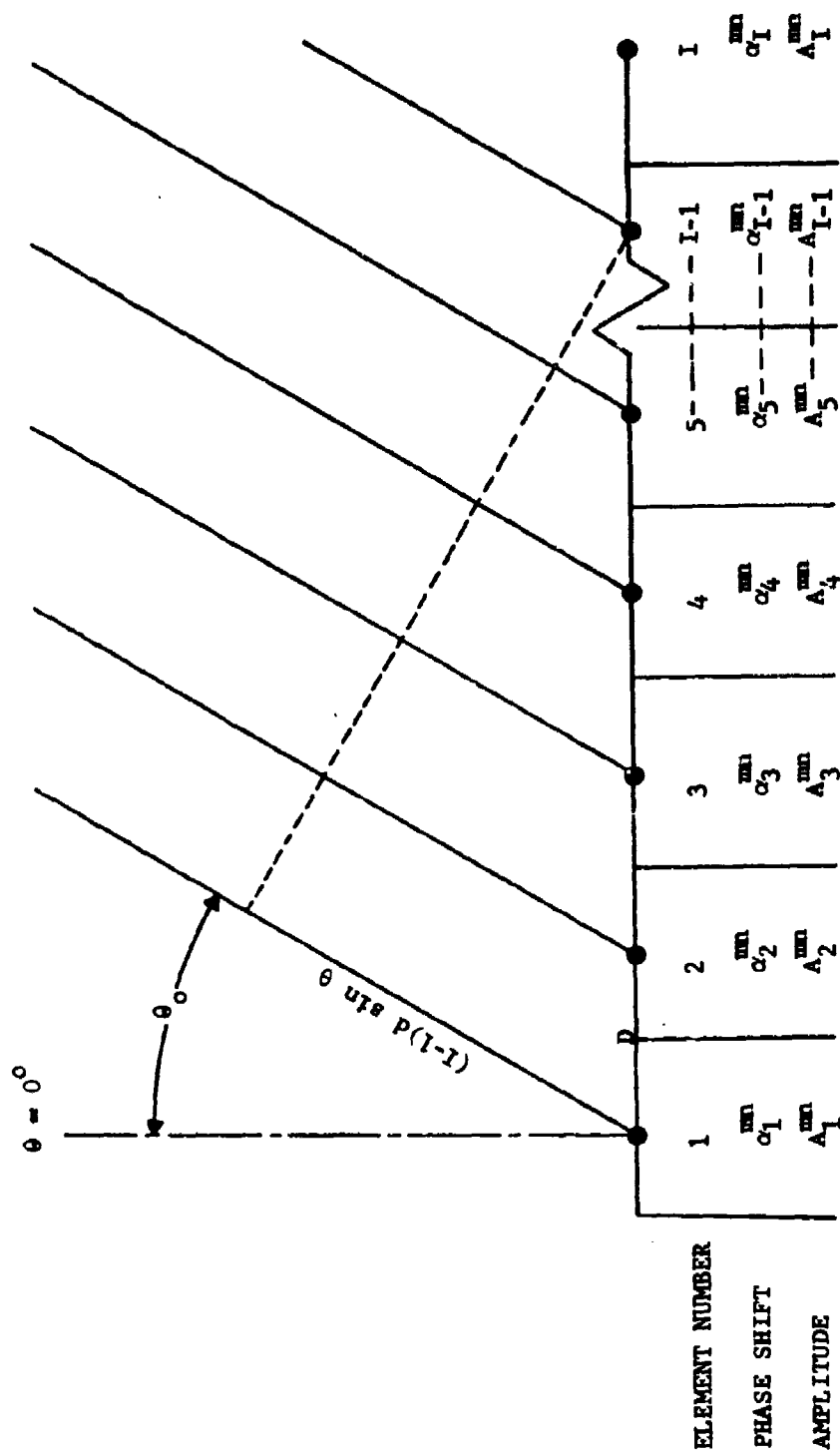
Figure 111. Sketch depicting geometry of waveguide array and pertinent variables.

elements propagate randomly-varying higher-order modes is defined [10]
as

$$\overline{P}(\theta) = \prod_{i=1}^{I}\left[\int_{A_i^{mn}}\int_{\alpha_i^{mn}} P(\theta)\ f_i^{mn}\ (\alpha_i^{mn})\ h_i^{mn}\ (A_i^{mn})\ d\alpha_i^{mn}\ dA_i^{mn}\right] \qquad (21)$$

where $f_i^{mn}(\alpha_i^{mn})$ = probability density for the random phase shift of the

$mn\underline{\text{th}}$ mode at the $i\underline{\text{th}}$ element,

$h_i^{mn}(A_i^{mn})$ = probability density for the random variations in the

peak far-field electric field amplitude for the $mn\underline{\text{th}}$

mode at the $i\underline{\text{th}}$ element, and

all other symbols are as previously defined. In Equation (21), the
random phase shift and amplitude variations are each assumed to be
statistically independent. As previously mentioned, the phase shift
variations are assumed to follow a Gaussian distribution. The prob-
ability density of the amplitude variations may be derived from the
assumed uniform probability density for the mode power variations pre-
viously defined by Equation (13). The resulting probability density is
for the peak far-field electric field amplitude is given as

$$h_i^{mn}(A_i^{mn}) = \frac{2A_i^{mn}}{\Delta A_i^{mn}} , \qquad (22)$$

where ΔA_i^{mn} is the interval over which A_i^{mn} varies randomly.

Equations (20) and (21) were used to derive an expression for the
average array pattern based on the stated phase shift and amplitude dis-
tributions. In the derivation, the statistical-average values of the
amplitude of a given mode are assumed to be invariant with bias voltage
and the statistical-average phase shift of a given mode is assumed to be a
linear function of bias voltage. This assumption is not very restrictive,

because the resulting average pattern equation is valid for situations where the average values and standard deviations of both the phase shifts and amplitudes of all the modes are different. Under the stated conditions, the average array pattern for both the parallel and cross-polarized far-field components are given as

$$\overline{P}(\theta) = \sum_{m,n} \left\{ F^{mn}(\theta) \ \overline{A^{mn}} \exp\left[-\frac{1}{2}\sigma_{mn}^2\right] \frac{\sin\left[I \ \frac{\Psi + \Delta\overline{\alpha}_{mn}}{2}\right]}{\sin\left[\frac{\Psi + \Delta\overline{\alpha}_{mn}}{2}\right]} \right\}^2$$

$$+ \sum_{\substack{m,n \\ p,q}} \left\{ \overline{A^{mn}} \ \overline{A^{pq}} \exp\left[-\frac{1}{2}\left(\sigma_{mn}^2 + \sigma_{pq}^2\right)\right] \right.$$

$$\times \left[2 \sum_{i=1}^{I} \cos \left[i \left(\overline{\alpha}_i^{mn} - \overline{\alpha}_i^{pq}\right) + \left(\gamma^{mn} - \gamma^{pq}\right)\right] \right.$$

$$\left. + 2 \sum_{\lambda=1}^{I-1} \sum_{\kappa=1+\lambda}^{I} \cos\left[(\lambda - \kappa)\Psi + \left(\overline{\alpha}_\lambda^{mn} - \overline{\alpha}_\kappa^{pq}\right) + \left(\gamma^{mn} - \gamma^{pq}\right)\right] \right] \right\}$$

$$+ \sum_{m,n} \left\{ \left[F^{mn}(\theta)\right]^2 \ \overline{\left(A^{mn}\right)^2} - \left[\overline{A^{mn}} \ \exp\left(-\frac{1}{2}\sigma_{mn}^2\right)\right]^2 \right\} I \ . \tag{23}$$

For the parallel or cross patterns, the sums in Equation (23) extend over all modes which have parallel or cross components, respectively. In the second sum, which contains products of the amplitude factors corresponding to each mode, the summation for a given polarization involves (1) products of all pairs of TE modes which have at least one different index, (2) products of all pairs of TM modes which have at least one different index, and (3) products of all pairs of TE and TM modes, including TE and TM mode pairs which have the same m and n indexes.

Equation (23) consists of three types of terms. The first summation is comprised of isotropic array factors for each mode multiplied by the corresponding amplitude and phase-shift standard-deviation factors of the modes. The second major summation involves pairs of statistical average cross products of the constituent array patterns corresponding to each mode. The third summation involves the mode element patterns and amplitude and phase deviation factors, but does not contain array factors.

The first and second summation determine the average scanning properties of the array since each of the two groups contains average phase shift terms within the arguments of the trigonometric functions. Each mode signal can have different scanning properties since the average phase shifts of the various mode signals are not necessarily the same. Consequently, based on the equation, the total out-of-band array pattern could have several sets of main beams and sets of grating lobes that scan through different angles as the in-band main beam is steered.

The third summation does not contain average phase shift factors

219

and, therefore, does not scan. However, the magnitude of this portion of the equation varies with spatial angle due to the presence of the element pattern factors of the mode signals. These terms determine the statistical average sidelobe level and are important in determining the overall shape of the average array pattern.

The average pattern equation indicates that the out-of-band characteristics of arrays of randomly-excited, multi-moding waveguide elements can be predicted and described if the statitistical parameters of the higher-order modes are known. Current knowledge of out-of-band mode statistical parameters as a function of phase shifter bias voltage is very limited. However, based on previous experimental investigations [2], the statistical parameters of the phase shift and amplitude variations of the out-of-band TE_{10} mode were derived as a function of bias voltage. The parameters of the other higher-order modes were not determined as a function of bias voltage in that study, although the limited data that were obtained at several discrete bias voltage settings indicate that the parameters for the other modes may be different from the TE_{10} out-of-band mode. However, in order to gain further insight into the behavior of out-of-band arrays, the assumptions are made in the remainder of this study that the various modal signals undergo the same random phase shift within a particular element and that the statistical phase shift parameters of all of the modes are equal to the experimentally-derived TE_{10} phase shift statistical parameters. No additional restrictions are placed on the statistical amplitude parameters. When the assumptions of equal intra-element modal phase shifts and statistical parameters are made, the expres-

sion for the average antenna pattern reduces to a simpler form. The expressions for the parallel-polarized array pattern is

$$
\bar{P}_p(\theta) = \left\{ \left\{ \left[F^{10}(\theta) \; \overline{A^{10}} \right]^2 + \left[F^{20}(\theta) \; \overline{A^{20}} \right]^2 \right. \right.
$$

$$
+ \left[2F^{10}(\theta) \; F^{20}(\theta) \; \overline{A^{10}} \; \overline{A^{20}} \cos (\gamma^{10} - \gamma^{20}) \right] \right\}
$$

$$
\times \exp \left[- \sigma_{10}^2 \right] \left[\frac{\sin \left[I \; \dfrac{\psi + \Delta\bar{\alpha}_{10}}{2} \right]}{\sin \left[\dfrac{\psi + \Delta\bar{\alpha}_{10}}{2} \right]} \right]^2 \right\}
$$

$$
+ I \left\{ \left\{ \left[F^{10}(\theta) \right]^2 \; \overline{(A^{10})^2} + \left[F^{20}(\theta) \right]^2 \; \overline{(A^{20})^2} \right. \right.
$$

$$
+ \left[2F^{10}(\theta) \; F^{20}(\theta) \; \overline{A^{10}} \; \overline{A^{20}} \cos (\gamma^{10} - \gamma^{20}) \right] \right\}
$$

$$
- \exp \left[- \sigma_{10}^2 \right] \left\{ \left[F^{10}(\theta) \; \overline{A^{10}} \right]^2 + \left[F^{20}(\theta) \; \overline{A^{20}} \right]^2 \right.
$$

$$
+ \left[2F^{10}(\theta) \; F^{20}(\theta) \; \overline{A^{10}} \; \overline{A^{20}} \cos (\gamma^{10} - \gamma^{20}) \right] \right\} \right\} \quad , \tag{24}
$$

and the cross-polarized array pattern is

$$
\bar{\Gamma}_c(\theta) = \left\{ \left\{ \left[F^{01}(\theta)\ \overline{A^{01}} \right]^2 + \left[F^{11}(\theta)\ \overline{A^{11}} \right]^2 + \left[F^{11}(\theta)\ _m\overline{A^{11}} \right]^2 \right. \right.
$$

$$
+ \left[2F^{01}(\theta)\ F^{11}(\theta)\ \overline{A^{01}}\ \overline{A^{11}} \cos\left(\gamma^{01} - \gamma^{11} \right) \right]
$$

$$
+ \left[2F^{01}(\theta)\ F^{11}(\theta)\ \overline{A^{01}}\ _m\overline{A^{11}} \cos\left(\gamma^{01} - _m\gamma^{11} \right) \right]
$$

$$
\left. + \left[2F^{11}(\theta)\ F^{11}(\theta)\ \overline{A^{11}}\ _m\overline{A^{11}} \cos\left(\gamma^{11} - _m\gamma^{11} \right) \right] \right\}
$$

$$
\times \exp\left[-\sigma_{10}^2 \right] \left[\frac{\sin\left[I\ \dfrac{\psi + \Delta\bar{\alpha}_{10}}{2} \right]}{\sin\left[\dfrac{\psi + \Delta\bar{\alpha}_{10}}{2} \right]} \right]^2 \right\}
$$

$$
+ I \left\{ \left\{ \left[F^{01}(\theta) \right]^2 \overline{\left(A^{10} \right)^2} + \left[F^{11}(\theta) \right]^2 \overline{\left(A^{11} \right)^2} + \left[F^{11}(\theta) \right]^2 \overline{\left(_m A^{11} \right)^2} \right. \right.
$$

$$
+ \left[2F^{01}(\theta)\ F^{11}(\theta)\ \overline{A^{01}}\ \overline{A^{11}} \cos\left(\gamma^{01} - \gamma^{11} \right) \right]
$$

$$
+ \left[2F^{01}(\theta)\ F^{11}(\theta)\ \overline{A^{01}}\ _m\overline{A^{11}} \cos\left(\gamma^{01} - _m\gamma^{11} \right) \right]
$$

$$
\left. + \left[2F^{11}(\theta)\ F^{11}(\theta)\ \overline{A^{11}}\ _m\overline{A^{11}} \cos\left(\gamma^{11} - _m\gamma^{11} \right) \right] \right\}
$$

$$
- \exp\left[-\sigma_{10}^2 \right] \left\{ \left[F^{01}(\theta)\ \overline{A^{01}} \right]^2 + \left[F^{11}(\theta)\ \overline{A^{11}} \right]^2 + \left[F^{11}(\theta)\ _m\overline{A^{11}} \right]^2 \right.
$$

$$
+ \left[2F^{01}(\theta)\ F^{11}(\theta)\ \overline{A^{01}}\ _m\overline{A^{11}} \cos\left(\gamma^{01} - \gamma^{11} \right) \right]
$$

$$
+ \left[2F^{01}(\theta)\ F^{11}(\theta)\ \overline{A^{01}}\ \overline{A^{11}} \cos\left(\gamma^{01} - \gamma^{11} \right) \right]
$$

$$
\left. \left. + \left[2F^{11}(\theta)\ F^{11}(\theta)\ \overline{A^{11}}\ _m\overline{A^{11}} \cos\left(\gamma^{11} - _m\gamma^{11} \right) \right] \right\} \right\} \quad , \qquad (25)
$$

222

where the leading subscript m on $_m\overline{A^{11}}$ and $_\gamma{}^{11}$ denotes the TM mode parameters. The element pattern factor is identical for the TE_{11} and TM_{11} modes, and therefore, is not distinguished by a subscript. The leading group of terms in each of Equations (24) and (25) (that is, the group of terms in the first set of outermost braces) determine the scanning properties and peak gain levels of the out-of-band main beam and grating lobes. In particular, the scanning properties are determined by the array factor which contains the average phase shift between elements. Since the statistical parameters of the various modal phase shifts were assumed equal, all of the modal components have the same scanning properties. The terms which multiply the array factor play a major role in determining gain as a function of the spatial angle, the signal strength of each mode, and the magnitude of the phase-shift standard deviation. Similarly, the last group of terms (that is, the group of terms in the second set of outermost braces) are of primary importance in determining the statistical average sidelobe level as a function of spatial angle and the mode statistics. These terms do not depend on the scan angle of the array.

When both the phase shift deviations and amplitude deviations approach zero, the exponential factor containing the phase shift deviation goes to unity, and the average value of the squared amplitude equals the average value of the amplitude squared. Consequently, the statistical average sidelobe terms disappear, and the remaining terms reduce to the expression for a non-random array of waveguide elements in which the various (non-random) modes propagate. For example, the

223

rallcl-polarization pattern for the deterministic equation is

$$P_p(\theta) \rightarrow P_p(\theta) = \left\{ F^{10}(\theta) \ A^{10} \ \frac{\sin\left[I \ \frac{\Psi + \Delta\alpha}{2}\right]}{\sin\left[\frac{\Psi + \Delta\alpha}{2}\right]} \right\}^2$$

$$+ \left\{ F^{20}(\theta) \ A^{20} \ \frac{\sin\left[I \ \frac{\Psi + \Delta\alpha}{2}\right]}{\sin\left[\frac{\Psi + \Delta\alpha}{2}\right]} \right\}^2$$

$$+ \left\{ 2F^{10}(\theta)F^{20}(\theta)A^{10}A^{20} \ \cos(\gamma^{10}-\gamma^{20}) \left[\frac{\sin\left[I \ \frac{\Psi + \Delta\alpha}{2}\right]}{\sin\left[\frac{\Psi + \Delta\alpha}{2}\right]} \right]^2 \right\} . \quad (26)$$

The effects of the random variations in amplitude and phase on the peak gain of the main beam and grating lobes can be discerned by inspection of the expressions for the average array pattern and the deterministic array pattern given by Equations (24) and (26), respectively. The average values of the amplitude factors are smaller than the corresponding deterministic amplitude factors; additionally, the exponential factor in the average pattern equation is less than unity. Therefore, the average peak gains of the main beam and the grating lobes are reduced by the random variations. This result also applies, of course, to the cross-polarized pattern.

As the Equations (24) and (25) show, the peak gain of the main beam and grating lobes, as well as the front sector median gain, will

224

vary with scan angle in a manner determined by the resultant element pattern. The resultant element pattern is a random superposition of the element patterns of the individual modes that are present. Therefore, the changes in peak gain and median gain as the array is scanned are a function of modal content.

b. Median Gain

The technique developed in the previous phased array study [3] for estimating front sector median gain can be applied in the current study. The estimation technique is partially based on an approximate analytical expression that relates the statistical-average real-number value of the average pattern to the statistical-average decibel value of the pattern. The expression is given as

$$\bar{p}(\theta) = \overline{10 \ Log_{10} \ [P(\theta)]} \approx 10 \ Log_{10} \ [\bar{P}(\theta)] - [2 \ dB] \left[\frac{\sigma_p(\theta)}{\bar{P}(\theta)} \right]^2 \tag{27}$$

$$- 10 \ Log_{10} \ [P_{iso}] \ ,$$

where

$\bar{p}(\theta)$ = statistical average decibel value of the average power at spatial angle θ,

$\sigma_p(\theta)$ = standard deviation of the power at spatial angle θ, and

$\bar{P}(\theta)$ = statistical average pattern given by Equation (23).

If the average patterns are normalized to isotropic level, the median gain may be approximated as

$$M = \frac{1}{181} \left[\sum_{q=1}^{181} \bar{P}(\theta_q) \right] - G_{iso} \ , \tag{28}$$

225

where

$\theta_q = (181 - q)$,

M = median gain of array relative to isotropic median gain, and

G_{iso} = median gain of isotropic radiator in decibels.

In order to use Equation (28), the behavior of the standard deviation of the average antenna pattern as a function of spatial angle must be determined. The spatial standard deviation can be determined from a knowledge of the cumulative probability distribution function for the random power. The cumulative distribution function is

$$F[P(\theta)] = \frac{1}{\tau(\theta)} \int_{o}^{P_o(\theta)} \exp\left[- \frac{[P(\theta) + \eta^2(\theta)]}{\tau(\theta)}\right] I_o(\beta)\, dP(\theta), \qquad (29)$$

where

$F[P(\theta)]$ = probability that $P(\theta) \le P_o(\theta)$,

η^2 = first group of terms in either Equation (24) or (25) obtained by letting σ_{10}^2 go to zero,

$\tau(\theta)$ = the second group of terms in either Equation (24) or (25) obtained by letting σ_{10} become very large,

$I_o(\beta)$ = modified Bessel function of the first kind and order n, and

$$\beta = \frac{\eta(\theta)\sqrt{P(\theta)}}{\frac{1}{2}\tau(\theta)}.$$

The spatial standard deviation may be derived with the aid of Equation (29). The standard deivation is, by definition,

$$\sigma_p(\theta) = \left\{ \frac{1}{\tau(\theta)} \int_0^\infty [P(\theta) - \overline{P}(\theta)]^2 \exp\left[-\frac{[P(\theta) + \eta^2(\theta)]}{\tau(\theta)} \right] I_0(\beta) \, dP \right\}^{\frac{1}{2}}. \quad (30)$$

The resulting expression for the spatial standard deviation is

$$\sigma_p(\theta) = \left\{ [\tau(\theta)]^2 + 2[\tau(\theta)] \, \eta^2(\theta) \right\}^{\frac{1}{2}}. \quad (31)$$

If the average pattern equations are expressed in terms of $\tau(\theta)$ and $\eta^2(\theta)$, the ratio of the standard deviation to the average power may be written as

$$\frac{\sigma_p(\theta)}{\overline{P}(\theta)} = \frac{\{[\tau(\theta)]^2 + 2[\tau(\theta)] \, \eta^2(\theta)\}^{\frac{1}{2}}}{\tau(\theta) + \eta^2(\theta)}. \quad (32)$$

In the sidelobe regions where the array factor contained in $\eta^2(\theta)$ produces a null, the ratio of the standard deviation to the average power is unity. In the main beam and grating lobe directions, the ratio is of the order $\sqrt{1/I}$, where I is the number of elements in the array. Because the angular extent of the front 180-degree sector is essentially occupied by sidelobes, the limiting value of the above ratio is close to unity over much of the array pattern, and therefore, can be set equal to unity in Equation (27). As a result the median gain can be

computed using Equation (28).

The standard deviation associated with the 180-degree median gain can be estimated directly as the square root of the sample variance. The sample variance is computed as the numerical average value of the square of the difference between the median gain and the gain of the average pattern at 181 sample points. However, the values of standard deviation obtained in this manner will generally be lower than the standard deviation computed for a particular random antenna pattern because the sidelobe variations have not been completely characterized. More accurate estimates appear possible through further an- ses.

D. Theoretical Calculations

Various calculations based on the preceding statistical equations were performed in order to (1) gain insight into the out-of-band pattern characteristics of randomly-excited arrays of waveguide elements involving higher-order mode propagation, and (2) assess the suitability of the statistical equations for describing and predicting the out-of-band pattern characteristics. In order to accomplish these objectives, the following types of calculations were made:

(1) In-band Antenna Patterns--In-band phased-array antenna patterns were calculated at selected scan angles to serve as reference data. For these calculated patterns, the TE_{10} mode of propagation was assumed, and the phase shifter responses were both linear and non-random.

(2) Out-of-band Antenna Patterns--Two basic types of out-of-band far-field phased-array antenna patterns were calculated.

228

These include statistical-average parallel- and cross-polarized patterns based on Equations (24) and (25), respectively, and individual random parallel-polarized and cross-polarized patterns based on inserting random modal phase-shift and amplitude values into Equation (20). Both the average patterns and the individual random patterns were calculated for three selected out-of-band frequencies for in-band scan angles corresponding to those of Item (1) above.

(3) Statistical Median Gain and Standard Deviation--These statistical values were determined for the computed in-band and out-of-band antenna patterns for the 180-degree azimuthal sector.

All of the calculations for both in-band and out-of-band frequencies were performed for a 20-element, one-dimensional array of waveguide elements whose inter-element spacing from center-to-center was chosen to be 0.53λ at the in-band frequency of 9.0 GHz. For the element spacing of 0.53λ, which is typical of the spacing for many actual arrays, the in-band scan limit for suppression of in-band grating lobes is about $\pm$ 60 degrees. The antenna patterns were computed and plotted with the aid of computer graphics techniques to facilitate the investigative efforts, and the calculations of median gain and standard deviation were similarly expedited by a computer program. When calculating the antenna patterns, median gains, and standard deviations, the power levels were determined at one-degree intervals over e front 180-degree sector. The choice of one-degree increments give dequate resolution of

pattern details commensurate with the scope and purposes of the current investigations. Accordingly, an occasional underestimation of pattern null depth or slight distortion of pattern lobes is deemed tolerable because this degree of resolution does not significantly affect the results.

In order to simplify the above calculations, the assumptions that the peak gain with respect to isotropic varies with scan angle according to the resultant element pattern and that the peak gain does not vary significantly with element spacing in terms of operating wavelength were made. The peak gain (in decibels) for a non-random array was then computed as the sum of the resultant element pattern gain, and the gain for a lossless array of isotropic radiators. The peak gain above isotropic for a non-random lossless, linear array is approximately equal to the number of elements, N, in the array when the element spacing is close to half-wavelength multiples [3]; for a 20-element array, the gain is about 13 dB relative to the isotropic gain level. When the element spacing is different from some half-wavelength multiple, deviations from the gain figure of N for an N-element linear array of lossless isotropic radiators are typically on the order of 1 or 2 dB for the scan angles and element spacings that were used is the theoretical calculations. In order to effect a standard for comparisons, the peak gain/isotropic for non-random situations was assumed to be 13 dB for the 20-element array for both the in-band and out-of-band antenna patterns. Scalar aperture theory was used to calculate the element gain relative to isotropic for non-random excitation of the TE_{10} mode for the in-band and the three out-of-band

frequencies. When the transmission coefficient at the interface of the aperture and free space are included, the gains of the TE_{10} mode element patterns at 9.0 GHz, 14.5 GHz, 15.7 GHz, and 18.0 GHz are approximately 2.5 dB, 7.5 dB, 8.5 dB, and 10 dB, respectively. The transmission coefficient improves as the frequency increases; therefore, the gain at 18.0 GHz is 10 dB. Because surface currents would flow on the outside of the waveguide element were it isolated in free space, the calculated gain levels are different from the gain levels that would be measured for a single waveguide element located either in free space or in an array. However, the calculated gain levels can serve as a suitable basis for comparison of in-band and out-of-band patterns in the current study.

The results of the theoretical calculations are presented and analyzed in the discussions that follow. In the analysis, emphasis is given to the characteristics of the theoretical data that are important from an EMC/EMI point-of-view. These include the scanning properties and gain levels of the out-of-band main beam, grating lobes, sidelobes, and the values of the 180-degree median gain and standard deviation of the out-of-band patterns.

1. In-Band Antenna Patterns

The antenna patterns of a 20-element waveguide array for the in-band 9.0 GHz frequency, which serve as reference data, are displayed in Figures 112 through 116 for scan angles of 0, 20, 40, 60, and 70-degrees, respectively. Each figure is a plot of the relative power expressed in decibels versus the azimuth angle, θ, which is measured from the broadside direction, $\theta = 0$ degrees. The isotropic gain level

231
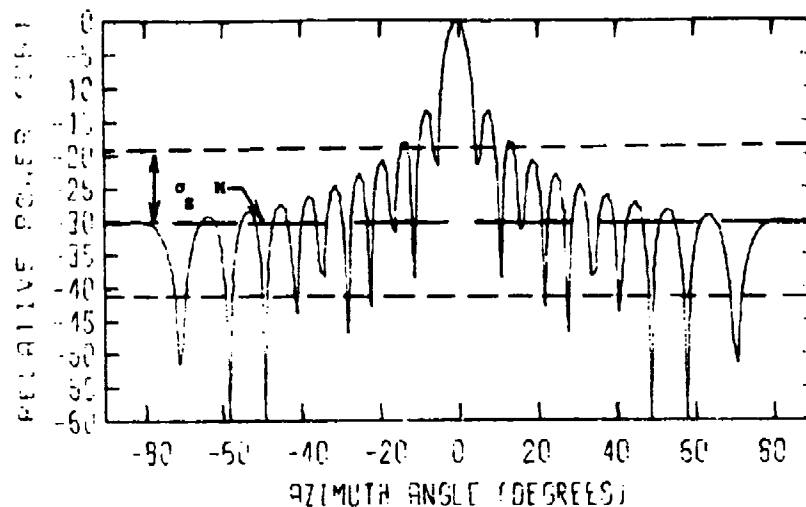
Figure 112. Antenna pattern for 9.0 GHz frequency for broadside
scan angle. The gain relative to an isotropic radiator
at the top of the chart is 15.5 dB, and the symbols M
and σ_g denote the 180-degree median gain and standard
deviation, respectively.

Figure 113. Antenna pattern for 9.0 GHz frequency for 20-degree
scan angle. The gain relative to an isotropic radiator
at the top of the chart is 15.5 dB, and the symbols M and
σ_g denote the 180-degree median gain and standard
deviation, respectively.

232
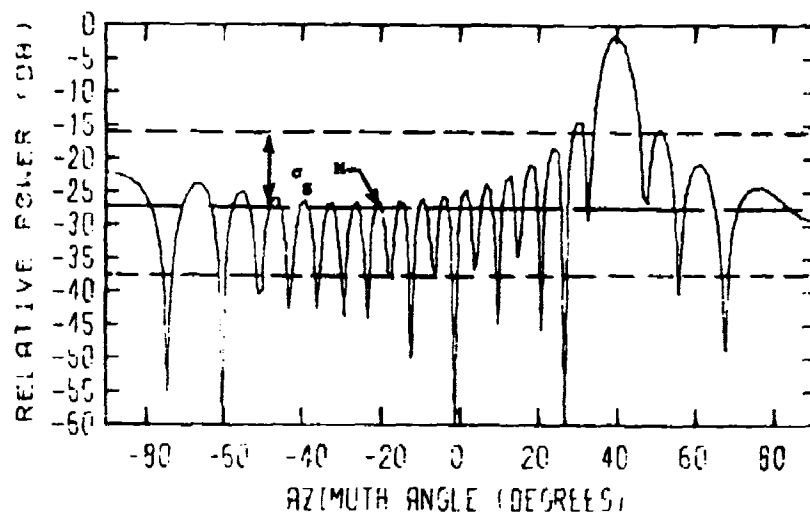
Figure 114. Antenna pattern for 9.0 GHz for 40-degree scan angle. The gain relative to an isotropic radiator at the top of the chart is 15.5 dB, and the symbols M and σ_g denote the 180-degree median gain and standard deviation, respectively.
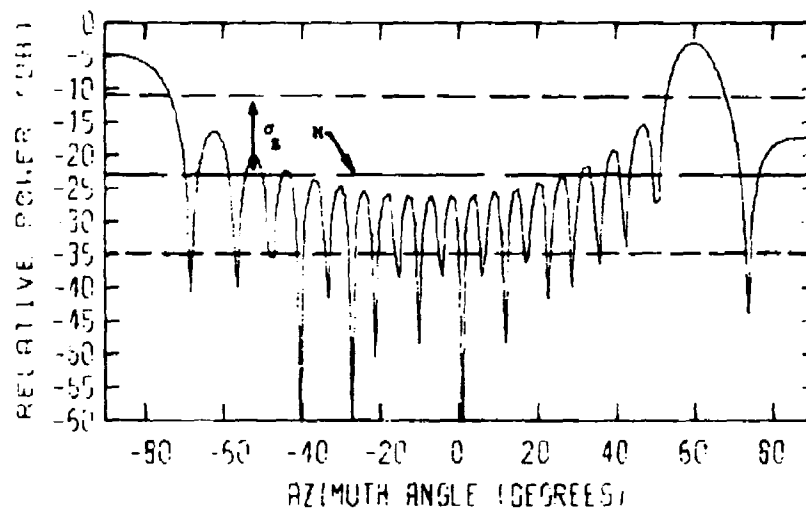
Figure 115. Antenna pattern for 9.0 GHz for 60-degree scan angle. The gain relative to an isotropic radiator at the top of the chart is 15.5 dB, and the symbols M and σ_g denote the 180-degree median gain and standard deviation, respectively.
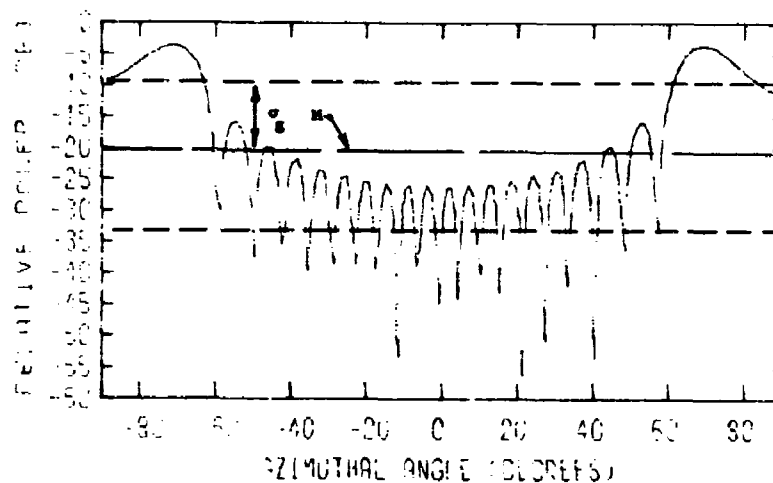
Figure 116. Antenna pattern for 9.0 GHz for 70-degree scan angle. The gain relative to an isotropic radiator at the top of the chart is 15.5 dB, and the symbols M and σ_g denote the 180-degree median gain and standard deviation, respectively.

234

for each pattern on each graph is -15.5 dB. The median gain and standard deviation over the 180-degree sector for each pattern are also shown in each figure. However, these theoretical in-band patterns are not random, and consequently their associated 180-degree cumulative gain distributions are not Gaussian. Therefore, the median gain and standard deviation should not necessarily be interpreted in the Gaussian sense.

The in-band patterns exhibit typical behavior. The broadside pattern shown in Figure 112 is characterized by a single main beam and by symmetrically-distributed sidelobes that decrease in magnitude for increasing angles off broadside. (Because the angular resolution of the computer-generated graphs was one degree, the depth of the first null on each side of the main bean is truncated.) As the array is scanned, the main beam and close-in sidelobes broaden, and the main beam gain decreases due to the spatial taper of the element pattern. A grating lobe begins to emerge in the endfire ($\theta = -90^{o}$) direction away from the scanning direction as the in-band scan limit of 60° is approached. The endfire grating lobe is esstentially formed when the main beam is steered to 60-degrees, as shown in Figure 115, and is essentially the mirror image of the main beam for the 70-degree scan angle, as shown in Figure 116.

The median gain and standard deviation both tend to generally increase as the main bean is scanned to large scan angles where the endfire grating lobe begins to emerge. However, the median gain and standard deviation increase slowly for scan angles of about 60 degrees or more, because the grating lobe is essentially already fully formed.

235

2. Out-of-Band Antenna Patterns

Two basic types of out-of-band antenna patterns were cal-
culated for the 20-element array of waveguide radiators. In particular,
statistical-average antenna patterns were computed from Equations
(24) and (25), and individual random antenna patterns were calculated
through the use of pseudo-random number generators and Equation (20).

The statistical phase-shift parameters used for the average
antenna pattern calculations were the ones derived from measured data
in previous phased-array studies [2,3]. In the current study, each
higher-order mode component was assumed to undergo the same random
Gaussian phase shift within a particular element and therefore varied
randomly in a Gaussian manner from element to element. The power
propagated in the various waveguide modes was assumed to vary randomly
with a uniform probability density both within each particular element
and from element to element. As discussed in the preceding subsection,
the statistical-average value of the total power propagated in all of
the modes in a particular element was constrained to equal one-half
the assumed constant input power incident on the ferrite phase shifter
contained in that element. The incident power was assumed to be two
watts and thus, the statistical-average output power was one watt.

The random antenna patterns were obtained by inserting random
values of phase shift and amplitude into Equation (20). Pseudo-
random number generators were used to generate the values of phase
shifts and amplitudes with specified Gaussian and uniformly dis-
tributed probabilities, respectively. The statistical parameters
of each distribution corresponded to the parameters for the average pattern.

236

Thus, the individual random pattern represents one of the possible antenna patterns that constitute the entire ensemble of random patterns for a specified choice of statistical parameters.

Both the average patterns and the random patterns were computed for the out-of-band frequencies of 18 GHz, 15.7 GHz, and 14.5 GHz, which are the same three out-of-band frequencies that were used in previous studies [2,3]. For the 18 GHz out-of-band frequency, the antenna patterns were computed for the same five in-band scan angles as for the in-band patterns. For the 15.7 and 14.5 GHz frequencies, the antenna patterns were computed only for the 0-degree and 40-degree scan angles. At each scan angle, antenna patterns were computed for various random mixtures of out-of-band modal contents in order to study the effects of modal content on the gain and median gain of the patterns. The following cases were studied at 18 GHz.

(1) The power was propagated in a single mode, for each one of the five allowed modes listed below:

    (a) TE_{10},

    (b) TE_{20},

    (c) TE_{01},

    (d) TE_{11}, and

    (e) TM_{11}.

(2) The power was simultaneously propagated in the TE_{10} and TE_{20} modes with equal statistical average power in each mode.

(3) The power was simultaneously propagated in the TE_{10}, TE_{20}, and TE_{01} modes with equal statistical average power in each mode.

237

(4) The power was simultaneously propagated in the TE_{10}, TE_{20}, TE_{01}, TE_{11}, and TM_{11} modes with the following mixtures of modal content:

(a) Equal statistical average power was in each mode.

(b) One-half the statistical average power was in the TE_{10} mode and the remainder was shared among the other four modes.

(c) The statistical average power was randomly distributed among the five modes.

For the 15.7 GHz frequency, the out-of-band array patterns were computed for simultaneous propagation of the TE_{10}, TE_{20}, and TE_{01} modes with equal average power in each mode. Similarly, the out-of-band array patterns for the 14.5 GHz frequency were calculated for simultaneous propagation of the TE_{10} and TE_{20} modes with equal average power in each mode.

The various antenna patterns are presented in Figures 117 through 153. Figures 117 through 147 are for the 18 GHz frequency, Figures 148 through 151 are for 15.7 GHz, and Figures 152 and 153 are for 14.7 GHz. Each figure consists of two parts. The (a) part of each figure, except Figure 147, is the statistical average pattern, and the (b) part is the individual random pattern for the particular frequency, choice of mode statistics, and in-band scan angle angle. The (a) and (b) parts of Figure 147 are the parallel and cross-polarized patterns, respectively, for a second random antenna pattern which is a memeber of the ensemble of possible patterns for the given statistical parameers. The median gain levels and standard

238
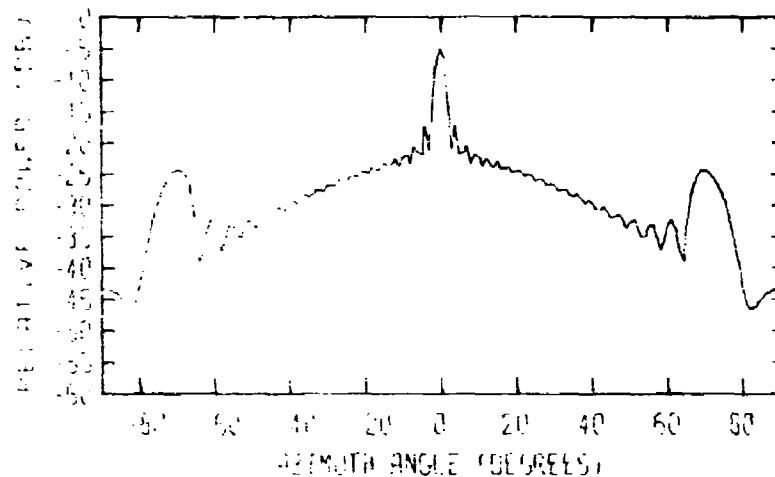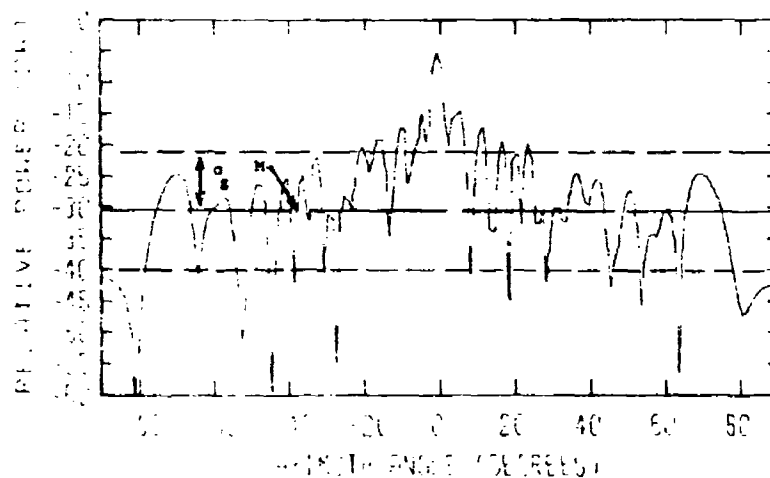
(a) Average Pattern

(b) Random Pattern

Figure 117. Statistical average and random out-of-band parallel polarized phased-array antenna patterns for the in-band scan angle of 0-degrees at 18.0 GHz involving the TE_{10} waveguide mode. The statistical average value of the randomly-varying modal power was 1.0 watt. The gain relative to an isotropic radiator at the tops of the charts is 23 dB, and the symbols M and σ_g denote median gain and standard deviation, respectively.

239

(a) Average Pattern

(b) Random Pattern

Figure 118. Statistical average and random out-of-band parallel-polarized phased-array antenna patterns for the in-band scan angle of 40 degrees at 18.0 GHz involving the TE_{10} waveguide mode. The statistical average value of the randomly-varying modal power was 1.0 watt. The gain relative to an isotropic radiator at the tops of the charts is 23 dB, and the symbols M and σ_g denote median gain and standard deviation, respectively.

(a) Average Pattern

(h) Random Pattern

Figure 11   Statistical average and random out-of-band parallel-
             polarized phased-array antenna patterns for the in-
             band scan angle of 0-degrees at 18.0 GHz involving
             the TE_{20} waveguide mode. The statistical average
             value of the randomly-varying modal power was 1.0
             watt.   The gain relative to an isotropic radiator
             at the tops of the charts is 23 dB, and the symbols
             M and σ_g denote median gain and standard deviation,
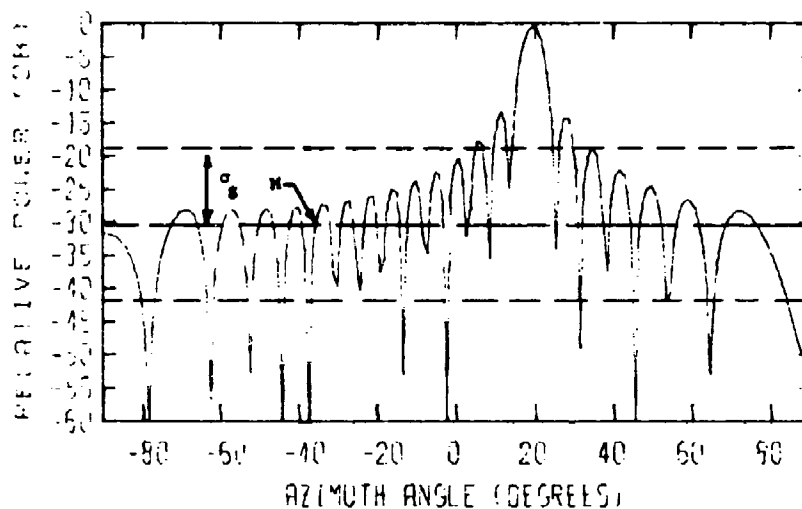   respectively.

(a) Average Pattern

(b) Random Pattern

Figure 120. Statistical average and random out-of-band parallel-polarized phased-array antenna patterns for the in-band scan angle of 40 degrees at 18.0 GHz involving the TE_{20} waveguide mode. The statistical average value of the randomly-varying modal power was 1.0 watt. The gain relative to an isotropic radiator at the top of the charts is 23 dB and the symbols M and σ_g denote median gain and standard deviation, respectively

(a) Average Pattern


(b) Random Pattern

Figure 121. Statistical average and random out-of-band cross-polarized phased-array antenna patterns for the in-band scan angle of 0-degrees at 18.0 GHz involving the TE_{01} waveguide mode. The statistical average value of the randomly-varying modal power was 1.0 watt. The gain relative to an isotropic radiator at the tops of the charts is 23 dB, and the symbols M and σ_g denote median gain and standard deviation, respectively.

(a) Average Pattern

(b) Random Pattern

Figure 122. Statistical average and random out-of-band cross-polarized phased-array antenna patterns for the in-band scan angle of 40 degrees at 18.0 GHz involving the TE_{01} waveguide mode. The statistical average value of the randomly-varying modal power was 1.0 watt. The gain relative to an isotropic radiator at the tops of the charts is 23 dB, and the symbols M and σ_g denote median gain and standard deviation, respectively.

(a) Average Pattern

(b) Random Pattern

Figure 123. Statistical average and random out-of-band cross-
polarized phased-array antenna patterns for the
in-band scan angle of C-degrees at 18.0 GHz involving
the TE_{11} waveguide mode. The statistical average
value of the randomly-varying modal power was 1.0
watt. The gain relative to an isotropic radiator
at the tops of the charts is 23 dB, and the symbols
M and σ_g denote median gain and standard deviation,
respectively.

(a) Average Pattern

(b) Random Pattern

Figure 124. Statistical average and random out-of-band cross-polarized phased-array antenna patterns for the in-band scan angle of 40 degrees at 18.0 GHz involving the TE_{11} waveguide mode. The statistical average value of the randomly-varying modal power was 1.0 watt. The gain relative to an isotropic radiator at the tops of the charts is 23 dB, and the symbols M and σ_g denote median gain and standard deviation, respectively.

(a) Average Pattern

(b) Random Pattern

Figure 125. Statistical average and random out-of-band cross-
polarized phased-array antenna patterns for the
in-band scan angle of 0-degrees at 18.0 GHz in-
volving the TM_{11} waveguide mode. The statistical
average value of the randomly-varying modal power
was 1.0 watt. The gain relative to an isotropic
radiator at the tops of the charts is 23 dB, and
the symbols M and σ_g denote median gain and
standard deviation, respectively.

(a) Average Pattern

(b) Random Pattern

Figure 126. Statistical average and random out-of-band cross-polarized phased-array antenna patterns for the in-band scan angle of 40 degrees at 18.0 GHz involving the TM_{11} waveguide mode. The statistical average value of the randomly-varying modal power was 1.0 watt. The gain relative to an isotropic radiator at the tops of the charts is 23 dB,and the symbols M and σ_g denote median gain and standard deviation, respectively.

(a) Average Pattern

(b) Random Pattern

Figure 127. Statistical average and random out-of-band parallel-
polarized phased-array antenna patterns for the in-
band scan angle of 0-degrees at 18.0 GHz involving
the TE_{10} and TE_{20} waveguide modes. The statistical
average value of the randomly-varying power in each
mode was 0.5 watt. The gain relative to an
isotropic radiator at the tops of the charts is 23
dB, and the symbols M and σ_g denote median gain and
standard deviation, respectively.

(a) Average Pattern

(b) Random Pattern

Figure 128. Statistical average and random out-of-band parallel-polarized phased-array antenna patterns for the in-band scan angle of 40 degrees at 18.0 GHz involving the TE_{10} and TE_{20} waveguide modes. The statistical average value of the randomly-varying power in each mode was 0.5 watt. The gain relative to an isotropic radiator at the tops of the charts is 23 dB, and the symbols M and σ_g denote median gain and standard deviation, respectively.

(a) Average Pattern

(b) Random Pattern

Figure 129. Statistical average and random out-of-band parallel-polarized antenna patterns for the in-band scan angle of 0-degrees at 18.0 GHz involving the TE_{10}, TE_{20}, and TE_{01} waveguide modes. The statistical average value of the randomly-varying power in each mode was 0.333 watt. The gain relative to an isotropic radiator at the tops of the charts is 23 dB, and the symbols M and σ_g denote median gain and standard deviation, respectively.

(a) Average Pattern

(b) Random Pattern

Figure 130. Statistical average and random out-of-band cross-polarized phased-array antenna patterns for the in-band scan angle of 0-degrees at 18.0 GHz involving the TE_{10}, TE_{20}, and TE_{01} waveguide modes. The statistical average value of the power in each mode was 0.333 watt. The gain relative to an isotropic radiator at the tops of the charts is 23 dB, and the symbols M and σ_g denote median gain and standard deviation, respectively.

252

(a) Average Pattern

(b) Random Pattern

Figure 131. Statistical average and random out-of-band parallel-polarized phased-array antenna patterns for the in-band scan angle of 40 degrees at 18.0 GHz involving the TE_{10}, TE_{20}, and TE_{01} waveguide modes. The statistical average value of the randomly-varying power in each mode was 0.333 watt. The gain relative to an isotropic radiator at the tops of the charts is 23 dB, and the symbols M and σ_g denote median gain and standard deviation, respectively.

(a) Average Pattern

(b) Random Pattern

Figure 132. Statistical average and random out-of-band cross-polarized phased-array antenna patterns for the in-band scan angle of 40 degrees at 18.0 GHz involving the TE_{10}, TE_{20}, and TE_{01} waveguide modes. The statistical average value of the randomly-varying power in each mode was 0.333 watt. The gain relative to an isotropic radiator at the tops of the charts is 23 dB, and the symbols M and σ_g denote median gain and standard deviation, respectively.
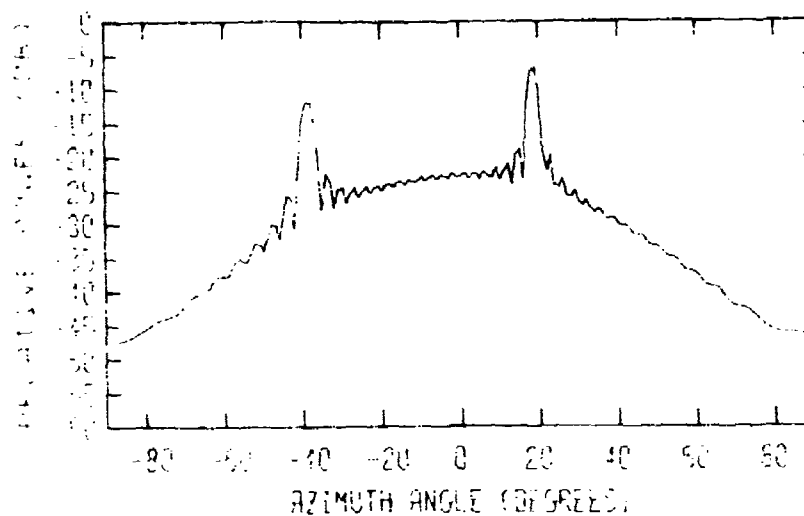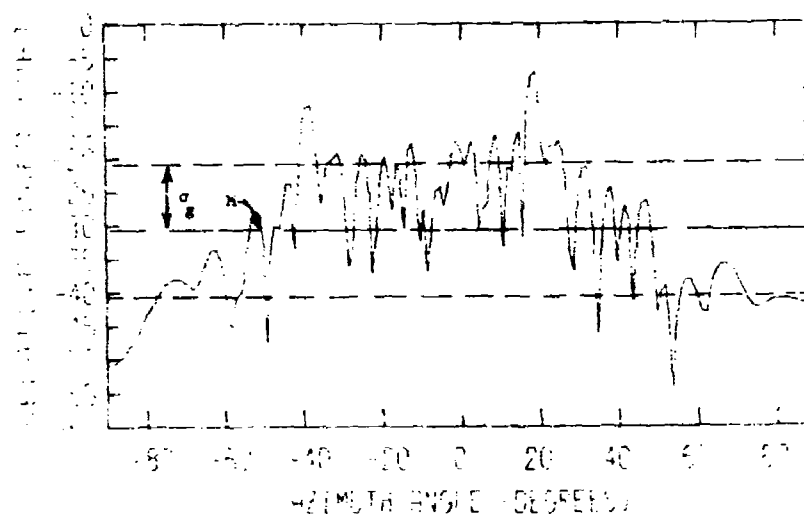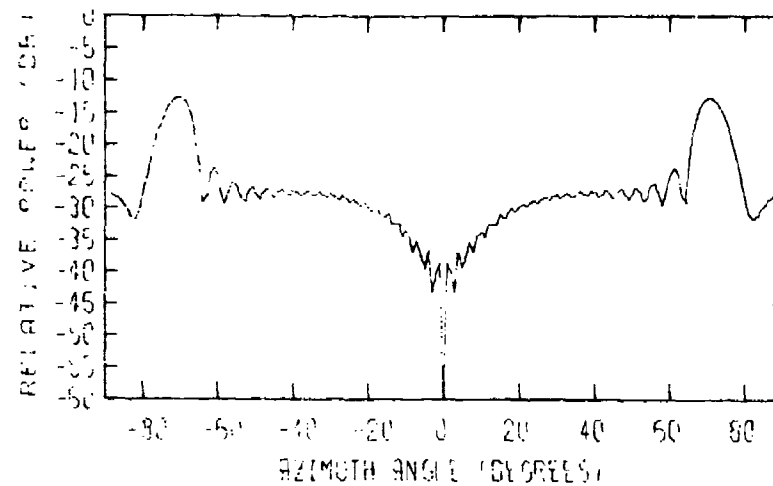
(a) Average Pattern

(b) Random Pattern

Figure 133.   Statistical average and random out-of-band parallel-
polarized phased-array antenna patterns for the in-
band scan angle of 0-degrees at 18.9 GHz involving
the TE_{10}, TE_{20}, TE_{01}, TE_{11}, and TM_{11} waveguide modes.
The statistical average value of the randomly-varying
power in each mode was 0.2 watt. The gain relative
to an isotropic radiator at the tops of the charts
is 23 dB, and the symbols M and σ_g denote median
gain and standard deviation, respectively.

(a) Average Pattern

(b) Random Pattern

Figure 134. Statistical average and random out-of-band cross-
polarized phased-array antenna patterns for the
in-band scan angle of 0-degrees at 18.0 GHz in-
volving the TE_{10}, TE_{20}, TE_{01}, TE_{11}, and TM_{11}
waveguide modes. The statistical average values
of the randomly-varying power in each mode was
0.2 watt. The gain relative to an isotropic
radiator at the tops of the charts is 23 dB, and
the symbols M and σ_g denote median gain and
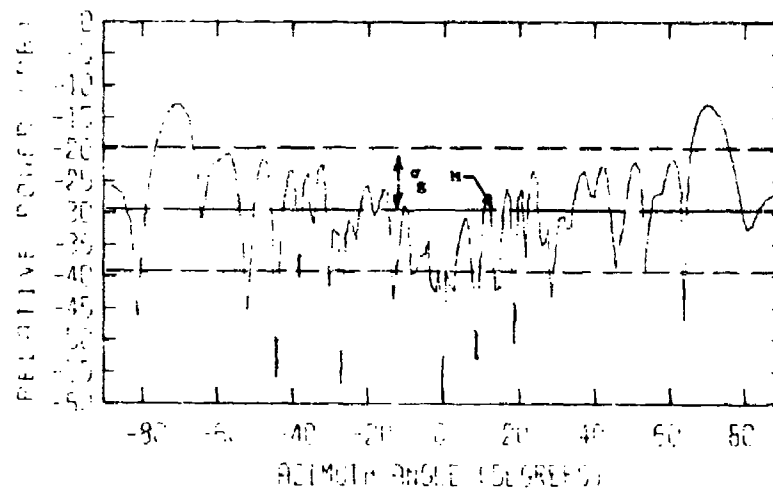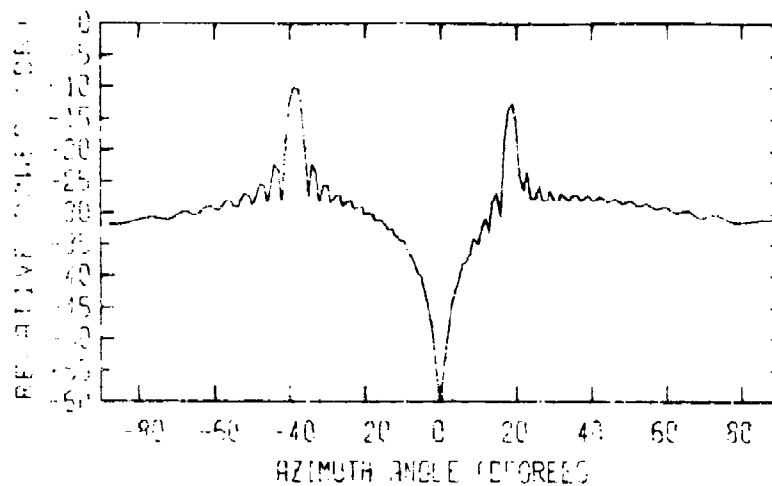standard deviation, respectively.
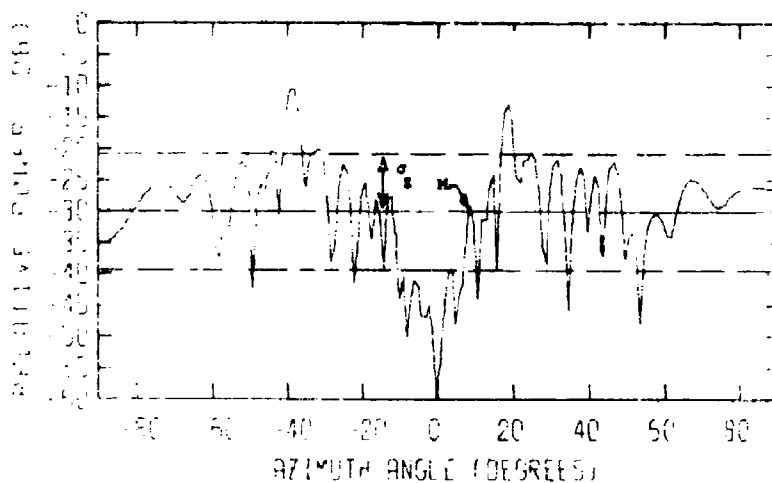
(a) Average Pattern

(b) Random Pattern

Figure 135. Statistical average and random out-of-band parallel-polarized phased-array antenna patterns for the in-band scan angle of 20 degrees at 18.0 GHz involving the TE_{10}, TE_{20}, TE_{01}, TE_{11}, and TM_{11} waveguide modes. The statistical average values of the randomly-varying power in each mode was 0.2 watt. The gain relative to an isotropic radiator at the tops of the charts is 23 dB, and the symbols M and σ_g denote median gain and standard deviation, respectively.

257

(a) Average Pattern

(b) Random Pattern

Figure 136. Statistical average and random out-of-band cross-polarized phased-array antenna patterns for the in-band scan angle of 20 degrees at 18.0 GHz involving the TE_{10}, TE_{20}, TE_{01}, TE_{11}, and TM_{11} waveguide modes. The statistical average value of the randomly-varying power in each mode was 0.2 watt. The gain relative to an isotropic radiator at the tops of the charts is 23 dB, and the symbols M and σ_g denote median gain and standard deviation, respectively.
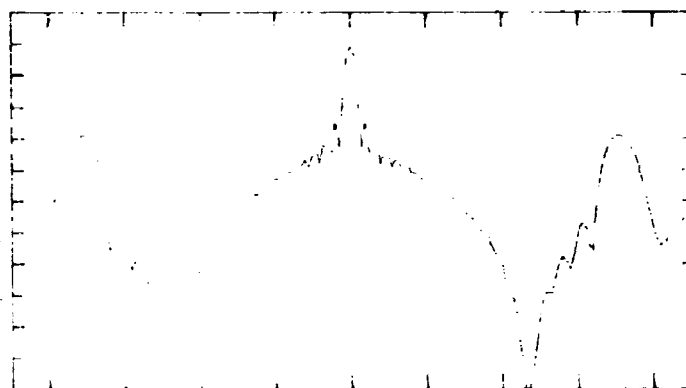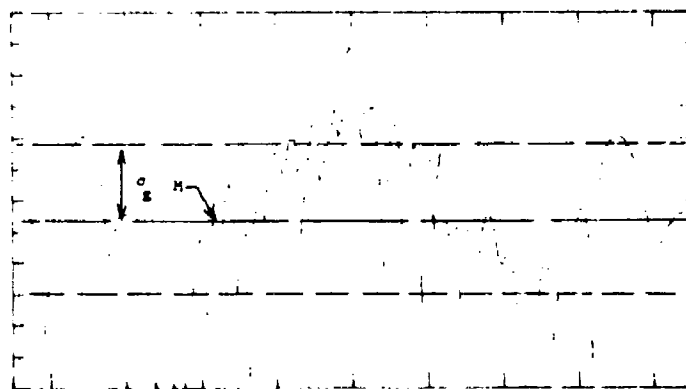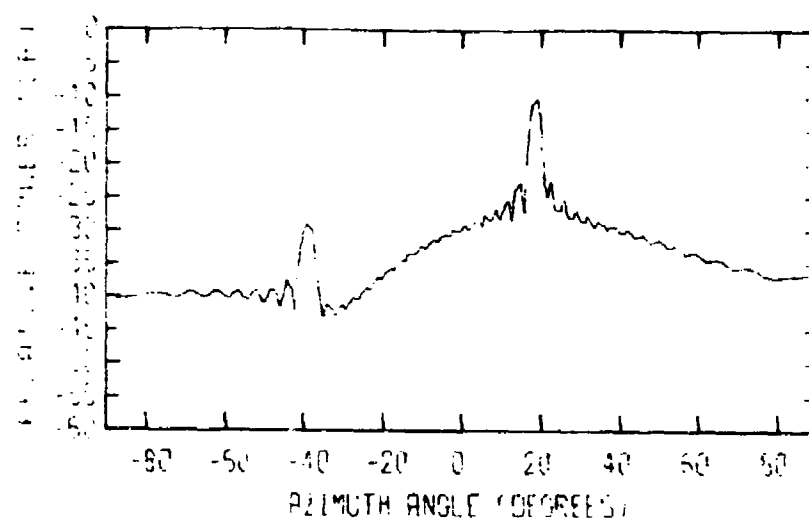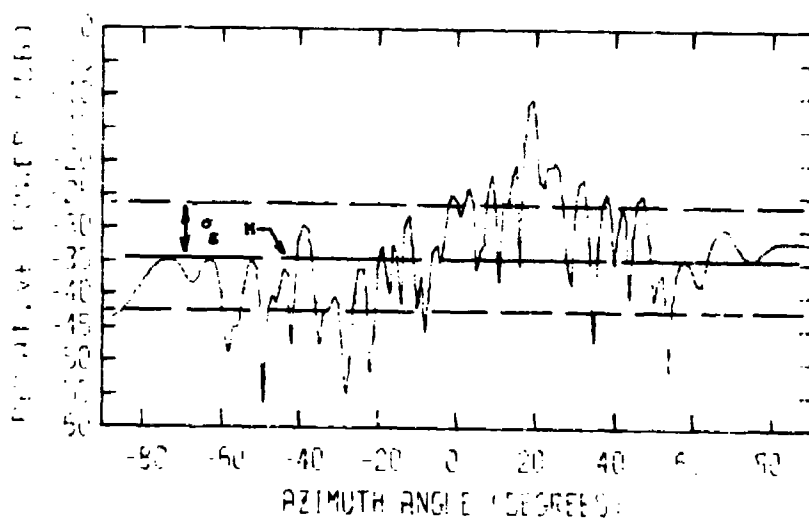
(a) Average Pattern

(b) Random Pattern

Figure 137. Statistical average and random out-of-band parallel-
polarized phased-array antenna patterns for the in-
band scan angle of 40 degrees at 18.0 GHz involving
the TE_{10}, TE_{20}, TE_{01}, TE_{11}, and TM_{11} waveguide modes.
The statistical average value of the randomly-varying
power in each mode was 0.2 watt. The gain relative
to an isotropic radiator at the tops of the charts
is 23 dB, and the symbols M and σ_g denote median
gain and standard deviation, respectively.
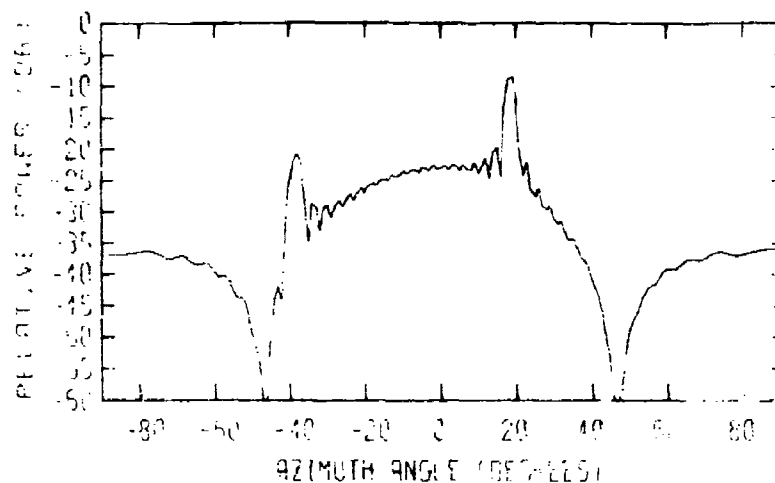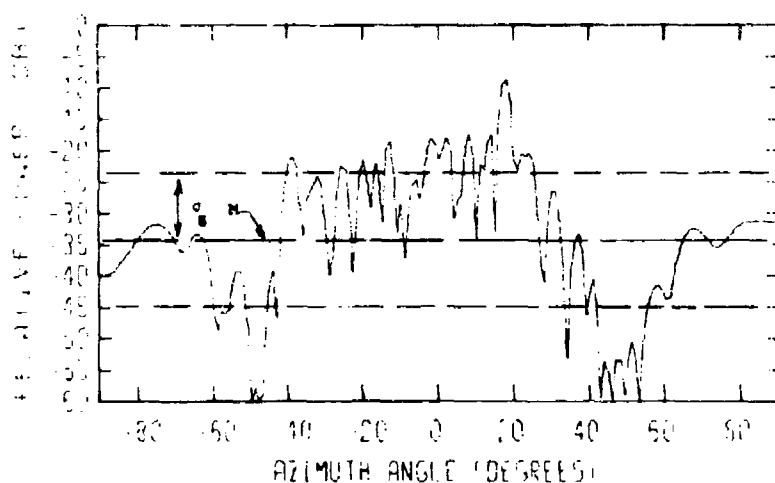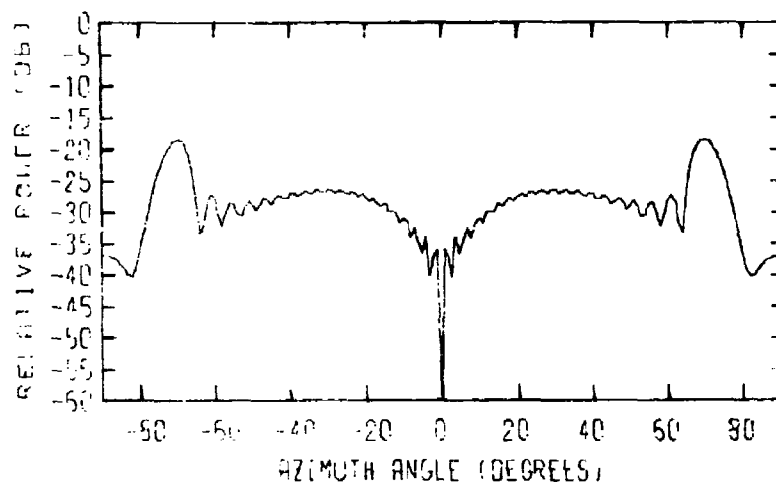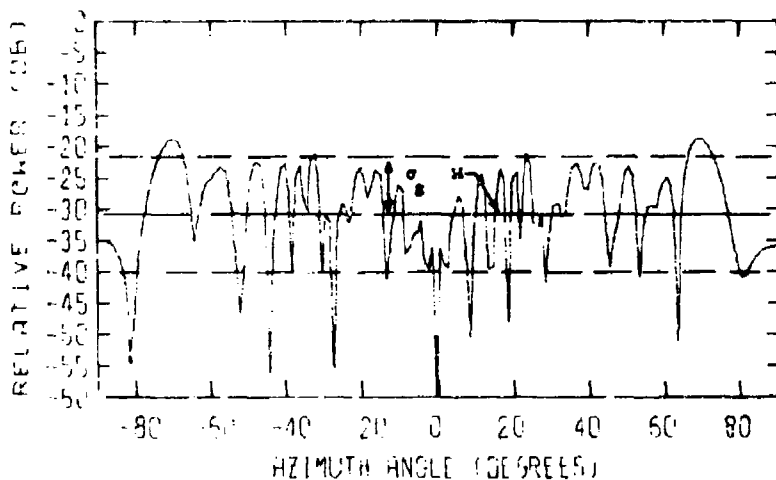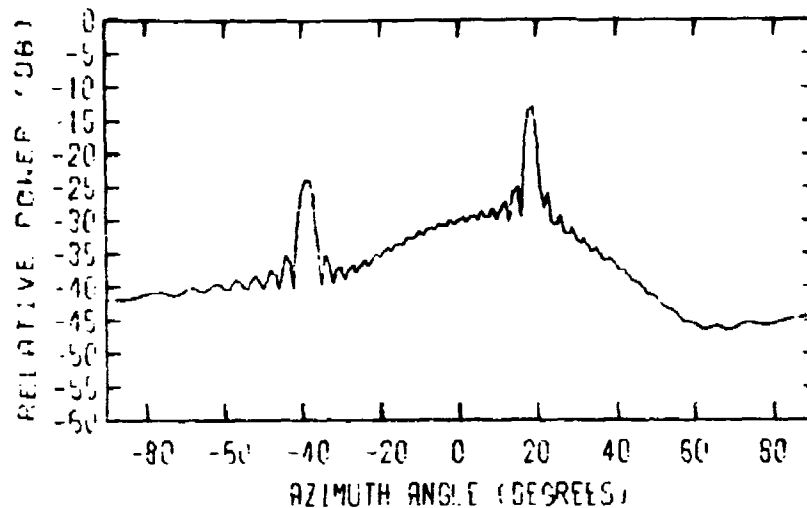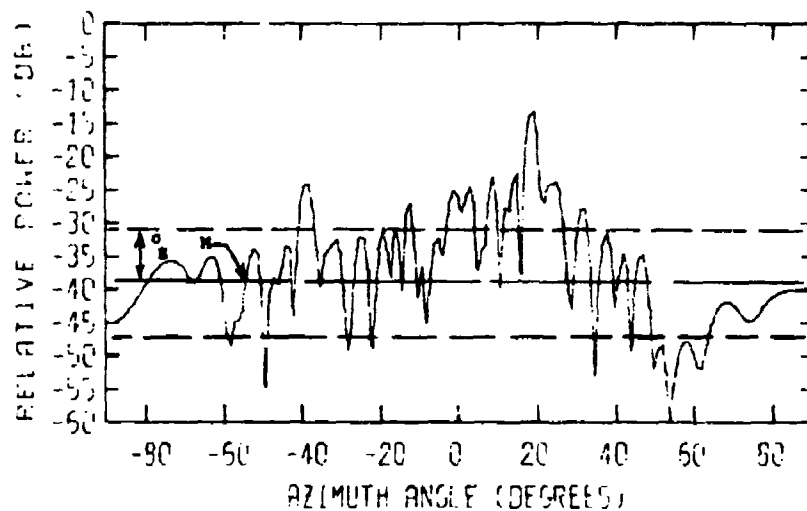
(a) Average Pattern

(b) Random Pattern

Figure 138. Statistical average and random out-of-band cross-polarized phased-array antenna patterns for the in-band scan angle of 40 degrees at 18.0 GHz involving the TE_{10}, TE_{20}, TE_{01}, TE_{11}, and TM_{11} waveguide modes. The statistical average value of the randomly-varying power in each mode was 0.2 watt. The gain relative to an isotropic radiator at the tops of the charts is 23 dB, and the symbols M and σ_g denote median gain and standard deviation, respectively.
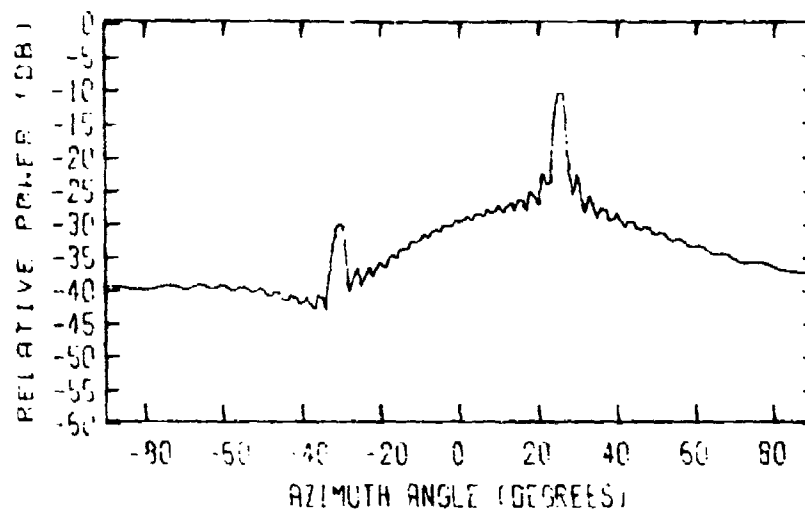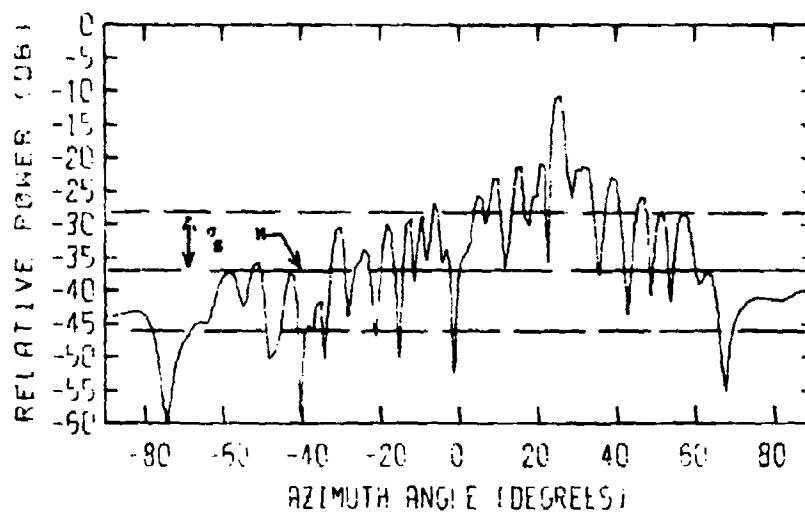
(a) Average Pattern

(b) Random Pattern

Figure 139. Statistical average and random out-of-band parallel-polarized phased-array antenna patterns for the in-band scan angle of 60 degrees at 18.0 GHz involving the TE_{10}, TE_{20}, TE_{01}, TE_{11}, and TM_{11} waveguide modes. The statistical average value of the randomly-varying power in each mode was 0.2 watt. The gain relative to an isotropic radiator at the tops of the charts is 23 dB, and the symbols M and σ_g denote median gain and standard deviation, respectively.
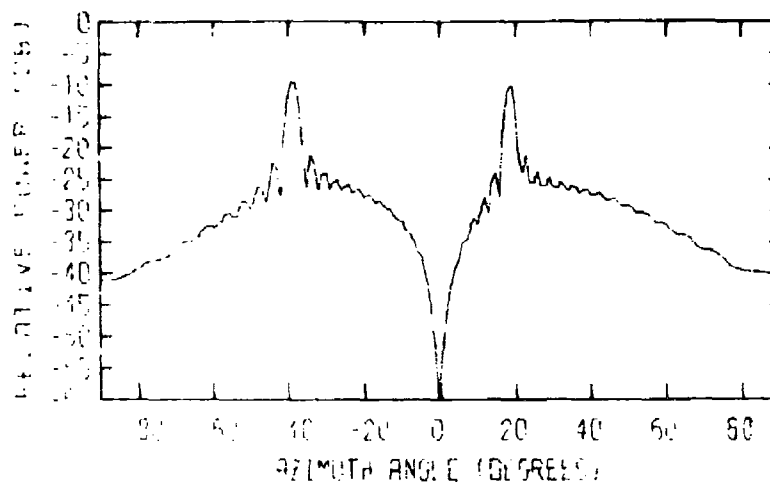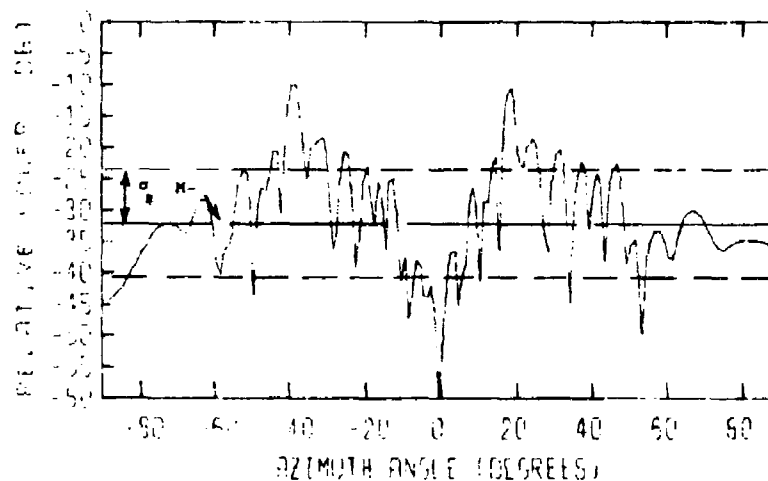
261
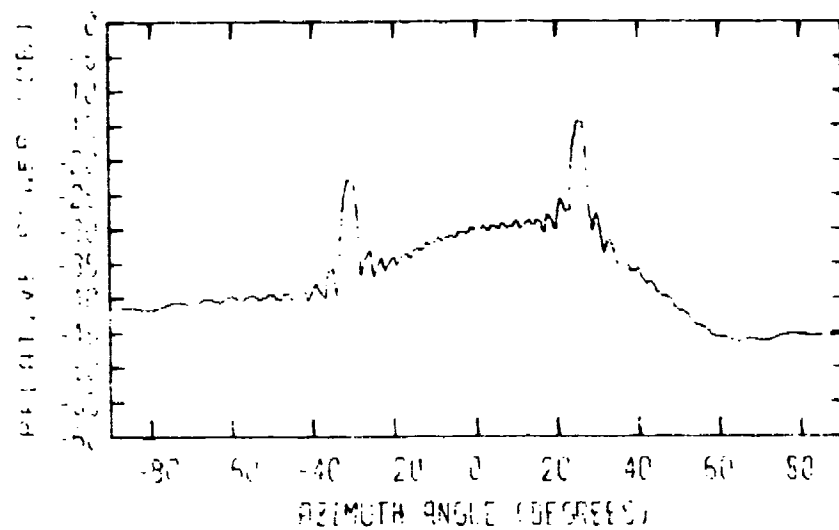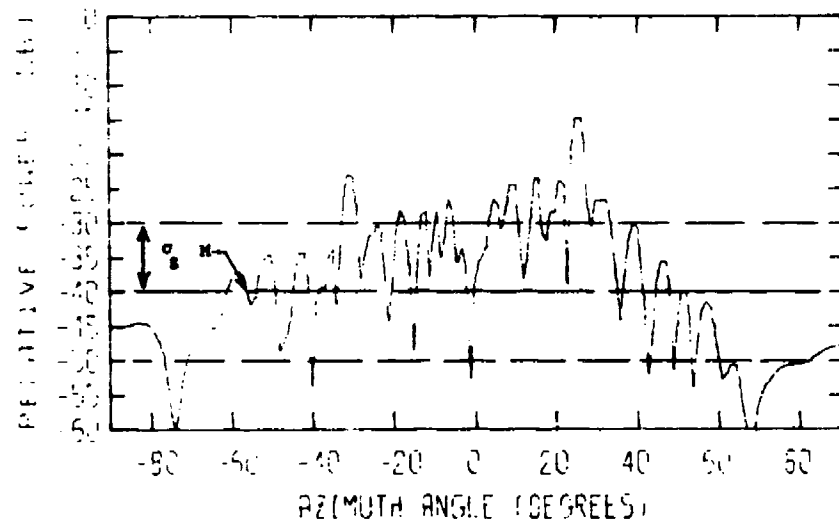
(a) Average Pattern

(b) Random Pattern

Figure 140. Statistical average and random out-of-band cross-
polarized phased-array antenna patterns for the in-
band scan angle of 60 degrees at 18.0 GHz involving
the TE_{10}, TE_{20}, TE_{01}, TE_{11}, and TM_{11} waveguide modes.
The statistical average value of the randomly-varying
power in each mode was 0.2 watt. The gain relative
to an isotropic radiator at the tops of the charts is
23 dB, and the symbols M and σ_g denote median gain and
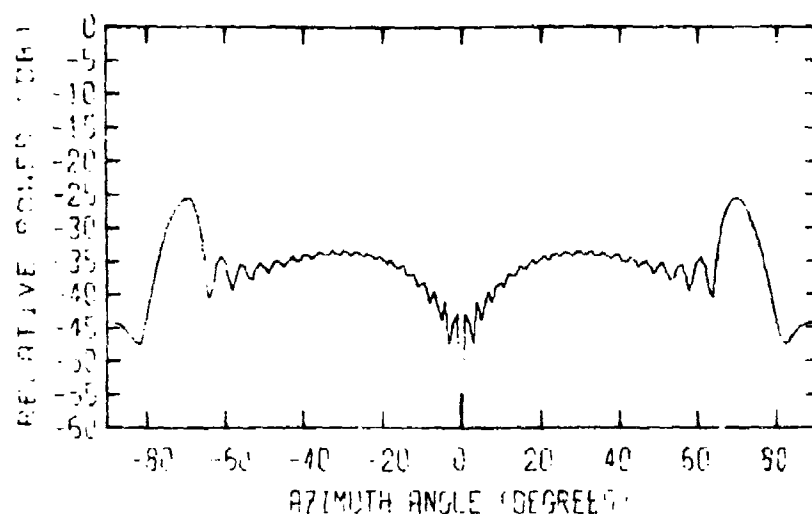standard deviation, respectively.

262
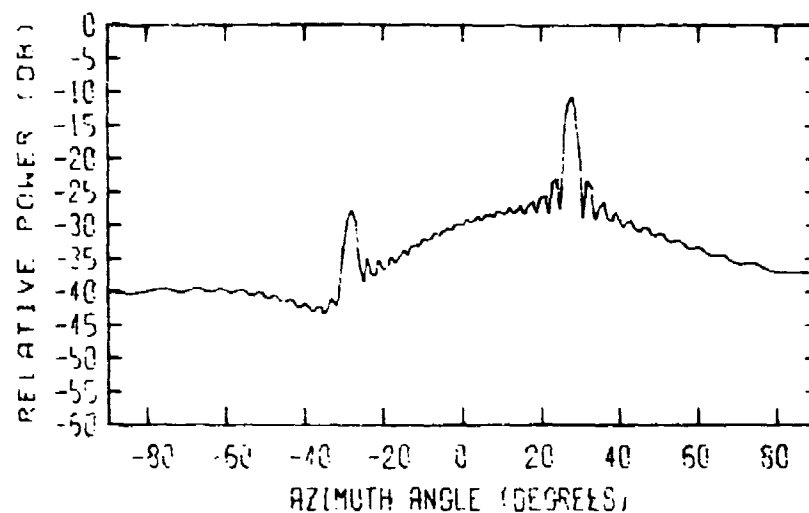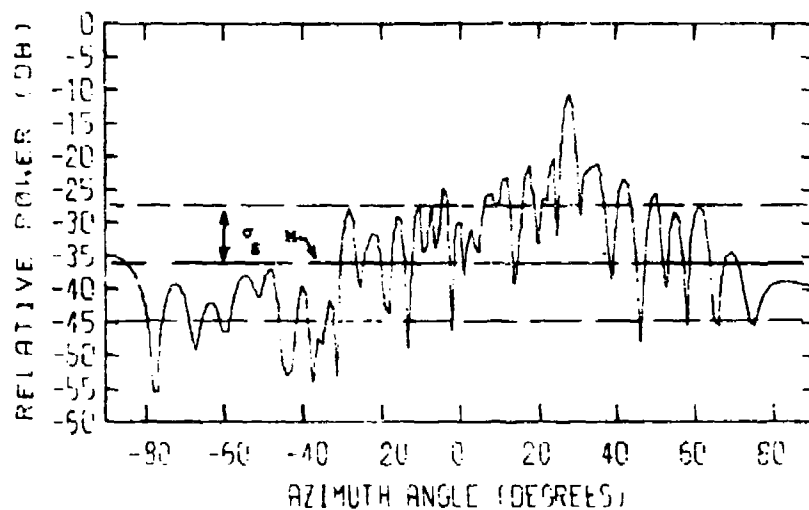
(a) Average Pattern

(b) Random Pattern

Figure 141. Statistical average and random out-of-band parallel-
polarized phased-array antenna patterns for the in-
band scan angle of 70 degrees at 12.0 GHz involving
the TE_{10}, TE_{20}, TE_{01}, TE_{11}, and TM_{11} waveguide modes.
The statistical average value of the randomly-varying
power in each mode was 0.2 watt. The gain relative
to an isotropic radiator at the tops of the charts is
23 dB, and the symbols M and σ_g denote median gain and
standard deviation, respectively.
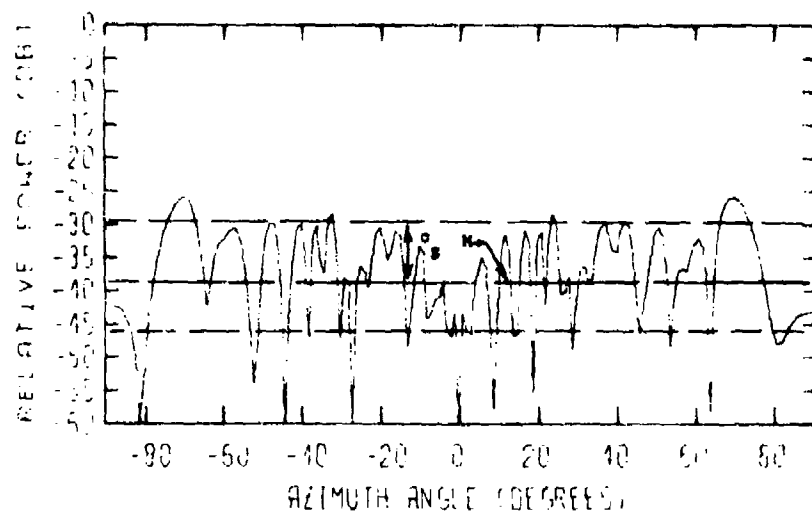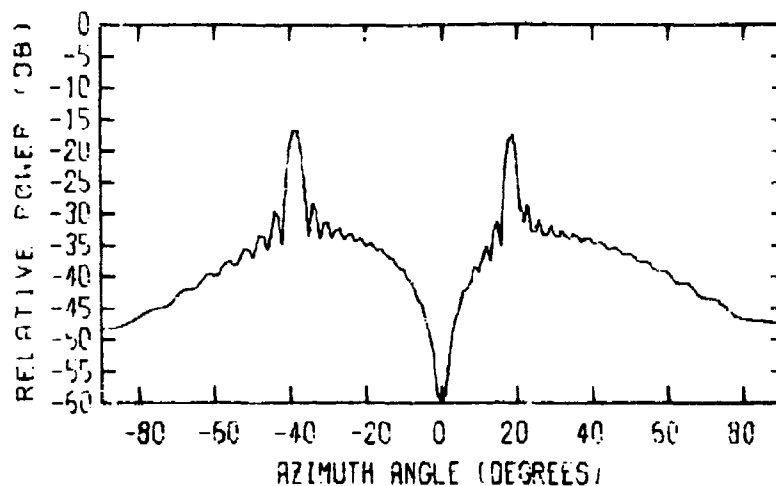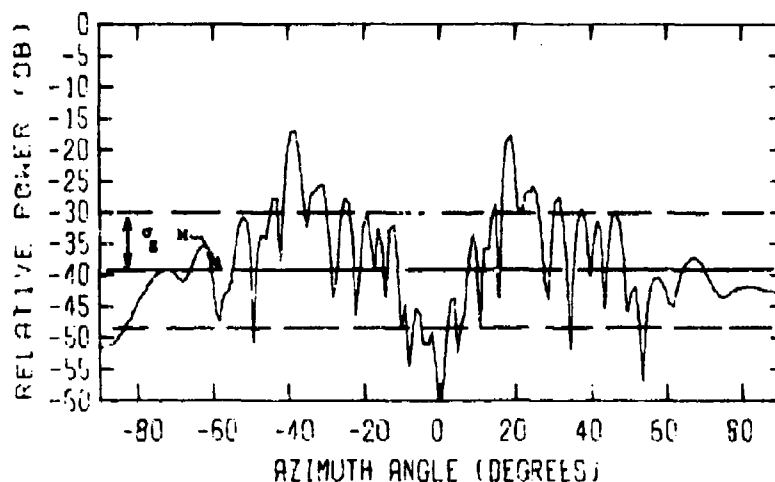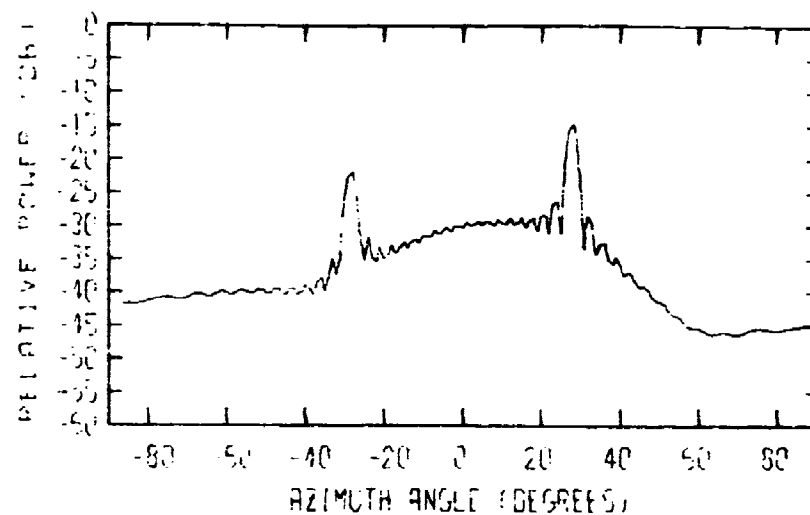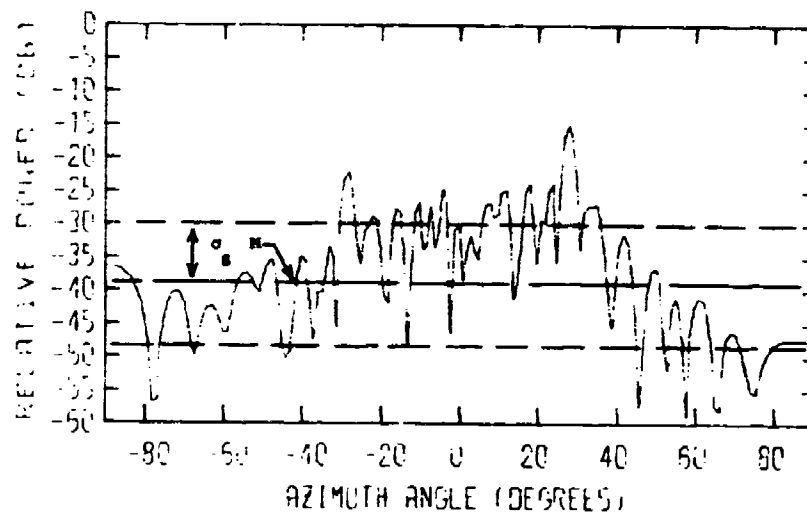
(a) Average Pattern

(b) Random Pattern

Figure <u>142</u>. Statistical average and random out-of-band cross-polarized phased-array antenna patterns for the in-band scan angle of 70 degrees at 18.0 GHz involving the TE_{10}, TE_{20}, TE_{01}, TE_{11}, and TM_{11} waveguide modes. The statistical average value of the randomly-varying power in each mode was 0.2 watt. The gain relative to an isotropic radiator at the tops of the charts is 23 dB, and the symbols M and σ_g denote median gain and standard deviation, respectively.
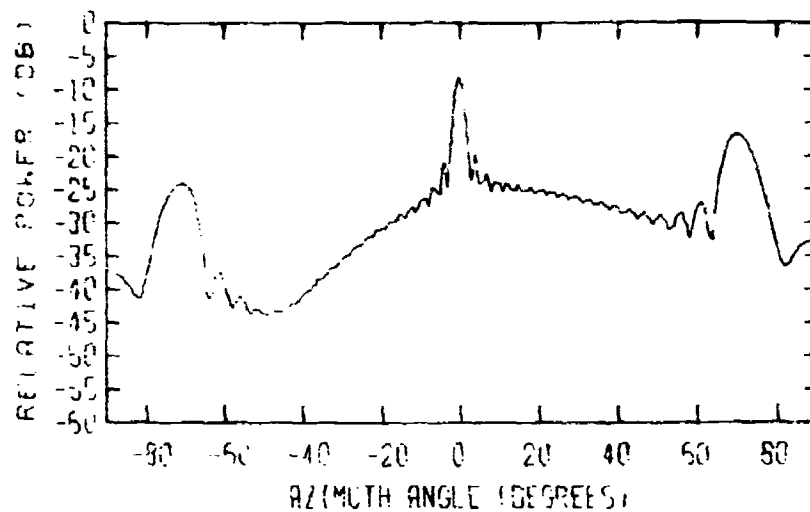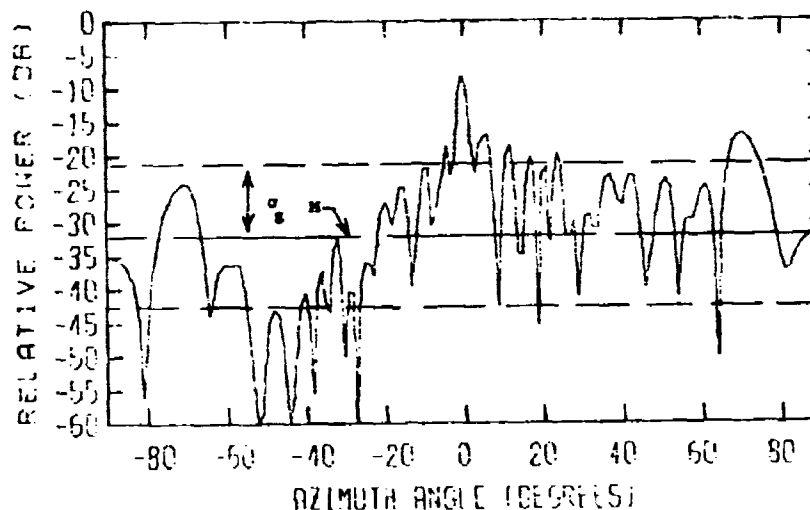
(a) Average Pattern

(b) Random Pattern

Figure 143. Statistical average and random out-of-band parallel-
polarized phased-array antenna patterns for the in-
band scan angle of 0-degrees at 18.0 GHz involving
the TE_{10}, TE_{20}, TE_{01}, TE_{11}, and TM_{11} waveguide modes.
The statistical average value of the randomly-varying
power in each mode was 0.5, 0.2, 0.1, 0.1, and 0.1
watt, respectively. The gain relative to an isotropic
radiator at the tops of the charts is 23 dB, and the
symbols M and σ_g denote median gain and standard
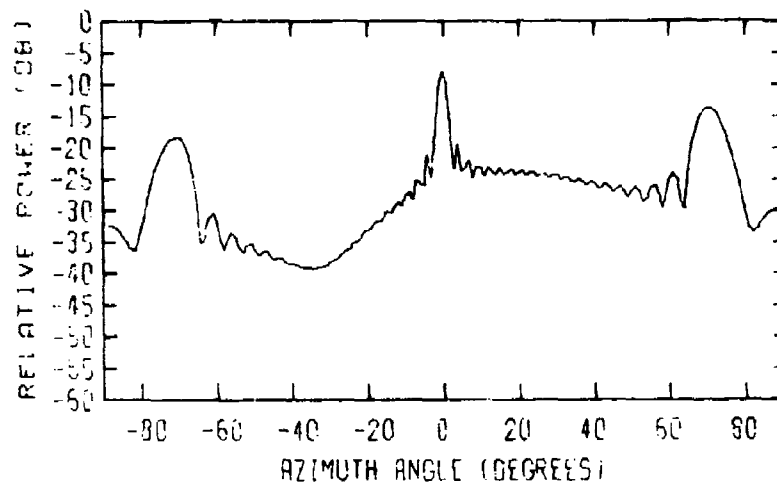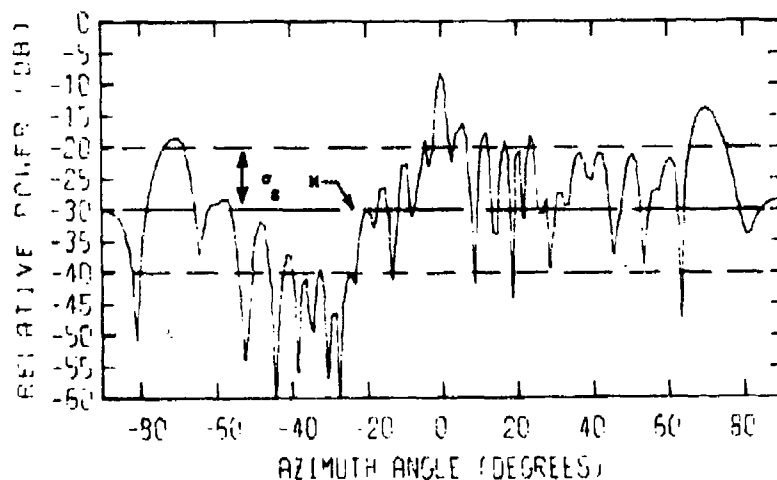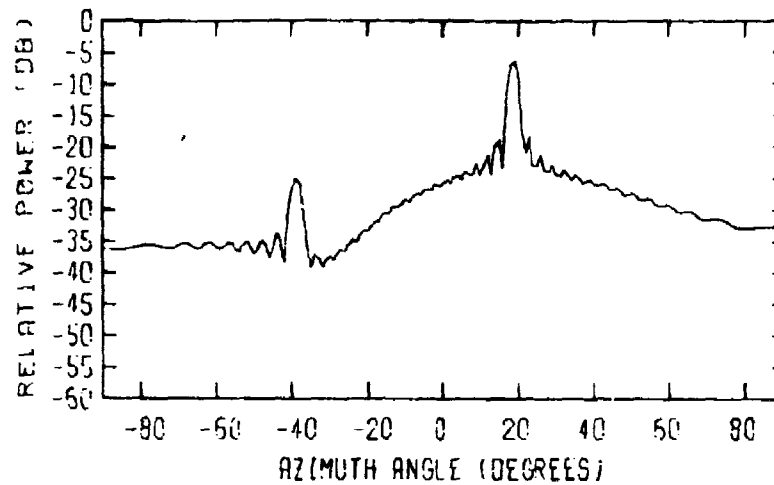deviation, respectively.

265
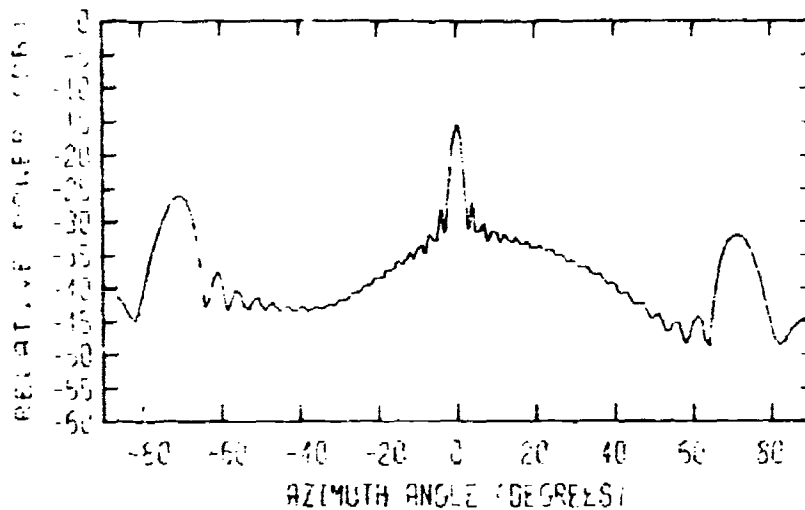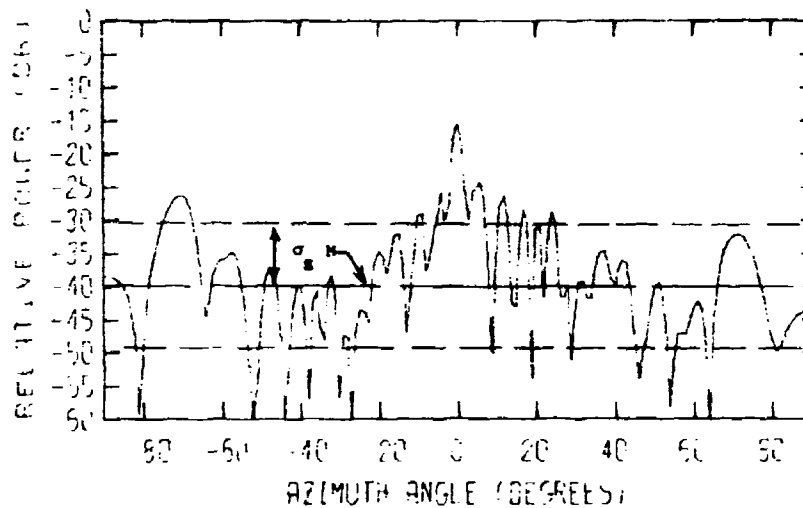
(a) Average Pattern

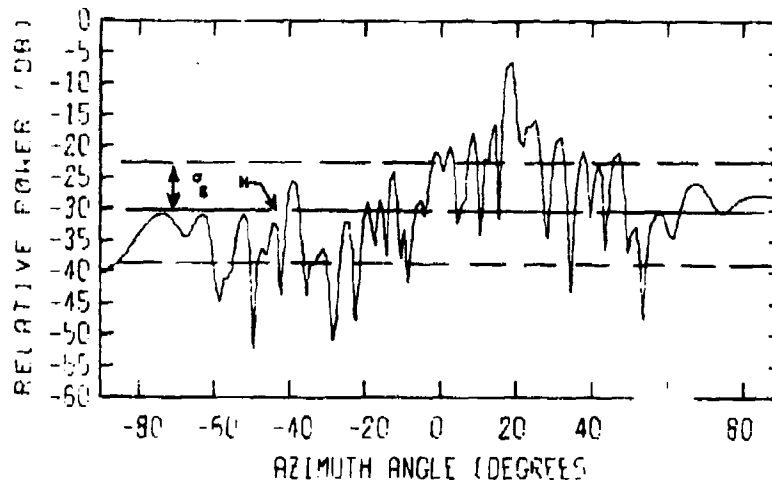

(b) Random Pattern

Figure 144. Statistical average and random out-of-band cross-
polarized phased-array antenna patterns for the in-
band scan angle of 0-degrees at 18.0 GHz involving
the TE_{10}, TE_{20}, TE_{01}, TE_{11}, and TM_{11} waveguide modes.
The statistical average value of the randomly-varying
power in each mode was 0.5, 0.2, 0.1, 0.1, and 0.1
watt, respectively. The gain relative to an isotropic
radiator at the tops of the charts is 23 dB, and the
symbols M and σ_g denote median gain and standard
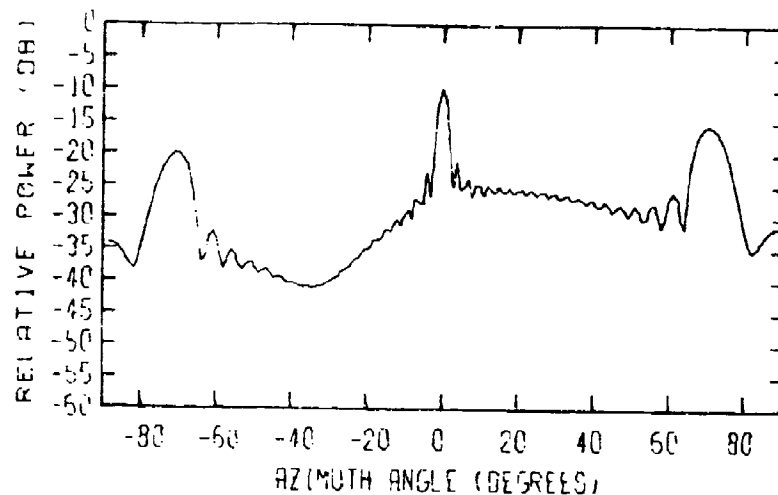deviation, respectively.
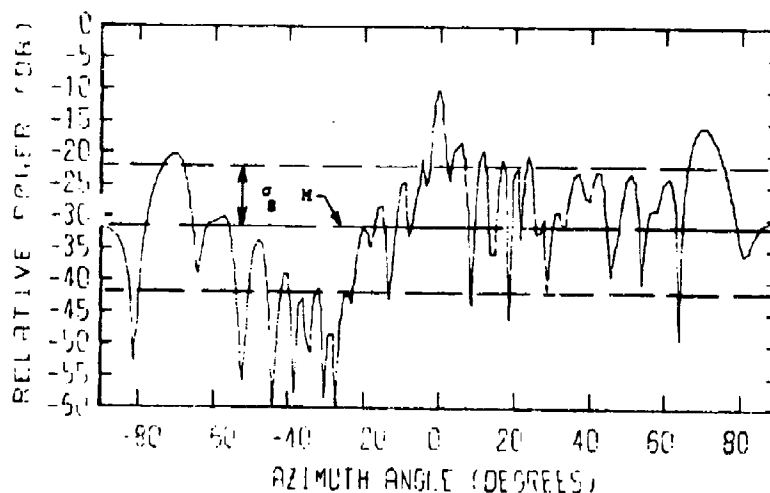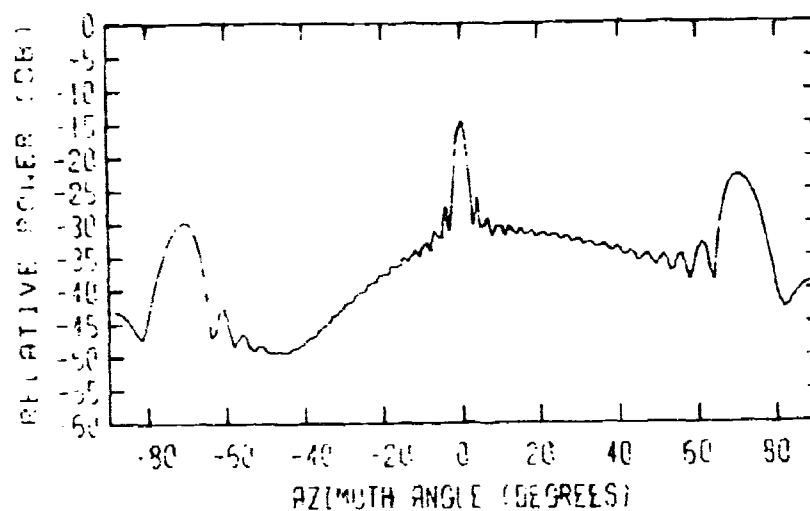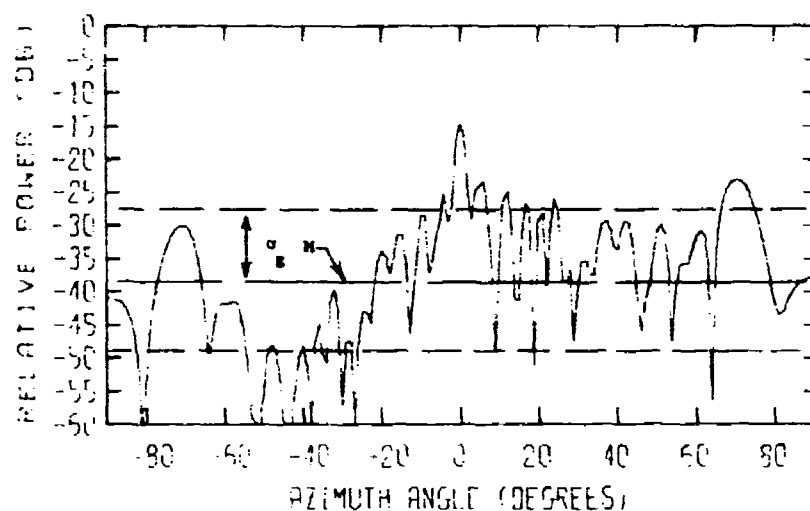
(a) Average Pattern

(b) Random Pattern

Figure 145. Statistical average and random out-of-band parallel-
polarized phased-array antenna patterns for the in-
band scan angle of 0-degrees at 18.0 GHz involving
the TE_{10}, TE_{20}, TE_{01}, TE_{11}, and TM_{11} waveguide modes.
The statistical average value of the randomly-varying
power in each mode was 0.11, 0.05, 0.43, 0.24, and
0.17 watt, respectively. The gain relative to an
isotropic radiator at the tops of the charts is 23 dB,
and the symbols M and σ_g denote median gain and
standard deviation, respectively.
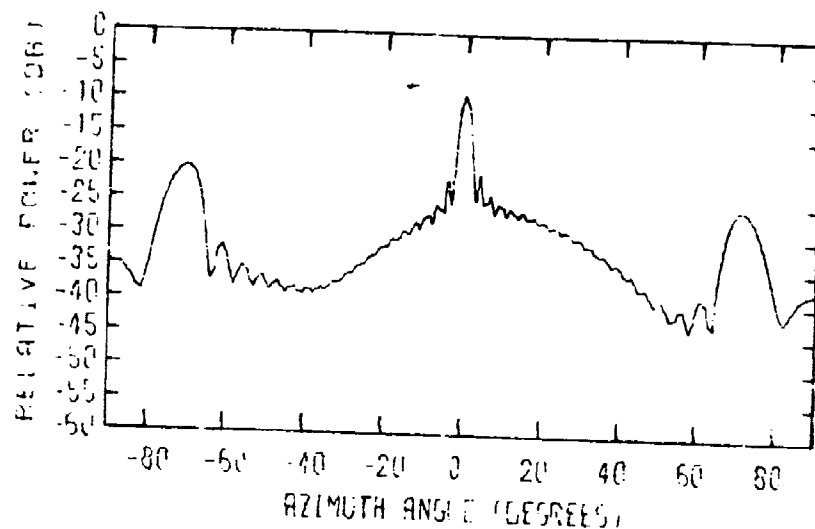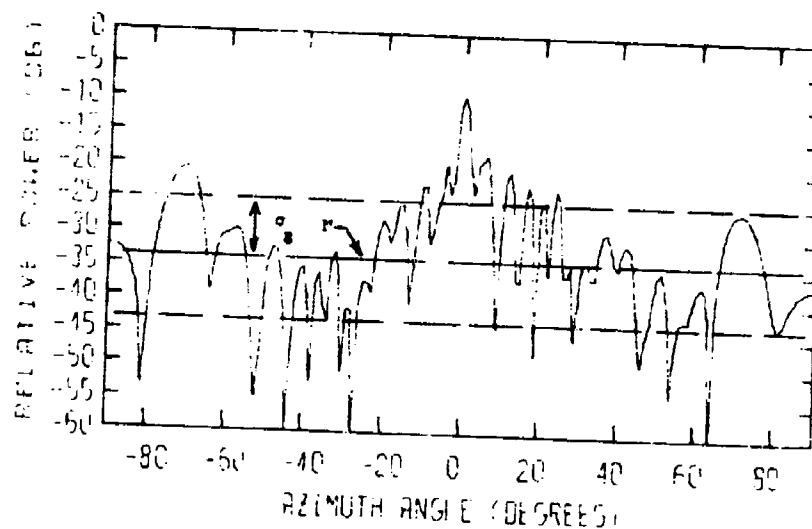
(a) Average Pattern

(b) Random Pattern

Figure 146. Statistical average and random out-of-band cross-polarized phased-array antenna patterns for the in-band scan angle of 0-degrees at 18.0 GHz involving the TE_{10}, TE_{20}, TE_{01}, TE_{11}, and TM_{11} waveguide modes. The statistical average value of the randomly-varying power in each mode was 0.11, 0.05, 0.43, 0.24, and 0.17 watt, respectively. The gain relative to an isotropic radiator at the tops of the charts is 23 dB, and the symbols M and σ_g denote median gain and standard deviation, respectively.
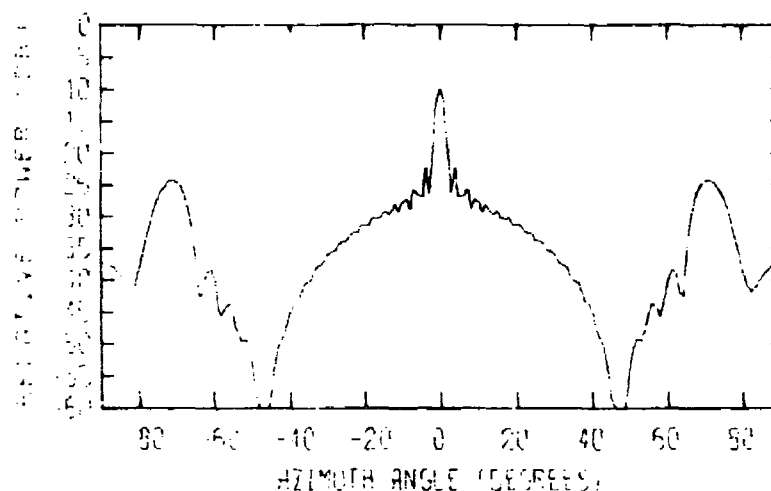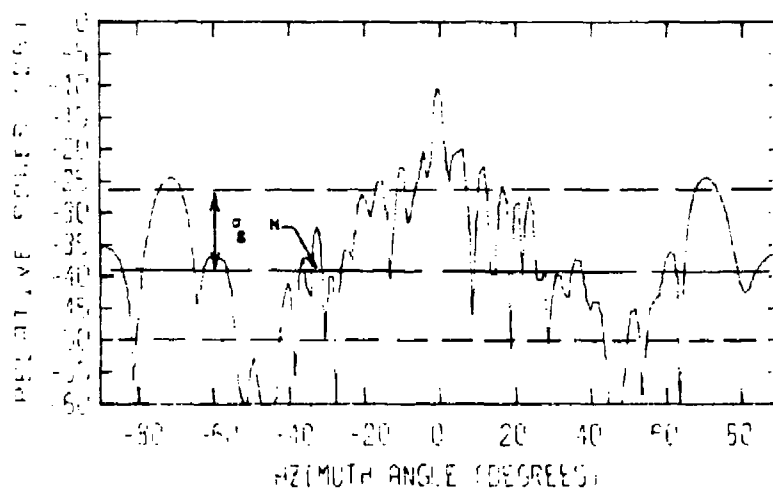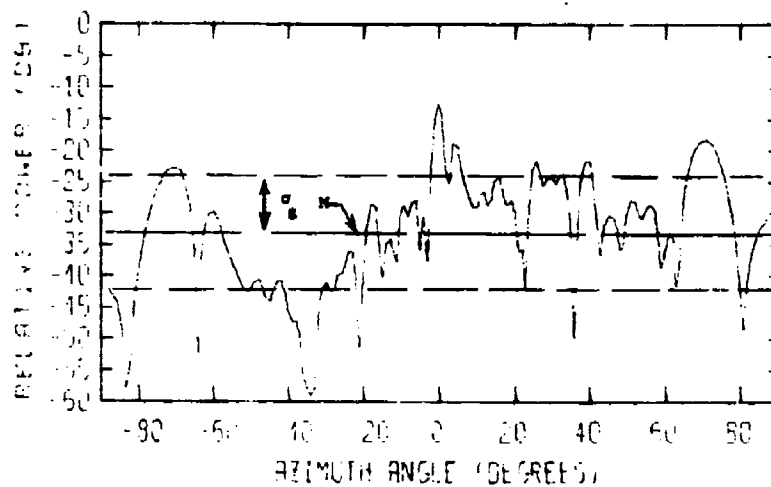
(a) Parallel
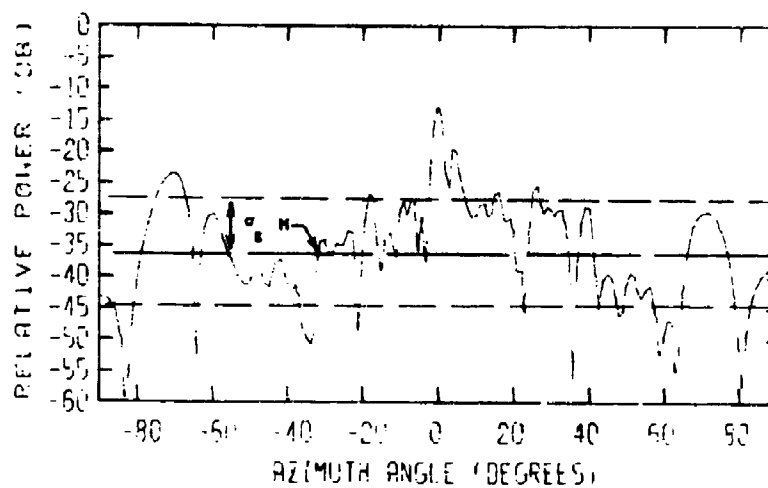
(b) Cross

Figure 147. Random out-of-band parallel and cross-polarized phased-array antenna pattern No. 2 for the in-band scan angle of 0-degrees at 18.0 GHz involving the TE_{10}, TE_{20}, TE_{01}, TE_{11}, and TM_{11} waveguide modes. The statistical average value of the randomly-varying power in each mode was 0.2 watt. The gain relative to an isotropic radiator at the tops of the charts is 23 dB, and the symbols m and σ_g denote median gain and standard deviation, respectively.
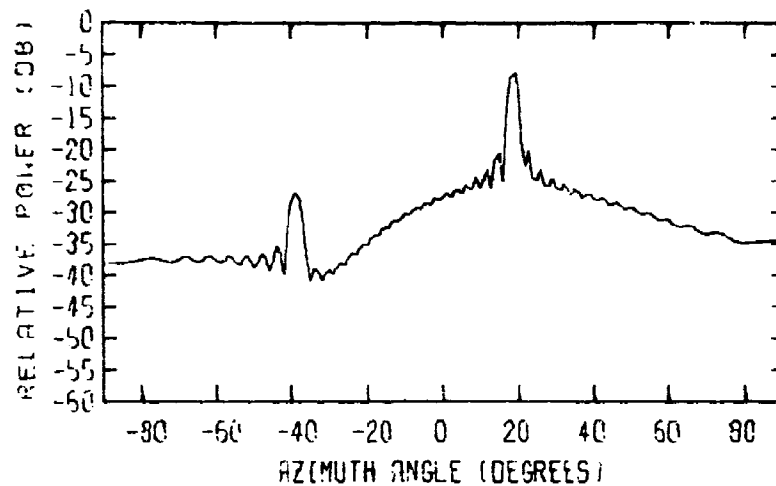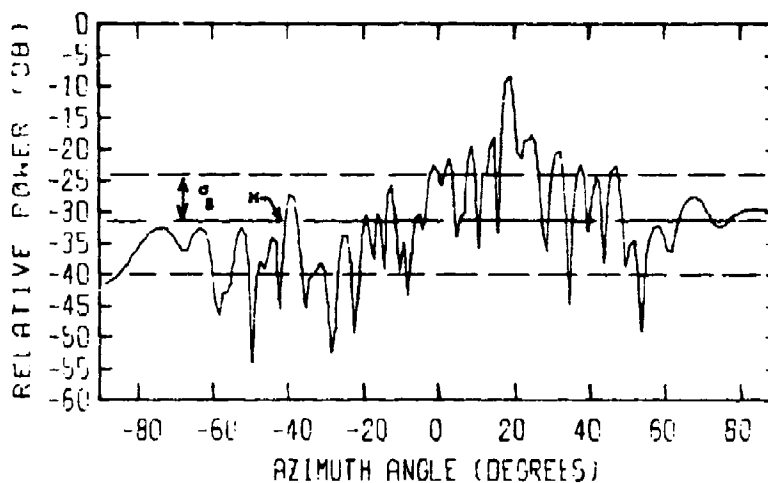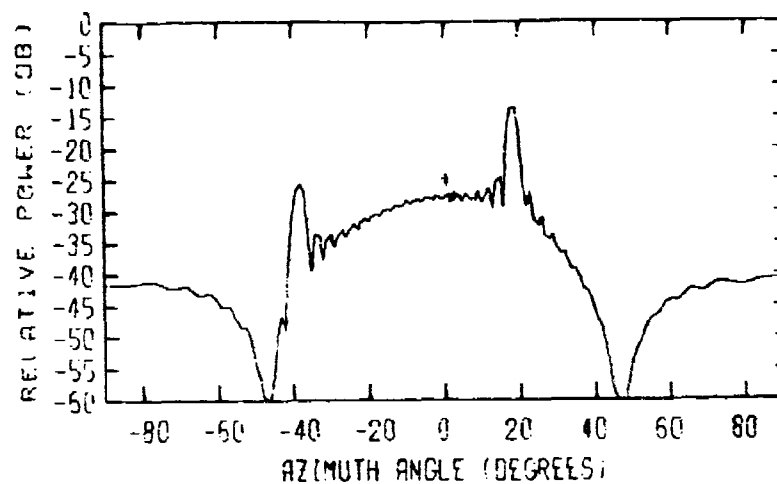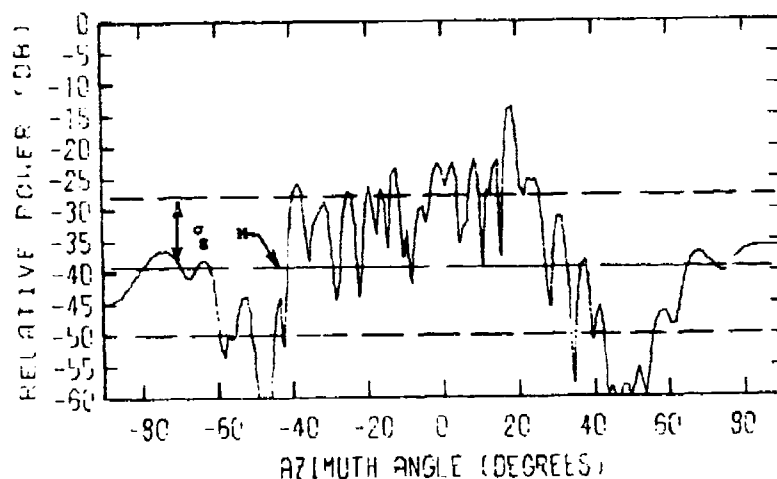
269
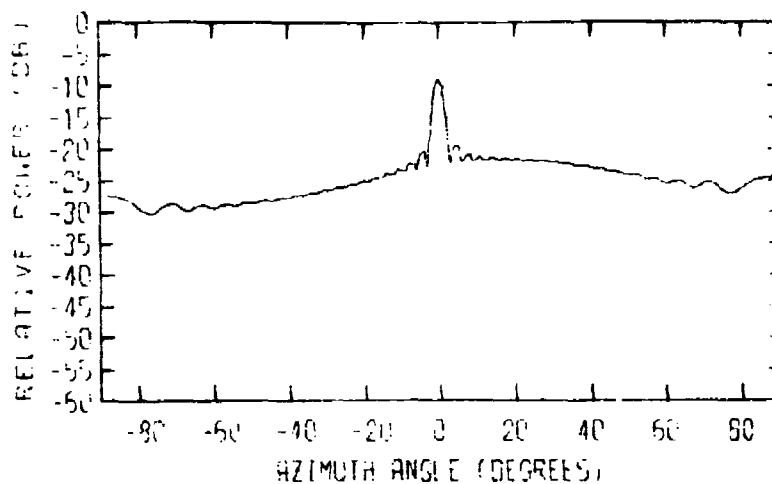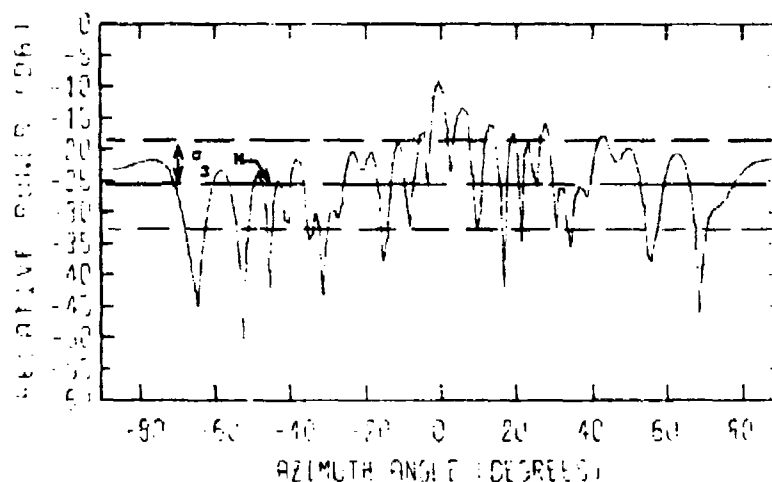
(a) Average Pattern

(b) Random Pattern

Figure 148. Statistical average and random out-of-band parallel-polarized phased-array antenna patterns for the in-band scan angle of 0-degrees at 15.7 GHz involving the TE_{10}, TE_{20}, and TE_{01} waveguide modes. The statistical average value of the randomly-varying power in each mode was 0.333 watt. The gain relative to an isotropic radiator at the tops of the charts is 19 dB, and the symbols M and σ denote median gain and standard deviation, respectively.
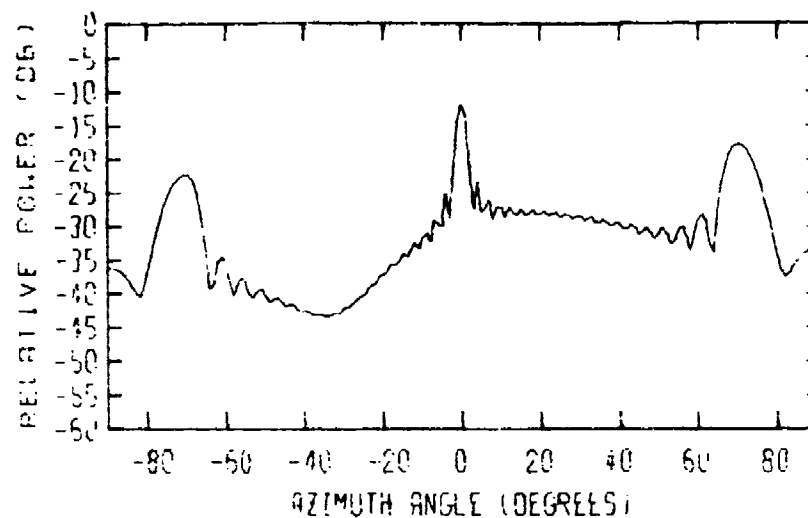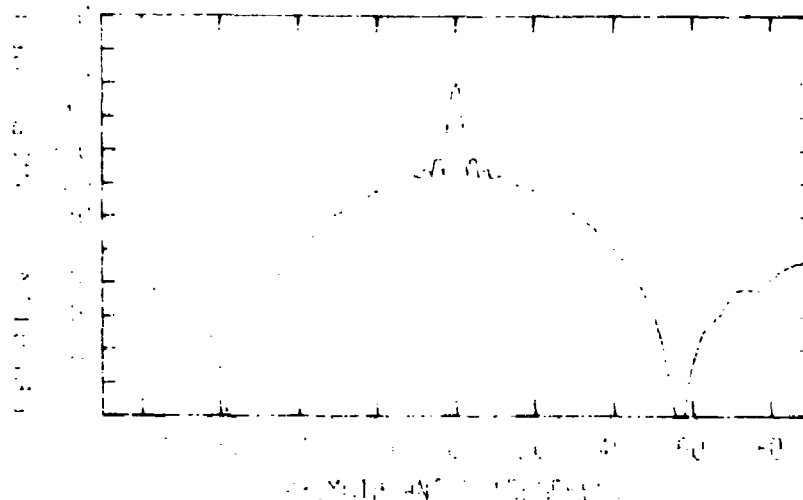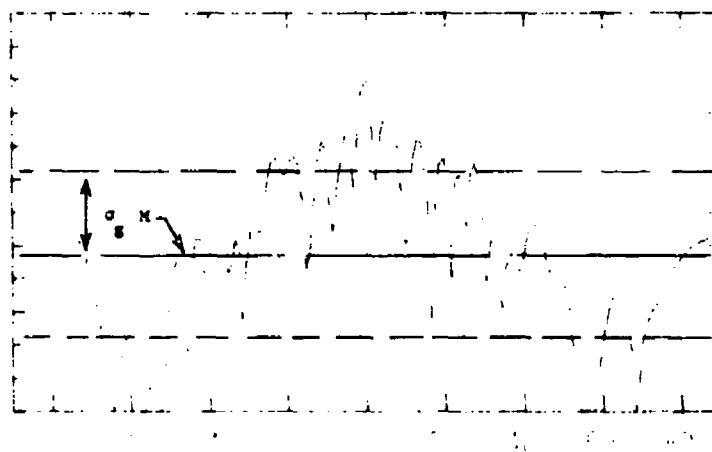
(a) Average Pattern

(b) Random Pattern

Figure 149. Statistical average and random out-of-band cross-
polarized phased-array antenna patterns for the in-
band scan angle of 0-degrees at 15.7 GHz involving
the TE_{10}, TE_{20}, and TE_{01} waveguide modes. The statis-
tical average value of the randomly-varying power
in each mode was 0.333 watt. The gain relative to
an isotropic radiator at the tops of the charts is
19 dB, and the symbols M and σ_g denote median gain and
standard deviation, respectively.

271
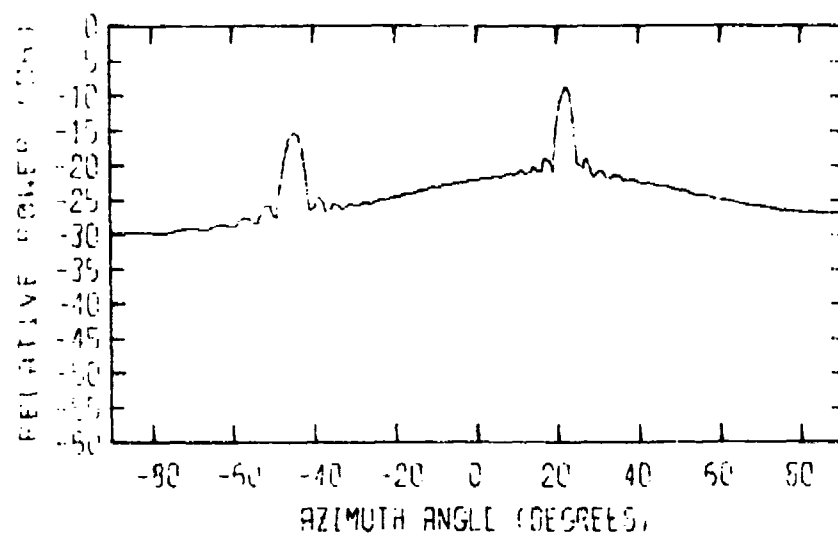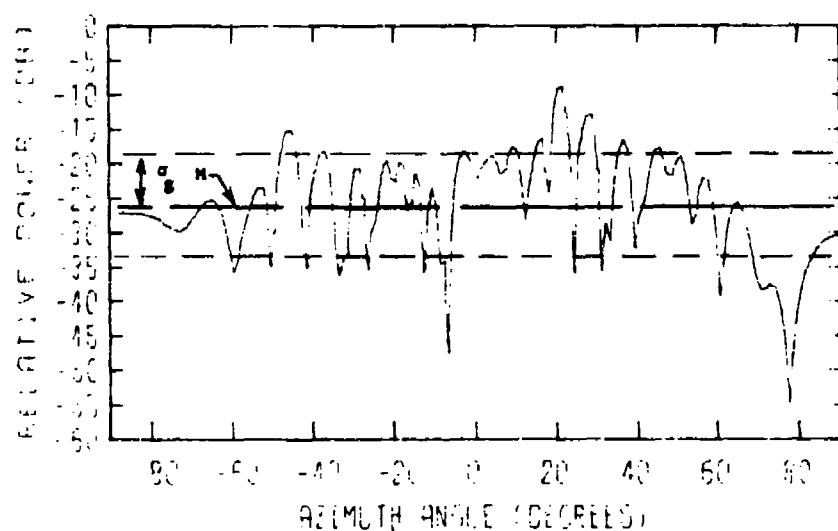
(a) Average Pattern

(b) Random Pattern

Figure 150. Statistical average and random out-of-band parallel-polarized phased-array antenna patterns for the in-band scan angle of 40 degrees at 15.7 GHz involving TE_{10}, TE_{20}, TE_{01} waveguide modes. The statistical average value of the randomly-varying power in each mode was 0.333 watt. The gain relative to an isotropic radiator at the tops of the charts is 19 dB, and the symbols M and σ_g denote median gain and standard deviation, respectively.
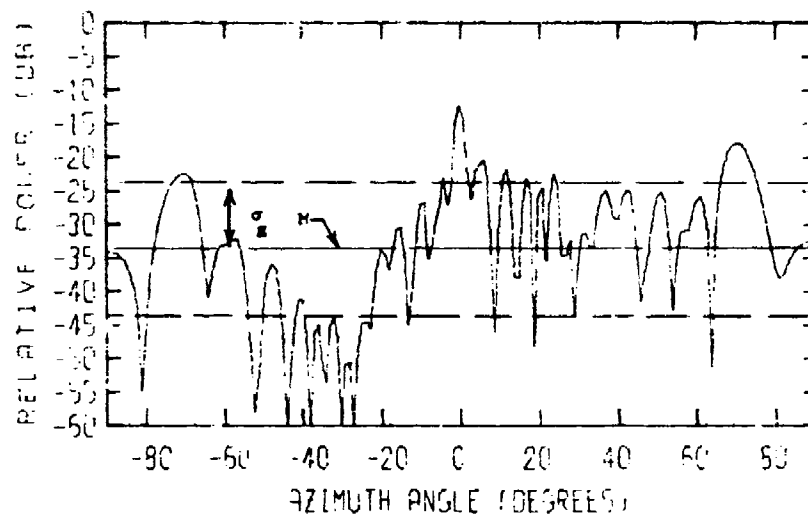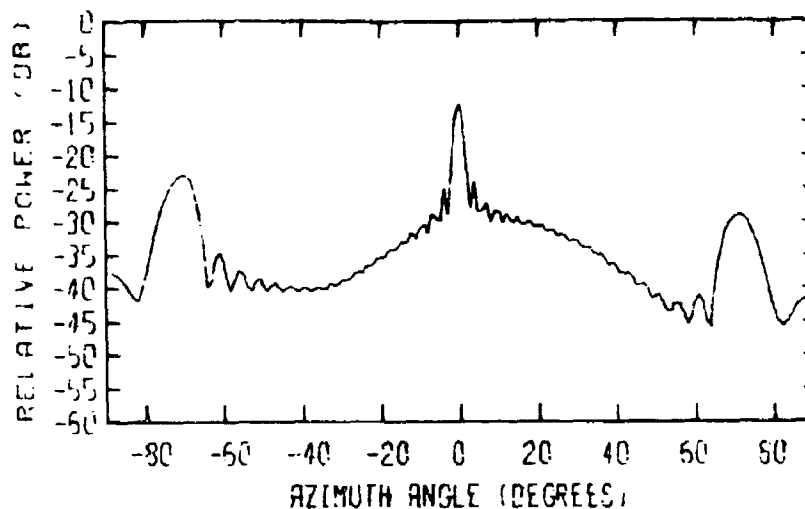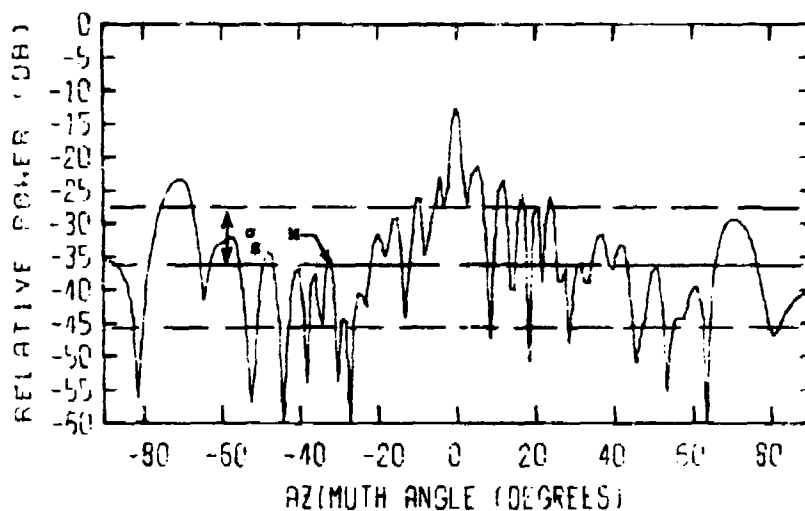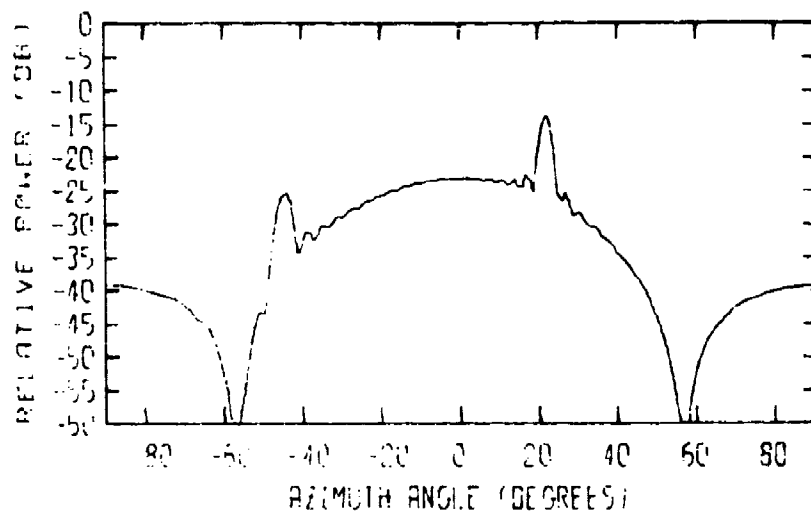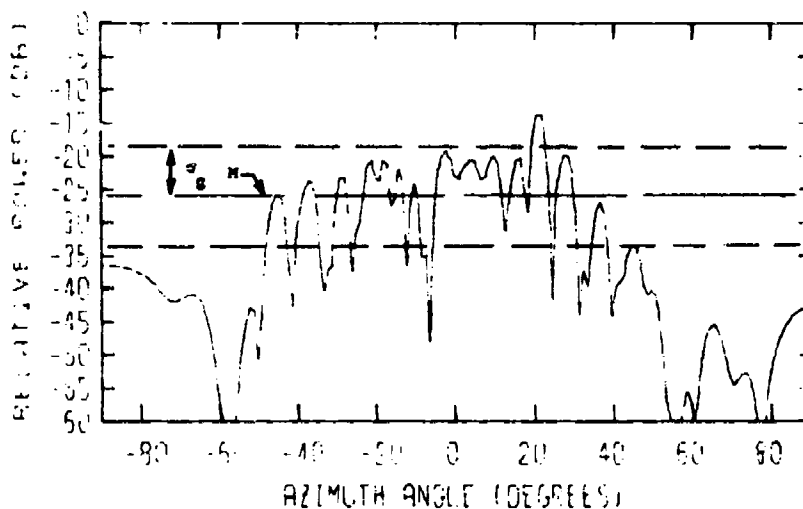
(a) Average Pattern

(b) Random Pattern

Figure 151. Statistical average and random out-of-band cross-polarized phased-array antenna patterns for the in-band scan angle of 40 degrees at 15.7 GHz involving the TE_{10}, TE_{20}, and TE_{01} waveguide modes. The statistical average value of the randomly-varying power in each mode was 0.333 watt. The gain relative to an isotropic radiation at the tops of the charts is 19 dB, and the symbols M and σ_g denote median gain and standard deviation, respectively.

273
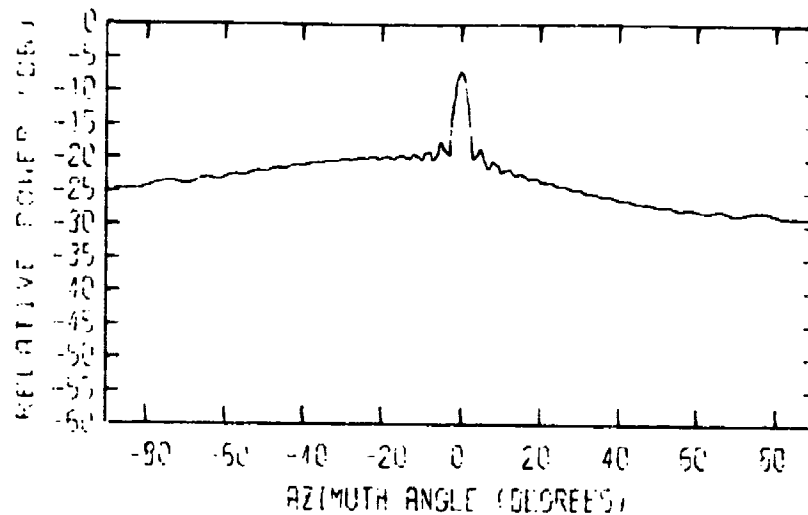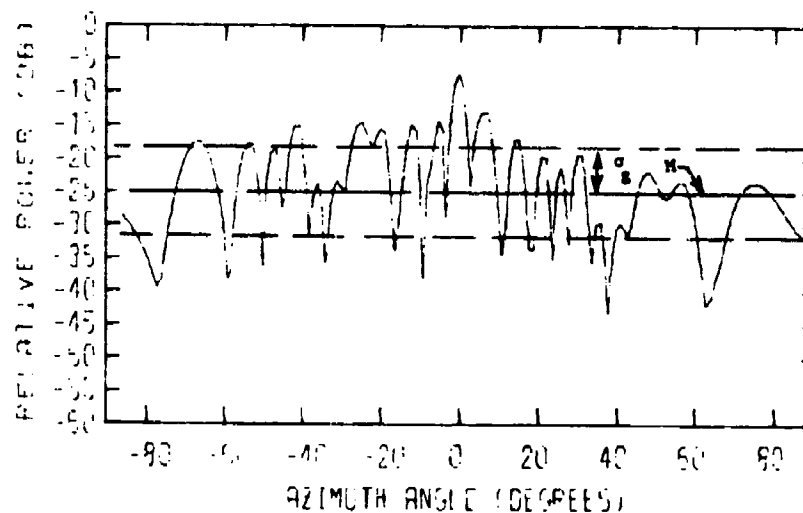
(a) Average Pattern

(b) Random Pattern

Figure _152_.   Statistical average and random out-of-band parallel-
polarized phased-array antenna patterns for the in-
band scan angle of 0-degrees at 14.5 GHz involving
the TE_{10} and TE_{20} waveguide modes. The statistical
average value of the randomly-varying power in each
mode was 0.5 watt.   The gain relative to an
isotropic radiator at the tops of the charts is 18
dB, and the symbols M and σ_g denote median gain and
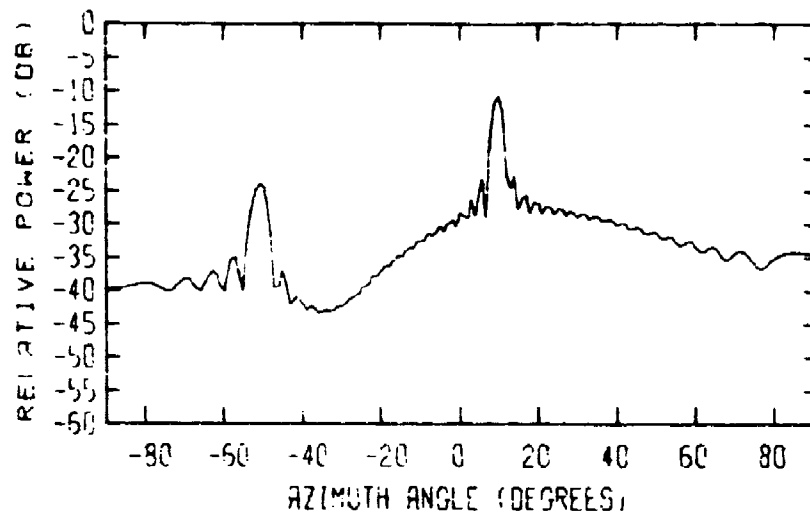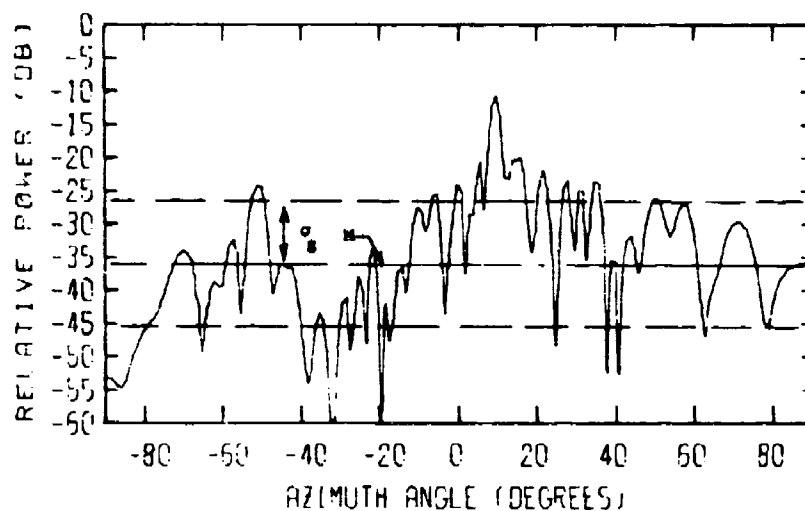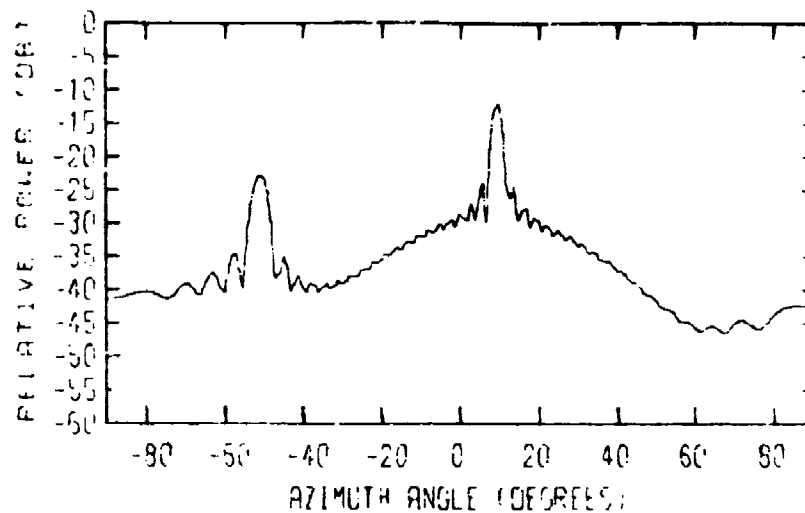standard deviation, respectively.
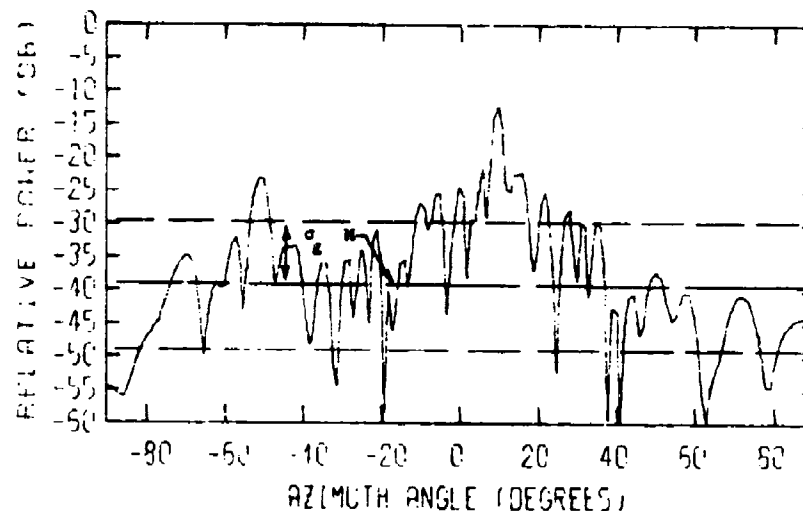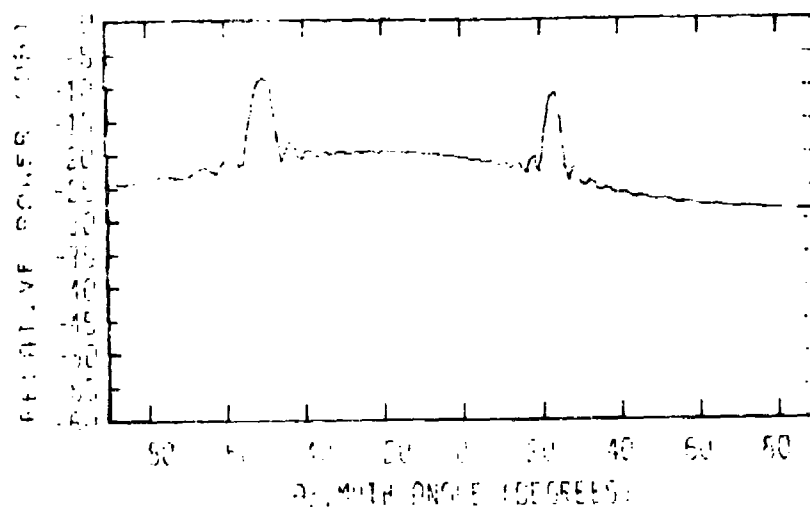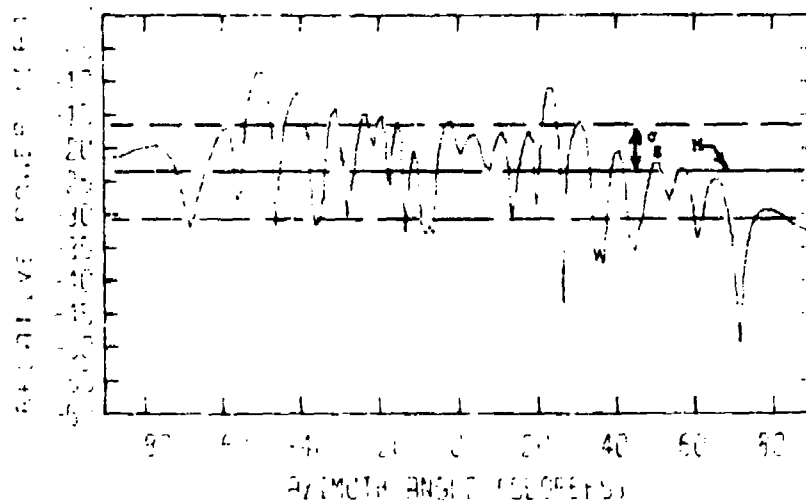
(a) Average Pattern

(b) Random Pattern

Figure 153. Statistical average and random out-of-band parallel-polarized phased-array antenna patterns for the in-band scan angle of 40 degrees at 14.5 GHz involving the TE_{10} and TE_{20} waveguide modes. The statistical average value of the randomly-varying power in each mode was 0.5 watt. The gain relative to an isotropic radiator at the tops of the charts is 18 dB, and the symbols M and σ_g denote median gain and standard deviation, respectively.

275

deviations of the random patterns in the various figures are indicated in the respective patterns by the dashed lines.

For the 18 GHz frequency, the figures are arranged according to modal content and in-band scan angle. Thus, Figures 117 through 126 are for propagation successively in the TE_{10}, TE_{20}, TE_{01}, TE_{11}, and TM_{11} waveguide modes for in-band scan angles of 0-degrees and 40-degrees. Figures 127 through 128 show the patterns for combined propagation energy in the TE_{10} and TE_{20} modes for equal average power in each mode. Figures 131 through 134 show the patterns obtained for combined propagation in the TE_{10}, TE_{20}, and TE_{01} modes for equal average power in each mode for the in-band scan angles of 0-degrees and 40-degrees. The antenna patterns involving combined propagation in all five out-of-band modes for equal average power in each mode for 0-degrees, 20-degrees, 40-degrees, 60-degrees, and 70-degrees scan angles are contained in Figures 133 through 142. In Figures 143 and 144 the relative amounts of statistical average power were selected based on experimental results obtained in a previous study [2], and the patterns shown in Figures 145 and 146 were obtained for a randomly-chosen set of statistical average power values in the five modes. Finally, Figure 147 shows the parallel- and cross-polarized antenna pattern obtained for a second set of phase shifts and amplitudes randomly distributed with the prescribed statistical parameters.

The patterns contained in Figures 148 through 151 are for combined propagation of the TE_{10}, TE_{20}, and TE_{01} modes for equal statistical average power in each mode at 15.7 GHz for the in-band scan angles of 0-degrees and 40-degrees. Similarly, Figures 152 and 153 show the

patterns for the frequency of 14.5 GHz at the same two scan angles for equal statistical average power in the TE_{10} and TE_{20} modes.

Several observations can be made from the antenna patterns shown in the various figures regardless of modal content, frequency, or polarization. The average patterns, displayed in the (a) part of the figures, show that (1) grating lobes occur, (2) the main beam and grating lobes tend to scan, (3) a reduction in peak gain occurs, (4) the far-out sidelobe levels are raised, and (5) the overall pattern shape is governed by the resultant statistical element-pattern. Since the phase shift statistics of each modal component were assumed to be identical to the statistics for the TE_{10} mode used in the previous phased-array study, the angular locations and scanning properties of the out-of-band grating lobes and main beam will be identical to those previously obtained for the isotropic array. The angular locations of the grating lobes and main beam are tabulated in Table XXI for convenience.

The general characteristics of the grating lobe and main beam as functions of scan angle and frequency may be summarized by referring to Figures 133 through 142 for 18 GHz and Figures 148 through 153 for 15.7 and 14.5 GHz. In particular, two grating lobes appear at $\pm$ 70 degrees for the 18-GHz patterns for the broadside in-band scan angle, and the grating lobe at +70 degrees moves out of the visible range for in-band positive scan angles. Both the average patterns and the individual patterns show this behavior. The out-of-band main beam and grating lobes tend to scan in the same direction but not in the same manner as does the in-band main beam.

TABLE XXI

OUT-OF-BAND POINTING DIRECTIONS OF MAIN BEAM AND GRATING LOBES FOR INDICATED IN-BAND SCAN ANGLE AND
OUT-OF-BAND FREQUENCY FOR A 20-ELEMENT ARRAY OF WAVEGUIDE RADIATORS

FREQUENCY (GHz)	IN-BAND SCAN ANGLE (DEGREES)	OUT-OF-BAND MAIN BEAM POINTING DIRECTION (DEGREES)	OUT-OF-BAND GRATING LOBE POINTING DIRECTIONS (DEGREES)
18.0	0	0.0	+70.0
	20	9.8	-50.7
	40	18.7	-38.6
	60	25.5	-30.8
	70	27.9	-28.4
15.7	0	0.0	-
	40	22.1	-44.8
14.5	0	0.0	-
	40	23.9	-49.9

This behavior is shown by the progressive movement of the out-of band main beam and grating lobes as the in-band main beam is scanned toward endfire. Although grating lobes for the 15.7 and 14.5 GHz frequencies do not occur for the broadside scan angle, they do move into the front sector when the array is scanned through the 40-degree in-band scan angle. The out-of-band scanning properties are due primarily to wider element spacings (in terms of wavelengths), random phase-shift characteristics, and the cycling errors that were previously discussed [3]. For the 14.5 GHz and 15.7 GHz out-of-band frequencies, the cycling error causes the main beam and grating lobe(s) to scan through smaller angles than they would if no cycling errors were present, whereas for the 18-GHz frequency, the cycling error causes the main beam and grating lobe(s) to scan through slightly larger angles than would otherwise occur. These effects are on the order of about 3 to 5 degrees for the 15.7-GHz and 14.5-GHz patterns, and about 1 to 2 degrees for the 18 GHz patterns. The random variations of modal power have no effect on the scanning properties of the array.

The reduction in the gain of the main beam and grating lobes for a given scan angle and frequency is primarily due to (1) random phase shift variations and (2) random variations of modal content. The gain reduction due to random phase shift responses at 18 GHz is about 1 to 2 dB, whereas for the 15.7 and 14.5-GHz frequencies, the phase shift variations cause gain reductions of about 3 to 5 dB, since they are larger than the variations at 18 GHz.

The significance of modal content on the peak gain levels can be seen by inspection of the main beam and grating lobe gain levels

in Figures 117 through 146. For example, examination of the main

beam gain level for the broadside in-band scan angle in the figures

shows that a main beam does not exist at all if propagation occurs

solely in the TE_{20}, TE_{11}, or TM_{11} modes. Similarly, propagation of

more than one mode causes a reduction in peak gain levels because

the total power is shared among the several propagating modes. For

example, the increasing reduction in the main beam gain for parallel

polarization for the broadside in-band scan angle as either one, two,

and three, or all five modes are propagated can be observed in Figures

117, 127, 129, and 133, respectively.

The detailed sidelobe structures of individual randomized patterns

can vary significantly. At any given angle, the sidelobes of the

individual randomized patterns vary significantly about the average

sidelobe levels due to phase shift variance of the phase shifters.

For example, the magnitude of the peak sidelobes of the 15.7 and 14.5

GHz patterns are typically greater than those for the 18 GHz patterns

because greater phase deviations occur at 15.7 and 14.5 GHz. However,

the peak sidelobe gain levels are usually within two standard de-

viations of the statistical average sidelobe level for every frequency

and scan angle. If a sufficiently large number of individual patterns

are sampled, the average of the sidelobe levels for the individual

patterns should tend toward the average sidelobe level of the average

antenna pattern. However, as all of the figures show, an average

sidelobe level depends on the modal content.

The overall structure of the various antenna patterns, both

parallel-polarized and cross-polarized, is a function of the element

radiation patterns of the various modes. Because the propagation
velocities of the various modes are different and the relative phases
and amplitudes of the modes in different elements vary randomly,
the resultant average pattern consists of random superpositions of
the electric-field patterns of the existing modes. The fact that
the overall array antenna pattern structure does not change as a
function of in-band scan angle indicates that the resultant element
pattern is scan-invariant. This fact is apparent from Figures 127
through 142 for 18 GHz and Figures 148 through 153 for 15.7 and 14.5
GHz. The resultant element pattern is, however, a function of the
relative phasing among the various modes which propagate within
each particular element. Consequently, if the relative phase shifts
of the modes within each particular waveguide element were different,
instead of equal as assumed in the current study, or if the point
of excitation of the various modes were chosen differently, then
the shape of the resultant element pattern would also be different
from those shown in the figures. In the general case where the intra-
element relative phases of the various modes have different average
phase shifts as a function of bias voltage, the overall pattern
shape may change slightly with in-band scan angle. However, this
possibility is based on limited analyses of the general statistical
expression for the average pattern given by Equation (23). Con-
sequently, further analysis involving the more complex situations
are needed before firm conclusions can be made.

The 180-degree median gains and standard deviations show certain
trends as functions of modal content and in-band scan angle. The

values of median gains and standard deviations for selected situations
which illustrate overall tendencies are tabulated in Tables XXII
through XXIV.

The effects of the modal content on the median gain may be dis-
cerned from the values tabulated in Table XXII for the in-band scan
angle of 0-degrees for all combinations of modal content. The median
gain for the parallel-polarized antenna patterns changes only about
2 to 5 dB for one, two, three, or five modes present and is always
greater than the in-band median gain for the broadside scan angle
regardless of which out-of-band modes are present. The median gain
of the cross-polarized pattern changes about 3 to 9 dB depending on
which modes are present, but is usually comparable in magnitude to
the median gain of the in-band parallel-polarized pattern.

The behavior of the median gain as a function of in-band scan
angle for a given modal content is indicated in Table XXIII for 18
GHz. Referring to the values in Table XXIII, the median gain for
the parallel-polarized pattern decreases from about -11 dB to -13 dB
as the array is scanned off broadside to 20-degrees. Similarly, the
median gain of the cross-polarized pattern also decreases from about
-13.5 dB to -16.0 dB as the array is scanned to 20-degrees. For
either polarization, the median gain changes only about 1 dB for other
scan angles. The initial decrease in median gain as the array is
scanned off broadside is due to the movement of a grating lobe out
of the 180-degree sector.

The median gains for the antenna patterns for 15.7 and 14.5
GHz, tabulated in Table XXIV for in-band scan angles of 0-degrees

TABLE XXI

MEDIAN GAINS AND STANDARD DEVIATIONS OF RANDOM ANTENNA PATTERNS AT 18.0 GHz FOR BROADSIDE IN-BAND SCAN
ANGLE FOR THE INDICATED POLARIZATIONS FOR PROPAGATION OF RANDOM AMOUNTS
OF POWER IN THE INDICATED OUT-OF-BAND WAVEGUIDE MODES

MODE	STATISTICAL AVERAGE POWER IN EACH MODE	MEDIAN GAINS* RELATIVE TO ISOTROPIC AND STANDARD DEVIATIONS* FOR INDICATED POLARIZATION**			
		Parallel		Cross	
		M(dB)	σ_g(dB)	M(dB)	σ_g(dB)
TE_{10}	1.0	- 8.0	$\pm$ 9.5	-	-
TE_{20}	1.0	- 5.0	$\pm$ 9.5	-	-
TE_{01}	1.0	-	-	-10.0	$\pm$12.0
TE_{11}	1.0	-	-	- 8.0	$\pm$ 8.5
TM_{11}	1.0	-	-	-15.0	$\pm$ 8.5
TE_{10} and TE_{20}	0.5	- 6.5	$\pm$10.0	-	-
TE_{10}, TE_{20} and TE_{01}	0.33	- 8.5	$\pm$10.0	-15.0	$\pm$12.0
TE_{10}, TE_{20}, TE_{01}, TE_{11} and TM_{11}	0.2	-11.0	$\pm$10.0	-13.0	$\pm$ 9.0
TE_{10}, TE_{20}, TE_{01}, TE_{11} and TM_{11}	***	- 9.0	$\pm$10.5	-17.0	$\pm$ 9.0

* M and σ_g denote median gain and standard deviation, respectively.
** The TE_{10} and TE_{20} have only parallel components and the TE_{01}, TE_{11} and TM_{11} have only cross components in the azimuthal plane.
***The statistical average values of the power propagated in the indicated modes were 0.5, 0.2, 0.1, 0.1 and 0.1 watts, respectively.

TABLE XXIII

MEDIAN GAINS AND STANDARD DEVIATIONS AT 18.0 GHz FOR THE INDICATED IN-BAND SCAN ANGLES FOR BOTH PARALLEL-POLARIZED AND CROSS-POLARIZED OUT-OF-BAND AVERAGE AND RANDOM ANTENNA PATTERNS OF A RANDOMLY-PHASED ARRAY OF WAVEGUIDE ELEMENTS PROPAGATING RANDOM AMOUNTS OF POWER IN THE TE$_{10}$, TE$_{20}$, TE$_{01}$, TE$_{11}$ AND TM$_{11}$ OUT-OF-BAND MODES*

ANTENNA PATTERN	IN-BAND SCAN ANGLE (DEGREES)	MEDIAN GAINS RELATIVE TO ISOTROPIC AND STANDARD DEVIATIONS** FOR INDICATED ANTENNA PATTERN POLARIZATION			
		Parallel		Cross	
		M(dB)	σ_g (dB)	M(dB)	σ_g (dB)
Average	0	-11.0	+ 7.0	-14.0	+ 6.5
Random		-11.0	+10.0	-13.5	+ 9.0
Average	20	-13.0	+ 6.0	-16.0	+ 7.0
Random		-13.0	+ 9.5	-16.0	+ 9.5
Average	40	-13.5	+ 6.0	-16.0	+ 7.0
Random		-11.5	+ 8.0	-14.5	+ 8.0
Average	60	-14.5	+ 6.0	-16.5	+ 7.0
Random		-14.0	+ 9.0	-17.0	+10.0
Average	70	-14.5	+ 6.5	-16.5	+ 7.0
Random		-14.0	+ 9.0	-16.0	+ 9.0

* The statistical average values of the randomly-varying power propagated in each mode were equal.

**M and σ_g denote median gain and standard deviation, respectively.

TABLE XXIV

MEDIAN GAINS AND STANDARD DEVIATIONS AT BOTH 15.7 AND 14.5 GHz FOR THE INDICATED IN-BAND SCAN ANGLES FOR BOTH PARALLEL-POLARIZED AND CROSS-POLARIZED OUT-OF-BAND AVERAGE AND RANDOM ANTENNA PATTERNS OF A RANDOMLY-PHASED ARRAY OF WAVEGUIDE ELEMENTS PROPAGATING RANDOM AMOUNT OF POWER IN THE INDICATED OUT-OF-BAND MODES

FREQUENCY (GHz)	TYPE OF ANTENNA PATTERN	IN-BAND SCAN ANGLE (DEGREES)	MODE	MEDIAN GAINS RELATIVE TO ISOTROPIC AND STANDARD DEVIATIONS** FOR INDICATED ANTENNA PATTERN POLARIZATION			
				Parallel		Cross	
				M(dB)	σ_g(dB)	M(dB)	σ_g(dB)
15.7	Average	0	$TE_{10}, TE_{20}, TE_{01}$	-8.0	$+\ 3.5$	-19.0	$+11.0$
	Random			-7.0	$+\ 7.0$	-18.0	$+12.5$
	Average	40		-7.5	$+\ 4.0$	-18.5	$+11.0$
	Random			-8.0	$+\ 7.5$	-18.0	$+13.0$
14.5	Average	0	TE_{10} and TE_{20}	-6.5	$+\ 4.0$	--	--
	Random			-6.0	$+\ 7.0$	--	--
	Average	40		-5.5	$+\ 4.5$	--	--
	Random			-4.5	$+\ 7.0$	--	--

* The statistical average values of the randomly-varying power propagated in each mode were equal.

**M and σ_g denote median gain and standard deviation, respectively.

and 40 degrees, also show a relative insensitivity to scan angle. The standard deviations for the 15.7-GHz and 14.5-GHz patterns are about 2 to 3 dB less than the corresponding standard deviations for 18 GHz. This trend is expected because the phase shift deviations are larger for these two frequencies than for 18 GHz.

The median gains computed for the statistical average patterns with the aid of Equation (28) are generally in reasonable agreement with the computed median gains of the corresponding random antenna patterns. However, the standard deviations are typically 1 to 3 dB lower than the standard deviations of the random antenna patterns. These results were anticipated, based on the analysis in the preceding subsection, because the current method for calculating the standard deviation of individual random patterns from the statistical average equation does not include the deivations in power about the average antenna pattern. However, suitable approximate analytical techniques for estimating this contribution to the total standard deviation can be subsequently developed.

E. EMC Implications

The results of the advanced theoretical investigations concerning the feasibility of statistical techniques for predicting and describing out-of-band phased-array phenomena for array of waveguide elements involving random propagation of higher-order modes indicate that statistical techniques are both feasible and potentially very useful for EMC applications. In particular, the results show that statistical techniques can be used to predict and describe out-of-

band pattern characteristics, as well as the statistical median gain and standard deviation, as a function of the in-band scan angle and the statistical parameters of the various higher-order modes. The investigations indicate that serious EMC problems in shipboard applications are possible, but that many of the undesirable characteristics of randomly-excited arrays can be predicted and described in terms of the statistical parameters of the out-of-band waveguide modes. The analyses indicate that out-of-band waveguide arrays are generally described by the following important characteristics which can have EMC significance:

(1) The out-of-band array may have antenna patterns which are both parallel-polarized and cross-polarized with respect to the in-band pattern;

(2) The out-of-band main lobe and grating lobe of both the parallel-polarized and cross-polarized patterns tend to scan within the in-band sweep sector but not at the same rate as the in-band main beam;

(3) The parallel-polarized out-of-band antenna patterns may scan at a rate different than the cross-polarized pattern;

(4) The out-of-band antenna pattern for either polarization sense may have several sets of out-of-band grating lobes and main beams that correspond to different modal components and which scan at different rates;

(5) The gain levels of the out-of-band main beam and grating lobes can be comparable to the gain of the in-band main beam and, consequently, may be of significant intensity

287

in EMC applications;

(6) The gain levels of the far-out sidelobes of the random antenna patterns are greater than the sidelobe levels for a non-random pattern; and

(7) The out-of-band median gains over the front azimuthal sector are typically greater than or comparable to the in-band median gain, and do not vary significantly with in-band scan angle.

The possible existence of both parallel-polarized and cross-polarized main lobes and grating lobes implies that interference problems will be potentially more severe in those spatial directions. However, the main lobes and grating lobes of the out-of-band patterns tend to scan when the in-band main beam is scanned. In general, it appears that several sets of out-of-band main beams and grating lobes corresponding to different modal components can be present for both polarizations and that each set of patterns may scan at different rates with respect both to each other and to the in-band main beam. Consequently, in planning shipboard antenna locations, these factors need to be considered. Therefore, the prediction of the angular location, scanning properties, and gain levels of the various possible out-of-band patterns are important factors affecting the electromagnetic effectiveness of ships.

The gain levels, with respect to isotropic, of the various out-of-band main lobes and grating lobes are reduced by the random phase and amplitude variations, but may be comparable to the in-band gain. Consequently, the peak gain levels of both the parallel and cross-

polarized out-of-band antenna patterns may be very significant in EMC applications.

The tendency of the far-out sidelobes to be increased in intensity can produce important consequences on shipboard interference problems, since considerable out-of-band power may be present in a wide angle radiation lobe. The gain levels of sidelobes can be of comparable magnitude to the out-of-band main beam or grating lobes for certain combinations of in-band scan angles and modal content. Hence, the severity of a potential coupling situation involving wide-angle sidelobes increases.

The median gains of the random out-of-band antenna patterns over the front 180-degree sector for both the parallel- and cross-polarized patterns appear to be generally greater than or comparable to the in-band median gain. The out-of-band median gains do not vary significantly with scan angle and consequently remain comparatively high regardless of in-band scan angle. The median gain levels calculated in the current study ranged typically from about -8 to -14 dB, depending primarily on modal content, and changed typically only about 2 dB with in-band scan angle. An analytical extension of the present statistical modal to planar shipboard phased arrays consisting of interacting waveguide elements will permit a more extensive description of the out-of-band pattern characteristics.

SECTION X

CONCLUSIONS

This report contains the results of various experimental and theoretical investigations. The experimental work was performed for in-band frequencies, whereas the theoretical phased-array work was performed for out-of-band frequencies. The results of these investigations extend the knowledge and range of usefulness of previously accomplished work [1-3].

The objectives of the investigations in the following areas were successfully met:

1) near-field effects of solid obstacles on far-field antenna performance for in-band frequencies,

2) near-field effects of open-mast structures on far-field antenna performance for in-band frequencies,

3) data additions and improvements to the computer program for shipboard siting of antennas,

4) possible improvements in far-field antenna performance due to dielectrically coating near-field obstacles, and

5) advanced phased-array investigations concerned with deriving a basic method for determining the out-of-band pattern characteristics and median gain.

In the first area, sets of empirical curves to specify the effects of totally enclosed (solid), metallic obstacles on various antenna performance characteristics were generated. In addition to the exploratory investigations to obtain basic information concerning open-mast structures, the open-mast work in the second area primarily was concerned with

empirically deriving antenna performance curves similar to those for the solid obstacles. In the third area, expansion of the computer data-base to include additional empirically-derived decoupling data and modification of the input routines to increase the flexibility of adding data and identifying the particular type of obstacle were accomplished. In the fourth area, initial exploratory tests involving a dielectric-coated cylindrical mast in the near field of an antenna were conducted to experimentally demonstrate that significant improvements in equivalent antenna gain are possible. Finally in the fifth area, the basic statistical model for predicting and analyzing out-of-band characteristics of future shipboard phased-array antennas was expanded to include radiation pattern shape and polarization properties of the array waveguide-elements. The following conclusions are based on these five areas of investigations.

A. Antenna-Performance Investigations With Solid Obstacles

These research investigations led to an expansion and further development of empirical curves and information that are needed to predict for more situations the far-field antenna performance of a directive antenna when an obstacle is located in its near field. This work, which yielded useful information concerning decoupling (antenna gain loss), beamshifts, beamwidths, and sidelobe levels, also extended the frequency range of coverage and expanded the number and types of solid obstacles investigated.

In general, the various trends in performance can depend on the following:

1) type of obstacle,

2) near-field distance of the obstacle from the antenna,

3) angle of the obstacle off the boresight direction between the target and the receiving antenna,

4) size of an obstacle,

5) polarization, and

6) frequency of operation.

The decoupling trends for the solid obstacles investigated under this program generally behave in the same manner as did the trends reported for the previously-conducted antenna performance investigations, with one major exception. For obstacles whose widths are approximately the same width as the antenna aperture, the monotonic decrease in the decoupling levels along the boresight direction was nonlinear for the S-band (3000 MHz) test frequency. Further, it appears that the empirical curves are asymtotically approaching a constant value for increasing obstacle distances along the boresight direction from the receiving antenna. Based on limited information, it appears that 0.2 of the far-field distance of the antenna may be a reasonable rule of thumb for estimating the obstacle distance for which further increases in the obstacle distance along the boresight direction produce no further significant decreases in decoupling. However, this conjecture needs to be further investigated.

The beamwidth, beamshift, and sidelobe behaviors for the various test situations and obstacle types were very similar to the behaviors previously reported for the flat sheet and cylindrical mast test cases. In addition, the extended antenna performance tests involving additional obstacles and an increased frequency range further showed that the antenna performance characteristics were not extremely sensitive to the obstacle type provided that the width of the obstacles, the polarization, the frequency, the

near-field obstacle distance, the obstacle angle off boresight, and the size of the obstacle were held constant for each type of obstacle. Therefore, it was possible to derive empirical average curves to display the beamwidths, beamshifts, and sidelobe levels, which eliminated the necessity of portraying separate sets of empirical curves for each type of obstacle.

B. Open-Mast Investigations

Much new information and a better insight into the potential problem areas associated with open masts were obtained from these investigations. In many respects, the near-field effects of open-mast obstacles and totally enclosed solid obstacles on the far-field performance of an antenna appear to be considerably different. The experimental tests at S-band, C-band, and X-band frequencies conducted with the two different open masts of different sizes and constructions yielded the following results.

1) Empirical curves for decoupling (gain loss) and for sidelobe levels were derived.

2) No significant changes in 3-dB beamwidths and no significant beamshifts occurred during the various tests; therefore, no empirical curves were generated.

3) The decoupling along the boresight direction for open masts was much lower than that for a solid obstacle of comparable width.

4) The decoupling levels along the boresight direction for both the 24-inch wide and 48-inch wide open masts were approximately the same and generally were approximately the same order of magnitude as that for a 6-inch solid obstacle.

294

5) Except at the X-band frequency, the decoupling level along
   the boresight direction for either open-mast obstacle was
   not dependent on the near-field distance of the open mast
   from the receiving antenna.

6) Along the boresight direction, rotation of either open mast
   produced only small changes in the decoupling levels and in
   the 3-dB beamwidth of an antenna. However, the changes in
   sidelobe levels due to obstacle rotation were often signifi-
   cant. Therefore, when sidelobe levels are critical, careful
   consideration should be given to factors such as obstacle
   orientation and construction.

7) The X-band tests indicated that the geometrical arrangement
   of the basic element members of an open mast can significantly
   affect the main-beam symmetry and the sidelobe levels. For
   monopulse antennas, beam asymmetries can crucially affect the
   tracking capabilities of the radar.

8) The open-mast decoupling levels as a function of the obstacle
   angle off the boresight direction were not generally as well-
   behaved as those for solid obstacles. The manner in which the
   curves vary appear to depend, in part, on the width of the
   obstacle, the near-field distance of the open mast from the
   receiving antenna, and the obstacle angle.

9) The changes in the sidelobe levels as a function of the obstacle
   angle off the boresight direction did not vary as greatly for
   the open masts as they did for solid obstacles of comparable
   widths. The range over which the sidelobes varied as a function

of obstacle angle was approximately the same for both the
24-inch wide and 48-inch wide open masts. Further, this
range was more nearly coincident with that which occurred
for 6-inch wide solid obstacles than those which occurred
for 24-inch and 48-inch wide solid obstacles.

C. Computer Program Modifications and Data Additions

The modifications and additions to the shipboard siting of antennas
computer program provide a significant increase in the capabilities of
the program. The inclusion of additional obstacle types allows a more
realistic simulation of practical shipboard antenna/obstacle configura-
tions, and the data for the additional frequency band permit a large number
of the radar frequency bands to be simulated. The fact that this large
increase in program capability was accomplished with a relatively small
number of program modifications attests to the fundamental simplicity and
utility of the program architecture.

Experience with the computer simulation of antenna/obstacle effects,
however, indicates that other additions to the program are needed to in-
crease its capability. These include the following:

1) expansion of the data base to include additional obstacle
    types, additional frequency bands, and larger antenna/
    obstacle separation ranges;

2) modification of the program to permit correlation between
    the data for various frequency bands on the basis of nor-
    malizing all physical dimensions to the operating wavelength,

3) modification of the program to permit more flexibility in the
    selection of the data to be used--In particular, it appears

296

desirable to "tag" each obstacle as to its specific type, which is not possible using the present program;

4) incorporation of additional data for different antenna types such as moderate gain fan beam and IFF antenna; and

5) provisions for subroutines and a data base for the estimation of the main-beam distortion, main-beam tilt, and sidelobe effects due to the obstacles.

The expanded capabilities of the program would provide a significant increase in the usefulness of the computer model in analysis of practical shipboard antenna/obstacle configurations.

D. Dielectric Coating Investigations

The results of brief experimental and theoretical investigations have shown that the application of dielectric materials to a circular totally-enclosed (solid) metal mast obstacle can produce beneficial effects relative to both improving the far-field performance of antennas and improving the isolation between near-field antenna pairs. Current indications are that even greater improvements are possible through the judicious choice of various electrical and physical parameters.

The results of the experimental investigations of a dielectric-coated mast obstacle specifically demonstrated the following.

1) Thin dielectric coatings on a circular metal mast located in the near field of a receiving antenna can enhance the propagation of vertically-polarized electromagnetic energy around the mast and reradiate it in the forward direction to produce a significant increase in received power.

297

2) Thin dielectric coatings on a circular metal mast in the near field of an antenna can significantly diminish the amount of horizontally polarized electromagnetic energy which would normally propagate around the mast and then be radiated from it in the forward direction, thus resulting in a significant increase in isolation.

3) The beneficial effects of EM field enhancement and isolation produced by the dielectric coating can extend over a wide frequency range and over a wide range of near-field obstacle locations on boresight.

4) The beneficial effects tend to be greater for obstacle locations which are physically closer to the receiving antenna where bare metal obstacles generally cause the greatest degradation of antenna performance.

Although these experimentally-observed facts are encouraging, the results for the particular dielectric-coated mast tested in this brief exploratory measurements program do not represent either an optimum situation or an upper limit on the possible electromagnetic benefits which might be obtained for different choices of parameters.

Prior theoretical considerations strongly indicated that a judicious choice of parameters can result in enhancement and/or isolation effects exceeding 20 dB (one way) and that the polarization response can be changed. These limited theoretical investigations previously conducted indicate that the electromagnetic scattering properties of dielectric-coated mast obstacles are a function of the following variables:

1. obstacle size, shape, and construction,

2. thickness of dielectric coating,

3. frequency,

4. polarization,

5. dielectric constant,

6. loss tangent, and

7. near-field obstacle distance.

Based on the experimentally derived behavior of one dielectric-coated mast and previous theoretical considerations involving several dielectric coated masts, it appears that dielectric materials can potentially be very useful in improving the electromagnetic effectiveness of directive antenna. However, additional experimental and theoretical investigations are greatly needed to develop and exploit this area of technology to achieve the maximum benefit/cost ratio.

E. Phased-Array Investigations

The results of the theoretical investigations concerning the feasibility of statistical techniques for predicting and describing out-of-band phased-array phenomena for arrays of waveguide elements involving random propagation of higher-order modes indicate that statistical techniques are both feasible and potentially very useful for EMC applications. A statistical analysis is necessary because the higher-order mode content of the elements which comprise the array antenna varies randomly at out-of-band frequencies. In particular, the results of this study show that statistical techniques can be used to predict and describe not only the out-of-band radiation

pattern characteristics but also the statistical median gain and standard deviation as a function of both the in-band scan angle and the statistical parameters of the higher-order mode signals.

The results of the investigations further indicate that out-of-band waveguide arrays involving propagation of higher-order modes exhibit characteristics that may present serious EMC problems in shipboard applications and that many of the undesirable characteristics of randomly-excited arrays can be predicted and described in terms of the statistics of the randomly-varying array parameters. The statistical analyses performed for a linear array of waveguide elements, which randomly propagate power in various higher-order modes, indicate that such arrays are generally described by the following characteristics:

(1) The out-of-band array may have antenna patterns that are cross polarized as well as polarized parallel with respect to the in-band pattern;

(2) The out-of-band main lobe and grating lobes of both the parallel-polarized and cross-polarized patterns tend to scan within the in-band sweep sector but not at the same rate as the in-band main beam;

(3) The parallel and cross-polarized out-of-band antenna patterns may scan at different rates;

(4) The out-of-band antenna pattern for either polarization sense may have several sets of out-of-band major lobes which correspond to different modal components and which scan at different rates;

300

(5) It appears that the gain levels of the out-of-band main lobe and grating lobes, based on the conventional definitions of antenna gain, may be comparable to the gain of the in-band main beam. However, the conventional methods of defining and computing antenna gain need to be investigated further to determine the range of applicability more precisely;

(6) The out-of-band median gains over the front azimuthal sector are typically greater than or comparable to the in-band median gain, but do not vary significantly with in-band scan angle.

Although the current investigations were conducted for a linear array of non-interacting waveguide elements, the results of the investigations strongly indicate that shipboard planar arrays of directive, interacting out-of-band waveguide elements can be similarly analyzed to derive EMC statistical prediction models.

SECTION XI

RECOMMENDATIONS

Successful conclusions of the five research tasks performed under this contract were achieved. Three of the tasks were continuations of previously initiated work, whereas two were initial exploratory efforts in nature. All of the research efforts significantly improved the existing situation. However, the results and conclusions of these investigations show that additional research is needed to provide the Navy the information necessary to further develop its topside electromagnetic-effectiveness prediction capability. Therefore, it is recommended that the following work be conducted to achieve this extended capability.

A. Extended Measured Data Base

It is recommended that the measured data base involving near-field obstacles be extended for (1) far-field antenna performance situations and (2) near-field antenna-to-antenna coupling situations.

1. Far-Field Antenna Performance

a) conduct investigations to determine the effects of the geometry of open-mast structural members on the far-field performance of fan-beam type antennas,

b) conduct investigations to determine the best-case and worst-case situations for open-mast/antenna configurations,

c) conduct open-mast/pencil-beam antenna investigations to determine the effects of different percentages of aperture blockages on antenna performance,

d) conduct open-mast/pencil-beam investigations to deter-
mine the effects of a given percentage of aperture
blockage for different open masts whose structural
members project a specified percentage of aperture
blockage onto the aperture of an antenna but are
distributed differently over the aperture of the
antenna, and

e) conduct investigations with a monopulse antenna to
determine the effects of solid obstacles and open-
mast structures on the null depth of the difference
pattern, pattern slope on each side of the null, gain
loss, and sidelobe levels.

2. Near-Field Antenna-to-Antenna Coupling

a) conduct boresight decoupling investigations to deter-
mine near-field effects of open-mast structures on
antenna-to-antenna coupling for the same near-field
antenna separation distances that were used in similar
tests with solid obstacles,

b) conduct a tradeoff study to determine expected antenna
coupling differences between various solid and open-
mast obstacle configurations, and

c) conduct investigations to identify relationships and
possible tradeoffs among the various open-mast/antenna
configurations involving near-field antenna coupling
and far-field antenna performance.

B. Main-Beam Distortion Investigations

It is recommended that a basic method be derived for theoretically predicting the distortions of directive spatial characteristics of the main beam due to various ship superstructure elements. It is further recommended that the investigations be initially focused in the following areas of endeavor:

1) assessment of potential analysis techniques,

2) development of initial first-order prediction algorithm,

3) validation of the initial algorithm, and

4) investigations to extend the algorithm.

C. Expanded Capabilities for Computer Program

It is recommended that the entire measured data base be incorporated into useful computer algorithms for analyzing the effects of near-field obstacles on (1) far-field antenna performance and (2) near-field antenna-to-antenna coupling.

1. Expanded Far-Field Analysis Capability

a) conduct work to expand the computer program to include the effects of near-field obstacles on beamwidths, beam-shifts, and sidelobe levels, and

b) determine the required modifications to input formats and output routines that are necessary to efficiently display the results and to allow the analyst the neces-sary flexibility to use the program.

2. Near-Field Antenna-Coupling Analysis Capability

a) conduct investigations to develop algorithms to deter-mine clear-site near-field antenna-to-antenna coupling

305

for both the main-beam to main-beam boresight situation
and for the main-beam misalignment situation,

b) conduct investigations to develop algorithms for antenna
coupling with near-field obstacles present between antenna
pairs that are either aligned or misaligned, and

c) develop the necessary input/output routines for the var-
ious situations.

D. Dielectric Coatings and Dielectric Obstacles

The results and conclusions of various investigations concerning di-
electric-coated circular metallic masts indicate that dielectric materials
can be applied to ship superstructural elements to reduce the severity of
the topside electromagnetic problems, thereby significantly improving the
performance of directive antennas and reducing the antenna siting problems.
It is recommended that a comprehensive theoretical and experimental re-
search program for developing and exploiting this existing potential be
initiated via the following tasks:

1) technology assessment of applicable state-of-the-art information,

2) theoretical investigations for determining critical factors for
guiding experimental investigations,

3) determination of obstacles and fabrication techniques for con-
structing test obstacles of various geometrical shapes,

4) experimental investigations to derive sets of curves illustrating
parametric relationships,

5) studies to investigate environmental feasibility of specific
dielectrics for shipboard applications, and

306

6) extended studies to determine feasibility of expanding di-
electric prediction capability.

It is anticipated that implementation of these recommended actions will
lead to many benefits. Among these benefits are the following:

1) An overview of potential uses of dielectrics for shipboard-
type applications will result;

2) Useful engineering curves for guiding topsiae designs that
utilize dielectrics to improve antenna performance will be
available;

3) Analytical solutions for cylindrical mast obstacles and a
determination of feasibility of deriving analytical solutions
for more complex shaped obstacles will result;

4) Many of the "fix-it-later" efforts will be eliminated through
better design;

5) Improved radar performance will result which will lead to an
increased capability to detect and respond to a threat;

6) The severity of many potential antenna siting problems will
be reduced or eliminated;

7) Increased benefit-to-cost ratios for future ship operations
will be possible, and

8) Framework necessary for future expansion to derive additional
long-term benefits will be provided.

E. Phased-Array Investigations

In order to extend the out-of-band statistical model to shipboard
arrays, it is recommended that theoretical and experimental work be

307

performed in the following areas to derive more comprehensive analytical expressions and provide more realistic statistical inputs into the model:

1) conduct theoretical out-of-band investigations and perform calculations for pattern characteristics and median gain for linear arrays of waveguide elements involving random variations of the relative phase shifts of the various modal components within each element,

2) extend the analyses in Item (1) to planar arrays of waveguide elements for representative classes of shipboard phased arrays,

3) conduct a theoretical and experimental investigation to determine the significance of inter-element mutual coupling on the statistical model as a function of both in-band and out-of-band frequencies and modal content,

4) perform additional experimental and theoretical out-of-band frequency investigations for both continuous and pulsed excitations involving several types of phase shifter devices for use in the investigations of Items (1) and (2) above,

5) conduct a power divider investigation for out-of-band frequencies to determine both analytically and experimentally the transmission and reflection characteristics of common power-divider networks, and

6) use near-field techniques to measure the near-field phase and amplitude distributions of a phased-array antenna at out-of-band frequencies to complement and validate the theoretical investigations.

Based on both the current and previously performed phased-array work, it is further recommended that investigations be performed in the following important problem areas:

1) experimentally determine the effects of typical shipboard obstacles on phased-array performance, for both in-band and out-of-band frequencies,

2) conduct experiments to assess the effects of large flux densities and voltage gradients on the characteristics of phase shifter devices, for both in-band and out-of-band frequencies,

3) conduct a study to identify the important parameters involved in the selection and placement of frequency filters to permit optimization of frequency filters for various phased-array feed systems, and

4) conduct out-of-band theoretical and experimental surface-wave investigations to identify conditions under which surface waves are generated and how they propagate on phased-array antennas.

SECTION XII

REFERENCES

1. F. L. Cain, C. E. Ryan, C. P. Burns, and B. J. Cown, "Near-Field Obstacle Effects and Phased-Array Studies", Georgia Institute of Technology, Final Engineering Report, Contract No. N00024-71-C-1120, January 1972.

2. F. L. Cain, C. E. Ryan, B. J. Cown, E. E. Weaver, "Electromagnetic Effectiveness Investigations of Near-Field Obstacle Effects, Antenna Coupling, and Phased Arrays", Georgia Institute of Technology, Final Engineering Report, Contract No. N00024-72-C-1274, June 1973.

3. F. L. Cain, B. J. Cown, E. E. Weaver, "Out-of-Band-Frequency Investigations of Near-Field Obstacle Effects and Phased Arrays", Georgia Institute of Technology, Final Engineering Report, Contract No. N00024-73-C-1141, February 1974.

4. C. E. Ryan and R. D. Nevels, "Final Report Consulting Services in Supoort of the Patrol Frigate Electromagnetic Effectiveness Analysis Program", Georgia Institute of Technology, Final Report, Subcontract No. A2MV-568343 to Prime Contract No. N00024-72-C-1444, August 1973.

5. T. F. Schmeckpeper and C. A. Bass, "A Computer Method of Shipboard Siting of Antennas", NRL Report 7144, Naval Research Laboratory, Department of the Navy, July 1970.

6. R. O. Niemi, "A Ship Modelling Program Description for the IBM 360/65", NELC Technical Note J411, Microwave Technology Division (Code 2300) Naval Electronics Laboratory Center, November 1971.

7. Dielectric Obstacle Investigations, Conducted In-House, Radar Division, Engineering Experiment Station, Georgia Institute of Technology, 1972.

8. M. Kerker, The Scattering of Light and Other Electromagnetic Radiation, Chapters 3-6, Academic Press (1969).

9. D. T. Paris and F. K. Hurd, Basic Electromagnetic Theory, Chapter 9, McGraw-Hill Book Company (1969).

10. A. Papoulis, Probability, Random Variables, and Stochastic Processes, Chapters 7 and 8, McGraw-Hill Book Company (1965).